An EPR and ENDOR Investigation of a Series of Cu(II) Transition Metal Complexes

Submitted for the degree of Doctor of Philosophy

by

Nadine Ritterskamp

School of Chemistry

Cardiff University

March 2019

Declaration

This work has not been submitted in substance for any other degree or award at this or any other university or place of learning, nor is being submitted concurrently in candidature for any degree or other award.

Signed …… (N. Ritterskamp) Date……

STATEMENT 1

This thesis is being submitted in partial fulfilment of the requirements for the degree of PhD.

Signed …….. (N. Ritterskamp) Date ……

STATEMENT 2

This thesis is the result of my own independent work/investigation, except where otherwise stated. Other sources are acknowledged by explicit references. The views expressed are my own.

Signed ……. (N. Ritterskamp) Date ……

STATEMENT 3

I hereby give consent for my thesis, if accepted, to be available for photocopying and for interlibrary loan, and for the title and summary to be made available to outside organisations.

Signed …… (N. Ritterskamp) Date ……

Acknowledgements

I would like to thank Prof. Damien Murphy for providing the opportunity to conduct this research and for his support and guidance. I would like to extend this thanks to Emma who has taken time to discuss results and pass on valuable advice. My gratitude extends to Andrea who always had an open ear for my queries and the time he took for discussing results, which I have really appreciated.

I also want to acknowledge all of the technical staff within the School of Chemistry, particularly James, Evelyn and Simon.

Special thanks go to some fantastic friends I have gained during my time in Cardiff; Jacob, you always helped out whenever you could. Kate, thank you for your friendship and all the talks we had on our tours in the main building. Emily, thank you for your friendship and love you provided.

Many thanks need to go to my family who always believed in me, even when I did not. Daniel, I wouldn't have done it without you. Thank you for being my big brother.

Abstract

Copper complexes have an enormous potential as cytotoxic compounds. Understanding the subtle interactions of these complexes and the variable modes of coordination with biologically relevant bases is mandatory from a biological perspective. However, in this thesis the more specific context is to investigate in detail the electronic and structural aspects of various copper complexes including $[Cu(acac)_2]$, $[Cu(acac)(N\text{-}N)]^+$ and the multidentate ligand based complex $[Cu(^aN\text{-}^bN\text{-}^aN)]$, and their interaction with target nitrogen bases.

Therefore, an in-depth study on the configurational aspects of adducts formed between $[Cu(acac)_2]$ and imidazole (Im) was performed using ENDOR, HYSCORE and DFT calculations, providing a detailed analysis of the decoded trans-equatorial $[Cu(acac)_2(Im)_{n=2}]$ conformation.

Based on *N*-imine coordinated complexes, a series of square planar Casiopeina Cu^{2+} complexes, consisting of one acetylacetonate and one diimine ligand, have been investigated by EPR and ENDOR spectroscopy. These diimine ligands were selected in light of the fact that the size of the aromatic diimine ligand may influence the therapeutic activity. Subtle but not neglectable electronic and structural changes of these $[Cu(acac)(N\text{-}N)]^+$ complexes were detected by using X-,Q- and W-band CW EPR and ^1H and ^{14}N ENDOR measurements, revealing distortion and strain effects in the ligand system.

Multidentate ligand based complexes $[Cu(^aN\text{-}^bN\text{-}^aN)]$ formed with e.g. di(2-picolyl)amine, tris(2-pyridylmethyl)amine and tris(2-aminoethyl)amine have been investigated by EPR and ENDOR spectroscopy. The focus of this investigation is to utilise ENDOR spectroscopy to examine copper complexes bearing inequivalent coordination nitrogen nuclei. Interesting electronical and structural features have been observed, illustrating the nature of the multidentate mixed nitrogen ligand.

Abbreviations

ABNO	9-azabicyclo[3.3.1]-nonane-N-oxyl
acac	Acetylacetone
a_{iso}	Isotropic Hyperfine Term
bipy	2,2‘-Bipyridine
$CHCl_3$	Chloroform
Cys	Cysteine
CW	Continous Wave
DBHB	5,5-Dibromohemi-bastadin-1
DFT	Density Functional Theory
DMF	Dimethylformamid
DMSO	Dimethyl Sulfoxide
DNA	Deoxyribonucleic Acid
dppz	Dipyrido[3,2-a:2',3'-c]phenazine
DSSC	Dye Sensitized Solar Cells
ENDOR	Electron Nuclear Double Resonance
EPR	Electron Paramagnetic Resonance
ESEEM	Electron Spin Echo Envelope Modulation
FTIR	Fourier-Transform Infrared Spectroscopy
Gly	Glycine
g_{iso}	Isotropic g-factor
Gua	Guanine
His	Histidine
hrs	hours
HYSCORE	Hyperfine Sublevel Correlation
Im	Imidazole
MBA	Methylbenzylamine
MeOH	Methanol
Met	Methionine
MW	Microwave
NMR	Nuclear Magnetic Resonance
OTf	Trifluoromethanesulfonate (triflate)

PGM	Platinum Group Metals
phen	1,10-Phenanthroline
PSC	Perovskite Solar Cells
Py	Pyridine
Py-bipy	2,3-Di(pyridine-2-yl)pyrazine
QSAR	Quantitative Structure-Activity Relationship
ROS	Reactive Oxygen Species
SOD	Superoxide Dismutase
SOMO	Singularly Occupied Molecular Orbital
TEMPO	2,2',6,6'-Tetramethylpiperidinyloxyl
THF	Tetrahydrofuran
Try	Tryptophan
Tol	Toluene
UV	Ultra-Violet
VT	Variable Temperature

Paper published and in progress

Published:

- Chapter 4, published in the journal *Inorganic Chemistry*:

  Understanding the Coordination Modes of [Cu^{2+})imidazole)$_{n=1,2}$] Adducts by EPR, ENDOR, HYSCORE and DFT Analysis
  N. Ritterskamp, K. Sharples, E. Richards, A. Folli, M. Chiesa, J. A Platts, D. M. Murphy, 2017, 56, 11862-11875

In Progress:

- Chapter 5, aiming to be published in *Inorganic Chemistry*:

  An EPR and ENDOR investigation of a series of Copper(II)-Casiopeina type coordination complexes [Cu(O-O)(N-N)]$^{+}$

- Chapter 6, aiming to be published in Inorganic Chemistry:

  The coordination chemistry of Cu(II) mixed nitrogen donor multidentate (*N*-amine and *N*-imine) ligands investigated by EPR

Contents

Chapter 1: Cu^{2+} Complexes in Electron Paramagnetic Resonance (EPR) Spectroscopy and their Relevance in Catalysis

To illustrate the importance of Electron Paramagnetic Resonance (EPR) spectroscopy one may first discover the rich source of available paramagnets in all kinds of research areas. As there is a rich source of paramagnets one must choose. Cu^{2+} has applications in biology, pharmacy, medicine and industry. For this reason, Cu^{2+} applications are given in this chapter and the relevance to use EPR spectroscopy.

1.1 Introduction

Transition metals have proven to be extremely important in a variety of disciplines such as medicine, biology, physics and chemistry, and are also important in industry from a catalysis perspective.[1–5] As a transition metal, copper is a very useful alternative in catalysis compared to the more expensive and toxic Platinum Group Metals (PGM) and is found predominantly in the coordination numbers Cu^{1+} and Cu^{2+}. In this Chapter, the focus will be mainly on the chemistry and coordination of Cu^{2+} complexes, which include *N*-imidazole and *N*-pyridine derivatives in the coordination sphere. The coordination number of Cu^{2+} complexes is predominantly four, five and six whilst the favoured structures are square planar, distorted tetrahedral and distorted octahedral, respectively.[6,7] Furthermore, a brief overview of the many reactions catalysed by copper will also be given. The importance of why EPR spectroscopic techniques are valuable in the study of Cu^{2+} *N*-donor rich complexes, will also be presented. Finally, the overall aims of this Thesis will be summarised and introduced later.

1.2 Metal centres in copper proteins

1.2.1 Proteins and metal proteins

Proteins are fundamental for the function of all living systems. They consist of amino acids, which form peptide bonds and consequently polypeptide bonds.[8]

Four examples of amino acids are shown in Figure 1a-d, including tryptophan (Try), methionine (Met), L-histidine (L-His) and cysteine (Cys). The general structure of the amino acids is based on one alpha carbon, at least one carboxyl group and a residue. In the cases presented in Figure 1a-d, the residue is either an imidazole derivative (L-His and Try), a thioether (Met) or a thiol (Cys) group. The peptide bond is formed by the reaction of the carboxyl group of one amino acid and the amino group of another amino acid. Consequently, polypeptides generate primary, secondary, tertiary and quarterly structures, forming the macrosystems known as proteins.

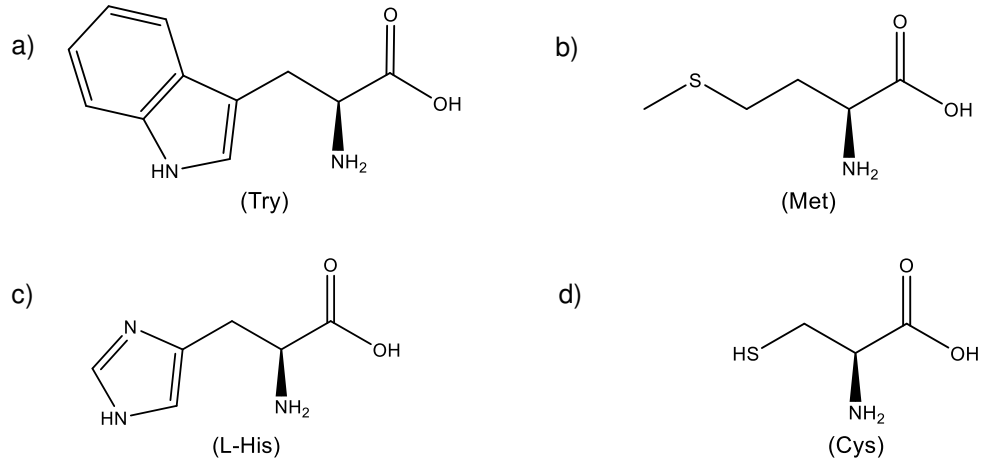

Figure 1.1 Four amino acids: a) Tryptophan (Try), b) Methionine (Met), c) L-Histidine (L His) and d) Cysteine (Cys). All of them include either a thioether, thiol or imidazole molecule, respectively, as a residue and functional group.[9,10]

However, introducing metals into proteins change their functionality. More precisely, the specific modification of these metals, such as the number, variety of metals, including the oxidation number, coordination number, electronic and chemical interactions, all have an impact on the reactivity and functions of these macrosystems, often loosely referred to as metalloproteins.[11–13] They are involved in processes such as photosynthesis of CO_2, called carbon fixation, or the conversion of molecular nitrogen into NH_3. The reactivity and conversion of small molecules takes place around the metal centres within the metalloproteins. Considering the metal themselves, the first row transition metals including V, Cr, Mn, Fe, Co, Ni, Cu and Zn are found to be frequently involved in metalloproteins.[11,14] In the next section, a summary of copper protein functions is presented followed by an outlook of the more common types of copper centres.

1.2.2 Copper proteins

Copper based proteins function as electron-transfer agents in photosynthesis and respiration or have a function in the metabolism of dioxygen (oxidase and oxygenase) and in the deactivation of harmful intermediates of O_2 reduction.[15–18]

The variety of metal centres in copper proteins is diverse and can be distinguished and categorised by three 'classical' protein copper centres, namely type 1, type 2 and type 3.[12,19,20] Copper type 1 centres are commonly found in 'blue' copper proteins, such as azurin and plastocyanin, which display electron transfer and antioxidative functions.[21,22] The intensified blue colour of these 'blue' copper proteins originated from the absorptions in the visible region of the spectrum from only symmetry-allowed electronic transitions of the metal.[23,24]

In general, type 1 copper centres have two imidazole residues from histidine (His) and one thiolate cysteine (Cys) strongly coordinated in a trigonal planar arrangement, whereby a weakly bound methionine (Met) coordinates from an axial position (Figure 1. 2a). The completed coordination environment of the type 1 copper centre is generally distorted in an irregular fashion and has been studied in various proteins.[11,22,25,26] The distortion in these type 1 centres causes the unpaired electron to be delocalized onto a sulphur ligand. As a result, the EPR spectrum of a type 1 centre has abnormally low A_{II} values in the EPR spectrum.[26]

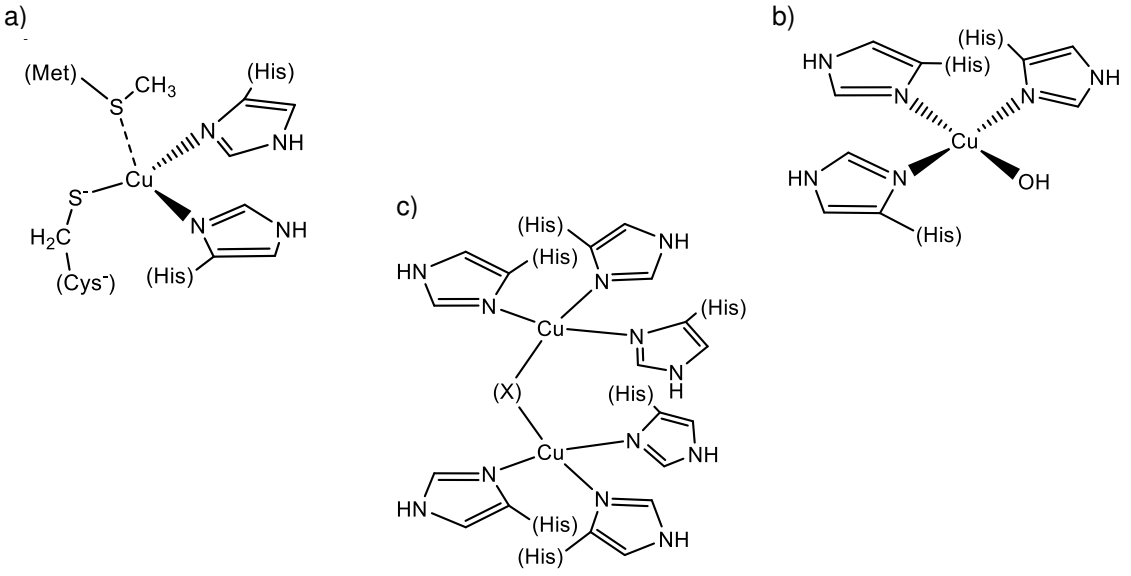

Figure 1.2 Illustrated are 'classic' copper protein centres, a) type 1, b) type 2 and c) type 3.[23]

The next copper centre is type 2, as illustrated in Figure 1.2b. Three imidazole residues from histidine and one hydroxyl group are coordinated to the copper in a square planar arrangement (Figure 1.2b). This 'non-blue' type 2 copper centre is EPR active but shows, in contrast to type 1, a normal EPR spectrum.[26] In the multicopper nitrite reductase from the bacterium *Achromobacter xylosoxidans*, the type 2 copper centre is the catalytic site, where nitrite is bound and reduced to NO.[27]

The last of the 'classic' copper centres in proteins is known as type 3, as illustrated in Figure 1.2c. In contrast to the above mentioned copper centres, type 3 is a dimer formed by two copper metals, linked or bridged by oxygen atoms. Its function is the uptake of O_2 in the Cu^{1+}-Cu^{1+} state until it is released in the Cu^{2+}-Cu^{2+} state.[28,29] Each of the two coppers in type 3 centres have three histidine molecules in a planar arrangement and in this respect, they are somewhat similar to type 2 centres (Figure 1.2b and c).

The copper type centres were introduced separately. But very commonly at least two of the three copper type centres can be present in metalloproteins. An example of this situation is laccase, a well known metalloenzyme. Laccase is a blue multi copper oxidase and catalyses the four-electron reduction of O_2 to water. The electron reduction depends on three different binding sites of the four copper centres present in laccase, namely type 1, type 2 and type 3.[20] Each of these copper centres have an important role to play in the catalytic mechanism. However, deciphering the mechanism is difficult as the shift of the wavelength between type 1 and 2 are very similar. Even with EPR, the mechanism is hard to unravel since both centres are EPR active simultaneously. In different cases, such as in Hemocyanine, ionizing radiation methods have been used to produce specific generations of reduced centres in enzymes. Thus decoupled Cu^{2+}-Cu^{2+} paramagnets were observed, revealing good Cu^{2+} EPR signals.[30]

1.3 Copper complexes in pharmacology

1.3.1 The role of copper in pharmacology applications

Adult humans only require an amount of about 150 mg of the trace element copper.[31] Deviation from this amount in the body can cause diseases, such as Wilson's disease, caused by acute copper deficiency and Menke's disease,

based on the disfunction of copper transport and copper storage mechanism. The neurodegenerative disease known as Lov Gehrig's disease, is caused by defects in the copper-dependent superoxide dismutase (SOD). Furthermore, copper may also be involved in neurodegenerative diseases such as Parkinson and Alzheimer.[4,31,32] Decoding the cause of copper-based dysfunctions is therefore vital to prevent such diseases and longer term develop suitable treatments.

1.3.2 Copper as a treatment for diseases

Copper is becoming increasingly used in the design of various pharmaceutical drugs used to treat a variety of diseases. For example, Martins *et al.*[33] designed copper complexes for the treatment of Chagase disease. This copper complex has trypancidal activity in vitro against *Trypanosoma cruzi*, which is the causative agent of Chagase disease. For the design of these copper complexes, the antibacterial agents levofloxacin and sparfloxacin were used. Additionally, nitrogen heterocyclic donor ligands, such as 1,10-phenanthroline were also used. Different copper complexes were designed, all bearing one antibacterial agent. The difference between the copper complexes were that some had a heterocyclic N-donor included and some were without this N-donor unit. Martins *et al.*[33] emphasised that i) coordinated heterocyclic N-donor ligands improve the anti-cruzi activity for the complex, and ii) [$Cu^{2+}Cl_2$(1,10-phenanthroline)(levofloxacin)] and [$Cu^{2+}Cl_2$(1,10-phenanthroline)(sparfloxacin)] were found to be the most active agents against *Trypanosoma cruzi* in their study.

Special attention has also been given to the design of anticancer drugs based on copper. Not only is it cheaper than the commonly used platinum group metals but also it has shown in many cases to be less toxic and more active.[14,34,35] The trend for the design of copper based drugs seem to be the use of planar, aromatic N, O or S-heterocyclic ligands which bind in the bi-, tri- or tetra-dentate mode to the transition metal.[36,37] The combination of chosen metal and ligand provides suitable membrane permeability, stabilization but still with selective reactivity, low toxicity, etc. These features are all important points for the design of efficient anticancer drugs.[34,38,39] In the following, specific anti-cancer drugs are briefly presented to illustrate the importance of imidazole and pyridine derivatives in the design of anti-cancer drugs.

The first cancer drug presented below is based on copper coumarins complexes. Coumarins are organic ligands belonging to the benzopyrone class and are found in living organisms.[40,41] They are commonly applied in the perfume and pharmaceutical areas. Usman *et al.*[42] have designed a distorted square planar $[Cu^{2+}(coumarin)(imidazole)]^{+}$ complex (Figure 1.3a) for the treatment of cancerous cells. Usman *et al.*[42] established that i) the complex undergoes only partly intercalation with the DNA at the minor groove, and ii) that partly intercalation occurs with the coumarin ligand. The coumarin ligand interacts with the base pair guanine residues Gua10 and Gua16 of the minor grove, as shown in Figure 1.3b. Consequently, electrostatic and hydrogen bonding occurs between the ligand and DNA bases.

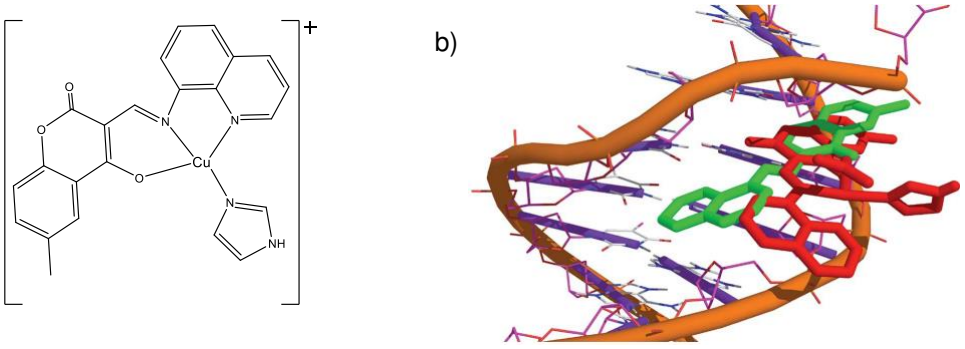

Figure 1.3 Illustration of a) the structure of $[Cu^{2+}(coumarin)(imidazole)]^{+}$ and b) the minor groove binding site conformation of the ligand (green) and the $[Cu^{2+}(coumarin)(imidazole)]^{+}$ (red).[42]

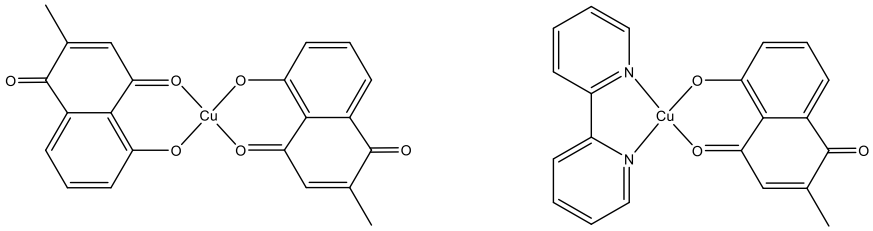

Figure 1.4 Structure of a) $[Cu^{2+}(plumbagin)]_2$]; (5-hydroxy-2-methyl-1,4-naphthoquinone; plumbagin) and b) $[Cu^{2+}(plumbagin)(2,2'\text{-bipyridine})]$. [37,43]

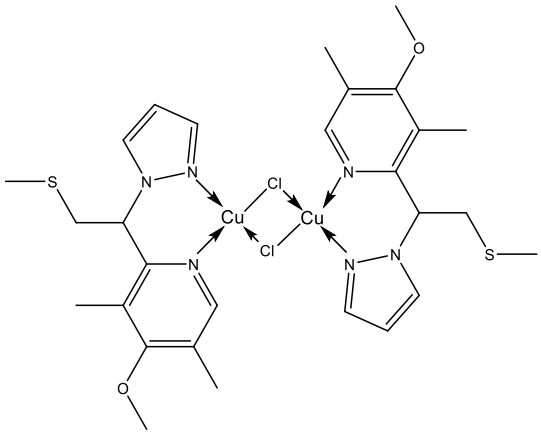

Figure 1.5 Pyrazolepyridine based copper complex with flexible thioether groups, which revealed good anticancer activities in HT1080 cells.[37,44]

Another ligand commonly used for anticancer drugs is plumbagin. The natural product plumbagin is an organic compound, which has also been used for rheumatoid arthritis and dysmenorrhea bruising.[37] In vitro cytotoxicity and activity against several cell lines have been observed for the plumbagin based complexes $[Cu^{2+}(plumbagin)]_2]$ and $[Cu^{2+}(plumbagin)(2,2'\text{-bipyridine})]$ (Figure 1.4a,b). Moreover, these complexes have demonstrated considerably higher activity against several cancer cell lines compared to cisplatin, which offers significant promise.[45]

Other anti-cancer drugs have used the pyrazolepyridine based ligands. The pyrazolepyridine ligand provides a $N_2Cu\text{-}CuN_2$ coordination sphere (Figure 1.5). A variety of these ligand types have been employed for the synthesis of cytotoxic active copper complexes. It has been shown that the sulphur binding ability strongly depends on the types of thioether fragments introduced in the ligand. As an example, Tardito *et al.*[44] found that the highest anticancer activities for HT1080 cells where found for complexes consisting of flexible thioether groups, such as the complex shown in Figure 1.5.

1.4 Copper complexes in advanced materials applications

There are many cases where copper based systems have also been successfully used for many years in the delivery and function of advanced materials. In the following sections, the industrial applications that involve copper complexes will be given.

1.4.1 Antifouling agents

The use of antifouling agents for tankers, boats and marine ships reduces the settling of microorganism, such as algae, barnacles, mussels and other systems, which can result in drag on the hull and subsequently skin friction drags. Preventing this settling reduces not only the economical losses, such as reduced speed and increased fuel consumption, but also increases the lifetime of the ship hulls. Different kind of antifouling agents have been designed and applied, from ultrasonic examples to organic polymers and special metal complexes containing Zn, Fe, Cu and Ti.[2,46] Bayer *et al.*[47] synthesized a 5,5′-dibromohemi- bastadin-1

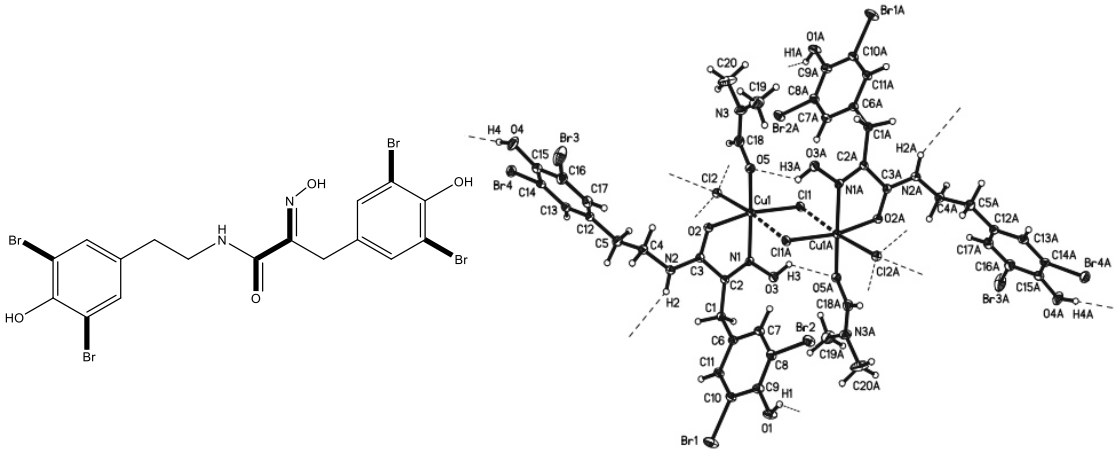

Figure 1.6 Schematic illustration of 5,5-dibromohemi-bastadin-1 (DBHB) ligand and $(DBHB(DMF)Cu^{2+}Cl_2)_2*4(CH_2Cl_2)$ complex.

(DBHB) ligand and associated copper DBHB complexes (Figure 1.6), which can suppress the settling of barnacle larvae on ship hulls by deactivating the copper active centre of Phenoloxidase. This copper containing enzyme is present in many living organisms and is involved in the firm attachment of mussels to the surfaces. Polymers of bastadin and its derivatives can coordinate to the copper centres and thereby inhibit its function, to prevent mussels from engaging with the hull surface. Trojers *et al.*[2] discussed the potential of Cu^{2+} antifouling agents for barnacles based on azole compounds, such as the imidazole containing biocide medetomidine. Elshaarawy and Janiak[48] in contrast developed Cu^{2+} complexes based on *N*-pyruvoyl anthranilate, revealing good antibacterial activity and inhibition of biofilm formation on surfaces.

1.4.2 Dye sensitized solar cells

The focus on renewable energy has been of interest for many decades. Therefore, it is not surprising that the development of dye sensitized solar cells (DSSC) and perovskite solar cells (PSC) have received a lot of attention. DSSCs employing Cu^{2+} and imidazole ligands were studied by Chen *et al*.[3] They combined Cu^{2+} and imidazole as auxiliary electron acceptors with electron donors, such as dithiophene or fluorine, to enhance the absorption intensity and extend the absorption range of the dye sensitizer in the visible and near infrared region. Karpacheva *et al*.[49] and Dragonetti *et al*.[50] used only the earth abundant elements to construct more environmentally and economically efficient DSSCs. Independent from each other, they designed promising copper complexes based on heteroleptic bisdiimine ligands. Apart from dye sensitized solar cells, Cu^{2+} complexes have also been designed and synthesized for applications as p-type dopants in solid-state perovskite solar cells (PSC) and have shown promising features.[51,52]

1.5 Copper complexes in catalysis

Most compounds and products formed in the petrochemical industry, including bulk chemicals, polymer production and fine chemicals for pharmaceuticals, all require the use of a catalyst at some stage of their production.[53–55] Catalysts are substances which decrease the activation energy of a chemical reaction and thereby increase the rate constants without being consumed themselves in the reaction. Many varieties of catalysts have been designed. Noteworthy is that the composition and structure of a catalyst itself can dictate the overall catalytic selectivity and activity of a particular reaction. For example, the two catalysts, boron phosphate and Mo_2C/Carbon, are active for ethanol conversion. However, the products are ethylene, diethyl ether or hydrogen and acetaldehyde, depending on the catalyst used.[56,57]

Three main types or areas of catalysis can be broadly defined, namely homogeneous, heterogeneous and enzymatic catalyst. In this section, only homogeneous and heterogeneous catalysts will be considered.

1.5.1 Copper in homogeneous catalysis

The reaction of a homogeneous catalyst takes place in the same phase as the reactant. The metal in the catalytic reaction cycle goes through different oxidation states. For copper catalysts, this can be Cu^0, Cu^{1+} and Cu^{2+}. Michelet *et al.*[58] studied a [((oxydi-2,1-phenylne)bis(diphenylphosphine))(2,9-dimethyl-4,7-diphenyl-1,10-phenanthroline)Cu^{1+}]PF_6 catalyst, where (oxydi-2,1-phenylne)-bis(diphenylphosphine) is a one electron rich chelating diphosphine ligand and (2,9-dimethyl-4,7-diphenyl-1,10-phenanthroline) is a one electron deficient phenanthroline ligand. This copper catalyst is activated using visible light. The proposed catalytic cycle involves an unusual $Cu^{1+}/Cu^{(1+)*}/Cu^0$ mechanism (Figure 1.7), when transforming organic halides into aryls or (cyclic)alkanes. Hoover *et al.*[43] reported a copper TEMPO catalyst involving a Cu^{1+}/Cu^{2+} mechanism for the aerobic oxidation of alcohols (Figure 1.8). This Cu^{1+}(2,2-bipyridine)(3-methyl-imidazole)/TEMPO catalyst was efficient for sterically unhindered primary alcohols. However, the catalytic activity was reduced for aliphatic and secondary alcohols. For this reason, Steve *et al.*[59] varied the structure of TEMPO and used various derivatives. By applying more oxidized nitroxyl derivatives, a decrease in the reaction rate was observed but an increase in rate occurred when less sterically encumbered bicyclic nitroxyl derivatives were used. Steve *et al.*[59] also reported a catalyst system which was efficient for primary, secondary allylic, benzylic and aliphatic alcohols. This catalyst consisted of (4,4′-dimethoxy-2,2′-bipyridine)Cu^{1+}(OTf) and ABNO (ABNO = 9-azabicyclo[3.3.1]-nonane-N-oxyl).

Employing copper in homogeneous catalysis has created a wide range of opportunities. One advantage of using copper is simply the aspect of a step towards economical and environmentally more friendly catalysis. Copper is an earth abundant metal, like Fe, Co and Ni. In some catalytic respects, the potential of copper in catalytic reactions has not been fully discovered. This may be the case for water splitting leading to hydrogen and oxygen production, which is an important reaction for clean energy conversion and storage.[60] Homogeneous copper based water splitting catalysts have a high reactivity, stability and low light absorption. However, the design of this copper based water splitting catalyst is

fairly recently and a considerable amount of work is required to better understand and optimise the reaction.[61,62]

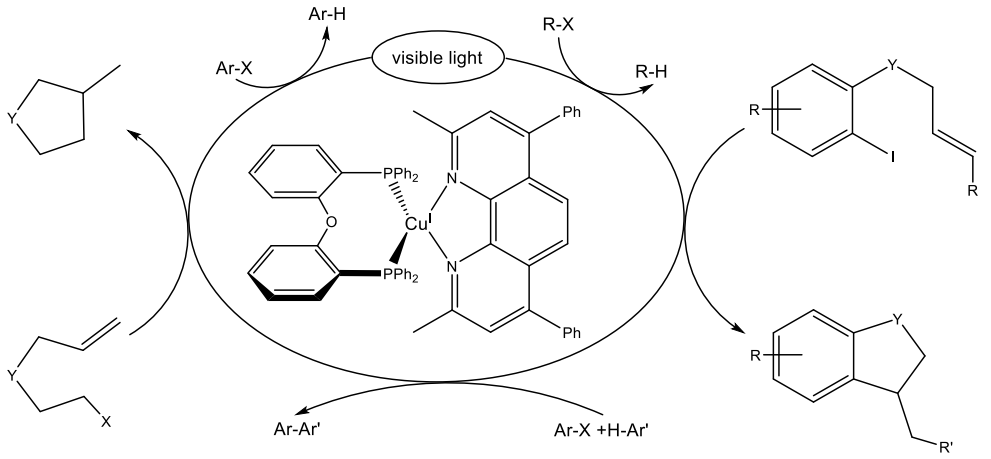

Figure 1.7 Catalytic cycle of the [((oxydi-2,1-phenylne)bis(diphenylphosphine))(2,9-dimethyl-4,7-diphenyl-1,10-phenanthroline)Cu^{1+}]PF_6 catalyst for the photoredox transformations of organic halides. This catalyst is efficient for reductions, cyclization and direct arylation of arenes .[58]

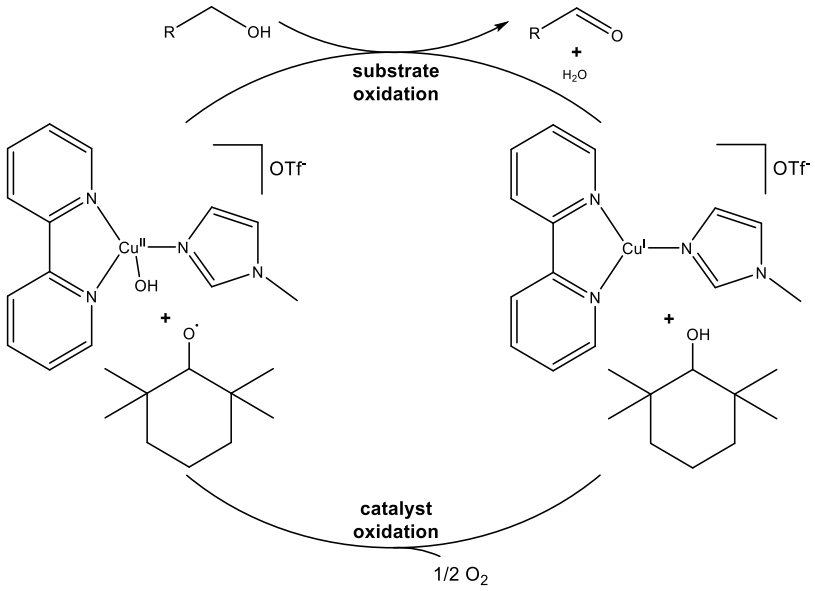

Figure 1.8 Simplified catalytic cycle for Cu^{1+}(2,2-bipyridine)(3-methyl-imidazole)/TEMPO catalysed aerobic alcohol oxidation.[43]

1.5.2 Copper in heterogeneous catalysis

Manufacturing sulphuric acid is traditionally based on a heterogeneous catalyst.[56,57] The reactants, sulphur dioxide and oxygen, are passed over a solid vanadium oxide catalyst. In this case, the catalyst is not in the same phase as the reactant. The two phases can be solid-liquid, solid-gas and liquid-gas (and liquid-liquid), which is in contrast to homogeneous catalysis. Well known examples of heterogeneous catalysts are based on zeolites which are crystalline

solids made up of SiO_4 building blocks.[54] ZSM, a type of zeolite, has been used for selective oxidations such as methane to methanol under mild conditions using H_2O_2 as an oxidant. In some cases, the selectivity was increased up to 97 % for the alcohol after doping ZSM with copper, which suppresses secondary oxidation reactions.[63]

Other heterogenous catalysts have been designed that integrate copper. Phnangboonehoo *et al.*[64] studied Cu_xCe_yMgz/Al_2O_3 for hydrogen production with low carbon monoxide via methanol steam reforming. Glinski *et al.*[65] described an experiment of dehydrogenation of cyclohexanol to cyclohexanone, using copper as the main catalyst and SiO_2 as the support material. Support materials help to improve the mechanical resistance and dispersion of the active catalytic phase. For dehydrogenation, a spectrum of copper-based support catalyst like Cu/SiO_2, Cu/MgO and Cu/Zn are commonly used, showing also the possible variation of metal oxide and metal combination catalysts.[58–61]

1.5.3 Bridging homogeneous, heterogeneous and enzymatic catalysis

As the awareness of developing more sustainable or green based catalysts continues, a solution for more environmentally and economical affordable catalysts has been the focus of considerable research in the past 10 years. Desirable features for catalyst design are for example recyclable, sustainable, more selective and active catalysts towards specific molecules. Using copper instead of the more expensive platinum group metals is a highly desirable goal. However, in the case of homogeneous catalysis, the catalysts are very often not reusable because they cannot be easily separated from the product. Over the years, different approaches have been attempted for example by attaching the catalysts onto a surface or by integrating homogenous catalysts into a porous scaffold, such as a metal organic frameworks (MOFs). Farrusseng *et al.*[70] and Corma *et al.*[71] gave an overview of MOFs and their modification using features from homogeneous, heterogeneous and enzymatic catalysis. Luz *et al.*[72] designed various copper containing MOF catalysts. They incorporated different Cu^{2+} catalysts such as [Cu^{2+}(2-hydroxypyrimidinolate)$_2$], [Cu^{2+}(imidazolate)$_2$], [Cu^{2+}(benzene-tricarboxylate)$_2$] and [Cu^{2+}(benzene-dicarboxylate)], which are all active and fully regioselective for click reactions. The resulting Cu-MOFs have been shown to be active and regioselective catalysts for the “click” reaction with

activity and selectivity as high as when using homogeneous catalysts. It was noticeable that the copper activity changes with the organic linker used in the MOF, meaning that CuN_4 based complexes are more active than CuO_4 containing centres.

1.6 Use of EPR to study copper nitrogen donor complexes

For paramagnetic Cu^{2+} based nitrogen complexes, Electron Paramagnetic Resonance (EPR) and the related hyperfine techniques such as Electron Nuclear Double Resonance (ENDOR), as described in Chapter 2, are ideal methods in which to examine the three dimensional structures of square planar nitrogen donor complexes and their interaction with secondary molecules.[9,22,73] In this Thesis, most of the Cu^{2+} complexes studied have either N-donors or are complexes that strongly coordinate N-based donor substrates, so a brief overview will be given here to demonstrate the utility of EPR in such systems.

The $[Cu(Im)_4]^{2+}$ complex (Im = N-imidazole) has been investigated by Van Camp *et al.*[74], using EPR and hyperfine measurements (ENDOR) (Figure 1.9a and b).

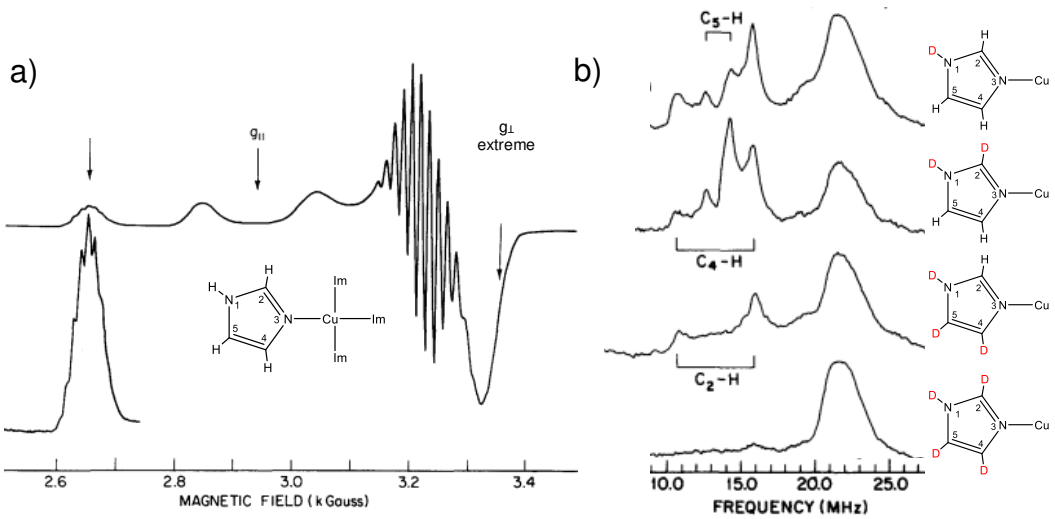

Figure 1.9 a) EPR spectrum of none deuterated Cu(imidazole)$_4$ and b) ENDOR spectra at the $g_{\perp}$ extreme position of selective deuterated imidazole protons of Cu(imidazole)$_4$.[74]

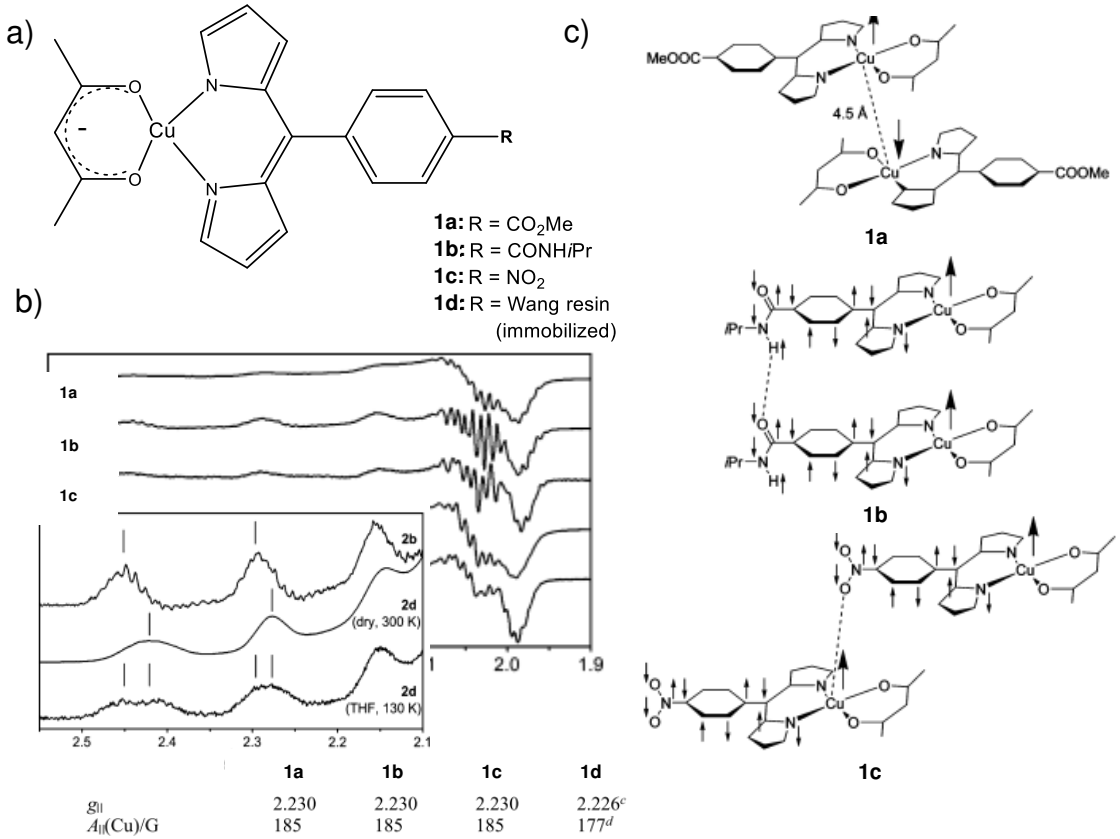

Figure 1.10 Substitutions (R) of the meso-Phenyldipyrromethene acetylacetonato Cu^{2+} complexes are shown in a). The corresponding anisotropic X-band EPR spectra and g_{II} and $^{Cu}A_{II}$ values of **1a**-**1c** (130 K, THF) and **1d** (300 K, solid; 130 K, THF) are given in b) and c) illustrates the polymer formation hold together by different forces for the complexes **1a**-**1c**.[77]

The aim of their study was to investigate the interaction of weakly coupled protons from the surrounding imidazole rings with the Cu^{2+} centre. Selective deuteration of the imidazole protons, as shown in Figure 1.9b, allowed the authors to obtain information on the molecular structure. The information was obtained via the interactions of the protons, neighbour nitrogen and remote nitrogen of the imidazole rings with the paramagnetic copper centre. Van Camp *et al.*[74] were able to identify the interactions to several nearby atoms on the ligand group such as the C_2-H (MHz), C_3-H (MHz), C_4-H (MHz) and C_5-H (MHz), as marked in Figure 1.9b.

García-Ramos *et al.*[75] studied isomeric effects on copper complexes by changing the position of the methyl group on the phenanthroline ligand. The resulting electronic changes were detected by EPR via the hyperfine coupling.

Changes in covalent bond strength of the Cu-L-bond was especially noticeable by the decrease of the $^{Cu}A_{II}$ coupling.

To prove that the coordination properties of synthetic imidazole differ from natural imidazole ligands, Andersson *et al.*[76] applied EPR, NMR and FTIR to the complexed imidazole substitutes formed with $Cu^{2+}Cl_2$ and $Zn^{2+}Cl_2$. They were able to show that the grade of substitution on the imidazole changes the electronic and steric preference. Indeed changes in the expected geometry were observed in the resulting EPR spectra.[9,76]

Heinze *et al.*[77] investigated four different heteroleptic Cu^{2+} dipyrromethene complexes with different substitutions (R) at the phenyl moiety, as shown in Figure 1.10a. These complexes are supposed to serve as molecular precursors for coordination polymers, as this has been of interest for magnetic and electronic materials and new classes of absorbents. These complexes form polymer chains, as shown in Figure 1.10c for complex **1a**-**1c**. The polymers are held together by forces of varying strength such as hydrogen bonds, coordination bonds and covalent bonds. X-band EPR spectroscopy confirmed that the primary coordination sphere around the copper centre is the same for all complexes (Figure 1.10, 2a-2d). The copper centre has a square planar N_2O_2 coordination (Figure 1.10a).[77] Due to immobilization of **1d**, via attachment on a surface, this complex is more restricted resulting in a smaller g_{II} and A_{II} compared to **1a**-**1c** (Figure 1.10b).

From a catalytical perspective, EPR is a useful tool to gain information on the change in oxidation states, interaction of the catalyst with the reactants and potentially the resulting intermediates.[13,78,79] It can also be used to study chiral interactions. If chiral substrates coordinate to the metal complex, small but different interactions with the metal centre occur. It is possible to observe these electronic differences using EPR. Murphy *et al.*[80] applied EPR and hyperfine measurements to visualize the diastereomeric interactions of copper salen complexes with chiral amines (MBA = methylbenzylamine) adducts. Hyperfine measurements such as ENDOR confirmed the weak covalent coordination of the *N*-amine of the MBA to the copper centre. Finally, W-band EPR measurements also revealed stereometric differences in the hyperfine coupling ^{Cu}A for the methylbenzylamine molecules coordination.

1.7 Aims of this work

The impact and importance of copper complexes in a diverse field of chemistry has been briefly illustrated above. It is clear that owing to this importance in many applications, it is vitally important to be able to study copper based complexes in depth, in order to better understand the structural, chemical and mechanistic aspects of their reactions. In this work, Cu^{2+} based complexes will be primarily studied. In particular, four different copper coordination spheres or ligand environments have been focussed on, including CuO_4, CuN_2O_2, CuN_3 and CuN_4, via EPR and ENDOR. As covered in the next Chapter, EPR can provide unrivalled access to information on the paramagnetic centre, allowing easier and more selective access to specific structural, chemical and physical information. In the following work, the purpose and importance of these copper ligand environments, including CuO_4, CuN_2O_2 and $CuN_{n=3-4}$, is briefly covered.

The bis(acetylacetonate) Cu^{2+} complex, labelled $[Cu^{2+}(acac)_2]$, is a simple biomimic copper centre possessing four oxygen atoms bound to the metal. $[Cu^{2+}(acac)_2]$ had been intensively studied via EPR spectroscopy (see Sharples *et al.*[81] and references therein). As a result, the structural and electronic properties of this prototypical complex are very well known. In this work, the interest is focused on the interaction of $[Cu^{2+}(acac)_2]$ with various imidazole derivatives, which are omnipresent in the coordination sphere of copper centres in nature. The aim is to investigate the structural transformations that occur in the adducts by different EPR and DFT methods, when imidazole derivatives coordinate to $[Cu^{2+}(acac)_2]$. This study will also give some insights into the N-donor coordination of imidazole(s).[9]

$[Cu^{2+}(acac)(1,10\text{-phenanthroline})]^+$ and $[Cu^{2+}(acac)(2,2'\text{-bipyridine})]^+$ are well known for their therapeutic properties (commercially used under the name Cu^{II}-Casiopeina) with potential anti-cancer activities.[82] However, little is known about the electronic properties of these complexes, which can be revealed by EPR and similarly, the inner and outer sphere ligand interactions, which can be probed by ENDOR in frozen solution. The interest here is therefore to use EPR and ENDOR to investigate a related diimine series of 2,2'-bipyridine and 2,2'-bipyrdidine derivatives to contribute to a better understanding of these anticancer drugs.

Di-(2-picolyl)amine metal complexes have also shown some promising capabilities for stoichiometric and catalytic transformations.[86–90] In this work, the focus is based on the copper version, $[Cu^{2+}(\text{di-(2-picolyl)amine})](NO_3)_2$ and their derivatives.[91] However, by comparison to the above mentioned complexes, which bear a single nitrogen environment, this system bears different nitrogen nuclei within the ligand and therefore it is important to explore how the complex ENDOR spectra could be analysed in such situations.

To summarise, Chapter 2 will present a brief theoretical treatment of the EPR and ENDOR techniques, with emphasis on the Cu^{2+} based systems. Chapter 3 will present a detailed experimental presentation of the studied copper complexes, including the methods and techniques used in this work. The focus of Chapter 4 is the detailed EPR and ENDOR investigation of the configuration and structural investigation of $[Cu^{2+}(acac)_2(Im)_{n=1,2}]$ adducts. Chapter 5 considers the structural EPR analysis of square planar $[Cu^{2+}(N\text{-}N)(O\text{-}O)]^+$ complexes. Finally, Chapter 6 uses EPR and ENDOR to describe the interactions of two different N-functional groups with the Cu^{2+} centre, before presenting a final concluding perspective in Chapter 7.

Scheme 1. 1. General illustration of the Cu^{2+} complexes including different types of N-ligands with oxygen or without oxygen donor groups.

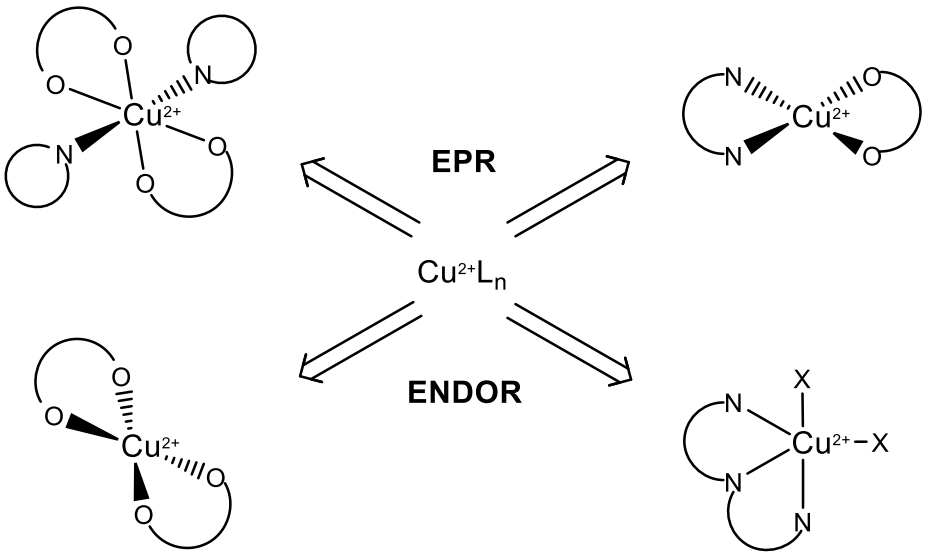

1.8 References

1. H. Zhai, Y. Li, L. Chen, X. Wang, L. Shi, R. Wang, J. Sun, *Nano Res.*, **2018**, 11, 1895–1904.
2. M. Andersson Trojer, A. Movahedi, H. Blanck, M. Nydén, *J. Chem.*, **2013**, 2013, 1–23.
3. X. Chen, Y. Liao, Y. Liu, C. Zhu, T. Chen, C. Zhong, *Dyes Pigment.*, **2017**, 139, 420–430.
4. R. F. Festa, D. J. Thiele, *Curr. Biol.*, **2011**, 21, 877–883.
5. Q. Fang, X. Zhao, Y. Huang, K. Xu, T. Min, P. K. Chu, F. Ma, *Phys. Chem. Chem. Phys.*, **2018**, 20, 553–561.
6. B. Murphy, B. Hathaway, Coord. *Chem. Rev.*, **2003**, 243, 237–262.
7. J. Echeverría, E. Cremades, A. J. Amoroso, S. Alvarez, *Chem. Comm.*, **2009**, 28, 4242–4244.
8. L. Holm, C. Sander, *Science.*, **1996**, 273, 595–602.
9. N. Ritterskamp, K. Sharples, E. Richards, A. Folli, M. Chiesa, J. A. Platts, D. M. Murphy, *Inorg. Chem.*, **2017**, 56, 11862–11875.
10. D. B. Tripathy, A. Mishra, J. Clark, T. Farmer, *C. R. Chim.*, **2018**, 21, 112-130.
11. R. H. Holm, P. Kennepohl, E. I. Solomon, *Chem. Rev.*, **1996**, 96, 2239-2314.
12. J. Liu, S. Chakraborty, P. Hosseinzadeh, Y. Yu, S. Tian, I. Petrik, A. Bhagi, Y. Lu, *Chem. Rev.*, **2014**, 114, 4366–4469.
13. E. I. Solomon, R. K. Szilagyi, S. DeBeer George, L. Basumallick, *Chem. Rev.*, **2004**, 104, 419–458.
14. C. Orvig, M. J. Abrams, *Chem. Rev.*, **1999**, 99, 2201–2204.
15. H. Chen, B. Su, T. Zhang, A. Huang, H. Liu, Y. Yu, J. Wang, *RSC Adv.*, **2017**, 7, 56093–56098.
16. D. Nikolova, C. Heilmann, S. Hawat, P. Gäbelein, M. Hippler, *Photosynth. Res.*, **2018**, 137, 281–293.
17. A. Lasorsa, G. Natile, A. Rosato, F. Tadini-Buoninsegni, F. Arnesano,*Curr. Med. Chem.*, **2018**, 25, 462–477.
18. Inesi, G., *IUBMB Life*, **2017**, 69, 211–217.
19. L. I. Ji-bin, D. R. McMillin, W. E. Antholine, *J. Am. Chem. Soc.*, **1992**, 114, 725–727.
20. R. Tamilarasan, D. R. McMillin, , *Biochem. J.*, **1989**, 263, 425–429.
21. K. Kataoka, K. Tsukamoto, R. Kitagawa, T. Ito, T. Sakurai, *Biochem. Biophys. Res. Commun.*, **2008**, 371, 416–419.
22. J. W. A. Coremans, M. van Gastel, O. G. Poluektov, E. J. J. Groenen, T. den Blaauwen, G. van Pouderoyen, G. W. Canters, H. Nar, C. Hammann, A. Messerschmidt, *Chem. Phys. Lett.*, **1995**, 235, 202–210.
23. S. Godlewska, J. Jezierska, K. Baranowska, E. Augustin, A. Dołęga, *Polyhedron*, **2013**, 65, 288–297.
24. R. Silavi, A. Divsalar, A. A. Saboury, *J. Biomol. Struct. Dyn.*, **2012**, 30, 752-772.
25. M. Prudêncio, R. R. Eady, G. Sawers, *Biochem. J.*, **2001**, 353, 259–266.
26. J. E. Roberts, J. F. Cline, V. Lum, H. Freeman, H. B. Gray, J. Peisach, B. Reinhammar, B. M. Hoffman, *J. Am. Chem. Soc*, **1984**, 106, 5324–5330.
27. J. H. Van Wonderen, D. N. Kostrz, C. Dennison, F. MacMillan, *Angew. Chem. - Int.*, **2013**, 52, 1990–1993.
28. T. E. Meyer, A. Marchesini, M. A. Cusanovich, G. Tollin, *Biochemistry*,

1991, 30, 4619–4623.
29. G. Hanson, L. Berliner, *Springer*, **2009**, 28, 1-666.
30. A. Pezeshk, J. Torres, M. T. Wilson, M. C. R. Symons, *J. Inorg. Biochem.*, **2001**, 83, 115–119.
31. M. Bost, S. Houdart, M Oberli, E. Kalonji, J.-F. Huneau, *J. Trace Elem. Med. Biol.*, **2016**, 35, 107–115.
32. T. Oka, A. Yokoya, K. Fujii, *Appl. Phys. Lett.*, **2011**, 98, 103701.
33. D. A. Martins, L. R. Gouvea, D. da Gama Jean Batista, P. Bernandino da Silva, S. R. W. Louro, M. Nazare C. Seiro, L. R. Teixeira, *BioMetals*, **2012**, 25, 951–960.
34. M. S. Islas, J. J. Martínez Medina, L. L López Tévez, T. Rojo, L. Lezama, G. A. Echeverría, O. E. Piro, E. G. Ferrer, P. A. M. Williams, *Inorg. Chem.*, **2014**, 53, 5724–5737.
35. S. G. Davila-Manzanilla, Y. Figueroa-de-Paz, C. Mejia, L. Ruiz-Azuara, *Eur. J. Med. Chem.*, **2017**, 129, 266-274.
36. H. K. Liu, P. J. Sadler, *Acc. Chem. Res.*, **2011**, 44, 349–359.
37. C. Santini, M. Pellei, V. Gandin, M. Porchia, F. Tisato, C. Marzano., *Chem. Rev.*, **2014**, 114, 815–862.
38. C. M. Ackerman, S. Lee, C. J. Chang, *Anal. Chem.*, **2017**, 89, 22–41.
39. L. Ronconi, P. J. Sadler, *Coord. Chem. Rev.*, **2007**, 251, 1633–1648.
40. S. P. Rohini, J*. Biofertil. Biopestic.*, **2014**, 5, 5–7.
41. M. Musa, J. Cooperwood, M. O. Khan, *Curr. Med. Chem.*, **2008**, 15, 2664-2679.
42. M. Usman, M. Zaki, R. A. Khan, A. Alsalme, M. Ahmadc, S. Tabassum, *RSC Adv.*, **2017**, 7, 36056–36071.
43. J. M. Hoover, B. L. Ryland, S. S. Stahl, *J. Am. Chem. Soc.*, **2013**, 135, 2357–2367
44. S. Tardito, I. Bassanetti, C. Bignardi, L. Elviri, M. Tegoni, C. Mucchino, O. Bussolati, R. Franchi-Gazzola, L. Marchio, J*. Am. Chem. Soc.*, **2011**, 133, 6235–6242.
45. Z.-F. Chen, M.-X. Tan, L.-M. Liu, Y.-C. Liu, H.-S. Wang, B. Yang, Y. Peng, H.-G. Liu, H. Liang, C. Orvig, *Dalton Trans.*, **2009**, 48, 10824-10833.
46. G. Borkow, J. Gabbay, *Curr. Med. Chem.*, **2005**, 12, 2163–2175.
47. M. Bayer, C. Hellio, J.-P. Maréchal, W. Frank, W. Lin, H. Weber, P. Proksch, *Mar. Biotechnol.*, **2011**, 13, 1148–1158.
48. R. F. M. Elshaarawy, C. Janiak, *Arab. J. Chem.*, **2016**, 9, 825–834.
49. F. M. Karpacheva, J. Malzner, C. Wobill, A. Büttner, E. C. Constable, C. E. Housecroft., *Dyes Pigment.*, **2018**, 156, 410–416.
50. C. Dragonetti, M. Magni, A. Colombo, F. Melchiorre, P. Biagini, D. Roberto, *ACS Appl. Energy Mater.*, **2018**, 1, 751–756.
51. C. Chen, W. Zhang, J. Cong, M. Cheng, B. Zhang, H. Chen, P. Liu, R. Li, M. Safdari, L. Kloo, L. Sun, *ACS Energy Lett.*, **2017**, 2, 497–503.
52. W. Zhang, P. Liu, A. Sadollahkhani, Y. Li, B. Zhang, F. Zhang, M. Safdari, Y. Hao, Y. Hua, L. Kloo, *ACS Omega*, **2017**, 2, 9231–9240.
53. A. Corma, H. García, F. X. Llabrés i Xamena, *Chem. Rev.*, **2010**, 110, 4606–4655.
54. K. Zhu, D. Wang, J. Liu, *Nano Res.*, **2009**, 2, 1–29.
55. P. Munnik, P. E. De Jongh, K. P. De Jong, *Chem. Rev.*, **2015**, 115, 6687-6718.
56. J. M. Thomas, W. J. Thomas, Principles and Practice of Heterogeneous Catalysis, *VCH*, Weinheim, **1997**.

57. R. J. Farrauto, C. H. Bartholomew, *Nachr. Chem. Tech. Lab.*, **1998**, 46.
58. B. Michelet, C. Deldaele, S. Kajouj, C. Moucheron, G. A Evano, *Org. Lett.*, **2017**, 19, 3576–3579.
59. J. E. Steves, S. S. Stahl, *J. Am. Chem. Soc.*, **2013**, 135, 15742–15745.
60. S. Liu, Y. J. Lei, Z. J. Xin, Y. Lu, H. Y. Wang, J. Photochem. Photobiol. A, **2018**, 355, 141–151.
61. P. Zhang, M. Wang, Y. Yang, T. Yao, L. Sun, *Angew. Chemie - Int.*, **2014**, 53, 13803–13807.
62. S. M. Barnett, K. I. Goldberg, J. M. Mayer, *Nat. Chem.*, **2012**, 4, 498–502.
63. Armstrong, R. D., Peneau, V., Ritterskamp, N., Kiely, C. J., Taylor, S. H. Hutchings., G. J., Chem. Phys. Chem., **2018**, 19, 469–478.
64. Y. Phongboonchoo, N. Thouchprasitchai, S. Pongstabodee, *Int. J. Hydrog. Energy*, **2017**, 42, 12220–12235.
65. M. Glinski, U. Ulkowska, E. Iwanek, *J. Chem. Educ.*, **2016**, 93, 1623–1625.
66. Y. Zhao, B. Shan, Y. Wang, J. Zhou, S. Wang, X. Ma, *Ind. Eng. Chem. Res.*, **2018**, 57, 4526–4534.
67. A. Romero, A. Santos, D. Escrig, E. Simón, *Appl. Catal. A Gen.*, **2011**, 392, 19–27.
68. V. Z. Fridman, A. A. Davydov, A. A. Davydov, *J. Catal.*, **2000**, 195, 20–30.
69. G. Soo Jeon, G. Seo, J. Shik Chung, *Korean J. Chem. Eng.*, **1996**, 13, 412-414.
70. D. Farrusseng, S. Aguado, C. Pinel, *Chem. Int.*, **2009**, 48, 7502–7513.
71. A. Corma, *Catal. Rev. - Sci. Eng.*, **2004**, 46, 369–417.
72. I. Luz, F. X. Llabrés I Xamena, A. Corma, *J. Catal.*, **2010**, 276, 134–140.
73. S. Van Doorslaer, E. Vinck, *Phys. Chem. Chem. Phys.*, **2007**, 9, 4620-4638.
74. H. L. Van Camp, R. H. Sands, J. A. Fee, *J. Chem. Phys.*, **1981**, 75, 2098-2107.
75. J. C. García-Ramos, R. Galindo-Murillo, A. Tovar-Tovar, A.-L. Alonso-Saenz, V. Gomez-Vidales, M. Flores-Alamo, L. Ortiz-Frade, F. Cortes-Guzman, R. Moreno-Esparza, A. Campero, L. Ruiz-Azuara, *Chem. Eur. J.*, **2014**, 20, 13730–13741.
76. M. Andersson, J. Hedin, P. Johansson, J. Nordström, M. Nydén, *J. Phys. Chem.*, **2010**, 114, 13146–13153.
77. K. Heinze, A. Reinhart, *Inorg. Chem.*, **2006**, 45, 2695–2703.
78. J. H. Spee, A. F. Arendsen, H. Wassink, S. J. Marritt, W. R. Hagen, H. Haaker, *FEBS Lett.*, **1998**, 432, 55–58.
79. N. A Sieracki, S. Tiana, R. G. Hadtb, J.-L. Zhangc, J. S. Woertinkb, M. J. Nilgesa, F. Suna, E. I. Solomonb, Y. Lu, *PNAS*, **2014**, 111, 924–929.
80. D. M. Murphy, I. Caretti, E. Carter, I. A. Fallis, M. C. Göbel, J. Landon, S. Van Doorslaer, D. J. Willock., *Inorg. Chem.*, **2011**, 50, 6944–6955.
81. K. M. Sharples, E. Carter, C. E. Hughes, K. D. M. Harris, J. A. Platts, D. M. Murphy, *Phys. Chem. Chem. Phys.*, **2013**, 15, 15214.
82. R. Horikoshi, Y. Funasako, T. Yajima, T. Mochida, Y. Kobayashi, H. Kageyama, *Polyhedron*, **2013**, 50, 66–74.
83. D. Venegas-Yazigi, E. Spodine, M. Saldias, A. Vega, V. Paredes-Garcia, R. Calvo, R. Costa de Santana, *Inorg. Chem.*, **2015**, 54, 3805–3814.
84. S. Menon, M. V Rajasekharan, J.-P. Tuchagues, *Inorg. Chem.*, **1997**, 36, 4341–4346.
85. K. C. Thatipamula, G. Bhargavi, M. V. Rajasekharan, *Polyhedron*, **2015**, 97, 182–187.

86. N. Niklas, F. Hampel, G. Liehr, A. Zahl, R. Alsfasser, C*hem. Eur. J.*, **2001**, 7, 5135–5142.
87. G. Olivo, M. Nardi, D. Vìdal, A. Barbieri, A. Lapi, L. Gómez, O. Lanzalunga, M. Costas, S. Di Stefano, *Inorg. Chem.*, **2015**, 54, 10141–10152.
88. R. S. Rarig, J. Zubieta, *J. Solid State Chem.*, **2002**, 167, 370–375.
89. J. England, R. Gondhia, L. Bigorra-Lopez, A. R. Petersen, A. J. P. White, G. J. P. Britovsek, *Dalton Trans.*, **2009**, 27, 5319.
90. Y. Shen, S. Zhu, R. Pelton, *Macromolecules*, **2001**, 34, 5812–5818.
91. M. Palaniandavar, S. Mahadcvan, M. Köckerling, G. Henkel, *J. Chem. Soc. Dalton Trans.*, **2000**, 2, 1151–1154.

Chapter 2: Background to EPR and ENDOR Spectroscopy

Advanced EPR spectroscopy techniques have in common that their fundamentals are based on Electron Paramagnetic Resonance (EPR) spectroscopy. In this chapter continuous wave (CW) EPR spectroscopy is discussed to further explain the principles of advanced EPR spectroscopy such as CW **E**lectron **N**uclear **D**ouble **R**esonance (ENDOR). Both, CW EPR and CW ENDOR, are crucial as they provide easy access to structural information. This is due the fact that EPR spectroscopy is high sensitivity to paramagnets and consequently only a small amount (mM) of paramagnetic sample is required compared to e.g. NMR. In addition, polycrystalline samples are also suitable for EPR. This is in contrast to for example X-ray, which requires single crystals for analysis.

2.1 Introduction

In this Chapter, the fundamental theory of **C**ontinuous **W**ave (CW) **E**lectron **P**aramagnetic **R**esonance (EPR) spectroscopy and CW **E**lectron **N**uclear **DO**uble **R**esonance (ENDOR) spectroscopy will be introduced. These two techniques enable one to study paramagnetic systems from a structural, configurational and electronic perspective, leading to insights into the coordination chemistry of the systems.[1,2] For a more detailed treatment of the subject area of EPR and ENDOR, the textbook *Electron Paramagnetic Resonance: A Practitioner's Toolkit* by Giamello and Brustolon is highly recommended.[1]

In simple terms, EPR spectroscopy is a technique based on the absorption of electromagnetic radiation in the microwave region by a paramagnetic species placed in an external magnetic field. At a specific microwave frequency and magnetic field, the absorption of electromagnetic radiation takes place. The absorption position is defined by the intrinsic characteristics of the paramagnetic species itself.

In the following sections, the reader will be introduced to the fundamentally important electron Zeeman and nuclear Zeeman terms, including the hyperfine coupling interaction and the superhyperfine couplings. Additionally, the spin-orbit

interaction will be briefly mentioned, as it is a crucial factor for the shift of the free electron *g* factor and in turn this is related to the structure and symmetry of the paramagnet. In this context, examples will be presented covering $3d^9$ metal systems, such as Cu^{2+}, since these species are the primary focus of this Thesis.

This Chapter will also examine the basic principles of ENDOR spectroscopy. ENDOR can be regarded as an advanced EPR technique, that monitors EPR and NMR transitions simultaneously. It provides information about the local environment around the paramagnetic centre and is useful for the structural analysis and the interactions of the paramagnet species with nearby EPR active nuclei.

2.2 CW Electron Paramagnetic Resonance (EPR) Spectroscopy

EPR spectroscopy is reliant on the presence of a paramagnetic system, containing an unpaired electron, including radicals or spin labels, transition metals, defects in single crystals or a variety of biological systems.[1,2] The simplest paramagnet is the free electron. The main characteristic of the electron from an EPR perspective, is the electron spin or electron magnetic momentum which has a specific behaviour when placed into an external applied magnetic field. Therefore, this vitally important property of the electron spin is introduced in the next section.

2.2.1 Electron Spin

The spin angular momentum ***S*** describes the rotation and direction of an electron spin in space, as described by a vector, with magnitude quantized in units of $\hbar$ ($\frac{h}{2\pi}$):

$$|S| = \sqrt{S(S+1)} \tag{2.1}$$

allowing a general projection of the spin orientation as $2S+1$.The electron spin is sometimes classed as 'spin-up (α-spin)' or 'spin down (β-spin)'. Conventionally, the components are defined as S_z along the z-axis of the Cartesian frame. This concept is illustrated in figure 2.1a with $S = +½, -½$, showing the two possible orientations for the electron, which has a spin angular momentum S of ½.

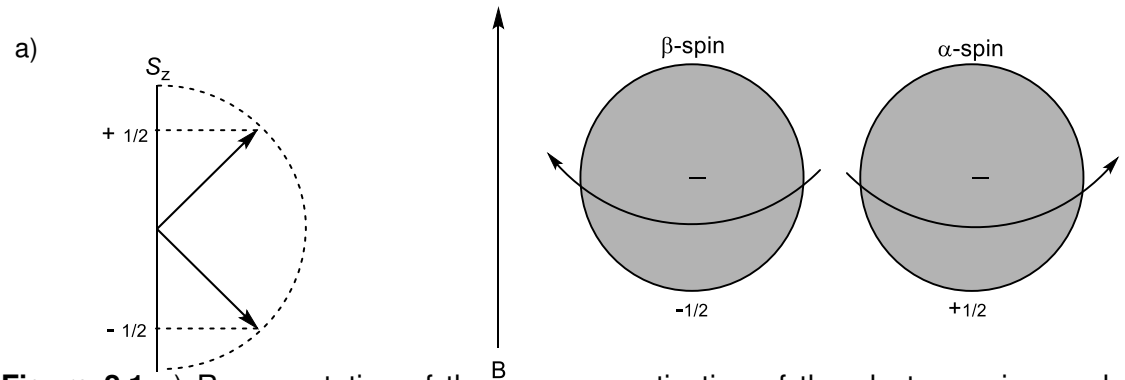

Figure 2.1 a) Representation of the space quantization of the electron spin angular momentum. The magnitude of the vectors are $[S(S+1)]^{1/2}$ in units of $\hbar$.[1] b) The two orientations of the electron magnetic dipole moments, μ_S, arising from the β- and α-spin states, aligned parallel or anti-parallel to the applied field (*z*-direction).[1]

The general definition for the possible orientations along S_z, for any given ***S***, are therefore, between $+S$ and $-S$ and are defined as:

$$m_S = -S, -S+1, \ldots, +S-1, +S \tag{2.2}$$

where m_S is the spin angular momentum quantum number. In addition to the electron spin orientation, the electron possesses a mass m_e and a charge *e*. Together with the mass m_e and charge, the spin creates a magnetic dipole moment labelled μ_S and given as:

$$\mu_S = -\gamma \boldsymbol{S}\hbar = -g_e \frac{e\hbar}{2m_e}\boldsymbol{S} = -g_e \mu_B \boldsymbol{S} \tag{2.3}$$

where γ is the gyromagnetic factor, g_e represents the free-electron factor and $\frac{e\hbar}{2m_e}$ (9.274×10^{-24} JT^{-1}) is the Bohr magneton (symbol μ_B). The negative sign in (2.3) is a result of the electron charge. Considering this and the two possible electron spin states, the electron magnetic dipole momentum can align either clockwise or anticlockwise (Figure 2.2). Defining the μ_S as oriented along the z-axis gives:

$$\mu_z = -g_e \mu_B m_S \tag{2.4}$$

giving a more accurate treatment when describing the electron in an applied magnetic field ***B***, as discussed in the next section.

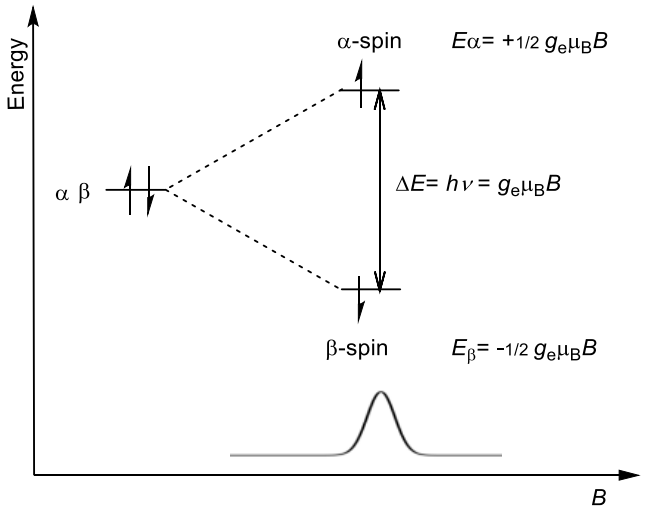

Figure 2.2 Illustration of the electron Zeeman effect (EZ). The spin states, α and β, are represented by up and down arrows at $\boldsymbol{B} = 0$ with the same energy. In the presence of a static magnetic field ($\boldsymbol{B} \neq 0$), the β-spin state is shifted to lower energy and the α-spin to higher energy. The energy separation is proportional to the magnetic field intensity and depends on the electron *g*-factor.

2.2.2 Electron Zeeman effect (EZ)

In the presence of an external magnetic field ***B***, the energy of the two degenerate spin states of the electron are lifted, and two different energy levels are created (Figure 2.2). This interaction between the electron spin and the applied field is called the electron Zeeman (EZ) effect and the energies of the two spin states, α and β, are given in energy terms as:

$$E_\alpha = h\nu = +\frac{1}{2} g_e \mu_B B \tag{2.5a}$$

$$E_\beta = h\nu = -\frac{1}{2} g_e \mu_B B \tag{2.5b}$$

The difference in energy between the two spin states, E_α and E_β, is given as the resonance energy ΔE with energy of:

$$\Delta E = h\nu = g_e \mu_B B \tag{2.6}$$

As a result, the EPR signal occurs at the magnetic field position corresponding to the resonance absorption of energy. However, to allow energy absorption the spin magnetic momentum must be conserved, and this leads to the EPR selection rule $\Delta m_S = \pm 1$. The EPR signal appears when the resonance energy matches the energy necessary to induce a transition from lower to upper spin states via the absorption of a photon, as presented in Figure 2.2.

In general, an isolated electron gives a rather uninformative EPR spectrum. For this reason, in the next sections the nuclear spin is introduced, and in particular the nuclear Zeeman effect will be described, along with a description of the interaction of the nuclear spin with the electron spin and the subsequent resulting EPR spectrum.

2.2.3 Nuclear Spin

In a similar manner to ***S***, the nuclear spin angular momentum ***I*** is also quantized in units of $\hbar$, as a vector with magnitude:

$$|\boldsymbol{I}| = \sqrt{I(I+1)} \tag{2.7}$$

where the number of discrete orientations, $I(I+1)$, is given by the magnetic quantum number $m_I = -I, -I+1 \ldots I-1, +I$. Therefore, the number of possible EPR lines for a system bearing non-zero nuclei is presented by $2nI+1$, where n = number of equivalent nuclei. Similar to the electron spin, the nuclear spin ***I*** has a magnetic momentum μ_I given by:

$$\mu_I = g_N \mu_N \boldsymbol{I} = g_N \frac{e\hbar}{2m_p} \boldsymbol{I} \tag{2.8}$$

where g_N is the effective g-factor, μ_N is the nuclear magneton ($= \frac{e\hbar}{2m_p} = 5.0508 \times 10^{-27}$ JT^{-1}), m_P is the mass of a proton and μ_I is established by coupling angular momenta of the nuclei. The nuclear isotopes have different spin quantum numbers, owing to the variations in the proton and neutron number. Subsequently, depending on the abundance of the isotopes, the profile of the resulting EPR spectrum will be dependent on the number of nuclear isotopes.[3,4] From a EPR perspective, the nuclear spin orientation and rotations are considered around the z-axis and given by:

$$\mu_z = g_N \mu_N m_I \tag{2.9}$$

2.2.4 Nuclear Zeeman Effect (NZ)

Without an external applied magnetic field, the two possible spin states of $I = ½$ are degenerate. If the external magnetic field is applied, two energy levels are produced (see Figure 2.3), with $m_I = -½$ at high energy and $m_I = +½$ at low energy. This interaction of the nuclear spin with the applied magnetic field ***B*** gives rise to the nuclear Zeeman interaction (NZ), expressed as:

$$E_{NZ} = -g_N \mu_N m_I B \tag{2.10}$$

The combined effect of the EZ and NZ interactions are shown in Figure 2.3 for a simple two spin system ($S = ½$, $I = ½$). In comparison to the energy gap between the EZ levels, the energy gap for the NZ splitting is much smaller, which is primarily due to the smaller μ_N of the nucleus.

2.2.5 Hyperfine Interaction (HF)

In addition to the interaction of the electron spin and nuclear spin with the applied magnetic field, the two spins can also interact with each other. The electron-nuclear interaction within an applied magnetic field ***B***, therefore, leads to a further splitting of the NZ energy level, as shown in Figure 2.3 and this is called the hyperfine interaction (HF). In contrast to the electron Zeeman effect, the nuclear Zeeman and hyperfine coupling interaction are significantly smaller compared to the electron Zeeman splitting energy.

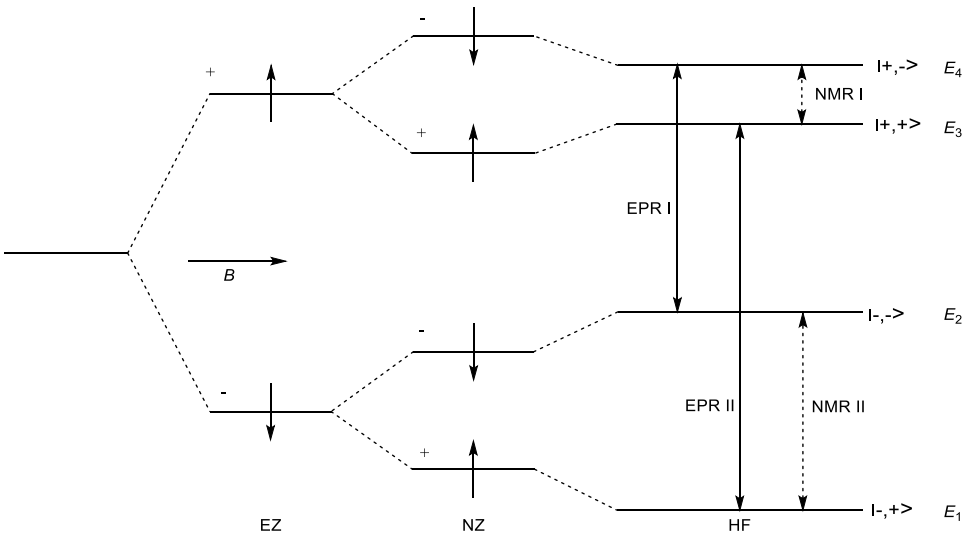

Figure 2.3 Energy level diagram of a two-spin system $S = ½$, $I = ½$, illustrating the effect of an applied magnetic field resulting in the electron Zeeman (EZ) splitting, nuclear Zeeman (NZ) splitting and hyperfine (HF) coupling. The two allowed EPR signals are marked with solid arrows and refer to the observed EPR signals labelled EPR I and EPR II. In this case g_N and a are positive and $a < g_N \mu_N \boldsymbol{B}$.[1]

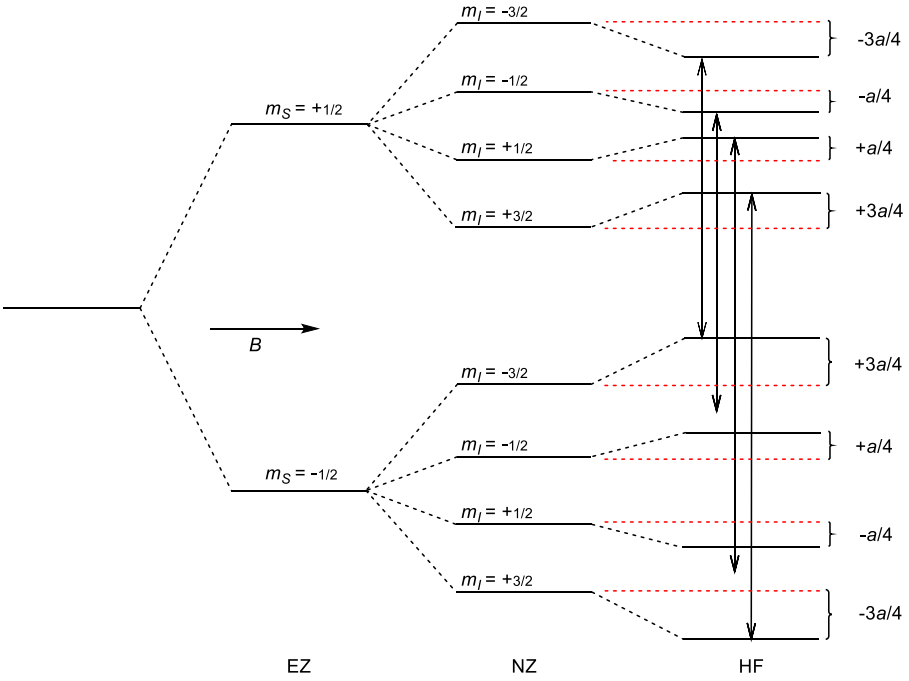

Figure 2.4 Energy level diagram for a two-spin system $S = ½$, $I = 3/2$. The allowed EPR signals are marked with arrows (solid). Electron Zeeman effect (EZ), nuclear Zeeman effect (NZ) and hyperfine coupling (HF) are illustrated.[1]

Nevertheless, the NZ and hyperfine terms create a non-negligible contribution to the spin Hamiltonian which can be described as:

$$E = g_e \mu_B B m_S - g_N \mu_N B m_I + a m_S m_I \tag{2.11}$$

where the first term describes the EZ energy, the second term describes the NZ energy and the final term describes the energy of the hyperfine interaction for a spin system with m_S and $m_I > ½$.

Applying a two-spin system of $S = ½$, $I = ½$ to (2.11) results in the following energy levels:

$$E_1 = -\frac{1}{2} g_e \mu_S B - \frac{1}{2} g_N \mu_N B - \frac{1}{4} a \tag{2.12a}$$

$$E_2 = -\frac{1}{2} g_e \mu_S B + \frac{1}{2} g_N \mu_N B + \frac{1}{4} a \tag{2.12b}$$

$$E_3 = +\frac{1}{2} g_e \mu_S B - \frac{1}{2} g_N \mu_N B + \frac{1}{4} a \tag{2.12c}$$

$$E_4 = +\frac{1}{2} g_e \mu_S B + \frac{1}{2} g_N \mu_N B - \frac{1}{4} a$$

The four discrete energy levels, labelled E_1, E_2, E_3 and E_4, for this two spin system are shown in Figure 2.3. The transitions between these energy levels which produce the observed EPR transitions are dependent on the intrinsic selection rules ($\Delta m_S = \pm 1$ and $\Delta m_I = 0$). According to these selection rules, the transitions, $E_2 \rightarrow E_4$ (labelled EPR I) and $E_1 \rightarrow E_3$ (labelled EPR II), shown in

Figure 2.3 are therefore allowed and result in a total of two EPR lines. Transition EPR I and EPR II are separated by the hyperfine coupling *a*. (2.12d)

A more complex energy splitting diagram is observed for systems bearing $I > ½$, for example the two spin system $S = ½$, $I = 3/2$ (Figure 2.4). Similar to the previous case described above, the EZ, NZ and HF effects are illustrated in the Figure 2.4, in this case showing four allowed energy transitions. The resulting EPR spectrum has four lines centred around the free electron *g*-factor and separated by the hyperfine coupling *a*.

2.2.6 Superhyperfine Interaction (shf)

In the above cases, it was assumed that the electron and interacting nucleus are in close proximity to each other, eg., as in the hydrogen atom, H•, for the two spin system $S = ½$, $I = ½$. However, the interaction of a nucleus with the electron can be remote, over extended distances, such as with ligand nuclei attached to a paramagnetic transition metal ion in a metal-complex. In this case, the interaction can be referred to as a superhyperfine interaction. Two limiting cases arise in such superhyperfine interactions; i) the ligand superhyperfine coupling is larger than the intrinsic EPR linewidth (so that the couplings can be readily measured by CW EPR techniques, for example), or ii) smaller or comparable to the EPR linewidth. In the latter case, advanced EPR techniques, such as ENDOR, are required to resolve these small superhyperfine interactions, and this will be discussed in more detail later in section 2.3.[1,5–7]

2.2.7 Anisotropy of g

In the above discussions, the *g*-factor has been considered as a scalar quantity; its magnitude is independent of the orientation of the paramagnetic system with respect to the magnetic field. In reality this is not the case, and in fact the *g* value can vary depending on the relative orientation of the sample with respect to the applied magnetic field, leading to an anisotropic **g** tensor. To explain the origin of the **g** tensor in more detail, the spin system is most conveniently described using a Cartesian coordinate system with defined directions of *x*, *y* and *z*. Depending on the symmetry of the spin system, the

resulting components **g** can be different. Commonly, such cases can be classified as *isotropic*, *axial* or *rhombic*.[8–10,11]

For many chemical systems, the *g*-value deviates from g_e due to the changes in symmetry and bonding in the paramagnetic complex. This means that the interaction of the electron spin with ***B*** will be orientationally dependent. The actual source of anisotropy in the **g** tensor is ultimately derived from the spin-orbit coupling.[1,12] As a result, a more accurate representation of **g** is given as:

$$\boldsymbol{g} = \begin{bmatrix} g_{xx} & 0 & 0 \\ 0 & g_{yy} & 0 \\ 0 & 0 & g_{zz} \end{bmatrix} \tag{2.13}$$

where g_{xx}, g_{yy} and g_{zz} are the components of the **g** tensor and the principal axes of the *g* frame.

2.2.8 Symmetry

In simple terms, the EPR spectrum can be defined based on the observed symmetry in **g**, which in turn provides valuable information on the structure and geometry of the paramagnetic system. The different types of symmetry include *isotropic*, *axial* and *rhombic*, as explained in the following sections.

2.2.8a Isotropic g

In an isotropic system, all three principal *g* values are equivalent (eg., $g_{xx} = g_{yy} = g_{zz}$). The isotropic signal is thus centred on g_{iso}:

$$g_{iso} = \frac{g_{xx} + g_{yy} + g_{zz}}{3} \tag{2.14}$$

An example of an isotropic spectrum is shown in Figure 2.5a, for an $S = ½$ spin system with no hyperfine coupling. Isotropy is typical observed for high symmetry systems, such as cubic, octahedral (O_h) and tetrahedral (T_d). However, fast averaging of the spectral parameters can occur for anisotropic spin systems due to rapid molecular tumbling leading to an isotropic *g* value.

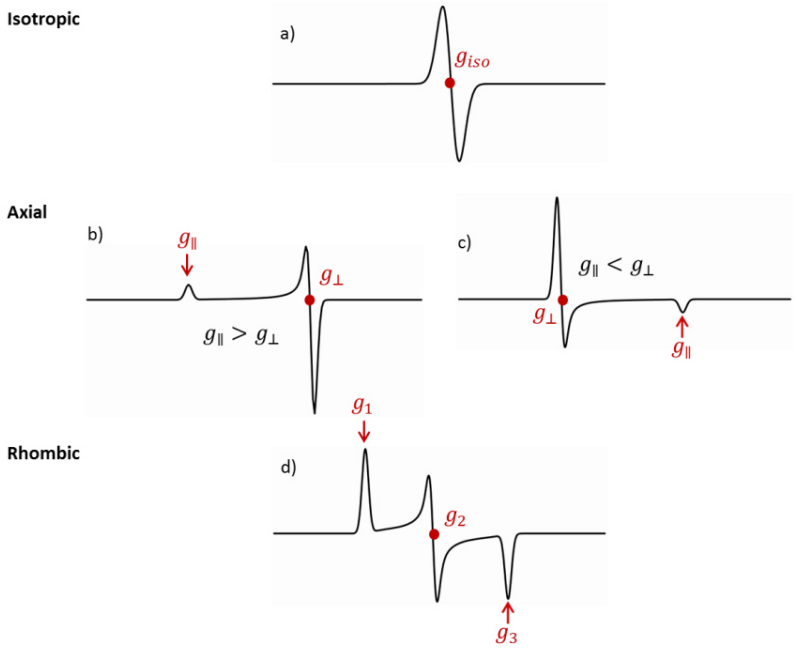

Figure 2.5 Simulated CW EPR spectra for an S = ½, I = 0 spin system in an a) isotropic, b-c) axial and d) rhombic symmetry environment. The positions of the g values are given in red. **B** increases from left to right.[13]

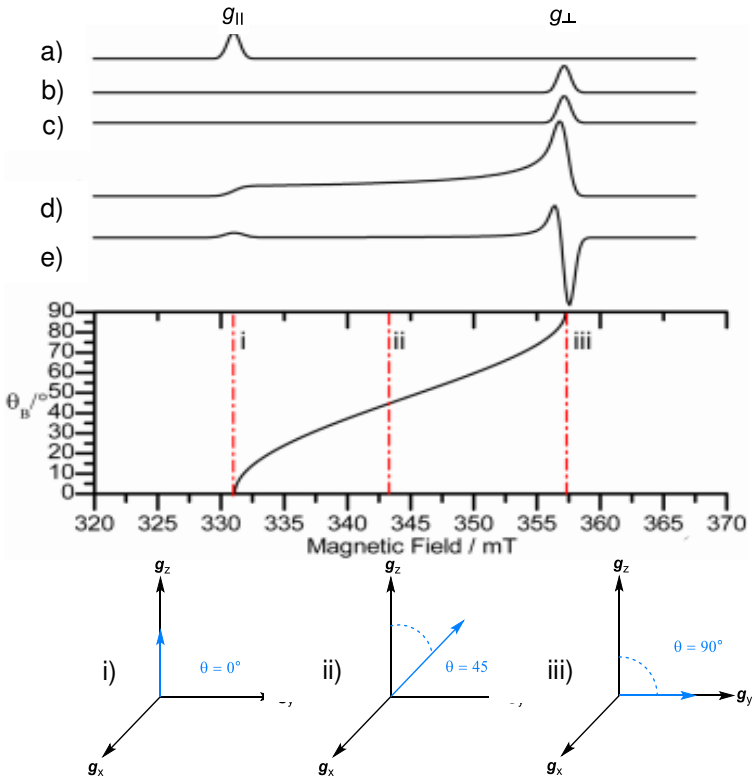

Figure 2.6 Simulated EPR profile for an axial spin system (S = ½) with $g_x = g_y = 1.9$, $g_z = 2.05$ and $g_{\parallel} > g_{\perp}$ at 9.5 GHz. The angular dependency profile of the **g** tensor is also shown. The EPR absorption profiles for the single crystal like orientations of g_x, g_y and g_z are illustrated in a), b) and c). In case a), g_z is parallel to ***B*** (θ = 0°), whereas in b) and c), g_x and g_y are parallel to ***B*** (θ = 90°). The plot in d) illustrates the absorption profile of the resulting powder spectrum containing randomly orientated paramagnets (as opposed to the single crystal example shown in a-c). The first derivative of the powder spectrum is then given in e). The highlighted points, labelled i-iii, represent the orientation of the magnetic field vector (***B***) with respect to the **g** tensor at magnetic field positions corresponding to i) 331 mT, ii) 343 mT and iii) 357 mT.[13]

2.2.8b Axial

Axial systems are typical observed for paramagnetic systems possessing square planar, trigonal and pyramidal structures. The axial symmetry is defined by the *g* values of $g_{xx} = g_{yy} \neq g_{zz}$, also abbreviated as $g_{\perp} = g_{xx} = g_{yy}$ and $g_{\parallel} = g_{zz}$. As a result, two limiting *g*-values are observed in the powder EPR spectrum, centred at $g_{\parallel}$ and the other centred at $g_{\perp}$. In Figure 2.5b, two possible situations are shown where $g_{\parallel} > g_{\perp}$ or $g_{\parallel} < g_{\perp}$, which simply depend on the symmetry and coordination of the metal complex. As mentioned earlier, the *g* value is dependent on the orientation in respect to ***B***, with $g_{\parallel}$ observed when the field is aligned parallel to the *g* frame ($\theta_B = 0°$) and $g_{\perp}$ is observed when the field is aligned orthogonal ($\theta_B = 90°$) to the *g* frame. This orientational dependency is best illustrated in Figure 2.6, showing the individual resonances (in absorbance mode) for *g* in the two extreme cases (Figure 2.6a-c). When $\theta_B = 0°$, the magnetic field is aligned along $g_{\parallel}$, resulting in one resonance line, whereas when $\theta_B = 90°$, the magnetic field is aligned parallel to $g_{\perp}$ producing a single line at this position. However, the powder EPR spectrum represents a sum of all possible orientations of the **g** tensor with respect to the applied field, and the absorption and derivative profiles for this powder pattern are shown in Figure 2.6d, e.

2.2.8c Rhombic

Finally, when all three axes are different due to spin systems possessing lower point group symmetries, the resulting **g** tensors takes the form $g_{xx} \neq g_{yy} \neq g_{zz}$. As a result, three different *g* values appear in the EPR spectrum due to the variations in the orientations of ***B*** relative to the *g* frame (Figure 2.5d).

2.2.9 Anisotropy of A

Two terms contribute to the hyperfine coupling interactions, namely, the isotropic Fermi contact interaction (a_{iso}) and the through space dipole-dipole interaction. These two hyperfine contributions are discussed below.

From a quantum mechanical perspective, there is a small probability that the electron may enter the nuclear volume. Inside the nucleus, the hyperfine field originating from the nuclear magnetic dipole is constant in all directions. This hyperfine interaction is called the *isotropic interaction*, or Fermi

(2.15)

contact interaction, and is a direct measure of the interaction between the electron and nuclear magnetic dipole moments as a result of the finite probability that the unpaired electron will be located at the nucleus. It arises exclusively for s- orbitals (or orbitals with partial s-character). The isotropic coupling, a_{iso}, is given by:

$$a_{iso} = \left(\frac{8\pi}{3}\right) g \mu_B g_N \mu_N |\psi(0)|^2$$

where $|\psi(0)|^2$ is the square of the absolute value of the unpaired electron wavefunction evaluated at the nucleus. The magnitude of the experimentally observed isotropic hyperfine coupling can thus be related to the electron spin density located at the nucleus, through the theoretically determined isotropic hyperfine coupling values.

The second contribution to the hyperfine coupling interaction occurs via the dipole-dipole interaction, also referred to as the anisotropic hyperfine coupling. The anisotropic hyperfine coupling describes the spatial interaction of the electron magnetic momentum with the nuclear magnetic momentum in energy terms E_{dip}, which is given by the classical term:

$$E_{dip} = (\mu_0/4\pi)\ [\mu_1 \cdot \mu_2/r^3 - 3(\mu_1 \cdot \boldsymbol{r})(\mu_2 \cdot \boldsymbol{r})/r^5] \tag{2.16}$$

and depends on the two magnetic momentum vectors in respect of their orientation and distance to each other. $\boldsymbol{r}$ is the vector relating the electron position in coordinate frame centred on the nucleus, and r is the electron-nucleus distance. μ_0 is the magnetic permeability of the vacuum.

Substitution of μ_1 and μ_2 with the electron spin and nuclear spin dipolar momentums μ_e and μ_N results in the following term:

$$E_{dip} = (\mu_0/4\pi) g \mu_B g_N \mu_N\ [\boldsymbol{S} \cdot \boldsymbol{I}/r^3 - 3(\boldsymbol{S} \cdot \boldsymbol{r})(\boldsymbol{I} \cdot \boldsymbol{r})/r^5] \tag{2.17}$$

where the electron is centred in a coordination frame, which is centred on the nucleus. The components of the frame are *x*, *y* and *z* and the position of the electron is described over the vector ***r***. This vector stays in correlation with the distance to the nucleus. However, the electron position is not localized but rather has a distribution in space. Therefore, the contribution to the hyperfine dipolar interaction energy E_{dip} has to be averaged over the electron distribution and can be expressed over the traceless dipolar hyperfine **T** tensor:

$$\boldsymbol{T} = \begin{bmatrix} T_{xx} & T_{xy} & T_{xz} \\ T_{yx} & T_{yy} & T_{yz} \\ T_{zy} & T_{zy} & T_{zz} \end{bmatrix} \tag{2.18}$$

2.2.10 Orientation

The importance of symmetry for paramagnetic systems, is reflected in the *g* values or **g** tensor. The change in position of the paramagnetic centre with respect to the magnetic field therefore has a direct impact on the profile of the resulting EPR spectrum. For clarification, the spherical positioning of the **g** tensor, regarding the magnetic field direction, is illustrated in Figure 2.7a, where the component B_z of the applied field is specified by the direction *Z'*. Furthermore, the orientation of the magnetic field vector with respect to the *g* principal axes is given in Figure 2.7b.

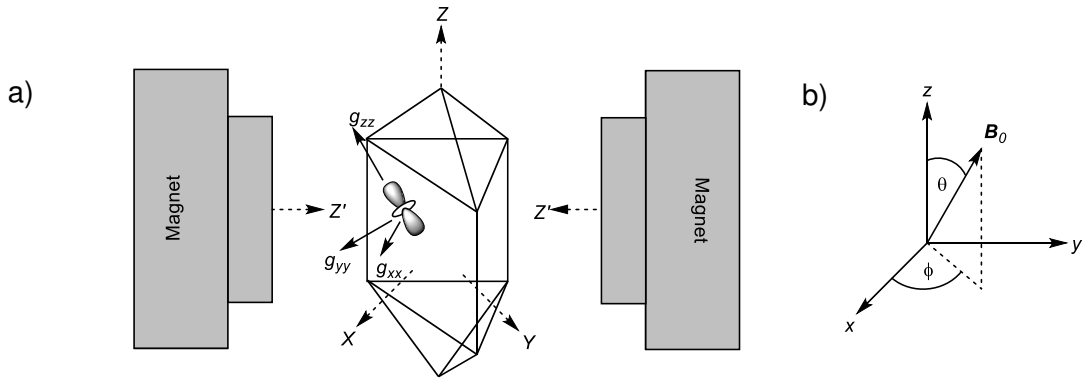

Figure 2.7 a) Schematic illustration of the independent axes systems relevant to EPR showing magnetic field axes, the principal **g** axes and the crystal axes, with b) representing the orientation of the magnetic field vector with respect to the **g** tensor axes *x*, *y* and *z*.[14]

First, the energy terms of the EPR resonance need to take into consideration the importance of sample orientation so the simple resonant equation is given as:

$$h\nu = \mu_B g(\theta, \varphi) B \tag{2.19}$$

with the polar angles θ and φ. These angles refer to the orientation of the B_0 vector within the molecular **g** tensor (Figure 2.7b). The individual components of ***B*** can be defined as B_x, B_y and B_z can be described using these polar angles as:

$$B_x = B sin\theta cos\varphi \tag{2.20a}$$
$$B_y = B sin\theta sin\varphi \tag{2.20b}$$
$$B_z = B cos\theta \tag{2.20c}$$

Considering, that the electron spin ***S*** can be expressed by the Pauli spin operator vector, $\hat{S}_x$, $\hat{S}_y$, $\hat{S}_z$ the spin Hamiltonian equation of the electron Zeeman splitting can finally be expressed as follow:

$$\hat{H} = \mu_B (B \sin\theta \cos\varphi \, g_{xx} \hat{S}_x + B \sin\theta \sin\varphi \, g_{yy} \hat{S}_y + B \cos\theta \, g_{zz} \hat{S}_z) \tag{2.21}$$

and provides a more accurate description of the structure and electronic configuration of the spin system.

2.2.11 Spin Orbit Coupling Interaction

In real paramagnetic systems, the unpaired electron will possess both spin and orbital angular momentum. When combined the effective magnetic momentum becomes:

$$\mu_e = \mu_B l + g\mu_B S \tag{2.22}$$

The spherical expansion of one atom is symmetrical, however, molecules usually have low symmetry. As a result, the orbital angular momentum is averaged to zero (quenched). Consequently, the orbital angular momentum is considered as almost absent and the electron angular momentum coupling is mostly due to the spin only contribution. A small amount of spin orbit coupling can be reintroduced leading to a small deviation of the *g* value from free spin ($\Delta g = g\text{-}g_e$). Hence, a shift of the resonance field intensity from the value corresponding to the free electron spin is observed. The deviation Δg is larger for metal complexes than for organic free radicals. Deviation of the *g* factor of the free electron gives, in general, important structural information. In the following section, the influence of spin orbit coupling is discussed in terms of transition metal ions with $3d^9$ electron configuration.

2.2.11a $3d^9$ Case (Cu^{2+})

The arrangement for the five d-orbitals d_{xy}, d_{xz}, d_{yz}, $d_{x^2-y^2}$ and d_{z^2}, of 3d metals varies for each possible molecule geometry.[15] Due to the orbital arrangement in space, the energy level of each d-orbital is different (Figure 2.8b) and referred to as the ligand field splitting. Metals ions such as Cu^{2+} ($3d^9$) can form complexes bearing octahedral, tetragonal or square planar geometries.

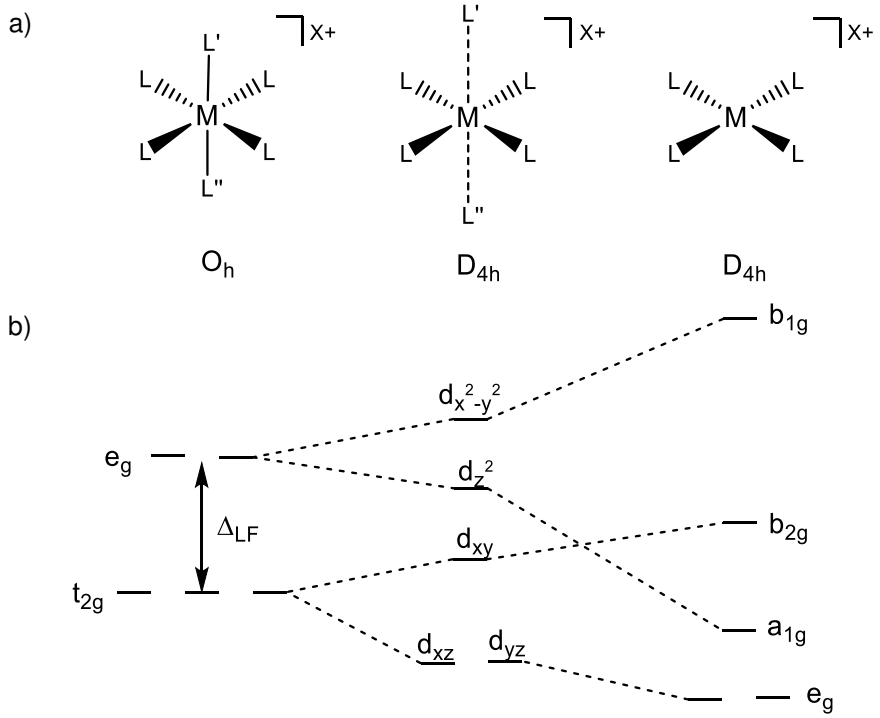

Figure 2.8 a) Splitting of the d-orbitals in an octahedral ligand field (O_h point group symmetry), caused by a Jahn-Teller distortion. The subsequent changes after a tetragonal distortion (D_{4h} symmetry caused by elongation along the *z* axis), and final removal of the ligands to produce a square planar arrangement (D_{4h} symmetry) are shown.[14]

The d-orbital splitting for each geometry can be influenced by distortion of the ligand due to, for example, elongating or compressing in the equatorial and/or axial plane (Figure 2.8a,b), as caused by a Jahn-Teller distortion.[16] Elongating the axial ligands L' and L" of the octahedral structure (Figure 2.8a) already leads to energy differences of the d-orbitals of the t_{2g} and e_g set (Figure 2.8b). Further elongation of L' and L", results in removal of L' and L" and consequently creates a square planar geometry. Comparing the d-orbital arrangement for the elongated octahedral and square planar geometry, a further shift in energy level is obtained (Figure 2.8a, b).

This is important as the arrangement of the d-orbital also determined the location of the unpaired electron for Cu^{2+}, $3d^9$ ion. Following the Pauli principle, the unpaired electron is found in the highest occupied d-orbital. As established earlier, the *g* values depend on the orientation of the spin system with respect to the applied field. Thus, changes in the crystal field splitting will in turn lead to anisotropic *g* values.

In theory, the unpaired electron for an elongated octahedral (D_{4h}) geometry, is located in the $d_{x^2-y^2}$, and well separated from other d-orbitals (Figure 2.8b).

However, spin orbit coupling can occur, leading to an admixture of the d-orbitals and introduces angular momentum. This in turn depends on the symmetry of the system and which orbitals can couple with which.

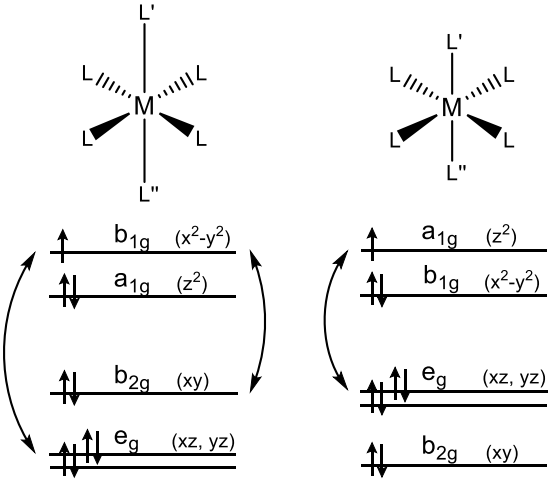

Figure 2.9 Splitting of the d-orbitals for D_{4h} symmetry, in elongated (left) and compressed (right) arrangements for a $3d^9$ ion. The orbitals which commute or mix with each other, under the influence of an applied field, are shown by the curved arrows. Crucially this field induced mixing introduces orbital momentum and therefore creates shifts in the *g* values.[14]

If a magnetic field is orthogonal to the *x*, *y* or *z* axes, the unpaired electron can couple from one orbital to another, inducing motion between suitable states of the correct symmetry. This motion between suitable states is equivalent to a rotation of the electron about the *x* (R_x), *y* (R_y) or *z* (R_z) axis. For D_{4h} symmetry, the corresponding irreducible representation for $d_{x^2-y^2}$ is B_{1g} (Figure A.1). Rotating the *z*-axis is presented by the irreducible representation A_{2g}. Coupling of A_{2g} and B_{1g} gives B_{2g}. According to the character table for point group D_{4h} (Figure A.1), $d_{x^2-y^2}$ can couple with d_{xy} as the ground state. The magnitude of the anisotropic *g* value for g_z is therefore:

$$g_{zz}(g_{||}) = g_e + \frac{8\lambda}{E_{(x^2-y^2)} - E_{xy}} \tag{2.23}$$

If the magnetic field is parallel to the *xy* plane, an *xy* rotation (R_x and R_y) is considered and transforms as E_g (A.1). Coupling of E_g with B_{1g} results in the irreducible representation E_g. For this reason, $d_{x^2-y^2}$ can admix the two degenerated d_{xz} and d_{yz} orbitals, contributing to the g_{xx} and g_{yy}.

$$g_{xx,yy}(g_{\perp}) = g_e + \frac{2\lambda}{E_{(x^2-y^2)} - E_{xz,yz}} \tag{2.24}$$

To summarize, if symmetry changes then the ligand field splitting changes, resulting in different energy states of E_0 - E_n and therefore anisotropic g values are produced which differ from g_e.

Similar to the g values, the anisotropic A values are also dependent on the symmetry and crystal field. Nevertheless, the prediction of the A values is not straightforward and depends upon factors such as the Single Occupied Molecular Orbital (SOMO) and the extent of electron delocalization on the corresponding nucleus. However, it is still possible to calculate the value of SOMO by comparing the experimental with the theoretical isotropic and uniaxial anisotropic hyperfine constants, where the isotropic and uniaxial hyperfine constants represent the unit spin density.

2.2.12 Linewidth broadening due to dynamic processes

Linewidth broadening can occur when dynamic processes are involved. To observe linewidth broadening, the difference in resonance frequency must be comparable in magnitude to the rate of the dynamic process. In the following section, an example is given, illustrating the impact of rotational diffusion. Rotational diffusion refers to the increase of molecular tumbling as illustrated in Figure 2.10 for the [Cu(acetylacetonate)$_2$] complex. The EPR sample was recorded at 140 K and 300 K, respectively. The CW X-band EPR spectrum recorded at 140 K (Figure 2.10a), exhibits the typical anisotropy of axial paramagnets. Recording the same EPR sample at 300 K, results in the EPR spectrum shown in Figure 2.10b, exhibiting an isotropic behaviour, where the

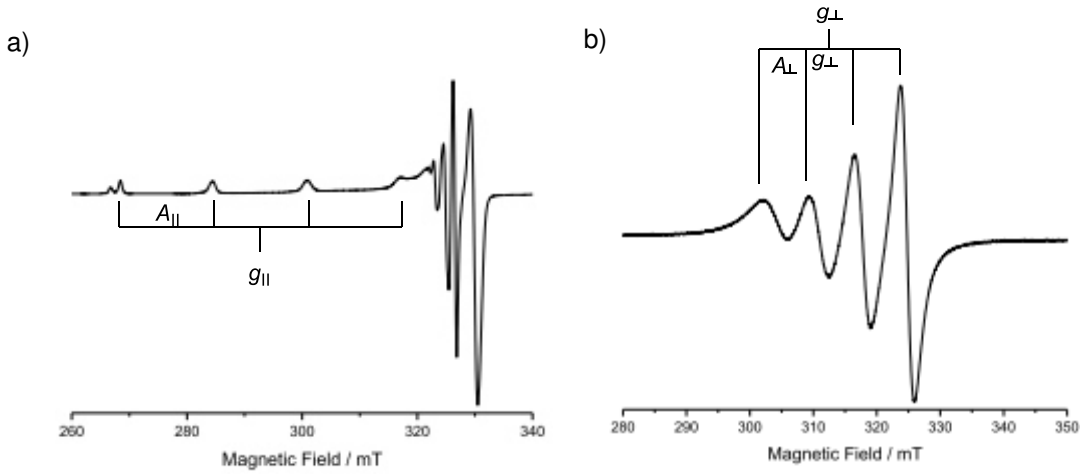

Figure 2.10 CW X-band EPR spectra of [Cu(acetylacetonate)$_2$] dissolved in DMF and $CHCl_3$ (1:1) recorded at a) 140 K and b) 300 K, showing the change in the line shape from anisotropic (140 K) to isotropic (300 K).

EPR lines are centred around g_{iso} and separated by a_{iso}. This occurs when the molecular tumbling is in the fast motion regime.[9] However to give a better understanding of the rotations, one need to consider the Stoke-Debye-Einstein relation:

$$\tau_C = \frac{1}{6D} = \frac{4\pi\eta r^3}{3kT} \tag{2.25}$$

where τ_c is the correlation relaxation time, *D* is the spherical diffusion coefficient, *r* is the hydrodynamic radius of the molecule modelled as a rotating sphere, $\boldsymbol{\eta}$ is the viscosity and *k* is the Boltzmann contribution.[17,18] Fast motion appears when $\frac{1}{\tau_c}$ is larger than the difference in resonance frequency for different molecular orientations. In contrast, slow motion is observed if $\frac{1}{\tau_c}$ is similar or smaller than the difference in resonance frequency for different molecular orientations. This phenomenon of fast motion and slow motion was observed for the example in Figure 2.10a and b, due to temperature changes. Influencing the correlation relaxation time, τ_c, can also be done by using high viscous solvents, by immobilization of the paramagnet system or using high pressures.[2,19,20]

Homogenous line broadening occurs when the paramagnetic species are all magnetically equivalent, whereas inhomogeneous broadening is observed if different individual electron spins exist in different environments or have different orientations with respect to the external magnetic field.[21] In solid state, the paramagnetic species are disordered, and the resulting spectrum is the sum of each orientation. Disorder might be a result of defects in the solid matrix or slightly different conformations in the solid phase. If a small variation of magnetic parameters is present, due to sample inhomogeneity, strain effects may be visible. This means that the *g*, *A* and *D* tensors appear in variation and effect the profile of the EPR spectrum.[22–24] Another type of inhomogeneous broadening is caused by weak resolved hyperfine interactions. Weak unresolved hyperfine interactions are not related to sample inhomogeneity and usually caused by many non-zero splitting nuclei. The non-zero splitting nuclei are too weak to split the EPR line. However, the combined effect of these nuclear interactions leads to line broadening.

2.3 CW Electron Nuclear DOuble Resonance (ENDOR) Spectroscopy

In cases where the hyperfine coupling is smaller than the intrinsic linewidth of the EPR signal, or when an accurate identification of the nucleus responsible for a hyperfine splitting is required, Electron Nuclear DOuble Resonance (ENDOR) spectroscopy can be used. If the anisotropy of *g* and *A* are known, the orientation selective approach can be used to extract further information on the nature of the hyperfine interaction. The focus of this section is to examine the basic principles of CW ENDOR spectroscopy and the importance of the orientation selective measurements will be explained in more detail later.

ENDOR allows one to elucidate the molecular structure of a paramagnetic system and provides information about the distance and orientation of atoms (nuclei) surrounding the paramagnetic centre. To obtain an ENDOR spectrum, microwave (EPR) and radio frequencies (NMR) are used simultaneously to induce electron and nuclear spin transitions. The principal step in the ENDOR measurement is to induce a saturated EPR transition (Figure 2.11a, b). At that EPR point the radio frequency (RF) is applied to induce the NMR transitions (Figure 2.11b, c). It should be noted, that EPR spectroscopy is more sensitive

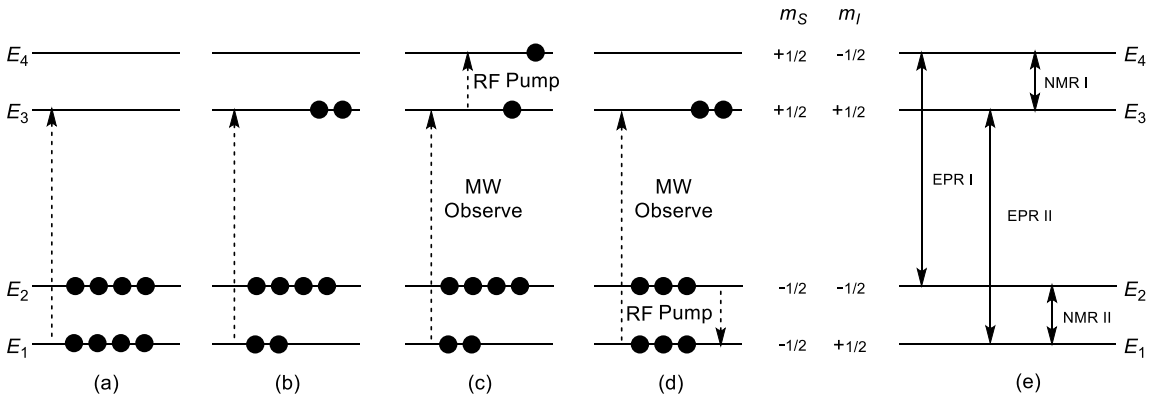

Figure 2.11 Energy level diagram for the two-spin system $S = ½$, $I = ½$, showing the effect of the applied microwave and radio frequencies at a) low microwave powers, b) saturating microwave power, c) saturating radio frequency power and (d) saturating radio frequency power.[14,25] The individual EPR and NMR transitions are illustrated in e).

compared to NMR spectroscopy. Perturbations to the EPR spectrum is thus caused by changes to the NMR transitions. Therefore, the NMR signal is only *indirectly* detected *via* the EPR spectrum (Figure 2.11d, c).[25]

The energy levels shown in Figure 2.11 pertain to the two spin system $S = ½$, $I = ½$. For this spin system, the EPR transitions were labelled EPR I ($E_2 \leftrightarrow E_4$) and EPR II ($E_1 \leftrightarrow E_3$), while the two NMR transitions were labelled NMR I ($E_3 \leftrightarrow E_4$) and NMR II ($E_1 \leftrightarrow E_2$). To induce the first EPR transition (EPR II) low microwave power is applied and resonance absorption occurs when the energy corresponding to the $E_1 \leftrightarrow E_3$ level difference (Figure 2.11a) is available. Due to rapid relaxation, the exited spins return quickly to the ground state, leaving an unsaturated EPR line. At higher microwave powers, the electron spin populations in the ground and excited state are almost equalized, resulting

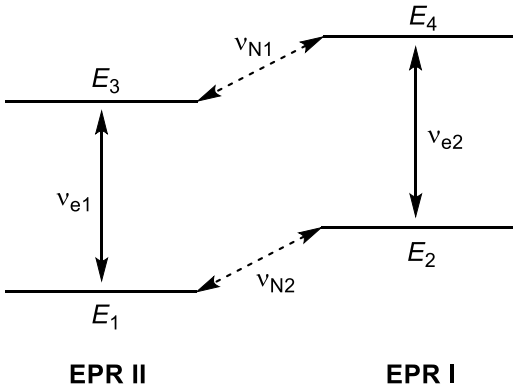

Figure 2.12 Energy levels for the two-spin system $S = ½$, $I = ½$, illustrating the allowed EPR (solid) and NMR (dashed) transitions, where ν_{e1} and ν_{e2} belonging to two different magnetic field positions in the EPR spectrum and ν_{N1} and ν_{N2} are the two ENDOR signals.[14]

in a saturated EPR signal for transition EPR II (Figure 2.11b). By applying a saturating RF, the NMR I transition $E_3 \leftrightarrow E_4$ is pumped which restores a population difference between the two EPR transitions $E_1 \leftrightarrow E_3$ (Figure 2.11c). Subsequently, the first ENDOR signal is thus obtained. Consecutively, the second RF transition NMR II ($E_1 \leftrightarrow E_2$) is pumped, resulting in an EPR signal enhancement and leading to the appearance of the second ENDOR signal (Figure 2.11d).

For convenience, these four energy levels are again illustrated in Figure 2.12. The allowed NMR and EPR transitions are now labelled in frequency terms as $\nu_{N1,2}$ (NMR) and $\nu_{e1,2}$ (EPR). In this case, the two lines appear at the frequency of $\nu_{e1,2}$ and are separated by the hyperfine coupling a. On the other hand, the two NMR lines in the ENDOR spectrum appear at the frequencies $\nu_{N1,2}$ but are also separated by the same hyperfine coupling value of a. This simple two spin system thus illustrates how the same value of a can be extracted from both the EPR and ENDOR spectrum. (2.26)

Crucially, the ENDOR spectrum does not just yield information on *a* (which is readily available from the EPR spectrum) but also the identity of the nucleus responsible for the coupling. The NMR transition frequency is actually defined by:

$$v_N = |v_L \pm \frac{a}{2}|$$

where $v_L \pm \frac{a}{L}$, defines the position of the ENDOR signals and v_L is the Nuclear Larmor frequency which is specific for each nucleus.[23,26,27]

In general, weakly and strongly coupled nuclei will lead to two limiting conditions in the ENDOR spectrum. The above pertains to nuclei with large nuclear Larmor frequencies, such as ^{1}H or ^{19}F, where $v_L > \frac{|a|}{2}$ at high fields. The same two ENDOR lines are observed when either EPR transition is observed (i.e., EPR I or EPR II). However, because ν_L is magnetic field dependent, the centre of the ENDOR lines observed by saturating EPR I or EPR II will be slightly shifted in frequency.

Alternatively, in some cases $\nu_L < |a|/2$. This is referred to as the *strong coupling* regime and occurs for nuclei such as ^{2}H, ^{13}C and ^{14}N particularly at low field. In this case, the two ENDOR lines are separated by $2\nu_L$ and centred at $|a|/2$. In this regime, the separation ($2\nu_L$) between the ENDOR resonances will be slightly different when either EPR line (i.e., EPR I or EPR II) is monitored owing to the magnetic field dependency of ν_L. The Larmor frequency at the selected field position (B) in the ENDOR experiment, can be calculated according to:

$$v_B = \frac{v_{L(350)} \cdot B}{B_{350}} \quad (2.27)$$

where B_{350} corresponds to a field value of 350 mT. As the ν_L is specific to individual nuclei, the hyperfine coupling *a* can be measured and assigned with high resolution and accuracy.[11,25]

2.3.1 Orientation Selective Hyperfine Measurements

A polycrystalline EPR spectrum can be considered as a superposition of resonances from randomly orientated molecules, so that as the applied field B is swept it adopts all possible orientations with respect to the chosen molecular frame. In orientation selective measurement (in particular for ENDOR), a series of hyperfine measurements are performed at a number of fixed magnetic field positions across the full width of the EPR spectrum. The hyperfine (2.28)

response at each field position arises only from the subset of molecules having orientations that contribute to the EPR intensity at that particular *B* field. The EPR resonance field positions, B_{res}, for given orientations (defined in terms of θ, ϕ) are expressed (to first order) as:

$$B_{res} = \frac{h\nu}{\mu_B g(\theta,\varphi)} - m_I A(\theta,\varphi)$$

where $A(\theta,\varphi)$ is the expression of the **A** tensor orientation via the polar angles θ and φ.

The profile of the hyperfine measurements recorded at different field positions can be used to determine the anisotropic **A** tensor, and hence the direction between an unpaired electron and an interacting nucleus of $I \neq 0$, through magnetic angle selection. To demonstrate the utility of orientation selective hyperfine measurements for the determination of the anisotropic *A* values, consider the case of a simple $S = ½$ spin system in axial symmetry and interacting with a remote nucleus (e.g., a ^{1}H, $I = ½$) producing small *A* values which will be buried under the intrinsic EPR linewidth (and so not visible by EPR). The EPR spectrum and corresponding angular variation in resonant field is shown in Figure 2.13. Orientation selective hyperfine measurements should be performed at the unique *single-crystal* like positions and additionally at different field positions between these extremes.

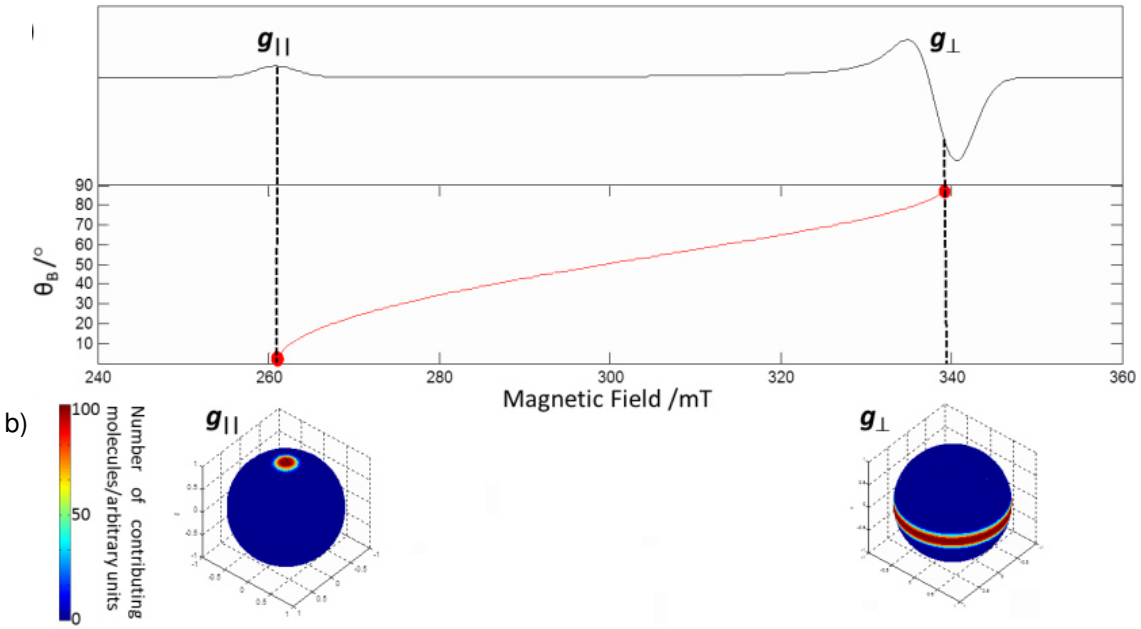

Figure 2.13 a) The turning points of an axial EPR spectrum ($S = ½$, $I = 0$) ($g_x = g_y = 2$, $g_z = 2.6$) are given by $g_{||}$ (0 °) and $g_\perp$ (90 °) are highlighted. The unit spheres corresponding to the orientation selection achieved at the field position corresponding to $g_{||}$ and $g_\perp$ are shown in b).[1,14]

In this axial system, at the magnetic field corresponding to $g_{\|}$ or $g_{\perp}$, the angle θ equals 0° or 90°. At all other B_{res} positions between these two extremes the exact value of θ and hence the angular curve in Figure 2.13, may be calculated as described earlier. For rhombic systems, the angle φ must also be considered in the angular dependency curve. The procedure for determining the anisotropic A values for the remote interacting nucleus will be demonstrated below for three cases.

2.3.2a Coincident g and A frame – Case 1

The simplest case one may consider is complete coincidence of the g and A frames for an $S = ½$ spin system in axial symmetry with $I = 0$ for the metal centre and where the electron interacts with a remote ligand proton ($I = ½$). A simple illustration of the alignment of these axes are shown in Figure 2.14a. The two z components of $g_{\|}$ and $A_{\|}$ are parallel to each other and orthogonal to the x and y axes ($g_{\perp}$, $A_{\perp}$). The resulting ^{1}H ENDOR spectra for this spin system are simulated and shown in Figure 2.14b, c. In the first case, the hyperfine couplings were simulated using a positive tensor of $^{H}A_1 = {}^{H}A_2 = {}^{H}A_{\perp} = 5$ MHz and $^{H}A_3 = {}^{H}A_{\|} = 10$ MHz (Figure 2.14b). In the second case, the tensor contains both positive

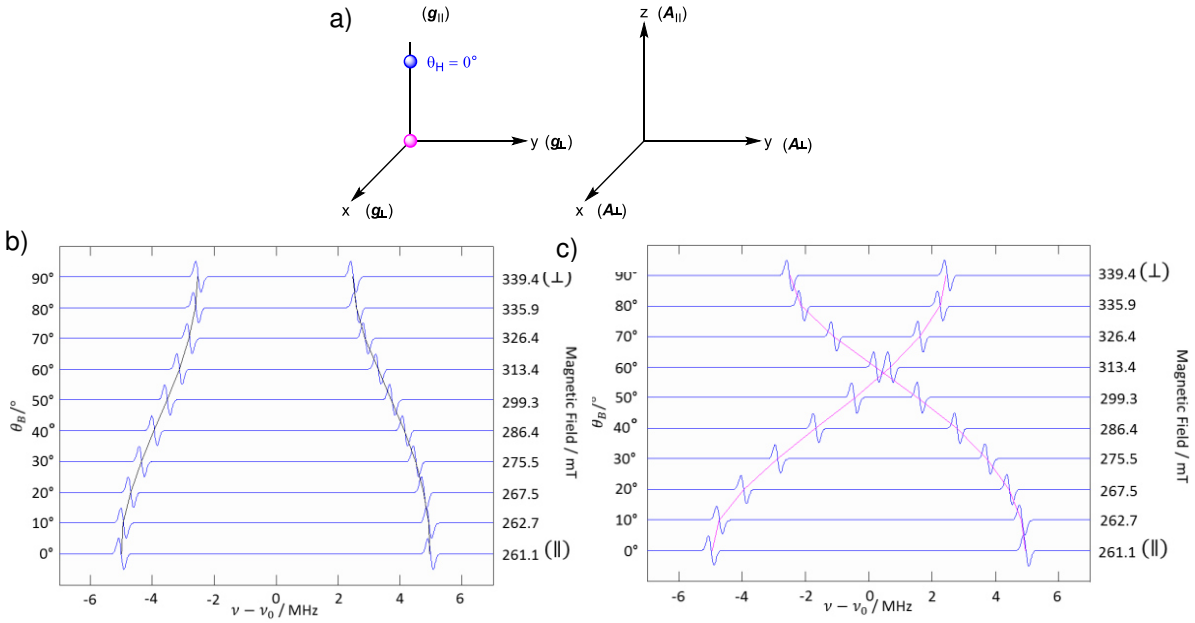

Figure 2.14 The field orientation (θ_B) dependence of the ^{1}H ENDOR for a system ($S = ½$, $I_{Ligand} = ½$, $I_{Metal} = 0$) with axial symmetry. a) the principal hyperfine frame of the proton is coincident with the g frame ($\theta_H = 0^{\circ}$). b) the angular dependency of the ENDOR spectra for a positive hyperfine tensor ($^{H}A_1 = {}^{H}A_2 = {}^{H}A_{\perp} = 5$ MHz, $^{H}A_3 = {}^{H}A_{\|} = 10$ MHz). In Figure c) a dipolar hyperfine tensor ($^{H}A_1 = {}^{H}A_2 = {}^{H}A_{\perp} = -5$ MHz, $^{H}A_3 = {}^{H}A_{\|} = 10$ MHz) is plotted and the profile is highlighted with a red trend line.[13]

and negative components, so that $^{H}A_{\perp}$ = -5 MHz and $^{H}A_{II}$ = 10 MHz (Figure 2.14c). In both cases the largest component of the tensor ($^{H}A_{II}$ = 10 MHz) is observed when θ_B = 0° (i.e., the applied magnetic field is aligned parallel to the *z* axis) while the smallest component ($^{H}A_{\perp}$ = 5 MHz) occurs when θ_B = 90°. At positions inbetween these fields, the hyperfine tensors have intermediate values of A_{II} and $A_{\perp}$. For the positive tensor, this means that the largest coupling of 10 MHz at the field position θ_B = 0°, gradually decreases to the smallest coupling of 5 MHz at the field position θ_B = 90°. However, for the purely dipolar tensor, with $^{H}A_{\perp}$ = -5 MHz, $^{H}A_{II}$ = 10 MHz, the coupling decreases from 10 MHz at the field position θ_B = 0°, until they cross after this field position, the coupling increases again up to 5 MHz at θ_B = 90°.

2.3.2b Coincident g and A frame – Case 2

The second case occurs when the *g* and *A* frame are coincident but orthogonal to each other as shown in Figure 2.15a. If the *g* and *A* frame are coincident but orthogonal to each other, the *A* frame is tilted by θ_H = 90° with respect to the z axis. At the selected orientation of θ_B =0°, g_{II} is aligned with the *x* axis of $A_{\perp}$. The angular dependency of the ^{1}H ENDOR spectra for this spin

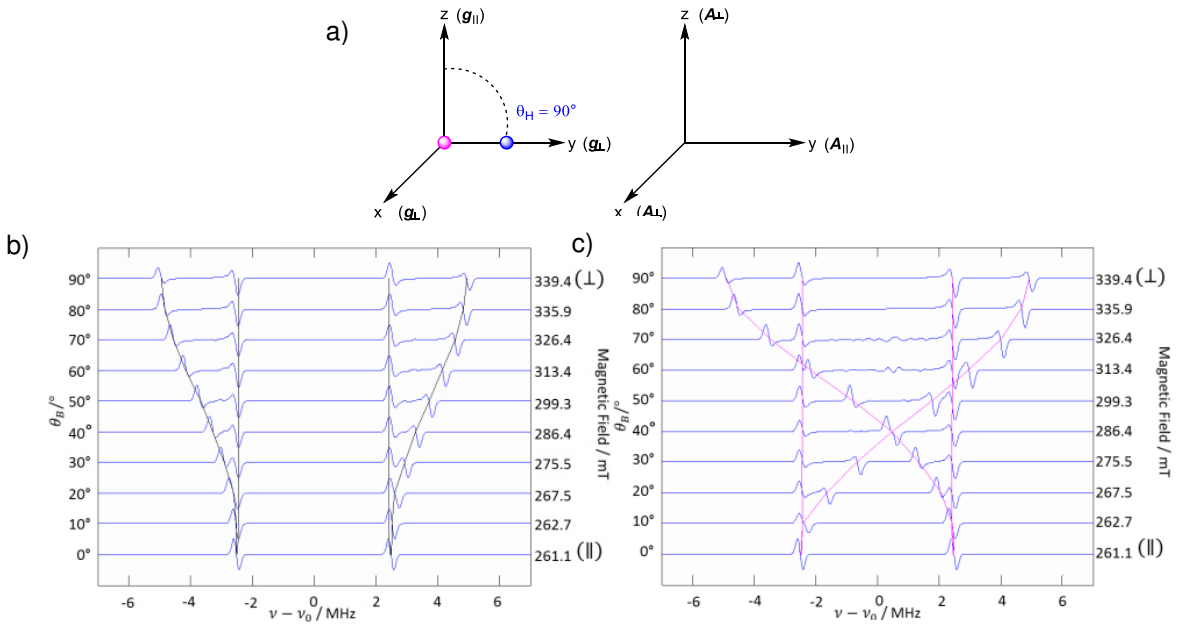

Figure 2.15 The field orientation (θ_B) dependence of the ^{1}H ENDOR for a system (S = ½, I_{Ligand} = ½, I_{Metal} = 0) with axial symmetry. a) shows that the parallel component of the hyperfine matrix of the protons lies in the perpendicular plane of the g matrix (θ_H = 90˚). b) illustrates an example plot for a positive hyperfine tensor of ($^{H}A_1 = {}^{H}A_2 = {}^{H}A_{\perp}$ = 5 MHz, $^{H}A_3 = {}^{H}A_{II}$ = 10 MHz) including a black trend line for the resulting hyperfine profile. c) illustrates

a dipolar hyperfine tensor ($^{H}A_1 = {}^{H}A_2 = {}^{H}A_\perp = -5$ MHz, $^{H}A_3 = {}^{H}A_\parallel = 10$ MHz) with red trend line of the resulting profile.[13]

system is illustrated in Figure 2.15b, c for positive ($^{H}A_\perp = 5$ MHz, $^{H}A_\parallel = 10$ MHz) (Figure 2.15b) and negative, or dipolar ($^{H}A_\perp = -5$ MHz, $^{H}A_\parallel = 10$ MHz) hyperfine tensors (Figure 2.15c). For both cases, a single proton coupling of $^{H}A_\perp = 5$ MHz at the field position $\theta_B = 0°$ is observed, since $A_\perp$ is aligned with $g_\parallel$. However, at $\theta_B = 90°$, two proton couplings are observed for the positive and dipolar proton hyperfine tensors. The two proton couplings are $^{H}A_\perp = 5$ MHz and $^{H}A_\parallel = 10$ MHz since $^{H}A_\parallel$ and $^{H}A_\perp$ are aligned with $g_\perp$ (Figure 2.15a). At intermediate field positions the contributions to the hyperfine coupling arises from $^{H}A_\parallel$ and $^{H}A_\perp$. Furthermore, as $^{H}A_\perp$ is aligned with $g_\parallel$ and $g_\perp$, the hyperfine coupling of 5 MHz, arises at each field position. This is true for both the positive hyperfine coupling tensor and the purely dipolar tensor. In the case of the positive hyperfine coupling, the $^{H}A_\parallel$ component gradually decreases from 10 MHz at $\theta_B = 90°$ to 5 MHz at $\theta_B = 0°$. In contrast to the positive hyperfine coupling, for the dipolar hyperfine coupling, $^{H}A_\parallel$ (10 MHz) decreases and at $\theta_B = 40°$ the lines cross and increase gradually to 5 MHz at the field position $\theta_B = 0°$.

2.3.2c Non-Coincident g and A axes – Case 3

In most real systems, the *g* and *A* frames are completely non-coincident, as shown below in Figure 2.16. In the specific example shown, the *z* axis of the proton frame is tilted by $\theta_H = 50°$ compared to the *g* frame, such that none of the three axes are aligned with the *g* frame. The resulting ^{1}H ENDOR spectra for such a system are therefore far more complicated than for the earlier cases described above, and simulation of the spectra is absolutely required to extract the correct hyperfine components.

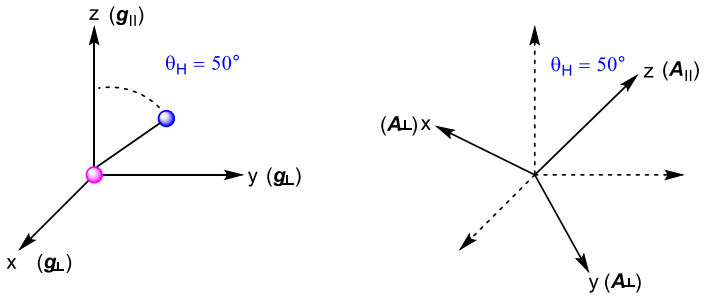

Figure 2.16 Orientation of the *g* and *A* frames relative to each other. The blue circle represents the change of the *A* frame by $\theta_H = 50°$. The resulting position overlaid on the *g* frame is also shown.[1,13]

2.3.3 Quadrupole Coupling (P)

All previously considered nuclear spin systems in this Chapter had I = ½. However, in this thesis Cu^{2+} complexes bearing coordinated ^{14}N-donor ligands, are studied. There are two isotopes of nitrogen, including ^{14}N and ^{15}N, with a nuclear spin of I = 1 and I = ½, respectively. However, since the natural abundance of ^{15}N is 0.364% this can be neglected for CW ENDOR studies; only the more abundant I =1 nucleus should be considered for EPR purposes.[1]

The quadrupole coupling is the interaction of the electric quadrupole moment Q of the nucleus for systems with $I \geq 1$, with the electric field gradient of the paramagnet.[28,29] Analysis of the resulting *nuclear-quadrupole parameter matrix* (**P**) therefore affords valuable information on the nature of the atomic orbitals at the nucleus and the electron distributions.

The quadrupole interaction, when smaller than the nuclear Zeeman and hyperfine interactions, only shifts the energy levels according to the nuclear states m_I. The quadrupole energy (or energy of alignment) is thus represented by the spin-Hamiltonian:

$$\hat{H}_0 = \boldsymbol{I} \cdot \boldsymbol{P} \cdot \boldsymbol{I} \tag{2.29}$$

Here **P** is a tensor which is traceless and symmetric as defined by:

$$\mathbf{P} = P\begin{bmatrix} 1 & 0 & 0 \\ & 1 & 0 \\ & & 2 \end{bmatrix} \tag{2.30}$$

and where P is given as:

$$P = \frac{e^2 qQ}{4I(2I \quad 1)} \tag{2.31}$$

The principal values of the nuclear quadrupole tensor are P_{xx} = [-($e^2qQ/4h$)](1-η), P_{yy} = [-($e^2qQ/4h$)](1+η), and P_{zz} = $e^2qQ/2h$. The asymmetry parameter (η) is equal to (P_{xx} - P_{yy})/P_{zz} with $|P_{zz}| > |P_{yy}| > |P_{xx}|$. Since the quadrupole tensor **P** is traceless, it is determined, apart from its orientation, by only two parameters. Usually in the literature and in this Thesis, the two quantities e^2qQ/h and η are reported. The dimensionless *asymmetry parameter* η also provides a measure of the field gradient deviation from uniaxial symmetry (ranging from η = 0 for uniaxial symmetry to η > 0 for rhombic symmetry).

2.4 Spectral simulation

Finally, it must also be stated that the above theory has demonstrated the wealth of information that can be accessed through the EPR and ENDOR measurements. The complexity of the experimental spectra, particularly the angular selective ENDOR, means that the accurate determination of the spin Hamiltonian parameters relies on computational simulation. Numerous simulation programmes are freely available, although throughout this Thesis the package *EasySpin* in *Matlab* has been used to analyse all spectra.

2.5 References

1. M. Brustolon, E. Giamello, Electron Paramagnetic Resonance: A Practitioner's Toolkit, *John Wiley & Sons*, **2009**.
2. K. Moebius, A. Savitsky*, J. Am. Chem. Soc.*, **2009**, 27, 1617-1659.
3. N. Ritterskamp, K. Sharples, E. Richards, A. Folli, M. Chiesa, J. A. Platts, D. M. Murphy, *Inorg. Chem.*, **2017**, 56, 11862–11875.
4. K. M. Sharples, C. Hughes, K. D. M. Harris, J. A. Platts, D. M. Murphy, *Phys. Chem. Chem. Phys.*, **2013**, 15, 15214–15222.
5. M. C. Lemon, M. Huyhn, A. G. Maher, B. L. Anderson, E. D. Bloch, D. C. Powers, D. G. Nocera, *Angew. Chemie Int. Ed.,* **2016**, 55, 2176–2180.
6. E. Carter, E. L. Hazeland,D. M. Murphy, B. D. Ward, *Dalton Trans.,* **2013**, 42**,** 15088-10596.
7. A. Weiss, P. Delpino, U. Bertsch, C. Panner, M. Mentler, L. Moroder, H. Kretschmar, F. Parak*, Vet. Microbiol.*, **2007**, 123, 358–366.
8. B. Bennett, J. M. Kowalski, *Methods Enzymol.*, **2015**, 563**,** 341–61.
9. S. Stoll, A. Schweiger, *Biol. Magn. Reson.*, **2007**, 27**,** 299–321.
10. S. Stoll, A. Schweiger, *J. Magn. Reson.*, **2006**, 178, 42–55.
11. S. Van Doorslaer, E. Vinck, *Phys. Chem. Chem. Phys.*, **2007**, 9**,** 4620-4638.
12. P. D. W. Boyd, A. D. Toy, T. D. Smith, J. R. Pilbrow, *J. Chem. Soc.*, **1970**, A, 1549–1563.
13. K. M. Sharples, Structural Characterisation of Cu II Complexes of Biological

Relevance and EPR and ENDOR investigation., *PhD Thesis*, Cardiff University, **2014**.
14. V. Chechik, E. Carter, D. M. Murphy, Electron Paramagnetic Resonance, *Oxford Chemistry Primers*, **2016**.
15. L. R. Falvello, *J. Chem. Soc., Dalton Trans.,* **1997***,* 4463–4475.
16. J. Echeverría,E. Cremades, A. J. Amoroso, S. Alvarez, *Chem. Commun.,* **2009**, 29, 4242–4244.
17. K. L. Ngai, *Magn. Prop.*, **1999**, 79**,** 1783–1797.
18. D. A. Turton, K. Wynne, K. *J. Phys. Chem. B*, **2014**, 118**,** 4600–4604.
19. J. McCoy,W. L. Hubbell, *Proc. Natl. Acad. Sci.*, **2011**, 108**,** 1331–1336.
20. J. Spencer, J. Stevens, C. Perry, D. M. Murphy, *Inorg. Chem.*, **2018**, 57, 10857-10866.
21. P. R. Cullis, *J. Magn. Reson.*, **1976**, 21**,** 397–418.
22. A. Ozarowski, I. B. Szymańska, T. Muziol, J. Jezierska, *J. Am. Chem. Soc.*, **2009**, 131, 10279-10292.
23. M. E. Owen, E. Carter, G. J. Hutchings, B. D. Ward, D. M. Murphy, *Dalton Trans.*, **2012**, 41**,** 11085–11092.
24. A. Savitsky, J. Niklas, J. H. Golbeck, K. Möbius, W. Lubitz, *J. Phys. Chem. B*, **2013**, 117, 11184-11199.
25. D. M. Murphy, R. D. Farley, *Chem. Soc. Rev.*, **2006**, 35, 249–268.
26. B. D. Howes, Z. H. Abraham, D. J. Lowe, T. Brüser, R. R. Eady, B. E. Smith, *Biochemistry*, **1994**, 33, 3171–3177.
27. B. Epel, C. S. Slutter, F. Neese, P. M. H. Kroneck, W. G. Zumft, I. Pecht, O. Pecht, Y. Lu, D. Goldfarber, *J. Am. Chem. Soc.*, **2002**, 124, 8152–8162.
28. H. A. Bechtel, A. H. Steeves, B. M. Wong, R. W. Field, *Angewandte Chemie*, **2008**, 120, 3011- 3014.
29. A. T. Taguchi, P. J., O'Malley, C. A. Wraight, S. A. Dikanov, *J. Phys. Chem. B*, **2014**, 118, 9225-9237.

Chapter 3: Experimental

3.1 Introduction

Within this Chapter an overview of the experimental procedures used throughout this thesis is given, including details of the characterisation techniques and synthesis methods. An outline of the instrumental setup of the EPR, ENDOR and HYSCORE spectrometer is also provided and the general sample preparation and measurement details are summarised.

HYSCORE and pulsed EPR and pulsed ENDOR spectra were recorded and analysed by Prof. Mario Chiesa.

3.2 Materials

3.2.1 Reagents

Reagents were commercially sourced from *Sigma Aldrich UK* at the highest purity level. The solvents were dried if necessary. Chloroform was dried over calcium hydride, whereas ethyl ether, tetrahydrofuran and toluene were purified using an *MBraun SPS-800* solvent purification system. Ultrapure water was obtained using a *Millipore milli Qplus 185* unit and deuterated solvents were obtained from *Sigma Aldrich UK* and *Goss Scientific* in sealed ampoules and used as received.

3.3 Synthetic Procedure

3.3.1 Preparation of [Cu(acac)(N-N)]CF_3SO_3 (N-N = bipy, phen or Py-bipy) [1]

The complexes [Cu(acac)(N-N)]CF_3SO_3, where N-N is 2,2'-bipyridine and 1,10-phenanthroline, hereafter labelled bipy and phen, respectively, used in this study were synthesised by *Kate Sharples*[2] according to the methods given by *Onawumi et al*[1]. This same synthesis route was also used for [Cu(acac)(N-N)]CF_3SO_3, where N-N is 2,3-di(2-pyridinyl)pyrazine, labelled as Py-bipy, as shown below.

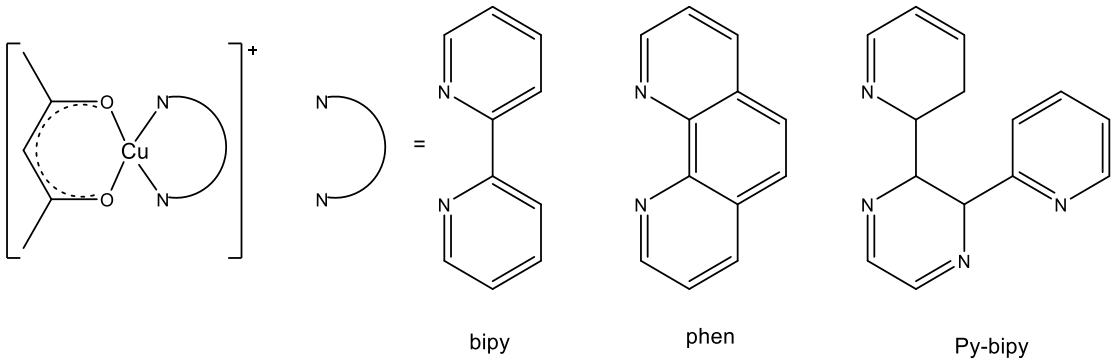

[Cu(acac)(2,2'-bipyrididne)]CF_3SO_3

$Cu(CF_3SO_3)_2$ (362 mg, 1 mmol) was dissolved in EtOH (10 mL) and acetylacetonate (103 µL, 1 mmol) was added. Afterwards solid diamine was added and a yellow solution was obtained. To the yellow solution an aqueous solution of NaOH (6 M, 200 µL) was added dropwise under stirring. The reaction was stirred at room temperature for 30 mins. and slowly evaporated for 72 hrs. which resulted in blue solid. This was washed with a small amount of cold ethyl ether. The product was isolated as teal plates (403 mg, 86 %).[2]

[Cu(acac)(1,10-phenanthroline)]CF_3SO_3

Prepared according to the preparation of [Cu(acac)(2,2'-bipyridine)]CF_3SO_3 using 1,10-phenanthroline (phen) (180 mg, 1 mmol). The product was isolated as teal plates (426 mg, 87 %).[2]

[Cu(acac)(2,3-di(pyridin-2-yl)pyrazine)]CF_3SO_3

Prepared according to the preparation of [Cu(acac)(2,2'-bipyridine)]CF_3SO_3 using 2,3-di(pyridin-2-yl)pyrazine (dpp4n) (234 mg, 1 mmol) instead. The product was isolated as a green solid with a yield of 0.070 g (9 %).

3.3.2 Preparation of [Cu(acac)(N'-N')]CF_3SO_3 [3]

[Cu(acac)(N-N)]CF3SO3, where N-N is dipyrido[3,2-a:2',3'-c]phenazine or dipyridol-2,3-phenazine-11-carboxylate, hereafter labelled dppz and dppCOOEt,

respectively, were synthesised by *Kate Sharples*[2] according to the method of *Chen et al.*[3]

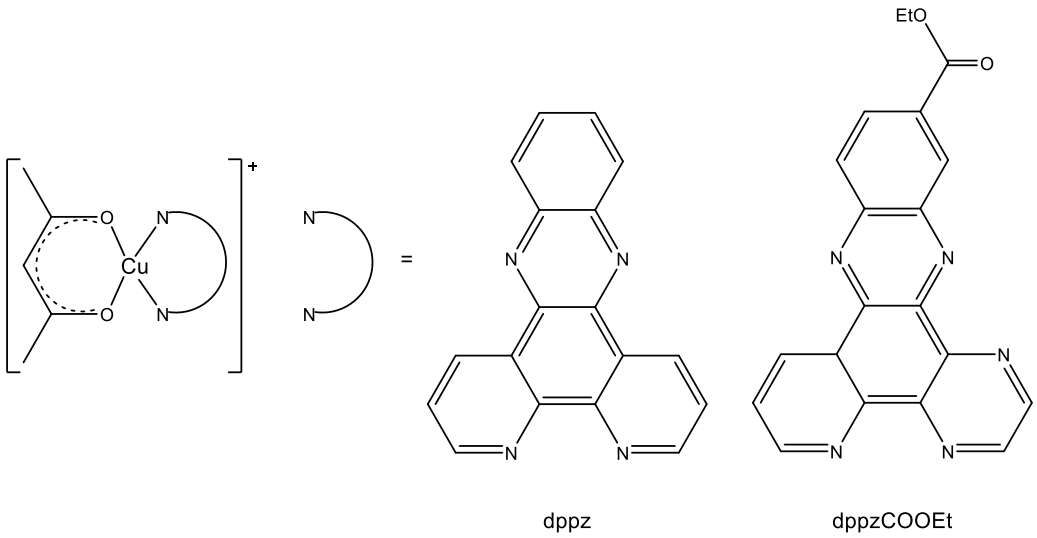

[Cu(acac)(dipyrido[3,2-a:2',3'-c]phenazine)]CF_3SO_3

Diimine was dissolved in MeOH (4 mL) and DMF (4 mL). The acetylacetone (10 µL, 97 µmol) was added and stirred for 10 min. KO^tBu was dissolved in H_2O and added dropwise to the yellow solution. A yellow precipitation was observed and then stirred for a further 30 min. To the yellow precipitation, $Cu(OTf)_2$ was dissolved in 1 mL H_2O. Immediately a green precipitation was observed and stirred for 6 h and then filtered. The product was recovered as a dark green solid (28 mg, 57%).[2]

[Cu(acac)(dipyridol-2,3-phenazine-11-carboxylate)]CF_3SO_3

Prepared according to the preparation of [Cu(acac)(dipyridol-2,2',3,3'-phenazine)]CF_3SO_3, using ethyl dipyridol-2,3-phenazine-11-carboxylate (dppzCOOEt) (354 mg, 1 mmol) instead. The product was recovered as a dark green solid (31 mg, 46%).[2]

3.3.3 Preparation of [Cu(di(2-picolyl)amine)]$(NO_3)_2$[4]

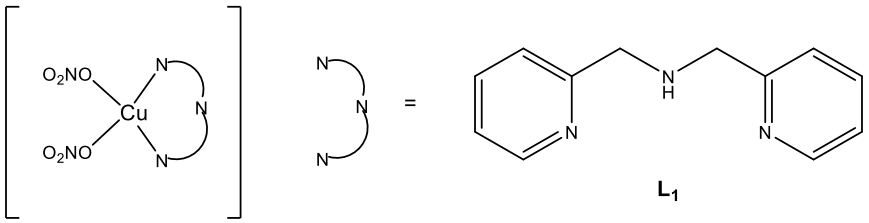

L_1

$Cu(NO_3)_2.3H_2O$ (24.1 mg, 0.1 mmol) was dissolved in 1 mL MeOH and added to di(2-picolyl)amine (**L_1**) (39.8 mg, 0.2 mmol) dissolved in 1 mL MeOH. The combined solution was stirred for 2 hrs. The dark blue powder was filtered and dried. A yield of 0.057 g (65 %) was obtained.

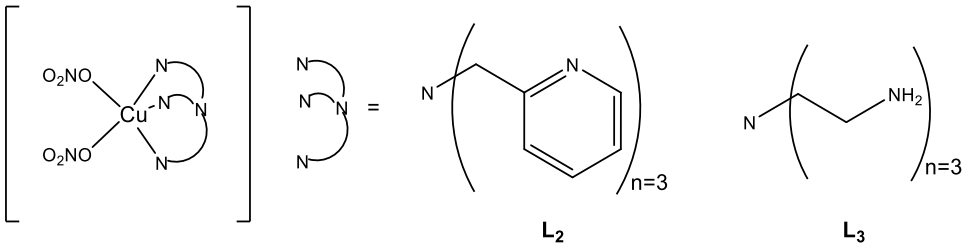

L_2 L_3

3.3.4 Preparation of [Cu(tris(2-pyridylmethyl)amine)$(NO_3)_2$]

Prepared according to the preparation of [Cu(di(2-picolyl)amine]$(NO_3)_2$ in section 3.3.3 using tris(2-pyridylmethyl)amine (**L_2**) (41.03 mg, 1 mmol) with the solvent system DMF:CHCl3 (1:1) instead. An Emulsion with purple precipitation was observed. After filtration, the product was obtained as a yellow solution.

3.3.5 Preparation of [Cu(tris(2-aminoethyl)amine)$(NO_3)_2$]

Prepared according to the preparation of [Cu(di(2-picolyl)amine]$(NO_3)_2$ in section 3.3.3 using tris(2-aminoethyl)amine (**L_3**) (30.26 mg, 1 mmol), with the solvent system DMF:CHCl3 (1:1) instead, resulting in a dark blue solution.

3.3.6. Preparation of [Cu(N-N)Cl_2] complexes

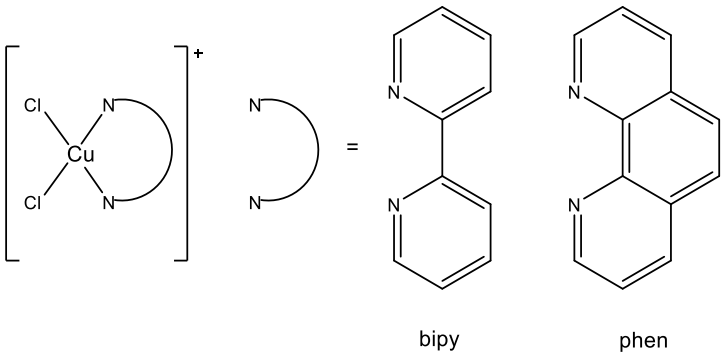

[Cu(2,2'-bipyridine)Cl_2] [5]

$CuCl_2$ (0.586 mg, 3.4 mmol) was dissolved in THF (2 mL) and acetonitrile (2 mL) and added to diimine (0.537 mg, 3.4 mmol). The solution was stirred for 24 hrs. A precipitation was observed, which was washed and air dried. The product was isolated as blue solid with a yield of 0.634 g (56 %).

[Cu(1,10-phenanthroline)Cl_2] [5]

Prepared according to the preparation of [Cu(2,2'-bipyridine)Cl_2] in section 3.3.6 using 1,10-phenanthroline (phen) (1.027 g, 5.7 mmol). The product was isolated as green solid with a yield of 1.70 g (84 %).

3.4 EPR characterisation

3.4.1 EPR and ENDOR measurements

The continuous wave (CW) X-band EPR measurements were performed on a *Bruker EMX* spectrometer utilizing an *ER4119HS resonator*, 100 kHz field modulation at 140 or 298 K, and typically using 10.17 mW MW power. The CW Q-band EPR and ENDOR measurements were recorded on a *Bruker Elexsys E500* spectrometer using a Bruker *ER5106 QT-E* Q-band resonator operating at 10 kHz field modulation and 10 K for ENDOR and for EPR at 100 kHz and 50 K. The CW ENDOR spectra were obtained using 5 dB RF attenuation (80 W) from an *ENI 3200L RF amplifier* at 100 kHz RF modulation depth and 0.5 mW microwave power. X-band Davies ENDOR measurements were recorded on *Bruker Elexsys E580* spectrometer and carried out using the following pulse

sequence: $\pi - T - \pi/2 - \tau - \pi - \tau$-echo. The experiments were done with MW pulse lengths of t_π = 256 ns, $t_{\pi/2}$ = 128 ns, and an interpulse time τ of 800 ns. An RF τ pulse of variable frequency and a length of 18 µs were applied during time T of 20 µs. The W-band EPR spectra were recorded at 20 K using at about 94 GHz using a Bruker Elexsys E-600 EPR spectrometer equipped with a E600-1021H TeraFlex resonator. A modulation amplitude of 7 Gauss was used.

3.4.2 Hyperfine Sublevel Correlation (HYSCORE) measurements

The HYSCORE experiments[6] were performed on a *Bruker Elexsys E580* spectrometer utilizing a Bruker *EN 4118X-MD4* pulsed EPR/ENDOR resonator at 10 K. The experiments were carried out with the pulse sequence $\pi/2 - \tau - \pi/2 - t_1 - \pi - t_2 - \pi/2 - \tau$-echo. The microwave pulse lengths $t_{\pi/2}$ = 16 ns and t_π = 16 ns were adopted. The time intervals t_1 and t_2 were varied in steps 16 ns starting from 100 to 3300 ns. The adopted shot repetition rate was 1 kHz. A four-step phase cycle was used for eliminating unwanted echoes. Spectra were recorded at two magnetic field positions, corresponding to B_0 = 338.6 mT ($g_\perp$ and B_0 = 283.2 mT) due to the single crystal-like position, m_I = -3/2, where only molecules with their g_z axis aligned along the external magnetic field are selected. The magnetic field was measured by means of *Bruker ER035 M* NMR gaussmeter. The choice of solvent system is dictated by the solubility of the studied system. However, potential for non-innocent interactions with the paramagnets and dielectric loss are important too, as an optimized glass is fundamental for structural analysis. It is important that, if the solution, including the paramagnet, is cooled down a glass with random ensemble of paramagnet is formed. Examples of suitable solvent system can be found in literature. In this project specifically, the solvent mixtures $CHCl_3$:DMF (1:1), acetonitrile:THF (1:1), EtOH:DMF (1:1) and H_2O:Glycerin (7:3) have been found to give a satisfactory glass. Samples for EPR X-band measurements were carried out at 0.02 mM and increased up to 0.03 mM for Q-band measurements. For $[Cu(acac)(N\text{-}N)]^+$ complexes a concentration of 0.03 mM (X-band) and 0.04 mM (Q-band) has been applied.

3.4.3 EPR sample preparation

EPR samples in frozen solution are required to be magnetically dilute, such that each paramagnet behaves independently. Otherwise magnetically concentrated samples tend to have significant line broadening caused by magnetic exchange, resulting in a loss in resolution and ultimately in structural information. To optimize the spectral resolution, the EPR samples are diluted on a molecular level, either in a solvent system or selection of single crystals.[7]

3.4.4 Experimental methods

Variable ratio studies with coordinating substrates

A series of solutions containing $[Cu(acac)_2]$ and imidazole in different ratios were prepared such that the ratio of copper to Im was systematically varied (0.5, 1, 2, 5, 10, 30, 40, and 50 equiv.) while the concentration of $[Cu(acac)_2]$ (0.02 M) and the composition of the $CHCl_3$:DMF (1:1) solvent was kept constant. The same procedure was used for variable ratio studies of $[Cu(acac)(N\text{-}N)]^+$ (0.03 M) complexes with either imidazole and L-histidine using copper to nitrogen base ratios of 1:2, 1:5, 1:10, 1:30, 1:50, 1:70 and 1:100. The composition of the solvent was kept constant within a series of measurements to ensure the quality of the frozen solution (140 K) and fluid solution (295 K) was unchanged.

For the variable study of $[Cu(NO_3)_2]$ with the ligand $\mathbf{L_1}$ (di(2-picolyl)amine), $\mathbf{L_2}$ (tris(2-pyridylmethyl)amine) or $\mathbf{L_3}$ (tris(2-aminoethyl)amine), the following procedure was applied. The variable ratio study was conducted for ratios of 1:0, 1:1, 1:2, 1:5, 1:10 and 1:50 of $[Cu(NO_3)_2]$ with either $\mathbf{L_1}$, $\mathbf{L_2}$ or $\mathbf{L_3}$. The general preparation was carried out in a DMF:$CHCl_3$ (1:1) solvent system. A 1 M Stock solution of $[Cu(NO_3)_2]$ was prepared and added to 1:1, 1:5, 1:10 or 1:50 (Cu^{2+}:**L**) equivalent solution of the desired ligand. The combined solution was stirred for two hrs and if necessary purified.

Variable Temperature Study

Variable temperature (VT) studies (10 K - 300 K) were typically conducted in 10 K increments. Progressive cooling of the cavity, as opposed to gradual heating of the cavity, combined with a flow of N_2 gas through the resonator helped

to limit condensation in the cavity. Samples were left at each operating temperature for *ca*. 10 mins in order to ensure the sample reached thermal equilibrium, before beginning the acquisition of the spectrum to prevent falsify results.

Saturation study

Saturation studies were conducted in 2-5 dB increments at a constant temperature of 300 K, 140 K or 10 K, respectively. For the acquisition of the spectrum, the scan number was set to a fixed value for each saturation study to ensure consistency in the results.

3.4.5 Spectral simulations

All of the EPR, ENDOR, and HYSCORE simulations were performed using the *Easyspin*[8] software package running within the *MathWorks MatLab* environment. The rotational correlation times for the different complexes were computed in *Easyspin*[8] assuming an isotropic rotational diffusion in the fast motion regime. Once a value of the correlation time is imposed, line widths were computed using the Kivelson formulas[9] within the Redfield limit (motional narrowing)[10].

3.5 DFT calculations

3.5.1 Geometry Optimisation

Geometries of all species were fully optimized without symmetry constraint using the *M06-2X*[11] meta-hybrid functional and basis set of 6-31+G(d,p)[12–14] on light atoms and Stuttgart-Dresden effective core potential and basis set on Cu[15] using the Gaussian09 suite[16]. The resulting geometries were used estimate EPR parameters in *ORCA*[17] using the hybrid *PBE0*[18] functional and basis of EPRII[18,19] for light atoms and the Core Properties all-electron basis set for Cu[20] with spin-orbit effects accounted for in a mean field approach.[21]

3.6 References

1. O. O. E. Onawumi, O. O. P. Faboya, O. A. Odunola, T. K. Prasad, M. V. Rajasekharan, *Polyhedron*, **2008**, 27, 113–117.
2. K. M. Sharples, PhD thesis: Structural Characterisation of Cu(II) Complexes of Biological Relevance; An EPR and ENDOR investigation, *Cardiff University*, **2014**.
3. G.-J. Chen, X. Qiao, P.-Q. Qiao, G.-J. Xu, J.-Y. Xu, J.-L. Tian, W. Gu, X. Liu, S.-P. Yan, *J. Inorg. Biochem.*, **2011**, 105, 119–126
4. M. Palaniandavar, S. Mahadcvan,M. Köckerling, G. Henkel, *J. Chem. Soc. Dalton Trans.*, **2000**, 2, 1151–1154
5. M. Boltz, A. Blanc, G. Laugel, P. Pale, B. Louis, *Chinese J. Catal.*, **2011**, 32, 807–811
6. P. Höfer, A. Grupp, H. Nebenführ, M. Mehring, *Chem. Phys. Lett.*, **1986**, 132, 279–282.
7. M. Brustolon, E. Giamello, *Electron Paramagnetic Resonance: A Practitioner's Toolkit*., *John Wiley & Sons*, **2009**.
8. S. Stoll, A. Schweiger, *J. Magn. Reson.*, **2006**, 178, 42–55
9. N. M. Atherton, *Chem. Soc. Rev.*, **1993**, 22, 293–298.
10. J. H. Freed, G. K. Fraenkel, *J. Chem. Phys.*, **1963**, 39, 326–34.
11. Y. Zhao, D. G. Truhlar, *Theor. Chem. Acc.*, **2008**, 120, 215–241.
12. R. Ditchfield, W. J. Hehre, J. A. Pople, *J. Chem. Phys.*, **1971**, 54, 724–728.
13. P. C. Hariharan, J. A. Pople, *Theor. Chim. Acta*, **1973**, 28, 213–222
14. T. Clark, J. Chandrasekhar, G. W. Spitznagel, P. V. R. Schleyer, *J. Comput. Chem.*, **1983**, 4, 294–301
15. M. Dolg, U. Wedig, H. Stoll, H. Preuss, *J. Chem. Phys.*, **1987**, 861.
16. M. J. Frisch, G.W. Trucks, H. B. Schlegel, G. E. Scuseria, M.a. Robb, J. R. Cheeseman, G. Scalmani, V. Barone, B. Mennucci, G. A Petersson, Gaussian 09, *Wallingford CT*, **2010**.
17. F. Neese, *Rev. Comput. Mol. Sci.*, **2012**, 2, 73–7.
18. C. Adamo, V. Barone, *J. Chem. Phys.*, 1**999**, 110, 6158–6170.
19. V. Barone, A. Polimeno, Chapter 7 of Electron Paramagn. Reson. A Pract. Toolkit, *Wiley and Sons*, **2008**, 251–284.
20. The ORCA basis set CoreProp was used. This basis is based on theTurboMole DZ basis developed by Ahlrichs and coworkers and obtained from the basis set library under ftp.chemie.uni-karlsruhe.de/ pub/basen.
21. F. Neese, A. Wolf, T. Fleig, M. Reiher, B. A. Hess, *J. Chem. Phys.*, **2005**, 122, 204107-204117.

Chapter 4: Understanding the Coordination Modes of [Cu^{2+}(imidazole)$_{n=1,2}$] Adducts by EPR, ENDOR, HYSCORE and DFT Analysis

This study highlights the relevance of imidazole as a model substrate in medical biological research. Interactions between Cu^{2+} complexes and imidazole substrates are thus potentially important as model systems for the better understanding of Cu^{2+} coordination chemistry, and of wider relevance to study proteins and nuclei acids. Therefore, in this Chapter a detailed discussion on the coordination mode and structure of the Cu-based Im adducts will be described using a combination of EPR, hyperfine techniques and density functional theory (DFT).

4.1 Introduction

Transition metal ions play important roles in biological systems.[1] Haemoglobin and Myoglobin, for example, are oxygen transporting Fe-proteins in the human body and both involve the oxidation state change from Fe^{2+} to Fe^{3+} for the oxygen transport. Zinc is also involved in diverse enzymatic activities and processes associated with the brain, muscle, bones, kidney, liver as well as the general immune system and is most likely found in the Zn^{2+} oxidation state. The human body contains about 100-150 mg of copper, both in the Cu^{+} and Cu^{2+} state, particularly in copper proteins such as superoxide dismutase and cytochrome c oxidase. All these metal proteins display high catalytic activities, structural and geometric flexibility and good chemo-selectivity. Therefore, metal proteins remain an ambitious field of research in medicinal inorganic chemistry, pharmaceutical chemistry and biochemistry.[2-4]

Transition metal ions not only interact with proteins and amino acids, but also with nucleic acids and their components.[1, 2] For this reason, transition metals and their complexes have now become an important area of investigation as potentially new classes of anticancer agents. A special interest has focussed on Cu^{2+} complexes as these systems have shown less toxicity and higher likelihood for clinical exploitation compared to other metal complexes based on Ru, As, Au,

V and Ti.[5, 6] Unlike these latter metals, copper has an endogenous presence in human body and has proven its potential as an anti-cancer agent, not least due to its active role in proteins.[6-8]

For anti-cancer drug design, the range of oxidation states, coordination geometries and ligand structures available to Cu complexes also enables and supports a wider range of ligand design flexibility.[2,9] Unlike cisplatin and its derivatives, Cu complexes are believed to non-covalently bind to DNA, either through major and minor grooves or via intercalation between base pairs.[5,7] Nevertheless, detailed structural information on how these metal complexes bind to receptors, base pairs and their mode of action, remains vital for the complete understanding of the anti-cancer activity and to facilitate a broader program of rational drug design.

For these reasons, many analytical techniques are employed to analyse metal interactions and binding, including NMR, UV-vis, circular dichroism, isothermal calorimetry and X-ray crystallography. However, for paramagnetic compounds, the resolution offered by NMR is often compromised and considerably diminished. In such cases, the sophistication of information extracted by NMR can be matched by using **E**lectron **P**aramagnetic **R**esonance (EPR) spectroscopy.[1,10-12] EPR in combination with related hyperfine techniques, including **E**lectron **N**uclear **DO**uble **R**esonance (ENDOR) and **HY**perfine **S**ublevel **COR**relation Spectroscopy (HYSCORE), are extremely powerful spectroscopic methods to investigate the electronic and geometric structure of metal complexes and their interactions in biological systems.[13-18] In this study, the coordination modes of copper complexes will be investigated by EPR techniques, illustrating the scale of information obtainable by this technique. Imidazole (abbreviated hereafter to Im) was chosen as a model substrate to study copper binding, primarily because it is common to both protein and nucleic acids, and since it is present in histidine residues and purine bases, respectively, thereby rendering it biologically relevance.[9,11,12,19]

Scheme 4.1 Structures of (**1**) Imidazole (Im), (**2**) 2-Methyl-imidazole (Im-**2**), (**3**) 4(5)-Methyl-imidazole (Im-**3**) showing resonance structures, (**4**) Benzimidazole (Im-**4**), (**5**) Histidine, (**6**) Guanine and (**7**) Adenine.

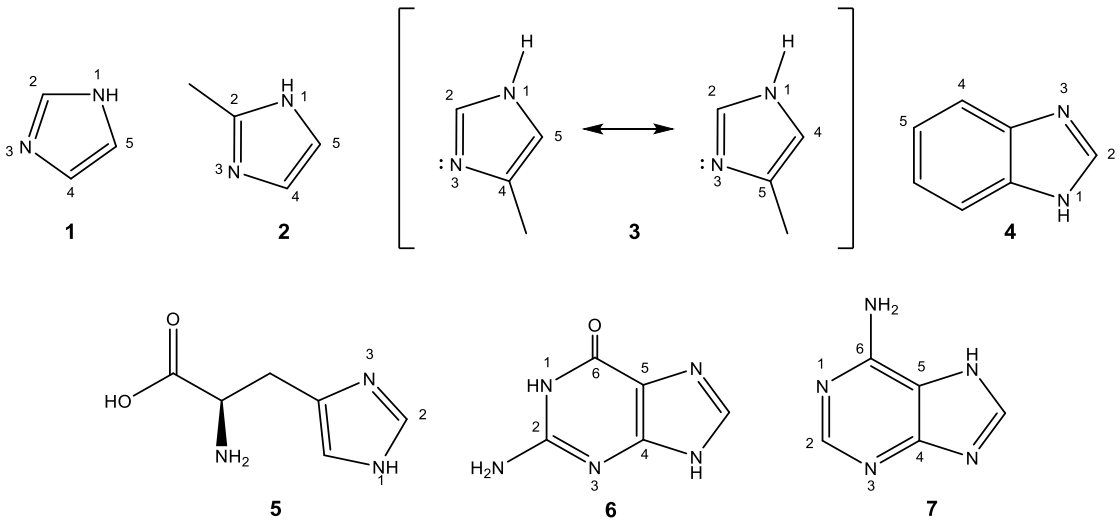

Coordination of imidazole to Cu^{2+} ions occurs readily, since in many copper proteins the imidazole ring of histidine coordinates by the imino nitrogen (N^3) and not by the amino nitrogen (N^1) of the imidazole unit. However, direct coordination of Cu^{2+} ions to DNA has been established to occur predominantly via the N^7 nitrogen of guanine (Scheme 4.1).[2,11]

It has been reported that Cu complexes bearing a variety of imidazole substitutes, such as methyl- and phenyl-benzimidazoles, have an impact on the related cytotoxicity. Indeed, detailed EPR and ENDOR studies of a Ru^{3+} based anticancer agent, including coordinated imidazole substrates, have been reported recently.[20,21] This study highlights the relevance of imidazole as a model substrate in medical biological research. Interactions between Cu^{2+} complexes and imidazole substrates are thus potentially important as model systems for the better understanding of Cu^{2+} coordination chemistry, and of wider relevance to study proteins and nuclei acids. Therefore, in this Chapter a detailed discussion on the coordination mode and structure of the Cu-based Im adducts will be described using a combination of EPR, hyperfine techniques and density functional theory (DFT).

4.2 Experimental Section

A detailed experimental section was already presented in Chapter 3. Therefore, only a brief summary of the key experimental points, relevant to this specific Chapter, are given here.

4.2.1 Materials

The bis(acetylacetano)-copper(II) complex, hereafter labelled [$Cu(acac)_2$], imidazole (**1**) (hereafter labelled Im), (**2**) 2-Methyl-imidazole (Im-**2**), (**3**) 4(5)-Methyl-imidazole (Im-**3**), (**4**) Benzimidazole (Im-4) and fully deuterated imidazole-d_4, were all purchased from *Sigma Aldrich* and used without further purification. Reagent grade $CHCl_3$ was purchased from *Fisher Scientific* and dried over calcium hydride. Reagent grade DMF was sourced from *Sigma Aldrich* and used as received. Deuterated solvents, including $CDCl_3$ and DMF-d_7, were obtained from *Goss Scientific* in sealed ampules and used without further purification.

4.2.2 Sample preparation

A series of solutions containing [$Cu(acac)_2$] and imidazole in different ratios were prepared such that the ratio of Cu^{2+} to Im was systematically varied (0.5, 1, 2, 5, 10, 30, 40 and 50 equiv.), whilst the concentration of [$Cu(acac)_2$] (0.02 M) and the composition of the $CHCl_3$:DMF (1:1) solvent was kept constant. The variable ratio study was monitored by CW X-band EPR in both frozen solution (140 K) and fluid solution (298 K). X-/Q-band CW EPR, CW ENDOR and X-band HYSCORE studies were conducted on samples containing [$Cu(acac)_2$]:Im molar ratios of 1:0 and 1:50 at 10 K using 0.03 M solutions prepared in $CDCl_3$:DMF-d_7 (1:1). All samples used for EPR, ENDOR and HYSCORE measurements were prepared on the bench. Dry $CHCl_3$ and DMF solvents were used to prepare the solutions.

4.3 Results and Discussion

4.3.1 CW EPR

The experimental and simulated CW EPR spectrum of the unbound [$Cu(acac)_2$] and bound [$Cu(acac)_2$]($Im_{n=1,2}$) complex in $CHCl_3$:DMF are shown in Figure 4.1 and the resulting spin Hamiltonian parameters for these complexes are listed in Table 4.1. For unbound [$Cu(acac)_2$] in frozen solution, it is known that the g and ^{Cu}A parameters depend subtly on the choice of solvent used.[22] In most cases, a well-defined signal is produced showing the ^{63,65}Cu isotope splitting, as evident on the low field hyperfine component. However, the solvent will have an impact on the resulting g and overall A values. Whilst very dry non-coordinating solvents, such as $CHCl_3$:Tol, give values of $g_{iso} = 2.117$ and $a_{iso} = 237$ MHz, weakly coordinating solvents such as $CHCl_3$:DMF, and even slightly wet $CHCl_3$:Tol solvents[22], produce notably different values, as in the current case with $g_{iso} = 2.135$ and $a_{iso} = 196$ MHz.

To investigate the nature and coordination mode of the adducts formed between [$Cu(acac)_2$] and Im, a speciation study was first performed by increasing the Cu:Im ratios from 1:0 up to 1:50 in the $CHCl_3$:DMF (1:1) solvent. Figure 4.2 illustrates the observed changes in the EPR spectra as the imidazole concentration was increased. At 1 equivalent of Cu:Im, a mixed EPR spectrum is observed, composed of unbound [$Cu(acac)_2$] bearing no Im coordination along with a second signal assigned to a bound [$Cu(acac)_2$Im] mono-adduct species. At 1:5 equivalent of Cu:Im, only this [$Cu(acac)_2$Im] mono-adduct is detected in the EPR spectrum. As the Cu:Im ratio is increased further, a third signal appears in the spectrum. This signal can be assigned to a [$Cu(acac)_2Im_2$] bis-adduct. At 1:50 equivalent of Cu:Im only this [$Cu(acac)_2Im_2$] bis-adduct is observed in the spectrum, as shown in Figure 4.3.

The experimental and simulated EPR spectra of the [$Cu(acac)_2Im_{n=1,2}$] mono- or bis-adduct, obtained at Cu:Im ratios of 1:5 and 1:50, are shown in Figure 4.1b and c, respectively. The [$Cu(acac)_2$Im] mono-adduct reveals a small increase in the g_3 value ($\Delta g_z = 0.022$) and a concomitant decrease in A_3 ($\Delta A_z = 48$ MHz) relative to the unbound [$Cu(acac)_2$] complex in the weakly coordinated $CHCl_3$:DMF (1:1) solvent system. These shifts in g_3 and A_3 are even larger when using dry non-coordinating $CHCl_3$:Tol (1:1) solvent ($\Delta g_z = 0.055$ and

ΔA_z = 100 MHz)[22] and are indicative of axial substrate coordination to the predominantly square planar Cu-O_4 environment in [$Cu(acac)_2$].[23] Comparing the coordinated Im adducts with various substituted pyridines for [$Cu(acac)_2$] in dry

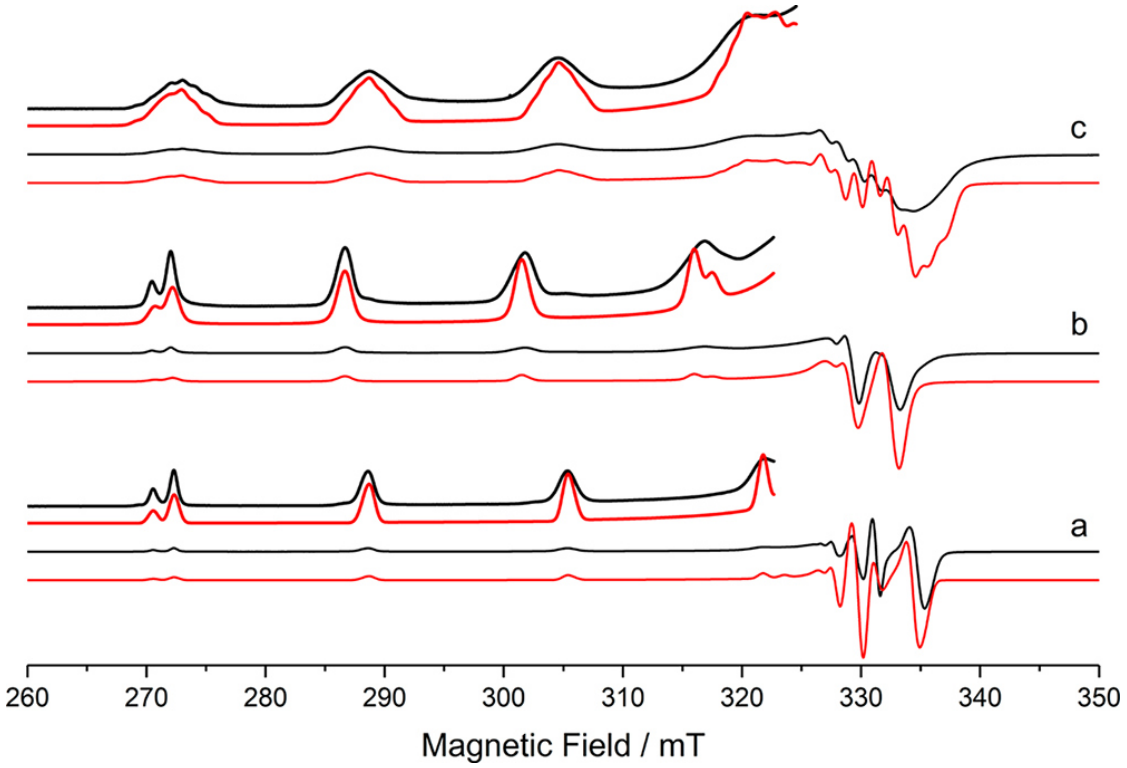

Figure 4.1 Experimental (black) and simulated (red) CW X-band EPR spectra of a) unbound [$Cu(acac)_2$], b) the [$Cu(acac)_2$Im] mono-adduct (Cu:Im ratio of 1:5) and c) the [$Cu(acac)_2Im_2$] bis-adduct (Cu:Im ratio 1:50). See Table 4.1 for spin Hamiltonian parameters.

Table 4.1 Spin Hamiltonian g and ^{Cu}A parameters for $[Cu(acac)_2Im_{n=0,1,2}]$ complexes and comparative literature values of *cis*-equatorial and *trans*-equatorial $Cu\text{-}O_4N_2$ type complexes.[a]

	g_1	g_2	g_3	g_{iso}	$^{Cu}A_1$	$^{Cu}A_2$	$^{Cu}A_3$	a_{iso}	**ref**
				unbound					
$[Cu(acac)_2]^f$	2.060[b]	2.060[b]	2.285[b]	2.135	-35[c]	-35[c]	-520[d]	-196[e]	*t.w*
$[Cu(acac)_2]^g$	2.048	2.052	2.252	2.117	-81	-58.5	572	-237	22
DFT	2.053	2.056	2.188	2.099	-130	-134	-891	-385	*t.w*
				monoadduct					
$[Cu(acac)_2Im]^f$	2.063[b]	2.063[b]	2.307[b]	2.114	26[c]	15[c]	472[d]	171[e]	*t.w*
$[Cu(acac)_2Im]^h$	2.060	2.060	2.260	2.127			557		
$[Cu(acac)_{2(}$Im-**2**$)]$	2.064	2.064	2.307	2.145	26[c]	15[c]	469[d]	170[e]	*t.w*
$[Cu(acac)_{2(}$Im-**3**$)]$	2.064	2.064	2.307	2.145	26[c]	15[c]	472[d]	171[e]	*t.w*
$[Cu(acac)_{2(}$Im-**4**$)]$	2.063	2.063	2.305	2.144	26[c]	15[c]	475[d]	172[e]	*t.w*
DFT	2.063	2.076	2.221	2.120	-34	-96	-855	-329	*t.w*
				bis-adduct					
$[Cu(acac)_2Im_2]^f$	2.059[b]	2.059[b]	2.288[b]	2.135	30	30	498[d]	186[e]	*t.w*
$[Cu(acac)_2($Im-**3**$)]^f$	2.063	2.063	2.289	2.138	30	30	496[d]	185[e]	*t.w*
				reference complexes					
	g_1	g_2	g_3	g_{iso}	$^{Cu}A_1$	$^{Cu}A_2$	$^{Cu}A_3$	a_{iso}	**ref**
				cis-equatorial					
$[Cu(acac)_2en]^i$	2.033	2.033	2.184	2.083	77	77	621		37
$[Cu(hfacac)_2bipy]^j$	2.056	2.056	2.299	2.137	77	77	486	213	38
$[Cu(nap)_2bipy]^k$	2.066	2.066	2.281	2.137			502		25
				Trans-equatiorial					
$[Cu(acac)_2Im_2]^h$	2.047	2.047	2.260	2.118			547		39
$[Cu(AcO)_2Im_2]^l$			2.267				486		18,32
$[Cu(nap)_2(4\text{-picoline})_2]^k$	2066	2.066	2.304	2.145			486		40
$DFT_{cis\text{-}mixed\ plane}$	2.070	2.109	2.248	2.142	47	-76	-834	-288	*t.w*
$DFT_{trans\text{-}axial}$	2.080	2.083	2.245	2.136	-21	-30	-843	-298	*t.w*
$DFT_{trans\text{-}equatorial}$	2.060	2.110	2.243	2.138	-151	154	-794	-264	*t.w*

[a]*t*w = this work; $^{Cu/N}A$ values given units of MHz. [b]±0.003. [c]±5. [d]±3. [e]±2. [f]$CHCl_3$:DMF (1:1). [g]$CHCl_3$:Tol (1:1). [h]DMSO:H_2O (90:10). [i]Single crystal. [j]Doped solid of [Zn(hfacac)2Bipy]:[Cu(hfacac)$_2$Bipy] (50:1). [k]CHCl3:CHCl2 (1:1). [l]H_2O. Ligand abbreviations: hfacac = hexafluoroacetylacetonate and nap = 2-nitroacetophenone.

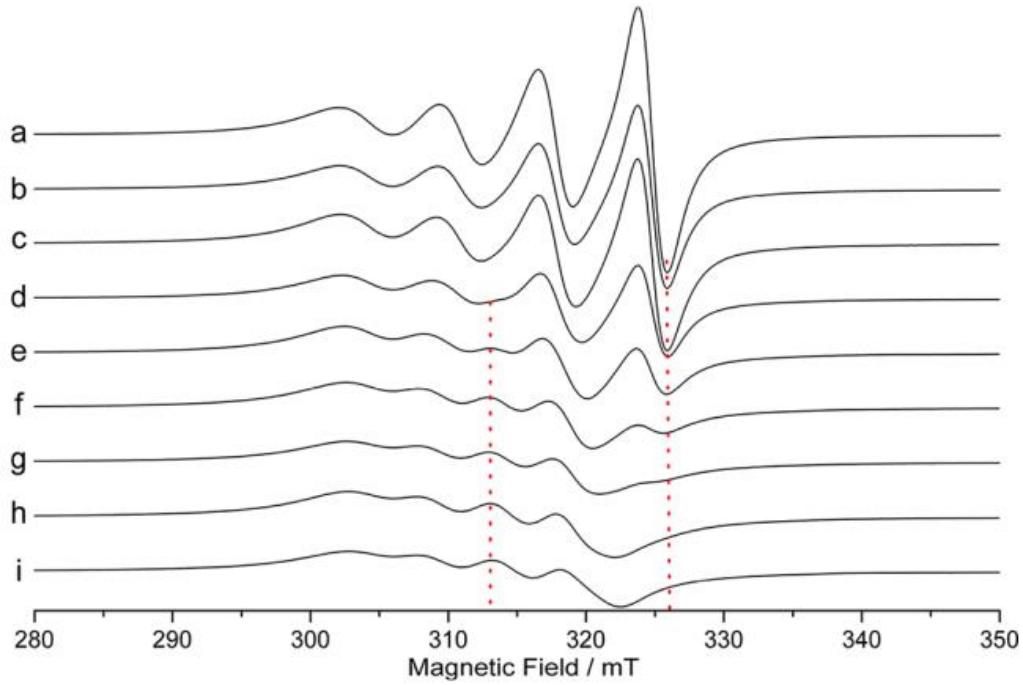

Figure 4.2 CW X-band EPR spectra (298 K) of $[Cu(acac)_2]$ recorded with increasing Cu:Im ratios of a) 1:0, b) 1:1, c) 1:2, d) 1:5, e) 1:10, f) 1:20, g) 1:30, h) 1:40 and i) 1:50.

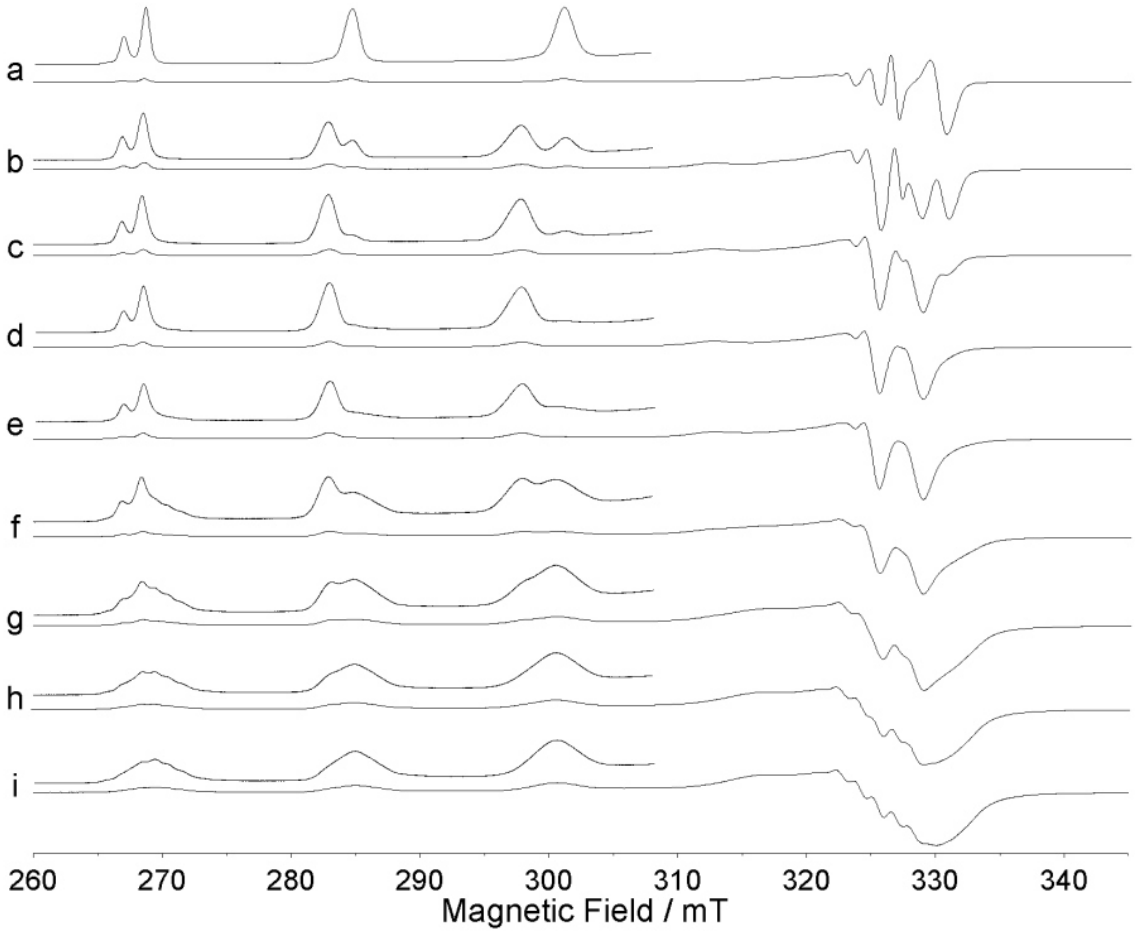

Figure 4.3 X-band CW EPR spectra (140 K) of $[Cu(acac)_2]$ in the presence of increasing ratios of imidazole; a) 1:0, b) 1:1, c) 1:2, d) 1:5, e) 1:10, f) 1:20, g) 1:30, h) 1:40 and i) 1:50.

non-coordinating $CHCl_3$:Tol suggested a stronger axial coordination of Im with $[Cu(acac)_2]$ than for the various substituted pyridines ($\Delta g_z = 0.043$, $\Delta A_z = 74$ MHz)[23] with $[Cu(acac)_2]$. This observation stands to reason considering that Im is a stronger base compared to pyridine. Mono-adducts of the type $[Cu(acac)_2Py]$, where Py refers to pyridine, methyl-pyridine or amine-methyl substituted pyridines, have already been formed at a Cu:Py ratio of 1:1. In addition, even at a Cu:Py ratio of 1:50, only $[Cu(acac)_2Py]$ mono-adducts were formed. Whereas the weakly coordinated $CHCl_3$:DMF solvent system currently used in this work contributes to the Cu:Im ratio of 1:5 required to form the axial $[Cu(acac)_2Im]$ mono-adduct. Nevertheless, the ^{14}N superhyperfine interaction in these axially coordinated square planar mono-adduct complexes bearing nitrogen bases, such as $[Cu(acac)_2Im]$, is not visible in the EPR spectrum due to the predominantly d_{xy} ground state for the Cu^{2+} ion.[23] Compared to substituted pyridine coordination, Im is able to coordinate more than once to $[Cu(acac)_2]$, which is observed at higher ratios of Cu:Im.

At a Cu:Im ratio of 1:50, a second Cu^{2+} signal is clearly visible in the EPR spectrum and appears at the expense of the $[Cu(acac)_2Im]$ mono-adduct signal, as see Figure 4.3g-i. The EPR signal of this adduct is predominantly axial and exhibits pronounced ^{14}N superhyperfine splitting in the parallel and perpendicular ^{Cu}A hyperfine components. Further analysis of the ^{14}N superhyperfine pattern suggests the presence of two equivalent nitrogen nuclei ($I = 1$) originating from two (equatorially) bound Im bases in a six-coordinate $[Cu(acac)_2Im_2]$ bis-adduct. According to the literature,[9,24] for equatorial bound nitrogen bases, it is reasonable to presume an equatorial Im coordination rather than a bis-axial coordination, which causes the large superhyperfine splitting. The simulated spin Hamiltonian g and ^{Cu}A parameters for this $[Cu(acac)_2Im_2]$ bis-adduct are listed in Table 4.1. For a more accurate determination of the ^{14}N hyperfine values, hyperfine measurements were used and the resulting ^{14}N values are given in Table 4.1. Therefore, it can be concluded that the structural nature of the $[Cu(acac)_2Im_2]$ bis-adduct cannot reliably be extracted from the frozen solution EPR spectrum alone.

Scheme 4.2 Schematic illustration showing a) unbound [Cu(acac)$_2$] and b) [Cu(acac)$_2$Im] axial mono-adduct and the structural isomers of the [Cu(acac)$_2$Im$_2$] bis-adducts, including c) *trans*-axial, d) *cis*-mixed plane, e) *trans*-equatorial and f) *cis*-equatorial.

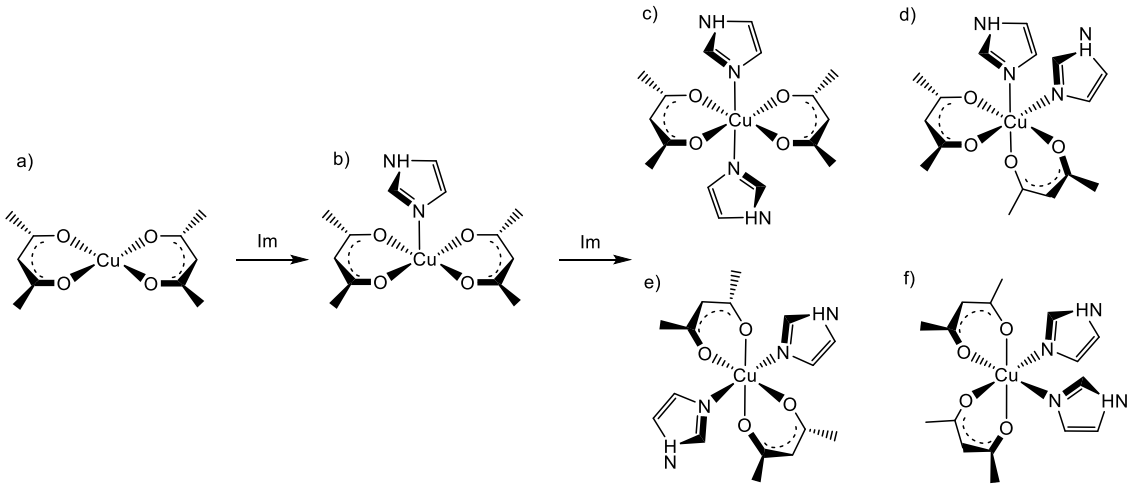

The observed *g* values ($g_\perp$ = 2.059 and $g_\parallel$ = 2.288) are consistent with a Cu^{2+} centre in an axially elongated tetragonal ligand field ($g_\parallel > g_\perp$).[24,25] Also, the ^{14}N superhyperfine pattern shown in Figure 4.1c and Figure 4.3i, indicates that both Im substrates must be coordinated in the equatorial (*xy*) plane and therefore limiting the plausible coordination geometries to *trans*-equatorial or *cis*-equatorial (Scheme 4.2). Comparing the Cu-O_4N_2 environments with *cis*-equatorial and *trans*-equatorial geometries based on the representative *g* and ^{Cu}A parameters, does not help to easily differentiate these geometries by EPR alone, primarily due to their reasonable variation in the *g* and ^{Cu}A values for both coordination isomers (Table 4.1). In addition, theory would suggest that the point group symmetries for MA_4B_2-type complexes for *trans*- and *cis*-equatorial isomers should produce different axial or rhombic **g** tensors. In practice the resulting distortion that occurs in the complexes coupled with the broad line-widths experienced in frozen solution does not allow one to detect their small differences in *g* and ^{Cu}A anisotropy at X- or Q-band frequencies. It can also be excluded that Im displaces the acac ligand in the complex, because the spectral features observed in Figure 4.1 are not consistent with those arising from [Cu(Im)$_4$].[11]

In addition, formation of the mono- and bis-adducts are expected to be temperature dependent as evidenced by the v.t. EPR spectra of the mono- and bis-adduct at 140 K and 298 K. At 140 K, the X-band EPR spectra showed a distribution of copper species, including those arising from unbound [Cu(acac)$_2$],

Table 4.2 Rotational correlation times and line width contributions for the room temperature (298 K) X-band CW EPR spectra of the $[Cu(acac)_2Im_{n=0,1,2}]$ complexes.[a]

species	lw m_I = +3/2	lw m_I = +1/2	lw m_I = -1/2	lw m_I = -3/2	τ_R
$[Cu(acac)_2]$	151.33	0.9 ± 0.1	15 ± 15	-10 ± 15	0 ± 15[b]
$[Cu(acac)_2Im]$	156.94	0.2	-14.1	88.2	2.4[c]
$[Cu(acac)_2Im_2]$	137.32	0.1	-21.4	42.1	18.3[b]

[a]The line widths (lw) of each of m_I line are given in MHz. The rotational correlation times (τ_R) are given in ps with uncertainties of [b]±10 ps. [c]±20 ps

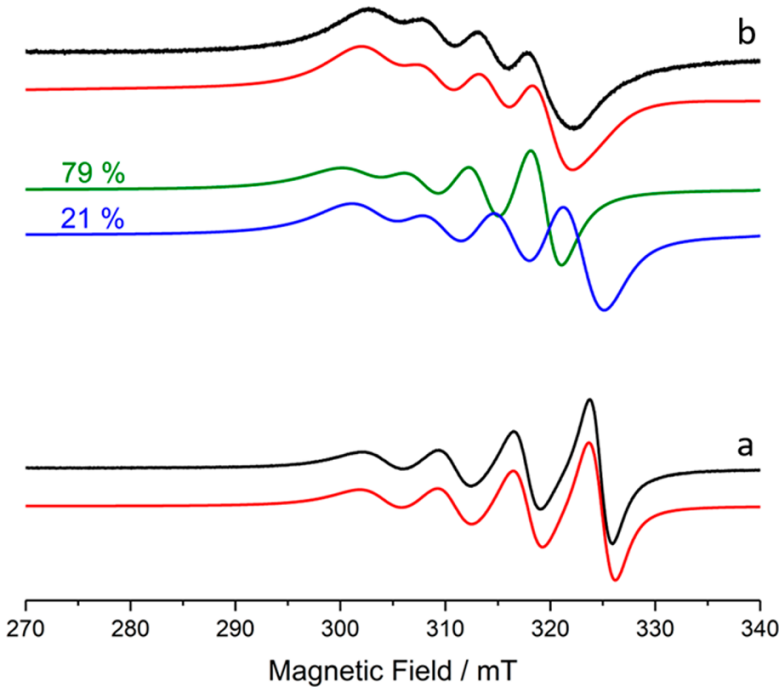

Figure 4.4 Experimental (black) and simulated (red) X-band CW EPR spectra (298 K) of $[Cu(acac)_2]$ recorded with a Cu:Im ratios of a) 1:0 and b) 1:50. The deconvoluted simulation of b), shown in the green and blue traces, is due to 79 % $[Cu(acac)_2Im]$ (green) and 21 % $[Cu(acac)_2Im_2]$ (blue). The spectra were recorded in a $CHCl_3$:DMF (1:1) solvent. The simulation parameters are listed in Table 4.2.

$[Cu(acac)_2Im]$ and $[Cu(acac)_2Im_2]$, depending on the ratios of Cu to Im used (see Figure 4.3). The mono-adduct was almost exclusively formed at a ratio of Cu:Im of 1:10 at 140 K, whereas the $[Cu(acac)_2Im_2]$ was dominant at a ratio of Cu:Im 1:50 (Figure 4.3). However, at 298 K, a wider distribution of copper adducts was observed in the X-band EPR spectra depending on the Cu:Im used. The isotropic EPR spectra were simulated by using the anisotropic spin Hamiltonian parameters listed in Table 4.1 and in the fast motional regime using *Easyspin*. The resulting rotational correlation times (τ_R) are given in Table 4.2. Representative examples of the simulated EPR spectra for the Cu:Im ratios 1:10 and 1:50 are shown in Figure 4.4. According to the analysis of the isotropic simulation, the EPR spectrum at a low ratio of Cu:Im (1:10) bears a contribution from both unbound $[Cu(acac)_2]$ (45.5 %) and $[Cu(acac)_2Im]$ (54.5 %). However, for a Cu:Im ratio of 1:50, the room temperature isotropic spectrum shown in Figure 4.4 contains a contribution of 79.0 % $[Cu(acac)_2Im]$ and 21.0 % $[Cu(acac)_2Im_2]$, unlike the 140 K equivalent spectrum in Figure 4.1 which revealed only the presence of the $[Cu(acac)_2Im_2]$ bis-adduct. It should also be noted that the integrated EPR signal intensity in the room temperature spectrum was found to decrease by *ca.* 45 % as the Im concentration in solution increased, as illustrated in Appendix, Figure C.1b. A similar trend was also found in the 140 K frozen solution EPR spectra. Anderson *et al.*,[11] also reported a reduced Cu^{2+} signal with high Im concentrations and ascribed the observations to the possible precipitation of coordination polymers, such as $[Cu(Im)_2(Im^-)]_n^{m+}$, and the bridging ligands for the coordination polymers were suggested to be anionic Im^-. Certainly, under basic conditions, deprotonation at the N^1 atom will produce an imidazolate anion (Im^-), which is well documented to bridge transition metal ions trough N^1 and N^3 coordination.[10,19,26-28] Moreover, imidazole bridges are present in SOD,[4] and other multimetal enzymes, that can mediate magnetic couplings between metal centers.[29-31] Therefore, although no precipitation was evident in the current study, it seems reasonable that the observed loss of Cu^{2+} signal is partially caused by spin-spin interactions occurring via Im^- bridged polymer complexes of the type $[Cu(acac)(Im)(Im^-)]_n^{m+}$, similar to those reported by Anderson *et al.*[11]

4.3.2 DFT analysis of the Cu-adducts

The geometry optimized structure of the axial mono-adduct was calculated and found to be square pyramidal with an Im ligand axially coordinated, as shown in Figure 4.5a. The resulting Cu-N distance has a length of 2.27 Å and all Cu-O distances range between 1.97 Å and 1.98 Å. The geometry optimized *cis*-mixed plane structure for the $[Cu(acac)_2Im_2]$ bis-adduct was characterized by one axial and one equatorial Im ligand (Figure 4.5b) at Cu-N distances of 2.35 Å and 2.08 Å, respectively. For the three equatorial positions of Cu-O, the distances were found to be between 1.99 Å and 2.01 Å and the axial Cu-O distance was 2.22 Å.

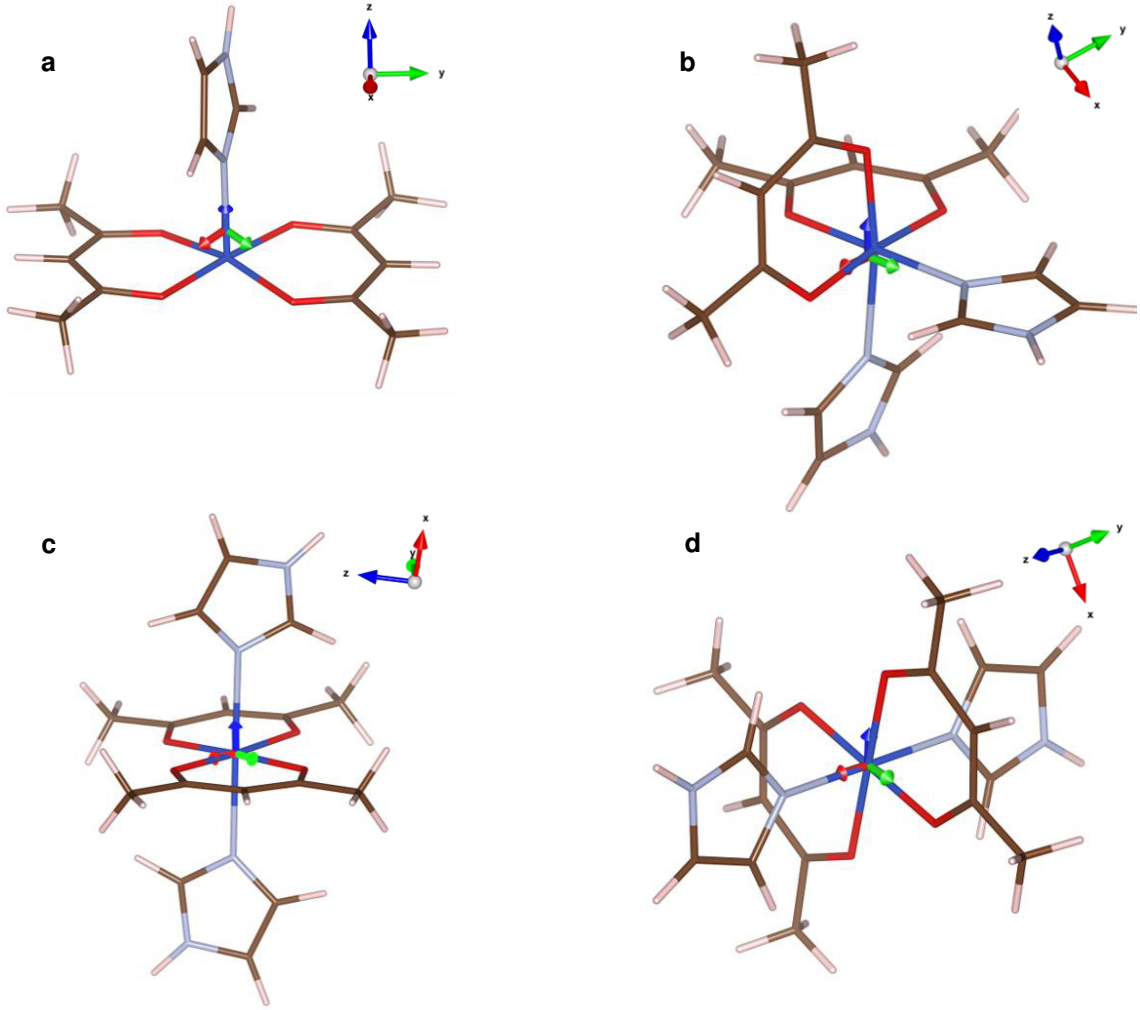

Figure 4.5 Geometry optimized structures for a) mono-axial $[Cu(acac)_2Im]$, b) cis-mixed plane, c) trans-axial, and d) trans-equatorial isomers of the $[Cu(acac)_2Im_2]$ adduct. In each structure, the *g* frame is reported on the Cu atom with the same colour coding as the molecular frame on the right-hand side of each structure: *x*, *y* (green) and *z* (blue).

The differences in the Cu-O distances can be explained by Jahn-Teller elongation of one Cu-N and one Cu-O bonds. The *trans*-axial [$Cu(acac)_2Im_2$] bis-adduct was found to have both of the Im ligands in the axial position with Cu-N distances of 2.35 Å and 2.34 Å. The Cu-O bond lengths range between 1.99 Å and 2.00 Å. In contrast, the *trans*-equatorial [$Cu(acac)_2Im_2$] adduct was established to be a Jahn-Teller distorted octahedral complex with both Im ligands occupying equatorial positions, as shown in Figure 4.5d, at Cu-N distances equal to 2.00 Å. Two Cu-O distances measure 2.05 Å and correspond to the equatorial oxygen atoms, while the remaining two Cu-O bonds, measuring 2.17 Å, are consistent with oxygen atoms in axial positions. It should be noted that the *trans*-equatorial structure was predicted to lie 23.0 kJ mol^{-1} higher in energy compared to the *trans*-axial structure and 17.3 kJ mol^{-1} higher than the *cis*-mixed plane at the *M06-2X (PBE0)* level and these energy differences are ascribed to the choice of functional and basis set used (Appendix, Table C.2).

4.3.3 CW ^{1}H ENDOR

In the case of [$Cu(acac)_2Im$], the geometry could be determined using EPR alone. In other words, to reliably distinguish between the two structural isomers of *cis*-mixed plane and *trans*-equatorial [$Cu(acac)_2Im_2$], EPR alone is not enough. Therefore, ^{1}H ENDOR experiments were used to discriminate between the possible structures formed in frozen solution. A complete angular selective ^{1}H ENDOR analysis can be used to extract structural information on the coordination geometry of the $Cu-O_4$ plane in [$Cu(acac)_2Im_2$].[23] To distinguish Im derived proton couplings from the bis(acetylacetonate) ligand in the Q-band ^{1}H ENDOR spectra, both protic and deuterated Im (Appendix, Figure C.3) were used (*i.e.,* [$Cu(acac)_2Im_2$] and [$Cu(acac)_2Im\text{-}d_4)_2$]. The remaining proton couplings observed in the Q-band ^{1}H ENDOR spectra must then arise from the proton of the bis(acetylacetonate) ligand itself. Looking at the ^{1}H ENDOR spectra of only the unbound [$Cu(acac)_2$][22] complex reveals couplings that arise from the methine protons, the averaged methyl group protons and a subset of methyl group protons undergoing hindered rotation on the EPR time scale such that a very anisotropic hyperfine tensor is produced. This hindered rotation was found to occur in 120° jumps creating a large $A_{dipolar}$ and a_{iso} component, which are always observed in the spectra and are greater than the fully averaged methyl group tensor.[22] Taking

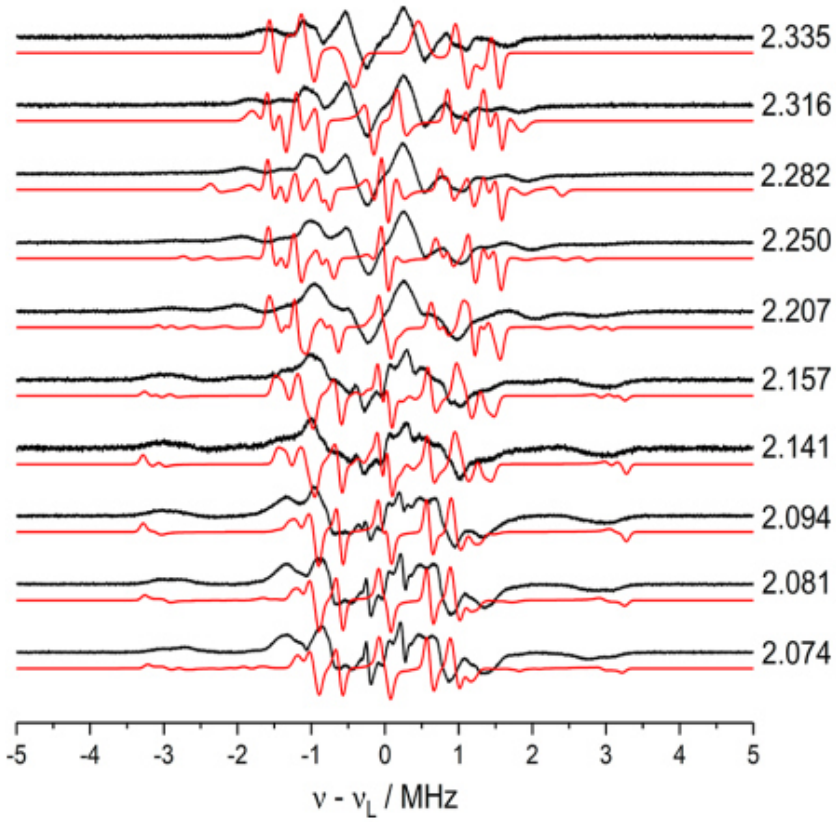

Figure 4.6 CW Q-band ^{1}H ENDOR spectra (10 K) of the $[Cu(acac)_2Im_2]$ bis-adduct dissolved in dry $CDCl_3$:DMF-d_7 (1:1) recorded at the field positions corresponding to the *g* values indicated beside each spectrum. Corresponding simulations are shown in red.

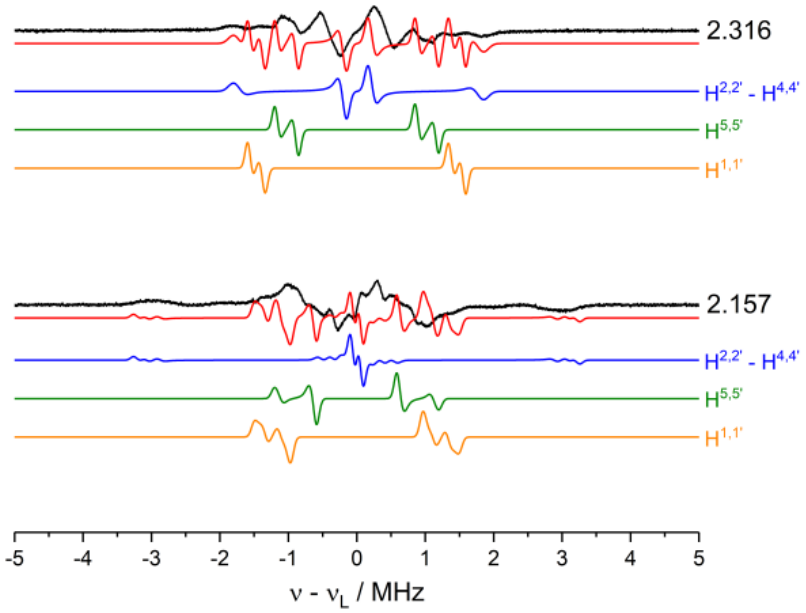

Figure 4.7 Experimental (black) and simulated (red) X-band ^{1}H ENDOR spectra (10 K) of the $[Cu(acac)_2Im_2]$ bis-adduct dissolved in dry $CDCl_3$:DMF-d7 (1:1), recorded at the two field positions corresponding to g = 2.316 and 2.57 (see Figure 4.1). The deconvoluted contributions to the simulations are: $H^{2,2'}$ – $H^{4,4'}$ (blue), $H^{5,5'}$ (green), $H^{1,1'}$ (orange).

Table 4.3 ^{1}H principal hyperfine values for $[Cu(acac)_2Im_2]$ complex dissolved in $CDCl_3$:DMF-d_7 (1:1).

atom	α	β	γ	A_x	A_y	A_z	a_{iso}
				$[Cu(acac)_2Im_{n=2}]$: experimental (ENDOR)			
set I (H^2/H^4)	20	45	-10	0.10	-0.14	6.55	2.17
set II (H^5)	10	75	0	1.21	1.17	2.43	1.60
set III (H^1)	30	20	-30	3.15	1.80	1.95	2.30
				Mono-adduct $[Cu(acac)_2Im_{n=1}]$: DFT			
H^4	-19.9	70.3	22.8	2.83	-1.47	-1.39	-0.01
H^2	-30.3	40.90	-33.90	-2.06	-1.83	3.98	0.03
H^5	-2.0	83.50	37.10	0.76	-0.48	-0.47	-0.06
H^1	-26.9	21.7	-42.5	-0.56	-0.56	0.90	-0.07
				cis-mixed $[Cu(acac)_2Im_{n=2}]$: DFT			
H^4	-25.4	32.2	11.8	-1.61	-1.80	3.38	-0.01
H^2	-3.0	56.0	-0.10	3.25	-1.65	-1.55	0.02
H^5	5.1	14.4	41.00	-0.48	-0.48	0.8	-0.05
H^1	-6.8	74.7	-4.8	0.83	-0.55	-0.54	-0.09
$H^{4'}$	1.7	87.8	-44.0	-0.65	6.03	0.17	1.85
$H^{2'}$	-2.6	88.8	36.60	-1.22	5.95	-0.54	1.40
$H^{5'}$	38.1	0.8	-55.10	0.33	2.11	0.24	0.89
$H^{1'}$	-1.2	87.2	13.9	0.47	2.42	0.65	1.18
				trans-axial $[Cu(acac)_2Im_{n=2}]$: DFT			
H^4	13.6	64.1	19.4	2.76	-1.39	-1.47	-0.03
H^2	-21.2	38.8	44.8	-2.01	-1.79	3.83	0.01
H^5	3.8	84.4	34.8	0.74	-0.47	-0.47	-0.07
H^1	-10.5	19.4	39.9	-0.57	-0.56	0.86	-0.09
$H^{4'}$	-13.5	64.9	48.6	2.69	-1.35	-1.43	-0.03
$H^{2'}$	16.5	39.5	26.1	-2.07	-1.83	3.92	0.01
$H^{5'}$	-6.0	86.2	39.2	0.74	-0.46	-0.47	-0.06
$H^{1'}$	0.6	20.6	35.2	-0.57	-0.56	0.88	-0.08
				trans-equatorial $[Cu(acac)_2Im_{n=2}]$: DFT			
H^4	24.3	44.6	-11.2	0.09	-0.14	6.55	2.16
H^2	31.3	55.3	-41.2	6.52	-0.44	-0.31	1.92
H^5	16.1	74.9	-4.8	0.51	0.47	2.43	1.14
H^1	32.8	21.1	-34.2	3.15	1.10	1.25	1.83
$H^{4'}$	29.1	45.2	-13.2	0.10	-0.14	6.55	2.17
$H^{2'}$	33.6	57.0	-43.0	6.50	-0.44	-0.31	1.92
$H^{5'}$	18.9	75.1	-5.4	0.51	0.46	2.43	1.13
$H^{1'}$	38.9	22.9	-40.1	3.14	1.09	1.24	1.82

[a]For comparison, the DFT calculated ^{1}H hyperfine tensors for the geometry optimized adducts are also listed. Euler rotation of hyperfine tensor **A** to **g** tensor is given as a set of three Euler angles based on the *zyz'* convention. Euler angles are in degrees and their uncertainties are listed in footnotes a and b. [b]±10°: hyperfine tensor principal values are in MHz with uncertainty. [c]±0.4 MHz: for the bis-adducts, the protons from one Im unit are labelled $H^{1\text{-}5}$, and for the second Im unit, they are labelled $H^{1'\text{-}5'}$.

Table 4.4 Experimental and DFT calculated ^{14}N hyperfine and nuclear quadrupole values of the $[Cu(acac)_2Im_2]$ bis-adduct.

label	α	β	γ	A_x	A_y	A_z	a_{iso}	$\lvert e^2qQ/h \rvert$	η	α'	β'	γ'
					$[Cu(acac)_2Im_{n=2}]$: experimental							
Imino $N^{3,3'}$ (ENDOR)	0 ± 10	0 ± 10	-90 ± 5	34.8 ± 0.2	43.5 ± 0.4	34.0 ± 0.4	37.4 ± 0.4	2.2 ± 0.1	0.2 ± 0.1	0 ± 10	0 ± 10	-90 ± 5
Amine $N^{1,1'}$ (HYSCORE)	85 ± 5	80 ± 10	0	1.5 ± 0.2	1.4 ± 0.2	2.5 ± 0.2	1.8 ± 0.2	1.4 ± 0.1	0.9 ± 0.1	15 ± 15	-10 ± 15	0 ± 15
					cis-mixed $[Cu(acac)_2Im_2]$							
Imino N^3	-0.7	88.8	7.3	-0.50	-1.42	-1.42	-1.11	3.4	0.2	-14.1	88.2	2.4
Amine N^1	-7.2	79.8	-1.7	0.02	-0.16	-0.16	-0.10	2.9	0.1	-21.4	42.1	18.3
Imino $N^{3'}$	-1.3	86.9	-1.8	29.25	35.95	28.55	31.25	2.7	0.4	-0.1	87.1	-0.5
Amine N1'	0	87.5	1.4	1.46	1.96	1.60	1.67	2.8	0.05	1.6	87.8	-35.1
					trans-axial $[Cu(acac)_2Im_2]$							
Imino N^3	5.7	1.1	108.6	-1.62	-1.64	-0.74	-1.33	3.4	0.2	24.4	11.6	23.7
Amine N^1	7.4	14.0	39.2	-0.17	-0.17	0.01	-0.11	2.9	0.1	5.2	63.3	44.5
Imino $N^{3'}$	6.6	1.4	-40.1	-1.61	-1.63	-0.73	-1.32	3.4	0.2	-35.6	14.5	57.1
Amine $N^{1'}$	-12.2	15.0	36.9	-0.16	-0.17	0.01	-0.11	2.9	0.1	-9.1	64.9	27.2
					trans-axial $[Cu(acac)_2Im_2]$							
Imino N^3	-6.9	8.3	-85.0	37.45	45.31	36.40	39.72	2.5	0.5	-9.3	9.2	-82.5
Amine N^1	-19.0	9.3	-72.40	2.25	2.83	2.40	2.49	2.9	0.05	11.0	57.2	-8.2
Imino $N^{3'}$	-6.1	10.5	-85.8	37.42	45.27	36.37	39.69	2.5	0.5	-8.0	11.6	-83.9
Amine $N^{1'}$	-15.5	11.7	-76.1	2.24	2.83	2.40	2.49	2.9	0.05	13.5	58.5	-9.5

The experimental values were obtained by ENDOR (for the imino $N^{3,3'}$) and HYSCORE (for the amine $N^{1,1'}$). Hyperfine tensor principal values quadrupole coupling are given in units of MHz; Euler angles, referred to the *g* frame, are given in degrees.

.

this knowledge into consideration in the ^{1}H ENDOR spectra of [Cu(acac)$_2$Im$_2$] with protic Im, the previously mentioned proton couplings of [Cu(acac)$_2$] are still visible in Figure 4.6. However, for clarity, only the ^{1}H ENDOR signals originating from the coordinated Im substrates are shown in the simulation and for this reason not all of the experimental lines are reproduced by the simulation. The resulting experimentally derived principal hyperfine values for the Im protons are listed in Table 4.3.

Three sets of hyperfine tensors were used to achieve a sensible and satisfactory fit to the experimental spectra. The simulation is shown in Figure 4.7 and the hyperfine tensors (I, II, and III) used for the simulation are given in Table 4.3. As a starting point for the simulation, however, DFT calculated hyperfine tensors were also used and modified slightly, as necessary, to match the experiment. Afterwards the resulting hyperfine values of [Cu(acac)$_2$Im$_2$] were compared to the theoretical DFT calculated ^{1}H hyperfine tensors (Table 4.3). The theoretical ^{1}H hyperfine of the Im derived protons of [Cu(acac)$_2$Im$_2$], are different for all cases, including the *cis*-mixed plane, *trans*-axial or *trans*-equatorial structures. However, the most closely matched set of couplings are found for the structures bearing one or two equatorially bound Im substrates; e.g., *cis*-mixed plane and *trans*-equatorial as illustrated in Scheme 4.2 and Figure 4.5b and d. This helps to assign the experimental values to the H^2/H^4 protons, H^5 protons and H^1 proton of the Im ligand. A less complex ENDOR spectrum is expected for the higher symmetry *trans*-equatorial structure, which contains two equivalent Im substrates. The *cis*-mixed plane structure has two inequivalent Im substrates, leading to more hyperfine couplings and consequently to a more complex ENDOR spectrum compared to the *trans*-equatorial structure. Even the angular selective ^{1}H ENDOR data seems to be more consistent with the *trans*-equatorial structure. Nevertheless, one cannot confidently discriminate between the *cis*- and *trans*-structures (Figure 4.5) based on the ^{1}H ENDOR measurements alone. For this reason, ^{14}N ENDOR and HYSCORE were additionally employed.

4.3.4 ^{14}N ENDOR and HYSCORE

Structural information about the coordination mode of the [Cu(acac)$_2$Im$_2$] adduct can be obtained from the ^{14}N superhyperfine pattern obtained in the CW X-band EPR spectrum, exhibited in Figure 4.1. However, line broadening effects

causes poor resolution in frozen solution spectra. For this reason, accurate determination of the nitrogen hyperfine data from the EPR spectrum is not straightforward. The ^{14}N hyperfine ($^{N}\mathbf{A}$) and quadrupole ($^{N}\mathbf{Q}$) tensors can in principle be determined by hyperfine techniques such as ENDOR and HYSCORE. The strongly coupled ^{14}N nucleus observed in the EPR spectrum (N^3, Scheme 4.1) can be analysed by ENDOR, whereas the remote ^{14}N of the Im ring (N^1, Scheme 4.1) can be detected by HYSCORE. When combined, these methods can be utilized to further investigate the structure of the bis-adduct. Indeed, Iwaizumi *et al*.,[18,32] demonstrated that ^{14}N ENDOR spectroscopy could be used to discriminate between copper complexes bearing pseudo planar arrays of donor sets, including N_4, *cis*-N_2O_2, and *trans*-N_2O_2. However, depending on the hybridized state of the nitrogen atoms or the changes in symmetry of the complex, this simple correlation between ^{14}N hyperfine and structure may be of limited diagnostic value and must be treated cautiously.

The angular selective CW Q-band ^{14}N ENDOR spectra were therefore recorded and the resulting experimental and simulated spectra are shown in Figure 4.8a. The spectra were successfully simulated using a single ^{14}N tensor, indicative of an equivalent nitrogen environment, with no evidence of a second strongly coupled nitrogen. The resulting parameters are listed in Table 4.4. The hyperfine tensor was found to deviate slightly from axial symmetry with the largest principal axes approximately directed to the copper ion. According to the DFT geometry optimized structures, the ^{14}N hyperfine tensor calculated for the imino N^3 nitrogen in the *trans*-equatorial adduct most closely matches the experimental values (Table 4.4).

In addition, angular selective X-band Davies ENDOR measurements were conducted to support the findings of the Q-band ENDOR experiments and are shown in Figure 4.8b. As expected at this frequency, the spectra contain overlapping signals from both ^{1}H and ^{14}N nuclei in the region between 10 – 25 MHz. The broad line width of the ^{14}N signals prevented the accurate determination of $^{N}\mathbf{A}$ and $^{N}\mathbf{Q}$. Hyperfine selective Davies ENDOR measurements were also performed to suppress the ^{1}H signals without reducing or distorting the ^{14}N signals. Whilst proton suppression was successful, the ^{14}N signal remained broad and poorly resolved, as commonly observed for strongly coupled nitrogen atoms in several copper proteins.[16,33]

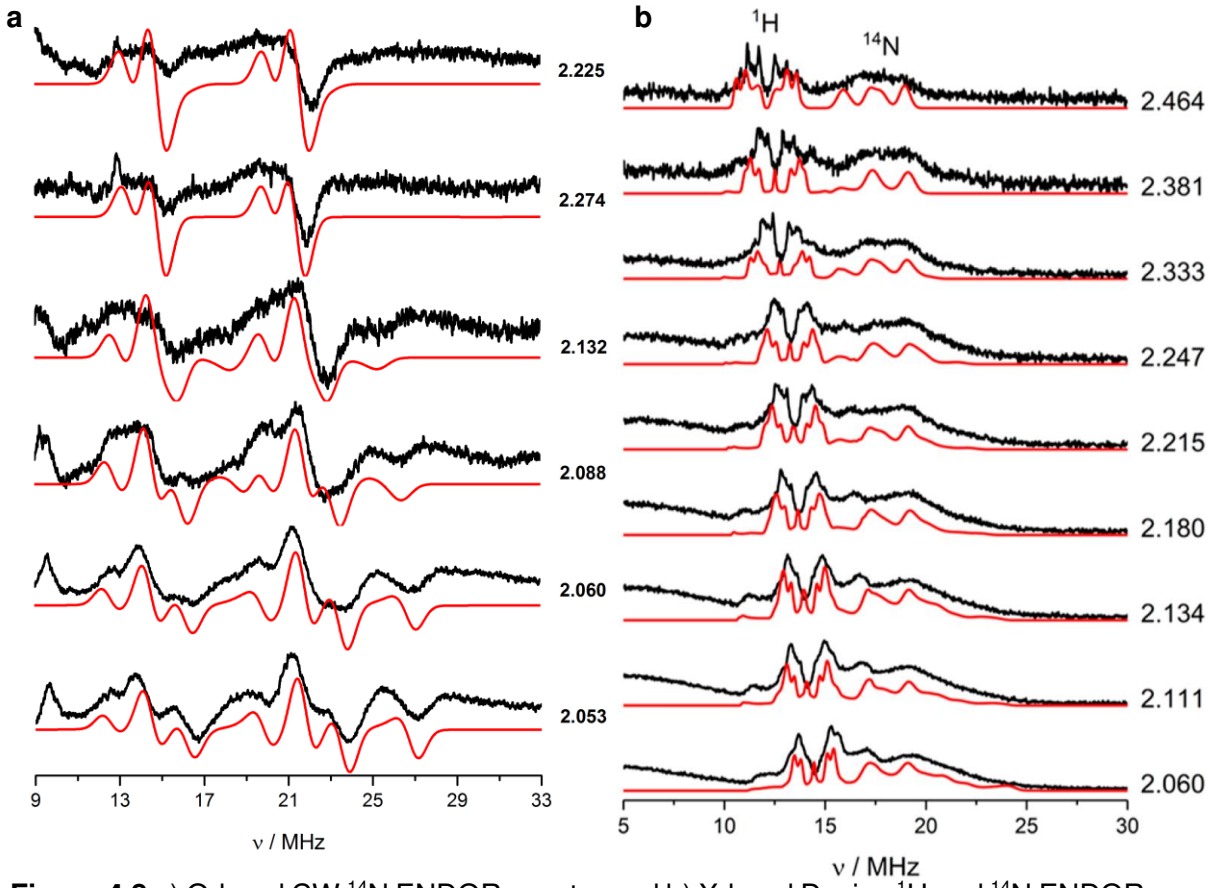

Figure 4.8 a) Q-band CW ^{14}N ENDOR spectra and b) X-band Davies ^{1}H and ^{14}N ENDOR spectra of the $[Cu(acac)_2Im_2]$ adduct dissolved in dry $CDCl_3$:DMF-d_7 (1:1). The spectra were measured at 10 K and recorded at the *g* values indicated beside each spectrum. The corresponding simulations are shown in red.

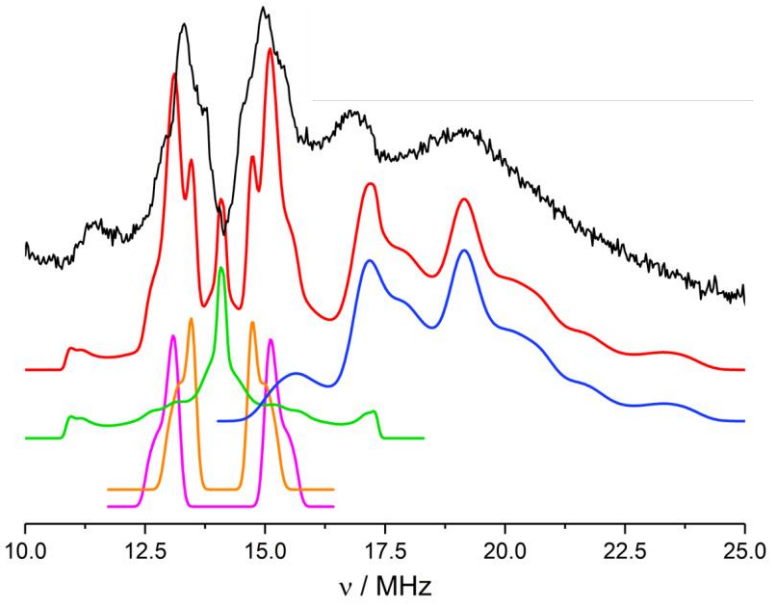

Figure 4.9 Experimental (black) and simulated X-band Davies ^{1}H and ^{14}N ENDOR spectra (10 K) of the $[Cu(acac)_2Im_2]$adduct dissolved in dry $CDCl_3$:DMF-d_7 (1:1), recorded at $g = 2.111$. The deconvoluted simulated contributions are as follow: imino N^3 (blue), $H^{2,4}$ (green), H^5 (orange), H^1 (magenta).

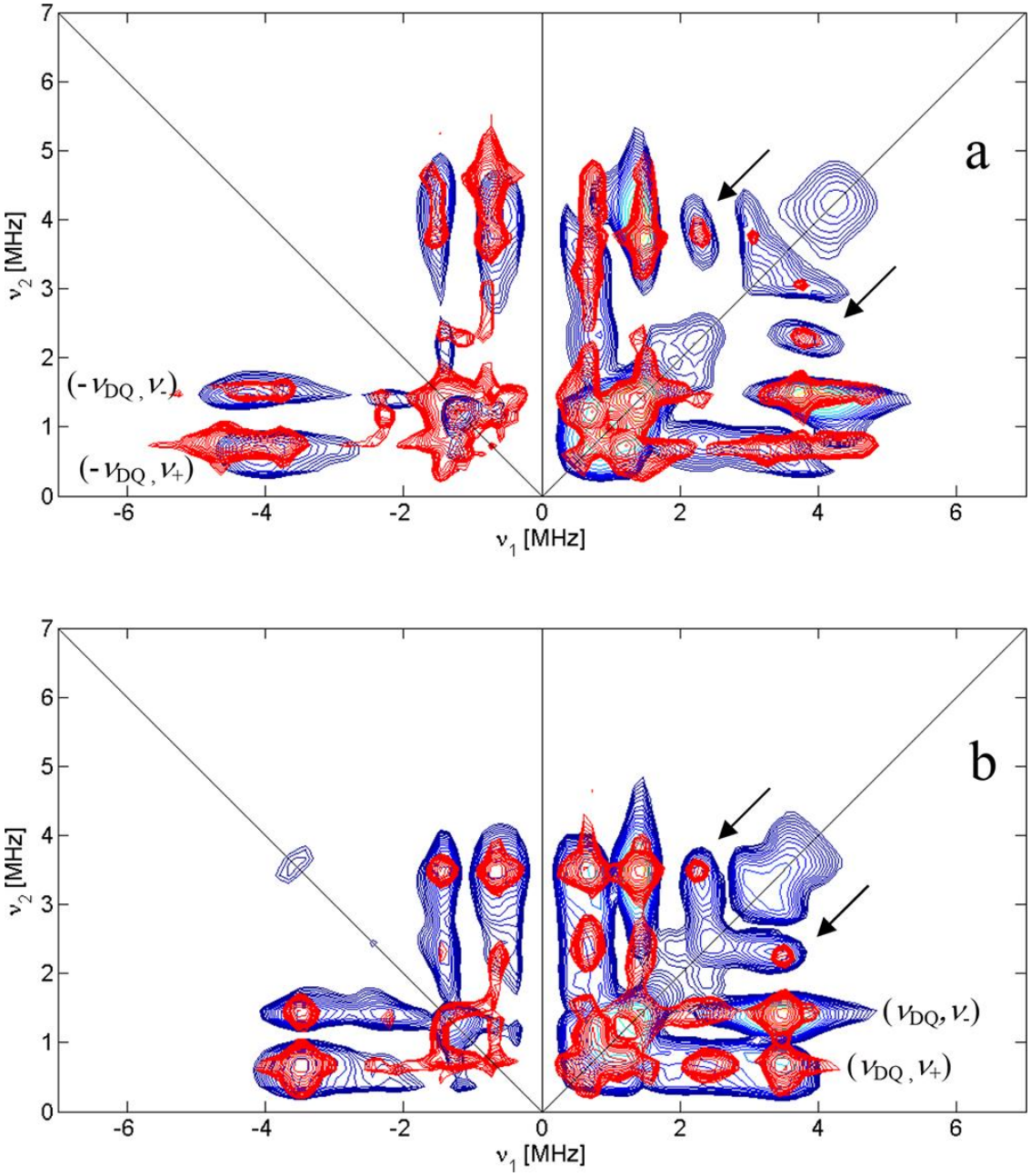

Figure 4.10 2D HYSCORE spectra of $[Cu(acac)_2Im_2]$ recorded at a) B_0 = 338.6 mT and τ = 176 ns, and b) B_0 = 283.2 mT and τ = 144 ns. Both spectra were recorded at 10 K. The assignments of these cross peaks are shown on the spectrum. The arrows indicate the combination peaks.

Nevertheless, an excellent fit to the experimental X-band Davies ENDOR was achieved using the ^1H and ^{14}N hyperfine tensors extracted from the Q-band spectra. The deconvoluted simulation of the Davies ENDOR is shown in Figure 4.9. The low anisotropy in the nitrogen hyperfine coupling is characteristic of Im coordination and is typical of δ dominant bonding as expected for Cu^{2+}-Im coordination.[9] Combined, these observations are consistent with equatorial coordination of Im to $[Cu(acac)_2]$.

The X-band HYSCORE spectrum of the $[Cu(acac)_2Im_2]$ adduct complex is shown in Figure 4.10 and characterized by cross peaks in both the (+,+) and (-,+) quadrants, arising from transitions associated with the remote amine ^{14}N nucleus of the imidazole ring (N^1). At X-band, the hyperfine coupling term for this specific ^{14}N interaction is approximately twice the nuclear Zeeman term, leading to the so-called cancellation condition, such that the two terms cancel out in one of the two M_s spin manifolds. The nuclear frequencies of this particular M_s manifold correspond to the nuclear quadrupolar resonance (NQR) frequencies ν_-, ν_+ and ν_0, which appear in the ESEEM spectra at 0.7 MHz (ν_+) and 1.4 MHz ($\nu_- \approx \nu_0$). A feature appearing at about 4 MHz in the ESEEM spectrum is due to the nuclear double-quantum transition frequency, ν_{DQ} of the other M_s manifold.[14,34,35] The HYSCORE spectrum recorded at the maximum echo intensity in Figure 4.10a, is dominated by elongated cross peaks appearing at (±0.65, +4), (±4, +0.65), (±1.4, +4) and (±4, +1.4) MHz, which correspond to (ν_+, ν_{DQ}) and ($\nu_-(\nu_0)$, ν_{DQ}) frequencies of the remote Im nitrogen nucleus, consistent with the ESEEM results. As reported by Mims and Peisach,[35] these frequencies correspond to a Fermi contact interaction term (a_{iso}) of 1.5 – 2.0 MHz, a nuclear quadrupole coupling $e^2qQ/h \approx 1.4$ MHz and an asymmetry parameter (η) of 0.9 - 1. In addition to these signals, two cross peaks at about (2.2, 3.9) and (3.9, 2.2) MHz are present in the (+,+) quadrant, associated with the combination frequencies due to the presence of at least two remote nitrogen nuclei coupled to the same electron spin.[36] The HYSCORE spectra were thus simulated by considering a three-spin system ($S = ½$, $I_a = 1$, and $I_b = 1$) with two equivalent nitrogen nuclei having spin Hamiltonian parameters typical for the remote ^{14}N nuclei of Im, as listed in Table 4.4. The simulations are displayed in red in Figure 4.10 and provide a convincing fit at both magnetic field settings. HYSCORE experiments, thus, indicate the presence of magnetically equivalent remote N^1 nitrogen atoms of the Cu coordinated Im rings.

*4.3.5 EPR spectra of $[Cu(acac)_2]$ with different imidazole derivatives (Im-**2** – **4**)*

It is also necessary to explore whether the formation of the $[Cu(acac)_2Im_2]$ bis-adduct is limited only to Im. Hence, a number of other Im derivatives, shown in Scheme 4.1 and including 2-methyl-imidazole (Im-**2**), 4(5)-methyl-imidazole (Im-**3**) and benzimidazole (Im-**4**), were also investigated. The EPR spectra of

$[Cu(acac)_2]$ dissolved in $CHCl_3$:DMF containing increasing ratios of Im-**2**, Im-**3** or Im-**4** are given in the Appendix C.1. The corresponding EPR spectra recorded at a Cu:Im ratio of 1:50 are shown in Figure 4.11. At Cu:Im-**2** – **4** ratios of 1:10, only the monoaxial $[Cu(acac)_2$(Im-**2** – **4**)] adducts were formed, see Appendix Figure C.1 and C.4, as revealed by the small change in the *g* and ^{Cu}A values, given in Table 4.1. Moreover, at higher concentrations (Cu:Im-**2** – **4** ratios of 1:50), no further changes were detected in the EPR spectra for Im - **2** and Im - **4** (Figure 4.11c and b, respectively). In contrast to these imidazole derivatives, the EPR spectra of Im – **3** exhibited the characteristic superhyperfine patterns observed earlier for $[Cu(acac)_2(Im)_2]$ (compare Figure 4.1c to Figure 4.11e), indicating the formation of the $[Cu(acac)_2$(Im–**3**$)_2]$ bis-adduct (Figure 4.11d).

The absence of any bis-adduct for Im – **2** and Im – **4** must be attributed to steric effects of the substrate, because the basicity for all of the Im-derivatives is relatively large. Im – **4** for example is clearly too bulky to form the *trans*-equatorial conformation, whereas the presence of a methyl group in position 2 of Im – **2** also prevents formation of the *trans*-equatorial coordination mode. In contrast, in the case of Im – **3**, tautomerization will effectively result in the methyl group occurring at position 5 (see Scheme 4.1), therefore pointing away from the ligand methyl groups of the acetylacetonate units and thus enabling the formation of the *trans*-equatorial structure.

4.3.6 Coordination mode of the $[Cu(acac)_2Im_2]$ adduct

Over the years, numerous Cu^{2+} complexes have been studied as model systems to explore the structure, coordination and binding in Cu^{2+} proteins. Invariably, studies of imidazole, substituted imidazoles and histidine interactions with Cu^{2+} ions or complexes have been undertaken using EPR, ENDOR and ESEEM,[15, 19, 26] largely because imidazole is an important component of many proteins and is, for example, the side chain in histidine and a constituent of purine bases. Although the imino nitrogen N^3 (Scheme 4.1) is the common binding site for the metal ions, in deprotonated Im, both nitrogens are sufficiently basic enough to facilitate binding. Therefore, the study of Im coordination is extremely important for the evaluation of the binding between metal ions and the imidazole residues of proteins. In many cases, the combined use of EPR and ENDOR or ESEEM was employed to determine the complete conformation of the coordinated

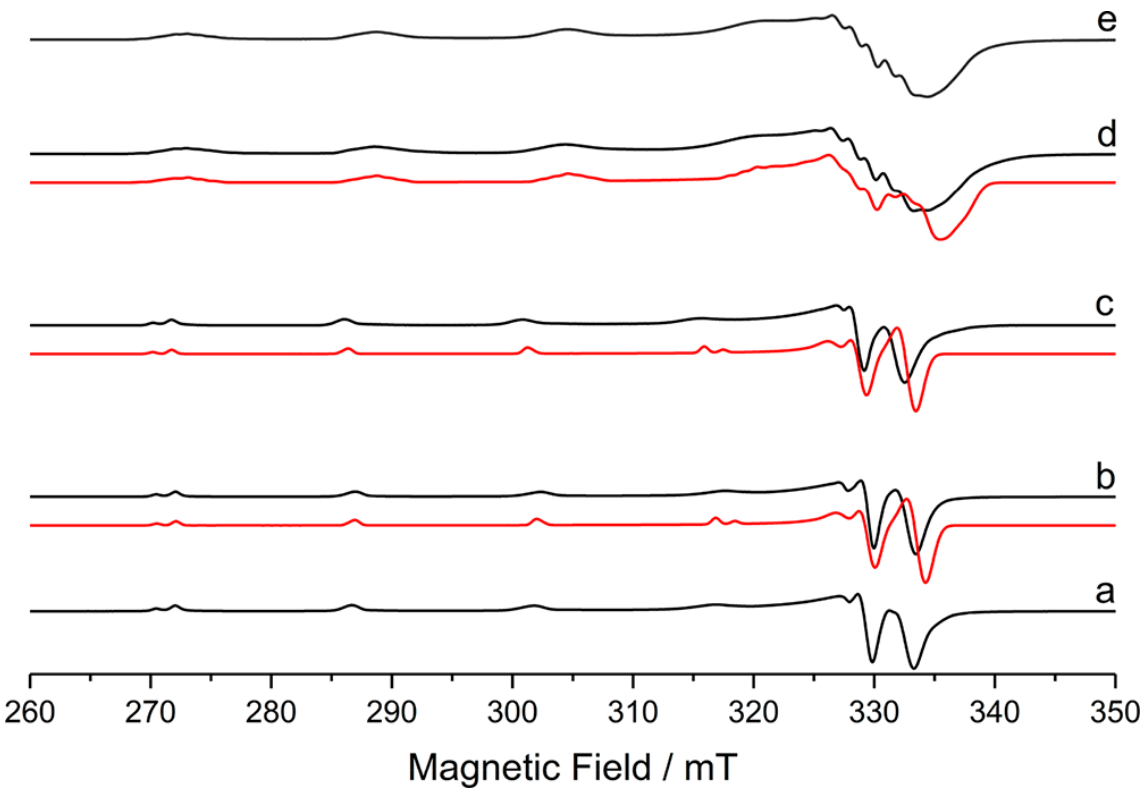

Figure 4.11 Experimental (black) and simulated (red) CW X-band EPR spectra of a) $[Cu(acac)_2Im]$, b) $[Cu(acac)_2(Im\text{-}\mathbf{4})]$, c) $[Cu(acac)_2(Im\text{-}\mathbf{2})]$, d) $[Cu(acac)_2(Im\text{-}\mathbf{3})_2]$ and e) $[Cu(acac)_2Im_2]$. The spectra were recorded at 140 K in a $CHCl_3$:DMF (1:1) solvent with a Cu:Im **1** – **4** ratio of 1:50 in all cases. The simulated spectra for a) and e) were shown earlier in Figure 4.1. The simulation parameters are listed in Table 4.1.

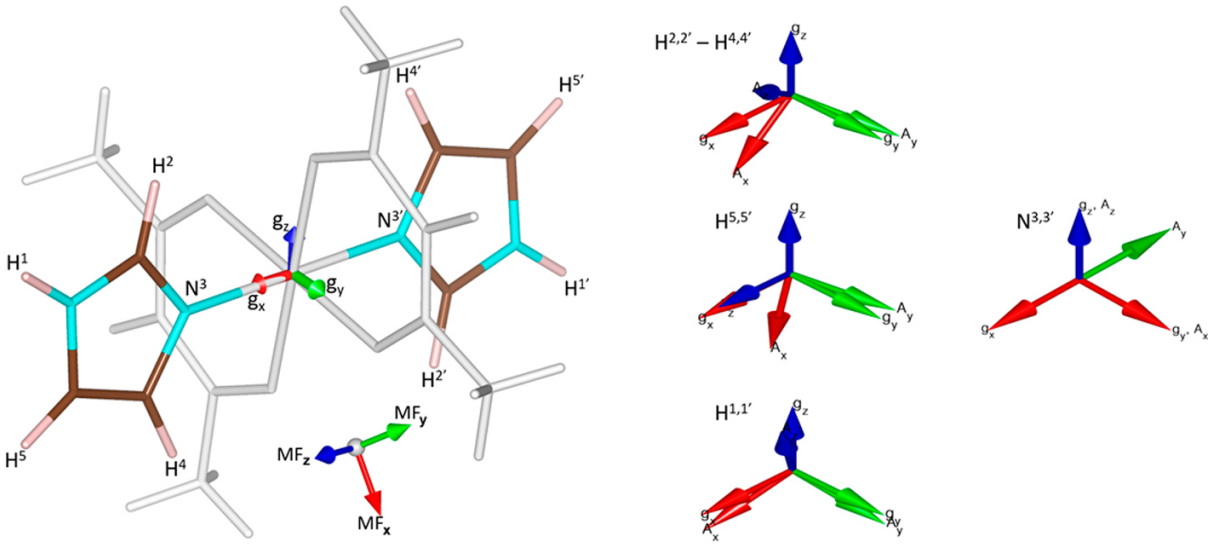

Figure 4.12 Geometry optimized DFT structure for the *trans*-equatorial $[Cu(acac)_2Im_2]$ adduct, showing the relative orientation of the ^{1}H and ^{14}N hyperfine tensors with respect to the **g**-frame.

substrates by analysis of the ^{1}H and ^{14}N hyperfine and (^{14}N) quadrupole parameters. However, a growing number of mixed chelate Cu^{2+} complexes containing the acetylacetonate ligand and a bidentate nitrogen-based N-N ligand, *i.e.,* $[Cu(acac)(N\text{-}N)]^{+}$, have received considerable interest recently owing to their cytotoxicity and DNA binding capabilities (Chapter 5), but the interaction of these mixed chelate complexes with imidazole has not been investigated to date.

In this Chapter, a number of possible conformations for the $[Cu(acac)_2Im_2]$ bis-adducts in solution were considered. Through a combined computational and experimental EPR approach, an accurate assignment to one particular coordination mode, *i.e., trans*-equatorial $[Cu(acac)_2Im_2]$, was established. Initially at low Im concentrations, the axial mono-adduct $[Cu(acac)_2Im]$ is formed, as confirmed by the small shift in g and ^{Cu}A values relative to the unbound $[Cu(acac)_2]$ complex (Table 4.1). At higher Im concentrations, a bis-adduct was formed, as revealed by the ^{14}N superhyperfine pattern on the $m_I = +3/2$ $^{63,65}Cu$ hyperfine component. Owing to the strong basicity of the Im substrate, the in-plane bis(acetylacetonato) ligands must rearrange themselves to facilitate the in-plane equatorial coordination of the two Im units. The resulting tetragonally distorted octahedral complexes contains a $Cu\text{-}N_2O_2$ plane with two coordinating nitrogens coming from the N^3 Im substrate. The g_x component of the **g** tensor is positioned along this equatorial N-Cu-N direction with the g_y component lying almost along the equatorial O-Cu-O direction and with g_z almost along the axial O-Cu-O direction (Figure 4.12). Orientation selective ^{1}H ENDOR revealed that the hyperfine couplings can be assigned to three sets of protons on the Im ring. The two protons adjacent to the imino N^3 nitrogen (H^2 and H^4) gave similar hyperfine tensors, according to the DFT calculations, which were indistinguishable in the experimental ENDOR spectra. The remaining two protons, labelled H^5 and H^1 in Scheme 4.1, produced sufficiently different hyperfine tensors so that all proton sets could be distinguished in the angular selective ^{1}H ENDOR simulations.

Angular selective ^{14}N ENDOR spectra were also recorded at X-band (Davies ENDOR) and Q-band (CW ENDOR) frequencies, yielding information on the hyperfine coupling and nuclear quadrupole coupling to the coordinating N^3 nitrogen listed in Table 4.4. The ^{14}N hyperfine tensor of the imino N^3 nitrogen was found to be nearly axially symmetric with the largest principal axis, $^{N}A_y$, orientated

almost directly along Cu-N bond direction and the g_x component (Figure 4.12). The experimental and theoretical ^{N}A values for the *trans*-equatorial $[Cu(acac)_2Im_2]$ structure were in excellent agreement with each other ([34.8, 43.5, 34.0] versus [37.4, 45.3, 36.4] MHz, respectively). The ^{N}A values for the *cis*-mixed plane and *trans*-axial structures were by comparison considerably smaller ([29.2, 35.9, 28.5] and [-1.62, -1.64, -0.74] MHz, respectively; Table 4.4). The experimental e^2qQ/h and η values were also typical for strongly coordinating nitrogens in Cu-N_2O_2-type complexes. The experimental ^{N}A values for the remote N^1 Im nitrogen, as determined by HYSCORE, were smaller compared to the theoretical values (Table 4.4) because DFT often overestimates these parameters for remote nitrogens. Nevertheless, the observed values were in the region expected for equatorially bound Im and were certainly larger than those predicted for the *cis*-mixed plane and *trans*-axial structures. Taken together, it is clear that the ^{14}N ENDOR and HYSCORE analysis is entirely consistent with the formation of the *trans*-equatorial $[Cu(acac)_2Im_2]$ adduct.

4.4 Conclusion

An experimental (EPR, ENDOR, HYSCORE) and computational study of imidazole coordination with a simple $[Cu(acac)_2]$ complex was undertaken. A growing number of cytotoxic Cu^{2+} based complexes contain the acetylacetonate ligand and therefore, a better understanding of how such complexes interact with imidazole, representing the side chain moiety of the amino acid histidine, is extremely important and timely. At a relatively low ratio of Cu to Im, a $[Cu(acac)_2Im_{n=1}]$ mono-adduct is formed. The Im was found to coordinate to the Cu in the axial position, as confirmed by the small shift in the g_3 value ($\Delta g_z = 0.022$) and the concomitant decrease in the $^{Cu}A_3$ value ($\Delta A_z = 48$ MHz) relative to the unbound $[Cu(acac)_2]$ complex. At higher ratios of Cu to Im, a $[Cu(acac)_2Im_2]$ bis-adduct is formed, as revealed by the superhyperfine pattern detected in the CW EPR spectra, which can be interpreted only based on two strongly coordinating and largely equivalent nitrogen nuclei. Different structural isomers of this bis-adduct are possible and detailed ^1H and ^{14}N hyperfine analysis reveals that the *trans*-equatorial conformer is formed. Three individual sets of ^1H tensors were detected in the ^1H ENDOR spectra and assigned to the H^2/H^4, H^5

and H^1 protons of Im (see Scheme 4.1 for labels). These values were consistent with either a *cis*-mixed plane or *trans*-equatorial structure for $[Cu(acac)_2Im_2]$. However, angular selective ^{14}N ENDOR (both CW and pulsed) provided more detailed insights into the hyperfine and quadrupole values for the coordinating imino N^3 nitrogen, and these parameters were in excellent agreement with the geometry optimized structure for the *trans*-equatorial $[Cu(acac)_2Im_2]$ adduct. Equally, the hyperfine and quadrupole values for the remote ^{14}N amine nucleus were determined by simulation of the X-band HYSCORE spectra, and a reasonably good agreement was achieved between theory and experiment. The ability of the coordinating ligand in the Cu-based complexes to flip between *cis*- and *trans*-conformations (from unbound to Im-bound adducts) must therefore be considered when designing novel cytotoxic Cu^{2+} based complexes for target interactions with proteins bearing imidazole residues.

4.5 References

1. C. M. Ackerman, S. Lee and C. J. Chang, *Anal. Chem.*, **2017**, 89, 22-41.
2. R. H. Holm, P. Kennepohl and E. I. Solomon, *Chem. Rev.*, **1996**, 96, 2239-2314.
3. C. Orvig and M. J. Abrams, *Chem. Rev.*, **1999**, 99, 2201-2204.
4. K. G. Strothkamp, *Acc. Chem. Res.*, **1982**, 15, 318-326.
5. H. K. Liu and P. J. Sadler, *Acc. Chem. Res.*, **2011**, 44, 349–359.
6. L. Ronconi and P. J. Sadler, *Coor. Chem. Rev.*, **2007**, 251, 1633-1648.
7. G. J. Chen, X. Qiao, P. Q. Qiao, G. J. Xu, J. Y. Xu, J. L. Tian, W. Gu, X. Liu and S. P. Yan, *J. Inorg. Biochem.*, **2011**, 105, 119-126.
8. C. Santini, M. Pellei, V. Gandin, M. Porchia, F. Tisato and C. Marzano, *Chem. Rev.*, **2014**, 114, 815-862.
9. R. J. Sundberg and R. Bruce Martin, *Chem. Rev.*, **1974**, 74, 471-517.
10. T. Higa, M. Moriya, Y. Shimazaki, T. Yajima, F. Tani, S. Karasawa, M. Nakano, Y. Naruta, O. Yamauchi, *Inorg. Chimica Acta*, **2007**, 360, 3304-3313.
11. M. Andersson, J. Hedin, P. Johansson, J. Nordstrom, M. Nyden, *J. Phys. Chem.*, **2010**, 114, 13146-13153.
12. P. Manikandan, B. Epel, D. Goldfarb, *Inorg. Chem.*, **2001**, 40, 781-787.
13. F. Jiang, K. D Karlin, J. Peisach, *Inorg. Chem.*, **1993**, 32, 2576-2582.
14. H. L. Flanagan, D. J. Singel, *J. Chem. Phys.*, **1987**, 87, 5606-5616.
15. H.J. Scholl, J. Huttermann, *J. Phys. Chem.*, **1992**, 96, 9684-9691.
16. H. L. van Camp, Y.H. Wei, C. P. Scholes, T. E. King, *Biochim. Biophysica Acta*, *Protein Struct.*, **1978**, 537, 238-246.
17. P. Höfer, A. Grupp, H. Nebenführer, M. Mehring, Chem. Phys. Letters, **1986**, 132, 279-282.
18. R. Miyamoto, Y. Ohba, M. Iwaizumi, *Inorg. Chem.*, **1992**, 31, 3138-3149.

19. P. Chaudhuri, I. Karpenstein, M. Winter, M. Lengen, C. Butzlaff, E. Bill, A. X. Trautwein, U. Florke, H. J. Haupt, *Inorg. Chem.*, **1993**, 32, 888-894.
20. O. Sanchez-Guadarrama, H. Lopez-Sandoval, F. Sanchez-Bartez, I. Gracia-Mora, H. Hopfl, N. Barba-Behrens, *J. Inorg Biochem.*, **2009**, 103, 1204-1213.
21. M. I. Webb, C. J. Walsby, *Dalton Trans.*, **2015**, 44, 17482-17493.
22. K. M. Sharples, E. Carter, C. E. Hughes, K. D. Harris, J. A. Platts, D. M. Murphy, *PhysChemChemPhys.*, **2013**, 15, 15214-15222.
23. E. Carter, K. M. Sharples, J. A. Platts, D. M. Murphy, *PhysChemChem Phys.*, **2015**, 17, 11445-11454.
24. D. Attanasio, I. Collamati, C. Ercolani, *J.Chem. Soc., Dalton Trans.*, **1974**, 1319-1324.
25. D. Attanasio, I. Collamati, C. Ercolani, *J. Chem. Soc.*, *Dalton Trans.*, **1973**, 2242-2247.
26. N. Masciocchi, G. Attilio Ardizzoia, G. LaMonica, A. Maspero, S. Galli, G. Sironi, *Inorg. Chem.*, **2001**, 6983-6989.
27. W. A. Alves, G. Cerchiaro, A. Paduan-Filho, D. M. Tomazela, M. N. Eberlin A. M. Da Costa Ferreira, *Inorg. Chimica Acta*, **2005**, 358, 3581-3591.
28. S. H. Rahaman, H. Chowdhury, D. Bose, G. Mostafa, H.-K. Fun, B. K. Ghosh, *Inorg. Chem. Comms.*, **2005**, 8, 1041-1044.
29. C. A. Koch and C. A. Reed, *J. Am. Chem. Soc*, **1989**, 11, 7645-7648.
30. K. G., L. S.J., W. J.V. and L. H.R., *J. Am. Chem. Soc.*, **1982**, 104, 717-725.
31. Y. F. Song, C. Massera, M. Quesada, I. A. Koval, P. Gamez, A. M. Manotti Lanfredi, J. Reedijk, *Eur. J. Inorg. Chem.*, **2004**, 4566-4571.
32. M. Iwaizumi, T. Kudo, S. Kita, *Inorg. Chem.*, **1986**, 25, 1546-1550.
33. G. H. Rist, J. S. Hyde, T. Vangard, *P.N.A.S.*, **1970**, 67, 79-86.
34. F. Jiang, J. McCracken, J. Peisach, *J. Am. Chem. Soc.*, **1990**, 112, 9035-9044.
35. W. B. Mims, J. Peisach, *J. Chem. Phys.*, **1978**, 69, 4921-4930.
36. J. McCracken, S. Pember, S. J. Benkovic, J. J. Villafranca, R. J. Miller, J. Peisach, *J. Am. Chem. Soc.*, **1988**, 110, 1069-1074.
37. E. Carter, E. L. Hazeland, D. M. Murphy, B. D. Ward, *Dalton Trans.*, **2013**, 42, 15088.
38. M. V. Veidis, G. H. Schreiber, T. E Gough, G. J. Palenik, *J. Am. Chem. Soc.*, 1969, 91, 1859-1860
39. S. Siddiqui, R. E. Shepherd, *Inorg. Chem.*, **1986**, 25, 3869-3876.
40. B. B. Wayland, V. K. Kapur, *Inorg. Chem.*, **1974**, 13, 2517-2520.

Chapter 5: An EPR and ENDOR investigation of a series of Copper(II)-Casiopeina type coordination complexes $[Cu(O\text{-}O)(N\text{-}N)]^+$.

A series of unbound casiopeina complexes with the general formula $[Cu(acac)(N\text{-}N)]^+$ have been prepared due to their relevance in pharmaceutical research. The electronic properties of these casiopeina complexes have been thoroughly explored through the spin Hamiltonian using EPR and ENDOR spectroscopy. Within the series of complexes studied, the diimine ligand (N-N) was systematically varied in size using 2,2'-bipyridine (bipy), 1,10-phenanthroline (phen), dipyridophenazine (dppz) and a pyridine substituted 2,2'-bipyridine ligand (Py-biby). These diimine ligands were selected in light of the fact that the size of the aromatic diimine ligand may influence the therapeutic activity.

5.1 Introduction

The casiopeinas are a class of mixed chelate, cationic copper complexes which have well known antineoplastic properties. They have the general formula $[Cu(O\text{-}O)(N\text{-}O)]^+$ or $[Cu(O\text{-}O)(N\text{-}N)]^+$, where O-O typically represents an acetylacetonate (acac) or salicylaldehydate (sal) chelate ligand, N-O denotes an aminoacidate or peptide, and N-N generally indicates an aromatic diimine such as 1,10-phenanthroline (phen) or 2,2'-bipyridine (bipy).[1] The most commonly studied derivatives are based on the [Cu(4,7-dimethyl-1,10-phenanthroline)(glycinato)]NO_3 complex[2–5] (labelled Cas II-gly) and the [Cu(4,4'dimethyl-2,2'-bipyridine)(acetylacetonato)]NO_3 complex[2,3,6,7] (labelled Cas III-ia); see Scheme 5.1. These complexes and numerous analogues[8–14] have been evaluated both *in vitro* and *in vivo*, and have demonstrated antineoplastic,[15] cytotoxic,[16] genotoxic[2,14] and antiviral activities. Notably, some casiopeinas have been found to be active on cisplatin-resistant cell lines,[4,17] whilst others have displayed improved anti-cancer activity compared to cisplatin.[18] Their potential to combat a broader spectrum of disease with fewer toxic side effects has therefore stimulated extensive studies on this class of complex.

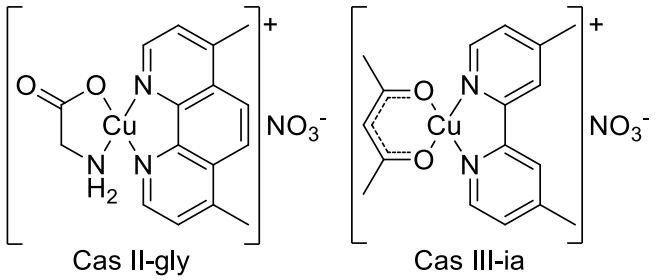

Cas II-gly Cas III-ia

Scheme 5.1 Structures of Cas II-gly and Cas III-ia casiopeina complexes.

The mode of action of these copper complexes however remains poorly understood. DNA has been established as its primary cellular target and the planar aromatic diimine ligand is known to bind DNA by intercalative[19–22] and non-intercalative interactions.[23] Once bound, the redox properties of the copper centre are capable of generating reactive oxygen species (ROS) which can cause oxidative damage to the DNA that is postulated to ultimately result in cell death.[23–26] Adduct formation between the copper complex and the DNA may induce conformational change within a strand of DNA and cause denaturation. This could also contribute to the therapeutic mechanism of casiopeinas. It has been demonstrated that cisplatin acts by forming inter-strand crosslinks between guanine bases causing the DNA to kink, preventing replication processes.[27–29]

Quantitative structure-activity relationship (QSAR) studies indicate that the biological activities of casiopeina type anticancer agents are affected by substitution effects on the ligands.[2] Physicochemical properties of the complex which may be influenced by ligand substitutions include the affinity towards DNA, the specificity of the DNA interaction and the redox potential of the copper centre. For instance, electron donating ligands on the diimine ligand were found to increase anti-tumour activity by modulating the redox chemistry of the copper centre.[2] In contrast, electron withdrawing groups present on the diimine ligand increased the stability of intercalative π-π interactions between the diimine and nucleobases of the DNA scaffold.[20] In addition, phen-type derivatives have been found to be more active than their bipy-type counterparts, suggesting that the size of the aromatic ring system of the diimine ligand influences the DNA affinity for the copper complex. Clearly, there is a delicate balance to achieve in order to optimise the performance of these complexes.

A complete description of the electronic and geometric structure of the casiopeina type complexes in both the ‘unbound’ state (free of DNA) and in the

bound DNA adduct, may therefore offer interesting insights into the therapeutic action of this class of compounds and ultimately contribute to the design of novel casiopeina inspired drugs with improved therapeutic activity. Electron Paramagnetic Resonance (EPR) and its related hyperfine techniques, such as Electron Nuclear Double Resonance (ENDOR), can offer a direct measure of this electronic and geometric information, as has in the past been demonstrated for the elucidation of the structure-function relationships in copper proteins,[30–32] and thus these methods have the potential to examine and interrogate the structure of these copper based therapeutics. A small number of papers have used EPR to study the covalency in the casiopeina complexes,[7] whilst Chikira *et al*.,[19,33] focussed on the $\boldsymbol{g}$ and $^{Cu}\boldsymbol{A}$ parameters when the copper complexes were intercalatively bound to DNA fibres. By comparison, no ENDOR studies of these complexes have been reported. Unlike EPR, ENDOR is able to probe the configuration of surrounding spin-active ligand nuclei, providing more detailed information on the overall electronic structure of the complex. Indeed the importance of electron distribution in these complexes was highlighted in an experimental and theoretical study by Ruiz-Azuara *et al*.[34] This level of detail in the electronic structure may be necessary in order to resolve subtle structural differences in the complexes which may have significant consequences in terms of activity.

In this work, we have therefore prepared a series of unbound casiopeina complexes with the general formula $[Cu(acac)(N\text{-}N)]^+$ and thoroughly explored their electronic properties through the spin Hamiltonian using EPR and ENDOR spectroscopy. Within the series of complexes studied, the diimine ligand (N-N) was systematically varied in size using 2,2'-bipyridine (bipy), 1,10-phenanthroline (phen), dipyridophenazine (dppz) and a pyridine substituted 2,2'-bipyridine ligand (Py-biby); see Scheme 5.2. These diimine ligands were selected in light of the fact that the size of the aromatic diimine ligand may influence the therapeutic activity.

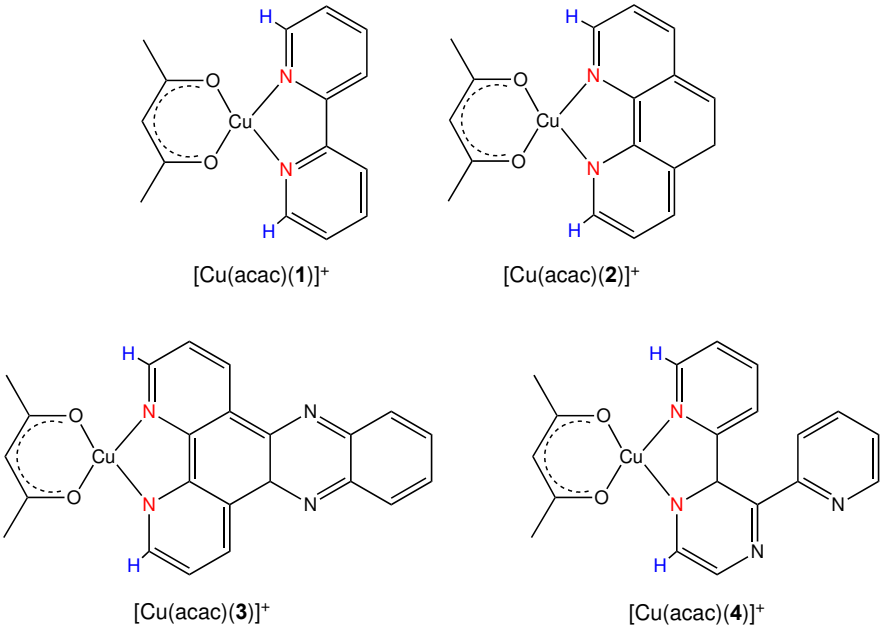

Scheme 5.2 Structures of the casiopeina type complexes with the general formula [Cu(acac)(N-N)]$^+$, where N-N represents 2,2'-bipyridine (bipy) [Cu(acac)(**1**)]$^+$, 1,10-phenanthroline (phen) [Cu(acac)(**2**)]$^+$, dipyridophenazine (dppz) [Cu(acac)(**3**)]$^+$ and the pyridine substituted 2,2'-bipyridine (Py-bipy) [Cu(acac)(**4**)]$^+$, using a CF_3SO_3 anions in all cases.

5.2 Experimental Section

5.2.1 Materials

The copper salt $Cu(CF_3SO_3)_2$ was sourced from *Sigma Aldrich*. Acetylacetone and the diimine ligands (2,2'-bipyridyl (bipy), 1,10-phenanthroline (phen), 2,3-bis(2-pyridyl)pyrazine (Py-bipy)) and L-Histidine (L-his) and imidazole (Im) were also bought from *Sigma Aldrich* and used as received. The dipyridophenazine (dppz) ligand were prepared and purified according to the procedure given in literature.[35]. Reagent grade EtOH, MeOH and DMF were purchased from *Sigma Aldrich* and used without further purification. Deuterated solvents; EtOD-d_6 and DMF-d_7 were sourced from *Goss Scientific* in sealed ampules and used as received.

5.2.2 Sample preparation

Complexes with the general formula of [Cu(acac)(N-N)]$^+$ were prepared using methods described in the literature[11,36,37]. Once isolated and purified, 0.03 M solutions of the [Cu(acac)(N-N)]$^+$ complexes were prepared in an

EtOH:DMF (1:1) solvent system and flash frozen to 140 K for X-band EPR analysis. Q-band EPR, ^{1}H and ^{14}N ENDOR studies were performed using 0.03 M solutions prepared in EtOD-d_6:DMF-d_7 (1:1) at 10 K. The same solvent system was used for W-band EPR studies with a sample preparation of 0.04 M

5.2.3 Variable Ratio studies

Speciation studies of adducts formed between $[Cu(acac)(N\text{-}N)]^{+}$ and nitrogen bases (N-base) at various $[Cu(acac)(N\text{-}N)]^{+}$:[N-base] molar ratios were monitored by X-band EPR (140 K) (N-base = imidazole (Im) and L-Histidine (L-his). A series of samples were prepared at a fixed $[Cu(acac)(N\text{-}N)]^{+}$ concentration of 0.03 M, whilst the molar equivalence of the N-base was systematically varied from 0 - 100 molar equivalents. The composition of the solvent system was kept constant within a series of measurements to ensure the quality of the frozen solution was unchanged.

5.2.4 EPR/ENDOR spectroscopy

The continuous wave (CW) X-band EPR measurements were performed on a Bruker EMX spectrometer utilizing an ER4119HS resonator, 100 kHz field modulation at 140 K or 298 K and typically using 10.17 mW MW power. The CW Q-band EPR and ENDOR measurements were recorded on a Bruker Elexsys E500 spectrometer using a Bruker ER5106 QT-E Q-band resonator operating at 10 kHz field modulation and 10 K for ENDOR (and at 100 kHz and 50 K for the EPR). The CW Q-band ENDOR spectra were obtained using 1 dB RF power from an ENI 3200L RF amplifier at 100 kHz RF modulation depth and 0.5 mW microwave power. The W-band EPR spectra were recorded at 20 K at about 94 GHz using a Bruker Elexsys E-600 EPR spectrometer equipped with a E600-1021H TeraFlex resonator. A modulation amplitude of 7 Gauss was used.

All of the EPR and ENDOR simulations were performed using the Easyspin[38] software package running within the MathWorks® MatLab® environment.

5.3 Results and discussion

5.3.1 CW-EPR

The experimental and simulated CW X-band EPR (140 K) spectra of the [Cu(acac)(**1-4**)]$^{+}$ complexes dissolved in ETOH:DMF are shown in Figure 5.1. The *g* values (Table 5.1) for the [Cu(acac)(**1-4**)]$^{+}$ complexes are similar to analogous Cu(II) complexes possessing a square planar geometry.[7,11,39] The influence of the varying aromatic ring size is barely perceptible in the *g* and ^{Cu}A values, in agreement with the derived DFT values. This suggests that the increasing diimine ring size and the possibility of greater spin delocalisation, has only a marginal influence of the *g* and ^{Cu}A values (Table 5.1).

To obtain more accurate *g*-values, the EPR spectra were also recorded at Q- and W-band frequencies. The multi-frequency EPR spectra for [Cu(acac)(**1**)]$^{+}$ are shown in Figure 5.2 (the corresponding spectra for [Cu(acac)(**2-4**)]$^{+}$ are shown in Appendix, Figure D1-2), where the spectra clearly illustrate the changes in EPR profile, going from a hyperfine dominated spectra to a spectrum where the *g* factors prevails.

Table 1 Experimental and DFT calculated *g* and ^{Cu}A spin Hamiltonian parameters for the [Cu(acac)(N-N)]OTf complexes.

	g_1	g_2	g_3	α	β	γ	$^{Cu}A_1$	$^{Cu}A_2$	$^{Cu}A_3$	α	β	γ	**ref.**
				Euler angles rotation of the g frame with respect to the molecular frame						Euler angles rotation of the A frame with respect to the molecular frame			
				/rad	/rad	/rad	/MHz	/MHz	/MHz	/rad	/rad	/rad	
[e][Cu(acac)(**1**)]$^+$	[a]2.052	[a]2.057	[a]2.250	[d]-3.00	[d]0.350	[d]-2.005	[b]30	[b]40	[c]550	[d]-0.007	[d]2.85	[d]0.0044	*t.w*
[e][Cu(acac)(**2**)]$^+$	[a]2.054	[a]2.058	[a]2.259	[d]-3.00	[d]3.10	[d]-3.00	[b]30	[b]40	[c]540	[d]-0.6862	[d]-3.0391	[d]0.0010	*t.w*
[e][Cu(acac)(**3**)]$^+$	[a]2.057	[a]2.057	[a]2.258	[d]-1.0998	[d]3.1346	[d]1.0991	[b]35	[b]35	[c]540	[d]0.4670	[d]0.0072	[d]0.0596	*t.w*
[e][Cu(acac)(**4**)]$^+$	[a]2.056	[a]2.056	[a]2.256	[d]0.55	[d]0.55	[d]0.5825	[b]35	[b]35	[c]540	[d]0.5690	[d]0.5690	[d]0.1927	*t.w*
[Cu(acac)(**1**)]$^+$	2.0427	2.0457	2.1479	-1.9045	0.3283	-0.1955	-127.4047	-129.3347	-857.0561	-1.7724	2.8131	1.9044	DFT
[Cu(acac)(**2**)]$^+$	2.0431	2.0464	2.1510	1.7724	3.1396	-1.3767	-127.6904	-130.6619	-858.3587	-3.0391	0.0019	-1.6862	DFT
[Cu(acac)(**3**)]$^+$	2.0433	2.0468	2.1538	-1.0998	3.1346	1.9991	-126.8962	-129.5250	-858.8942	0.4670	0.0072	1.0596	DFT
[Cu(acac)(**4**)]$^+$	2.0422	2.0459	2.1493	-0.9515	1.5732	1.5825	-123.3794	-131.4145	-852.2420	0.8328	1.5690	-2.1927	DFT
							$^{Cu}A_1$	$^{Cu}A_2$	$^{Cu}A_3$	α	β	γ	
										Euler angles rotation of the A frame with respect to the g frame			
							/MHz	/MHz	/MHz	/rad	/rad	/rad	
[Cu(acac)(**1**)]$^+$							-129.3347	-127.4047	-857.0561	0.0052	0	0	DFT
[Cu(acac)(**2**)]$^+$							-130.6619	-127.6904	-858.3587	0.0052	0	0	DFT
[Cu(acac)(**3**)]$^+$							-129.5250	-126.8962	-858.8942	0.0017	0	0	DFT
[Cu(acac)(**4**)]$^+$							-852.2420	-131.4145	-123.3794	-0.0017	1.5656	-0.7261	DFT

t.w = this work. ^{Cu}A is given in MHz. [a]± 0.03 [b]± 5 MHz [c]± 4 MHz [d]± 0.26 rad. Diimine ligands, (**1**) 2,2'-bipyridine (bipy), (**2**) 1,10-phenanthroline (phen), (**3**) dipyridophenanzine (dppz), (**4**) 2,3-bis(2-pyridyl)pyrazine (Py-bipy). Solvent system; [e]EtOH:DMF (1:1).

As seen in the W-band spectra for [Cu(acac)(**1**)]$^+$ (Figure 5.2), the *g* values reveal a small but noticeable rhombic symmetry. A similar behaviour was also found for [Cu(acac)(**2**)]$^+$, whereas both [Cu(acac)(**3**)]$^+$ and [Cu(acac)(**4**)]$^+$ retain a distinct axial set of *g* values (Figure 5.3 and Table 5.1). In Figure 5.3 the experimental and simulated W-band spectra of [Cu(acac)(**1-4**)]$^+$ are shown together. These observations suggests a greater degree of distortion in the Cu(II)-N_2 plane for bipy and phen compared to the dppz and Py-bipy ligands which enable the Cu(II) ion to retain a more localised axial environment.[40]

The ^{14}N superhyperfine splitting, caused by the two nitrogen atoms ($I = 1$) of the diimine, are clearly visible in the X-band EPR spectra (Figure 5.1), both at low $g = g_{||}$ field position ($m_I = + 3/2$) and at the higher $g = g_{\perp}$ position. However, the contributions to the spin Hamiltonian parameters from the two ^{63,65}Cu isotopes and the ^{14}N nuclei could not be accurately determined from the X-band EPR spectra alone. In general, large ^{14}N superhyperfine couplings can be directly observed in the X-band EPR spectra of Cu(II) nitrogen macrocycles.[41–45] The presence of such well-resolved features in Figure 5.1 arises from the considerably large magnitude of the ^{14}N coupling. As the *g*-anisotropy is responsible for the overlap of g_1, g_2 and g_3 features, accurate determination of the *g*-values due to the superimposed ^{14}N superhyperfine pattern requires the higher microwave frequencies. However, at higher microwave frequencies the ^{14}N superhyperfine splitting is lost due to strain effects, which become first order at Q and W-band. For example, the *g*-strain effect is 10 times larger at W-band frequencies compared to X-band, and as a result the hyperfine splitting resolution is lost. To successfully extract the superhyperfine couplings, and for ^{14}N the additional quadrupole coupling, angular selective ENDOR measurements are required. For this reason, ^{14}N and ^{1}H ENDOR spectra were also recorded. ENDOR spectroscopy provides more information on the extent of spin delocalisation onto the surrounding ligand nuclei. By recording the ENDOR data at selected magnetic field positions, one can observe spectra from copper complexes having a specific orientation with respect to the external magnetic field, providing unique insights into the Cu(II) paramagnetic centre and its non-zero nuclei surrounding.[46,47]

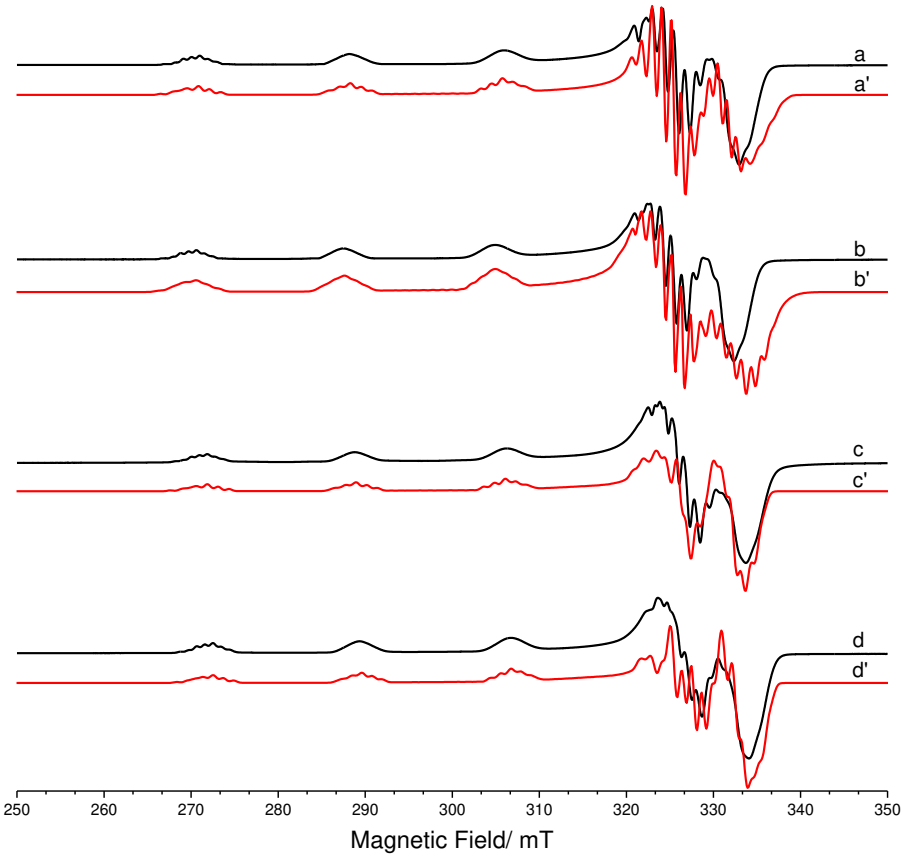

Figure 5.1 X-band CW-EPR spectra (recorded at 140 K) of a) [Cu(acac)(**1**)]$^{+}$, b) [Cu(acac)(**2**)]$^{+}$, c) [Cu(acac)(**3**)]$^{+}$ and d) [Cu(acac)(**4**)]$^{+}$, using a OTf counterions in all cases. All complexes dissolved in EtOH:DMF (1:1). Corresponding simulations are shown in red trace (a′-d′).

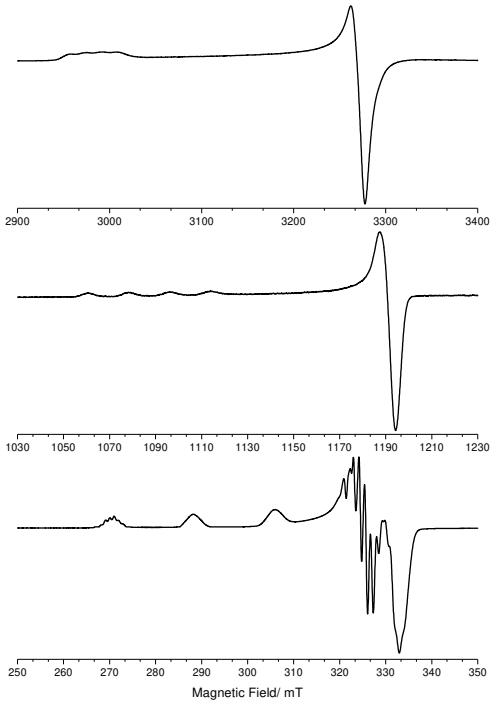

Figure 5.2 Multi-frequency CW EPR spectra of 2,2'-bipyridine (bipy) [Cu(acac)(**1**)]$^{+}$ recorded at X-, Q- and W-band frequency. All spectra measured at 10 K. All complexes dissolved in EtOH:DMF (1:1).

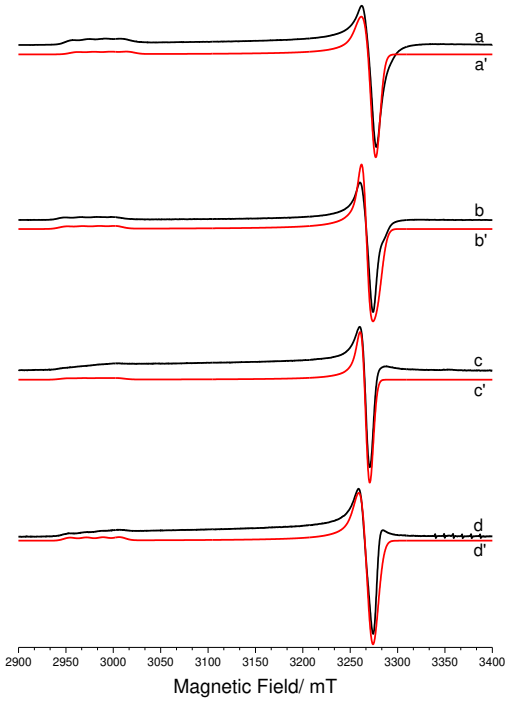

Figure 5.3 W-band CW-EPR spectra (recorded at 10 K) of a) [Cu(acac)(**1**)]$^{+}$, b) [Cu(acac)(**2**)]$^{+}$, c) [Cu(acac)(**3**)]$^{+}$ and d) [Cu(acac)(**4**)]$^{+}$, using a OTf counterions in all cases. All complexes dissolved in EtOH:DMF (1:1). Corresponding simulations are shown in red trace (a′-d′)

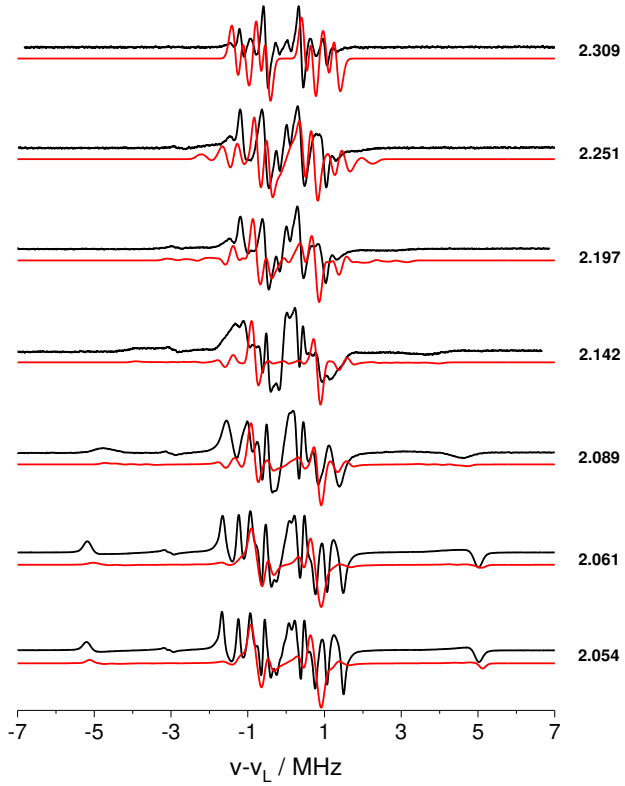

Figure 5.4 Q-band CW ^{1}H ENDOR spectra (measured at 10 K) of [Cu(acac)(**1**)]$^{+}$ dissolved in EtOH:DMF (1:1) recorded at the field positions corresponding the labelled *g*-values. Corresponding simulations shown in red trace.

Table 2 Experimental and DFT calculated ^{1}H principal hyperfine values for the [Cu(acac)(N-N)]OTf complexes.

Atom No.		$^{1H}A_1$	$^{1H}A_2$	$^{1H}A_3$	α	β	γ	**ref.**
					Euler angles rotation of the A frame with respect to the molecular frame			
		/MHz	/MHz	/MHz	/rad	/rad	/rad	
[e][Cu(acac)(**1**)]+								
H-Imine	27H/3H	[a]2.10	[a]3.30	[b]10.20	-1.60	1.60	-2.10	*t.w*
Methine	6H	[d]1.10	[d]-1.80	[d]-2.70	-0.50	0.50	-1.00	*t.w*
Methyl (1)	---	1.10	1.60	1.80	1.00	-1.70	-2.00	*t.w*
Methyl (2)	---	[a]-0.90	[d]1.60	[d]-1.00	0	0	0	*t.w*
[e][Cu(acac)(**2**)]+								
H-Imine	27H/30H	[a]2.30	[a]3.60	[a]10.00	-0.80	1.60	-2.00	*t.w*
Methine	6H	[d]1.50	[d]-2.10	[d]-2.80	0	0.70	-1.00	*t.w*
Methyl (1)	---	1.50	1.60	1.80	-0.20	0.40	2.40	*t.w*
Methyl (2)	---	[d]-0.90	[d]1.60	[d]-1.00	0	0	0	*t.w*
[e][Cu(acac)(**3**)]+								
H-Imine	27H/30H	[a]2.90	[a]2.90	[a]9.80	1.70	1.70	1.70	*t.w*
Methine	6H	[d]2.10	[d]-2.10	[d]-3.00	0	1.00	-1.00	*t.w*
Methyl (1)	---	1.50	1.50	2.20	0.5	0.5	-0.60	*t.w*
Methyl (2)	---	[d]-0.90	[d]1.60	[d]-1.00	0	0	0	*t.w*
[e][Cu(acac)(**4**)]+								
H-Imine	33H/36H	[a]3.00	[a]3.00	[a]10.00	1.70	1.70	1.70	*t.w*
Methine	26H	[d]2.10	[d]-2.10	[d]-3.00	0	1.00	-1.00	*t.w*
Methyl (1)	---	1.40	1.40	2.20	0.50	0.50	-0.60	*t.w*
Methyl (2)	---	[a]-0.90	[a]1.60	[a]-1.00	0	0	0	*t.w*
Atom No.		$^{1H}A_1$	$^{1H}A_2$	$^{1H}A_3$	α	β	γ	**ref.**
					Euler angles rotation of the A frame with respect to the g frame			
		/MHz	/MHz	/MHz	/rad	/rad	/rad	
[Cu(acac)(**1**)]+								
H-Imine	27H	3.0944	4.6294	11.2683	0.3144	1.4689	0.6301	DFT
H-Imine	31H	3.0956	4.6311	11.2696	-0.3272	1.5928	-2.7361	DFT
Methine	6H	0.8800	-2.2499	-3.0904	-2.9551	0.3422	-1.2292	DFT
H-Methyl	8H	0.5127	-2.6452	-3.3541	1.8033	1.1932	-1.9232	DFT
H-Methyl	9H	0.8553	-2.4482	-3.2436	-0.5095	0.5108	0.6142	DFT
H-Methyl	10H	1.9335	2.6694	4.9599	-0.2986	1.2249	2.4297	DFT
H-Methyl	12H	0.8570	-2.4468	-3.2426	-2.6530	0.6337	-2.7028	DFT
H-Methyl	13H	0.5115	-2.6459	-3.3545	1.7137	2.0408	2.9216	DFT

H-Methyl	14H	1.9325	2.6683	4.9590	0.1734	1.1856	1.7921	DFT
[Cu(acac)(**2**)]+								
H-Imine	27H	3.3818	4.6888	11.0554	-0.0001	1.5675	1.701878	DFT
H-Imine	31H	0.2193	0.4127	2.3182	-0.0038	1.5681	1.164614	DFT
Methine	6H	0.8747	-2.2766	-3.1357	-3.0306	0.0133	-0.11896	DFT
H-Methyl	8H	0.5056	-2.6852	-3.4054	2.0622	0.9502	-1.01325	DFT
H-Methyl	9H	0.8503	-2.4869	-3.2935	-1.0289	0.6729	2.086045	DFT
H-Methyl	10H	2.0009	2.7514	5.0599	0.1357	1.6278	0.286984	DFT
H-Methyl	12H	0.8566	-2.4826	-3.2905	-2.1159	0.6723	-2.09954	DFT
H-Methyl	13H	0.5014	-2.6863	-3.4056	1.0821	0.9515	0.99543	DFT
H-Methyl	14H	1.9968	2.7471	5.0557	-0.1362	1.6301	-0.30297	DFT
[Cu(acac)(**3**)+								
H-Imine	27H	3.2377	4.5865	10.9852	0.0046	1.5743	1.6608	DFT
H-Imine	31H	0.2385	0.4290	2.3445	-0.0057	1.5770	1.1353	DFT
Methine	6H	0.8867	-2.2507	-3.0975	-0.3742	0.0189	0.3320	DFT
H-Methyl	8H	0.5177	-2.6614	-3.3735	2.0511	0.9406	-1.0423	DFT
H-Methyl	9H	0.8502	-2.4682	-3.2638	-1.0190	0.6808	2.0428	DFT
H-Methyl	10H	1.9679	2.7079	5.0069	-0.1253	1.5092	-2.8868	DFT
H-Methyl	12H	0.8575	-2.4629	-3.2603	-2.1125	0.6652	-2.1349	DFT
H-Methyl	13H	0.5131	-2.6627	-3.3737	1.0822	0.9565	0.9625	DFT
H-Methyl	14H	1.9639	2.7036	5.0028	-0.1422	1.6300	-0.3401	DFT
[Cu(acac)(**4**)]+								
H-Imine	33H	3.0380	4.7215	11.3327	1.0669	2.8135	-1.0142407	DFT
H-Imine	36H	3.1572	4.6423	11.1289	1.5682	3.0895	-0.6905183	DFT
Methine	26H	0.8623	-2.2832	-3.1320	1.7407	1.5997	-2.2027207	DFT
H-Methyl	27H	0.6436	-2.5991	-3.3733	0.1317	0.9775	1.56622162	DFT
H-Methyl	28H	0.6653	-2.6233	-3.3890	0.1665	2.1243	0.35674377	DFT
H-Methyl	29H	2.1081	2.8642	5.1711	1.6006	1.1056	-0.6363181	DFT
H-Methyl	30H	0.6598	-2.5740	-3.3066	-0.5391	0.8233	0.57390318	DFT
H-Methyl	31H	0.6664	-2.5497	-3.2970	-2.5906	0.8413	-1.8399565	DFT
H-Methyl	32H	1.9161	2.6503	4.9292	1.5739	1.6940	-0.629672	DFT

t.w = this work. [1]HA given in MHz. a±0.2 b±0.5 [c]±0.26 rad, [d]±0.1. Diimine ligands, (**1**) 2,2'-bipyridine (bipy), (**2**) 1,10-phenanthroline (phen), (**3**) dipyridophenanzine (dppz), (**4**) 2,3-bis(2-pyridyl)pyrazine (Py-bipy). Solvent system; [e]EtOH-d_6:DMF-d_7 (1:1).

5.3.2 ^{1}H ENDOR

The Q-band angular selective experimental and simulated ^{1}H ENDOR spectra of [Cu(acac)(**1**)]$^{+}$ are shown in Figure 5.4. The analogous ^{1}H ENDOR spectra for the [Cu(acac)(**2-4**)]$^{+}$ complexes are shown in Appendix, Figure D3 and D4. All four complexes produce a similar ^{1}H ENDOR pattern with large couplings arising from the imine ^{1}H (labelled blue in Scheme 5.2 above). For this reason, only the ENDOR spectra of [Cu(acac)(**1**)]$^{+}$ will be described in detail here, and the necessary comparisons between the resulting spin Hamiltonian parameters of the other three [Cu(acac)(N-N)]$^{+}$ complexes (see Table 5.2) will be discussed accordingly.

A distinct feature of these type of copper complexes are the large couplings for the imine protons, as reported elsewhere in literature. The large coupling is attributed to the conjugation of the imine proton with the coordinating nitrogen atoms, resulting in significant unpaired spin density delocalising over the proton.

The maximum coupling for [Cu(acac)(**1**)]$^{+}$ is observed at the field position corresponding to g = 2.054, with a value of 10.20 MHz (Figure 5.4). The two remaining hyperfine components of the hyperfine tensor were postulated to be 2.10 MHz and 3.30 MHz and these can be readily assigned to the H-imine proton.

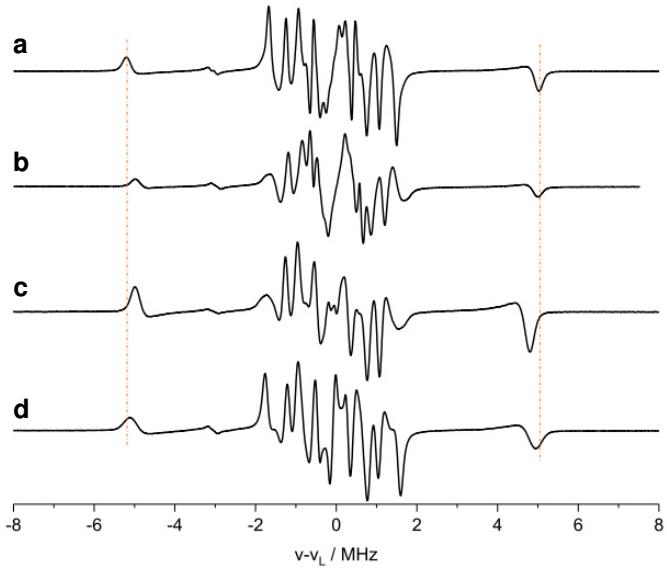

Figure 5.5 CW Q-band ^{1}H ENDOR spectra (10 K) of a) a) [Cu(acac)(**1**)]$^{+}$, b) [Cu(acac)(**2**)]$^{+}$, c) [Cu(acac)(**3**)]$^{+}$ and d) [Cu(acac)(**4**)]$^{+}$, dissolved in EtOD-d_6:DMF-d_7 (1:1), recorded at the field positions corresponding to g = 2.05.

Overall the ^{1}H imine coupling for the [Cu(acac)(**1-4**)]$^{+}$ complexes follow the same trend, possessing a positive ^{1}H tensor with a considering rhombic character for [Cu(acac)(**1**)]$^{+}$ (^{1H}A = [2.10 3.30 10.20] MHz) and [Cu(acac)(**2**)]$^{+}$ (^{1H}A = [2.30 3.60 10.00] MHz) in contrast to the more axial ^{1H}A-tensor values for [Cu(acac)(**3**)]$^{+}$ (^{1H}A = [2.90 2.90 9.80] MHz) and [Cu(acac)(**4**)]$^{+}$ (^{1H}A = [3.00 3.00 10.00] MHz). In summary, the largest hyperfine components for the [Cu(acac)(**1-4**)]$^{+}$ complexes were found to be 10.20 MHz (bipy), 10.00 MHz (phen), 9.80 MHz (dppz) and 10.00 MHz (Py-bipy), respectively, and this subtle variation in $^{1H}A_3$ can be clearly seen below in Figure 5.5.

The decrease in magnitude of the coupling appears to correlate with the increase size of the diimine ligands and suggests that the imine protons are very sensitive to the delocalisation of the spin density over the aromatic ring system. For example, the coupling magnitude is greatest for 2,2'-bipyridine, where the spin density is delocalised over two six-membered rings whilst it is smallest for the dppz ligand, where the spin density is localised over a more extended aromatic ring system.

This trend was not only observed experimentally but also was predicted by DFT calculations (Table 5.2) and are in good agreement with the observed experimental hyperfine value for the ^{1}H-imine protons. Also, the small increase of the largest hyperfine coupling value for Py-bipy was also observed in the DFT calculation. The pyridyl residue is substituted on the 2,2'-bipyrdine ring. Even so, the diimine is still fully aromatic, the delocalisation effect is similar to the bipyridine and this explains the hyperfine coupling value of 10.00 MHz. Simulation of the complete angular selective ^{1}H ENDOR spectra of [Cu(acac)(**1**)]$^{+}$ is given in Figure 5.4. The imine derived resonances were accounted for using the proton tensor above, whilst the acetylacetonato ligand derived resonances were accounted for by a combination of the methine protons (Scheme 5.2) and the combined variation of rotational and hindered methyl group protons.

It should be noted that the components of the methine tensor in [Cu(acac)(**1**)]$^{+}$, and the other complexes described herein, are slightly different compared to [Cu(acac)$_2$], which has been thoroughly investigated by Sharples *et al.*[48]. Slight differences in the values might be explained from the fact that the [Cu(acac)(N-N)]$^{+}$ complexes were recorded in EtOD-d$_6$:DMF-d$_7$ (1:1), whilst the [Cu(acac)$_2$][48] complexes were recorded in CDCl$_3$:Tol-d$_8$ (1:1) and this

may account for the slight differences. However, the proton labelled Methyl (1) (Table 5.2) is not in agreement with the reported couplings and might be due to the fact that different angles have been applied.

5.3.3 ^{14}N ENDOR

The ^{14}N superhyperfine patterns observed in the CW X-band EPR spectra (Figure 5.1a-d) are a rich source of structural information and can help to understand the coordination of the different sized diimine ligands on the copper centre. In order to extract the hyperfine and nuclear quadrupole values of the ^{14}N nuclei from the diimine ligand, Q-band CW ENDOR measurements were conducted on each sample [Cu(acac)(**1-4**)]$^+$. The experimental and corresponding simulations for [Cu(acac)(**1**)]$^+$ are shown in Figure 5.6. The corresponding ^{14}N ENDOR spectra for the [Cu(acac)(**2-4**)]$^+$ are given in Figure D6I-II and D7 in the Appendix. The ^{14}N couplings are well resolved, enabling one to simulate the angular selective profile more accurately than for the ^{14}N couplings observed in the X-band EPR spectra in Figure 5.1.

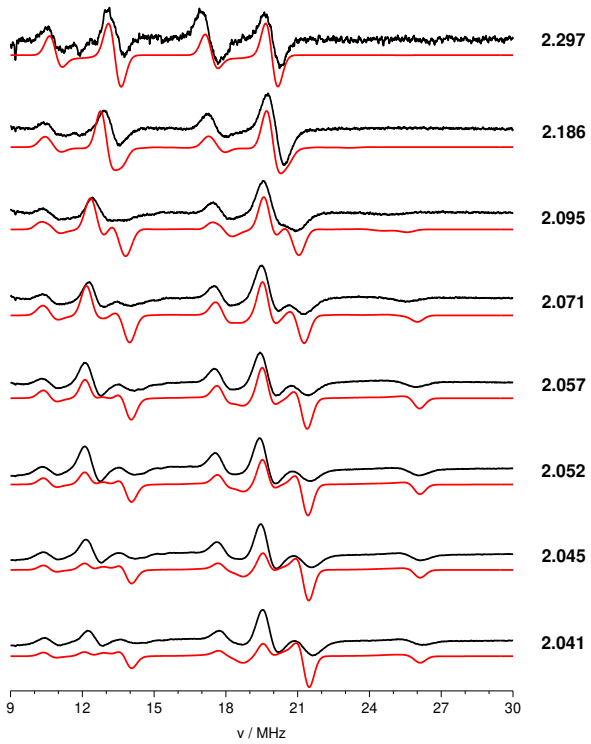

Figure 5.6 Q-band CW ^{14}N ENDOR spectra (measured at 10 K) of [Cu(acac)(**1**)]$^+$ dissolved in EtOH:DMF (1:1) recorded at the field positions corresponding the labelled *g*-values. Corresponding simulations shown in red trace.

The resulting couplings are given in Table 5.3. The hyperfine and quadrupolar coupling from the ^{14}N ($I = 1$) nuclei in [Cu(acac)(**1**)]$^+$ and [Cu(acac)(**2**)]$^+$ complex are of rhombic symmetry with the largest hyperfine coupling found as $^{14N}A_3$ = 40 MHz or 38.7 MHz, for both complexes respectively. In the case of [Cu(acac)(**3**)]$^+$ and [Cu(acac)(**4**)]$^+$ complex, the hyperfine and quadrupole appear to be of more axial symmetry with the largest hyperfine coupling of $^{14N}A_3$ = 38.8 MHz and 39.1 MHz, respectively. For the ^{14}N ENDOR measurements, it is given that the size of the diimine ligand has a subtle impact on the magnitude of the hyperfine coupling, in the following order for the largest coupling $^{14N}A_3$ for the [Cu(acac)(**1-4**)]$^+$ with, 40 MHz (bipy), 38.7 MHz (phen), 38,8 MHz (dppz) and 39.1 MHz (Py-bipy). This is analogous to the trends observed with the ^1H data.

5.3.4 DFT data

The DFT data, used to calculate the spin Hamiltonian parameters via ORCA, was obtained from the geometry optimised structures, shown below in Figure 5.7 for [Cu(acac)(**3**)]$^+$. The corresponding structures for [Cu(acac)(**1,2,4**)]$^+$ are shown in Appendix, Figure D5. The relative orientation of the *g*-frame with respect to the molecular frame is indicated in the figure. The ^{14}N hyperfine tensor is also found to be largely coincident with the g-frame.

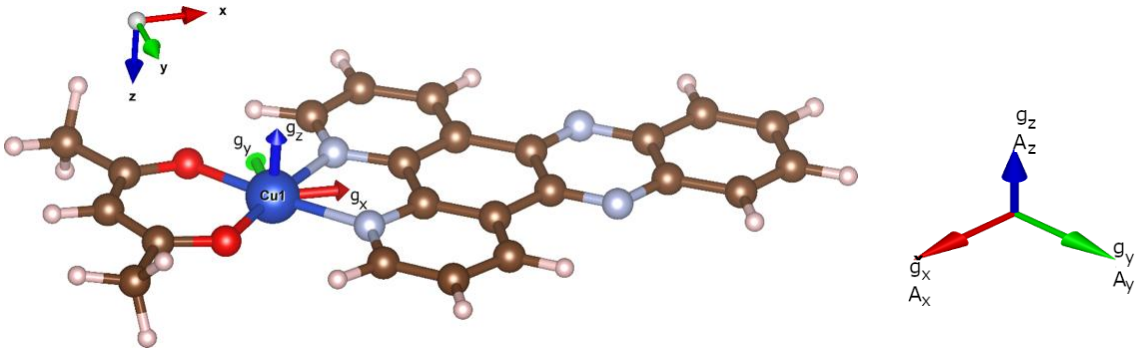

Figure 5.7 Geometry optimised structure for [Cu(acac)(**3**)]$^+$. The *g*-frame is reported on the Cu atom with the same colour coding as the molecular frame on the right-hand side of the structure: *x* (red), *y* (green) and *z* (blue).

Table 3. Experimental and DFT calculated ^{14}N principal hyperfine and quadrupole values for the [Cu(acac)(N-N)]OTf complexes.

		$^{14N}A_1$	$^{14N}A_2$	$^{14N}A_3$	α	β	γ	Q_1/h	Q_2/h	Q_3/h	α	β	γ	$\lvert e^2qQ/h\rvert$	η	ref.
					Euler angles rotation of the A frame with respect to the molecular frame						Euler angles rotation of the Q frame with respect to the molecular frame					
		/MHz	/MHz	/MHz	/rad	/rad	/rad	/MHz	/MHz	/MHz	/rad	/rad	/rad			
[d][Cu(acac)(**1**)]$^+$		[a]30	[a]31	[a]40	[b]1.5	[b]1.6	[b]-1.3	[c]0.75	[c]0.90	[c]-1.65	[b]1.6	[b]1.7	[b]1.3	--	--	*t.w*
[d][Cu(acac)(**2**)]$^+$		[a]28.7	[a]29.7	[a]38.7	[b]1.5757	[b]1.5679	[b]-2.5749	[c]0.7375	[c]0.9061	[c]-1.6436	[b]1.4278	[b]1.5743	[b]-1.5355	--	--	*t.w*
[d][Cu(acac)(**3**)]$^+$		[a]29.3	[a]29.3	[a]38.8	[b]1.5	[b]1.6	[b]2.8	[c]0.8	[c]0.8	[c]-1.6	[b]1.65	[b]1.65	[b]3.1413	--	--	*t.w*
[d][Cu(acac)(**4**)]$^+$		[a]30	[a]30	[a]39.3	[b]1.4	[b]1.6	[b]0.6248	[c]0.8	[c]0.8	[c]1.6	[b]1.5781	1.5781	[b]3.1413	--	--	*t.w*
[Cu(acac)(**1**)]$^+$	15N	31.7721	32.7737	42.8043	1.4399	1.8669	-1.6681	0.5645	0.8205	-1.3851	1.7194	1.2824	2.9980	2.774	0.185	DFT
[Cu(acac)(**1**)]$^+$	16N	31.7801	32.7820	42.8142	1.8061	1.7940	-0.4115	0.5646	0.8205	-1.3851	0.3622	1.3602	-2.8977	2.774	0.185	DFT
[Cu(acac)(**2**)]$^+$	15N	30.7777	31.7936	41.3123	1.5757	1.5679	-0.5829	0.5376	0.8061	-1.3437	0.6278	1.5743	-3.1355	2.691	0.200	DFT
[Cu(acac)(**2**)]$^+$	16N	30.7696	31.7853	41.3023	1.5725	1.5757	-2.5749	0.5375	0.8061	-1.3436	2.5300	1.5652	-3.1386	2.691	0.200	DFT
[Cu(acac)(**3**)]$^+$	15N	31.1116	32.1086	41.7706	1.5684	1.5648	-0.6246	0.5280	0.8081	-1.3360	0.6672	1.5781	3.1413	2.676	0.210	DFT
[Cu(acac)(**3**)]$^+$	16N	31.1082	32.1051	41.7660	1.5625	1.5719	0.5401	0.5279	0.8081	-1.3360	-0.5828	1.5706	3.1315	2.676	0.210	DFT
[Cu(acac)(**4**)]$^+$	8N	31.5948	32.5856	42.3062	2.9361	0.7899	-0.3355	0.6747	0.8741	-1.5488	-2.8197	0.7464	0.4336	3.102	0.129	DFT
[Cu(acac)(**4**)]$^+$	13N	31.5528	32.5525	42.6313	0.2430	1.1701	2.3117	0.5357	0.8229	-1.3586	0.8807	1.1271	-1.8202	2.721	0.211	DFT
		$^{14N}A_1$	$^{14N}A_2$	$^{14N}A_3$	α	β	γ	Q_1/h	Q_2/h	Q_3/h	α	β	γ	$\lvert e^2qQ/h\rvert$	η	ref.
					Euler angles rotation of the A frame with respect to the g frame						Euler angles rotation of the Q frame with respect to the g frame					
		/MHz	/MHz	/MHz	/rad	/rad	/rad	/MHz	/MHz	/MHz	/rad	/rad	/rad			
[Cu(acac)(**1**)]$^+$	15N	31.7721	42.8043	32.7737	0.7592	0.0052	0.2059	0.8205	-1.3851	0.5645	0.6213	0.0087	0.2932	2.774	0.185	DFT
[Cu(acac)(**1**)]$^+$	16N	31.7801	42.8142	32.7820	-0.7435	0.0052	-0.2234	0.8205	-1.3851	0.5646	-0.6039	0.0070	-0.3124	2.774	0.185	DFT
[Cu(acac)(**2**)]$^+$	15N	41.31	30.78	31.79	0.6929	0.0052	-0.1169	-1.3437	0.8061	0.5376	0.7802	0.0052	-0.1606	2.691	0.200	DFT
[Cu(acac)(**2**)]$^+$	16N	41.30	30.77	31.79	-0.7278	0.0052	0.1536	0.8061	-1.3436	0.5375	0.7627	0.0052	0.1885	2.691	0.200	DFT
[Cu(acac)(**3**)]$^+$	15N	41.7706	31.1116	32.1086	0.7487	0.0070	-0.1658	0.8081	-1.3360	0.5280	-0.7313	0.0087	-0.2147	2.676	0.210	DFT
[Cu(acac)(**3**)]$^+$	16N	41.7660	31.1082	32.1051	-0.7610	0.0070	0.1780	0.8081	-1.3360	0.5279	0.7243	0.0087	0.2217	2.676	0.210	DFT
[Cu(acac)(**4**)]$^+$	8N	42.3062	31.5948	32.5856	-0.0227	0.2025	0.8360	0.8741	-1.5488	0.6747	-0.2059	1.3614	-0.6685	3.102	0.129	DFT
[Cu(acac)(**4**)]$^+$	13N	32.5525	31.5528	42.6313	-0.1623	1.3753	-0.3962	0.5357	0.8229	-1.3586	-0.1379	1.3334	-0.4451	2.721	0.211	DFT

t.w = this work. ^{14N}A is given in MHz. [a]±3 MHz, [b]±0.26 rad, [c]± 0.1 MHz. Diimine ligands, (**1**) 2,2'-bipyridine (bipy), (**2**) 1,10-phenanthroline (phen), (**3**) dipyridophenanzine (dppz), (**4**) 2,3-bis(2-pyridyl)pyrazine (Py-bipy). Solvent system; [d]EtOH-d_6:DMF-d_7 (1:1).

5.3.5 Adduct study

As the copper casiopeina complexes are used for the intercalation with DNA, it was deemed necessary to investigate the adduct formation properties of the complexes with a series of N-based donor substrates. Guanine and adenine are not dissolvable in the solvent system adopted in the current studies, and for this reason only the model substrates of imidazole and L-histidine were investigated. The CW X-band EPR spectra (140 K) of $[Cu(acac)(\mathbf{1})]^+$ dissolved in EtOH:DMF are shown in Figure 5.8, with increasing ratios of added imidazole (abbreviated Im). To investigate the nature and coordination mode of the adducts formed between $[Cu(acac)(N\text{-}N)]^+$ and imidazole, a speciation study was performed by increasing the Cu:Im ratios from 1:0 to 1:100 in EtOH:DMF (1:1) solvent.

At a ratio of 1:2 (Cu:Im) a shift to lower field position for the $^{Cu}A_3$ value is clearly observed, indicating the coordination of one imidazole to the square planar copper complex in the axial position. A similar observation was observed in the previous Chapter 4, for the $[Cu(acac)_2]$ complex.[49] In addition at least one additional Im substrate binds to the $[Cu(acac)(\mathbf{1})]^+$ complex, as noted by the appearance of a second signal. This second signal increases when the concentration of Im increases, with the steady decrease in the first signal. Similar trends have been observed for $[Cu(acac)(\mathbf{2})]^+$ (see Appendix, Figure D8). On the contrary, in the case of $[Cu(acac)(\mathbf{3})]^+$ and $[Cu(acac)(\mathbf{4})]^+$ (Figure D8II and D9), the coordination of one imidazole, forming a square pyramidal complex, appears to be the only dominant species. Only small traces of a second bis-adduct species, especially at high Cu:Im ratios of 1:50, 1:70 and 1:100, can be observed. A variable ratio study was also conducted for L-histidine (L-his) with $[Cu(acac)(\mathbf{1})]^+$ and $[Cu(acac)(\mathbf{2})]^+$ (Figure D10I-II). The coordination trend of L-his is from an axial position, forming square pyramidal $[Cu(acac)(\mathbf{1\text{-}2}]^+$ adducts. For completeness the EPR spectra are given in the supporting information (Figure D10I-II).

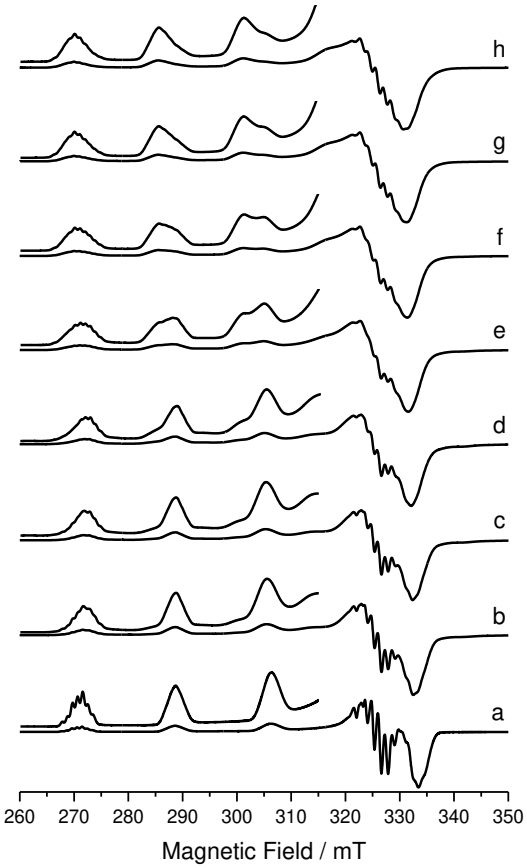

Figure 5.8 CW X-band EPR spectra (140 K) of [Cu(acac)(**1**)]$^+$ recorded with increasing Cu:Im ratios, a) 1:0, b) 1:2, c) 1:5, d) 1:10, e) 1:30, f) 1:50, g) 1:70 and h) 1:100.

5.4 Conclusions

Copper casiopeina type complexes have been studied for many years, as they are showing promising potential as therapeutic agents. In general, casiopeina complexes have shown to possess less toxic side effects compared to existing cis-platinum drugs. The therapeutic mechanism of the casiopeina still remains unclear and many approaches have been made, such as structural modifications of the complex and spectroscopic studies, to explore this mechanism. To this date, no ENDOR spectroscopic studies have been reported in the literature. ENDOR spectroscopy has proven to be a powerful tool for unravelling the structure-function relationships in proteins, particularly in copper protein chemistry. This tool could therefore be extended to copper based therapeutics.

Therefore, a series of unbound casiopeina complexes with the general formula [Cu(acac)(N-N)]$^+$ were prepared, and their electronic properties

examined through EPR and ENDOR spectroscopy. Within the series of complexes studied, the diimine ligand (N-N) was systematically varied in size using 2,2'-bipyridine (bipy), 1,10-phenanthroline (phen), dipyridophenazine (dppz) and a pyridine substituted 2,2'-bipyridine ligand (Py-bipy). These diimine ligands were selected in light of the fact that the size of the aromatic diimine ligand may influence the therapeutic activity. The EPR spectra, recorded in ETOH:DMF (1:1) were characterised by rhombic *g* and *A* values for [Cu(acac)(**1**)]$^+$ and [Cu(acac)(**2**)]$^+$, with predominantly axial parameters for [Cu(acac)(**3**)]$^+$ and [Cu(acac)(**4**)]$^+$, indicating that the size of the diimine ligand can influence the EPR symmetry. The diimine ligand bipy and phen might have small but not negligible strain effect on the coordination to the copper centre. As a result, a very small distortion of the resulting square planar geometry might occur, which can be detected by EPR spectroscopy.

Differences between the four complexes were also detected in the ^{1}H ENDOR data. The magnitude of the largest imine hyperfine component observed at 90 °, was found to be sensitive to size of the diimine ligand. Larger couplings were observed for smaller aromatic ring systems, *i.e.,* bipy, due to the restricted spin delocalisation. Smaller couplings were observed for larger aromatics ligands (*i.e.,* dppz), where spin delocalisation is more diffuse. This observation was confirmed by ^{14}N ENDOR measurement revealing a decrease of the largest $^{14N}A_3$ coupling for the [Cu(acac)(**1-4**)]$^+$, from 40 MHz (bipy), to 38.7 MHz (phen), to 38,8 MHz (dppz) and to 39.1 MHz (Py-bipy). The spin distribution in the diimine ligand could provide valuable information on DNA intercalation. The π-π interactions involved in the intercalation may influence the spin density distribution in the diimine ligand and be manifested as changes in the magnitude of the largest imine hyperfine component in the ^{1}H ENDOR spectra. The adduct study with heterocycle nitrogen molecules has shown the tendency of Im and L-his to coordinate in the axial position. However, further investigations need to be carried out to gather a wider picture of the possible interaction with heterocycle nitrogen molecules such as nitrogen bases.

5.5 References

1. C. Santini, M. Pellei, V. Gandin, M. Porchia, F. Tisato, C. Marzano, *Chem Rev*, **2014**, 114, 815-862.
2. M. E. Bravo-Gómez, J. C. García-Ramos, I. Gracia-Mora, L. Ruiz-Azuara, *J. Inorg. Biochem.*, **2009**, 103, 299-309.
3. L. Becco, A. Rodríguez, M. E. Bravo, M. J. Prieto, L. Ruiz-Azuara, B. Garat, V. Moreno, D. Gambino, *J. Inorg. Biochem.*, **2012**, 109, 49-56.
4. A. De Vizcaya-Ruiz, A. Rivero-Muller, L. Ruiz-Ramirez, G. E. N. Kass, L. R. Kelland, R. M. Orr, M. Dobrota, *Toxicol. in Vitro*, **2000**, 14, 1-5.
5. C. Trejo-Solís, G. Palencia, S. Zúñiga, A. Rodríguez-Ropon, L. Osorio-Rico, S. T. Luvia, I. Gracia-Mora, L. Marquez-Rosado, A. Sánchez, M. E. Moreno-García, A. Cruz, M. E. Bravo-Gómez, L. Ruiz-Ramírez, S. Rodríguez-Enriquez ,J. Sotelo, *Neoplasia*, **2005**, 7, 563-574.
6. F. Carvallo-Chaigneau, C. Trejo-Solís, C. Gómez-Ruiz, E. Rodríguez-Aguilera, L. Macías-Rosales, E. Cortés-Barberena, C. Cedillo-Peláez, I. Gracia-Mora, L. Ruiz- Azuara, V. Madrid-Marina, F. Constantino-Casas, *Biometals.*, **2008**, 21, 17-28.
7. A. Tovar-Tovar, L. Ruiz-Ramírez, A. Campero, A. Romerosa, R. Moreno-Esparza, M. J. Rosales-Hoz, *J. Inorg. Biochem.*, **2004**, 98, 1045-1053.
8. M. O'Connor, A. Kellett, M. McCann, G. Rosair, M. McNamara, O. Howe, B. S. Creaven, S. McClean, A. Foltyn-Arfa Kia, D. O'Shea, M. Devereux, *J. Med. Chem.*, **2012**, 55, 1957-1968.
9. M. E. Katsarou, E. K. Efthimiadou, G. Psomas, A. Karaliota, D. Vourloumis, *J. Med. Chem.*, **2008**, 51, 470-478.
10. R. Horikoshi, Y. Funasako, T. Yajima, T. Mochida, Y. Kobayashi, H. Kageyama, *Polyhedron*, **2013**, 50, 66-74.
11. O. O. E. Onawumi, O. O. P. Faboya, O. A. Odunola, T. K. Prasad, M. V. Rajasekharan, *Polyhedron*, **2008**, 27, 113-117.
12. N. r. Aliaga-Alcalde, P. Marqués-Gallego, M. Kraaijkamp, C. Herranz-Lancho, H. den Dulk, H. Görner, O. Roubeau, S. J. Teat, T. Weyhermüller, J. Reedijk, *Inorg. Chem.*, **2010**, 49, 9655-9663.
13. P. P. Silva, W. Guerra, J. N. Silveira, A. M. d. C. Ferreira, T. Bortolotto, F. L. Fischer, H. n. Terenzi, A. Neves, E. C. Pereira-Maia, *Inorg. Chem.*, **2011**, 50, 6414-6424.
14. A. M. Madalan, M. Noltemeyer, M. Neculai, H. W. Roesky, M. Schmidtmann, A. Müller, Y. Journaux, M. Andruh, *Inorg. Chim. Acta*, **2006**, 359, 459-467.
15. J. Serment-Guerrero, P. Cano-Sanchez, E. Reyes-Perez, F. Velazquez-Garcia, M. E. Bravo-Gomez, L. Ruiz-Azuara, *Toxicol. in Vitro*, **2011**, 25, 1376-1384.
16. A. De Vizcaya-Ruiz, A. Rivero-Müller, L. Ruiz-Ramirez, J. A. Howarth, M. Dobrota, *Toxicology*, **2003**, 194, 103-113.
17. C. H. Ng, S. M. Kong, Y. L. Tiong, M. J. Maah, N. Sukram, M. Ahmad and A. S. B. Khoo, *Metallomics*, **2014**, 6, 892-906.
18. M. Devereux, D. O'Shea, M. O'Connor, H. Grehan, G. Connor, M. McCann, G. Rosair, F. Lyng, A. Kellett, M. Walsh, D. Egan, B. Thati, *Polyhedron*, **2007**, 26, 4073-4084.
19. M. Chikira, Y. Tomizawa, D. Fukita, T. Sugizaki, N. Sugawara, T. Yamazaki, A. Sasano, H. Shindo, M. Palaniandavar, W. E. Antholine, *J.*

Inorg. Biochem., **2002**, 89, 163 173.
20. R. Galindo-Murillo, J. Hernandez-Lima, M. Gonzalez-Rendon, F. Cortes-Guzman, L. Ruiz-Azuara, R. Moreno-Esparza, *Phys. Chem. Chem. Phys.*, **2011**, 13, 14510-14515.
21. T. Hirohama, Y. Kuranuki, E. Ebina, T. Sugizaki, H. Arii, M. Chikira, P. Tamil Selvi, M. Palaniandavar, *J. Inorg. Biochem.*, **2005**, 99, 1205-1219.
22. R. Galindo-Murillo, L. Ruiz-Azuara, R. Moreno-Esparza, F. Cortes-Guzman, *Phys. Chem. Chem. Phys.*, **2012**, 14, 15539-15546.
23. R. Alemón-Medina, J. L. Muñoz-Sánchez, L. Ruiz-Azuara, I. Gracia-Mora, *Toxicol. in Vitro*, **2008**, 22, 710-715.
24. J.-i. Ueda, M. Takai, Y. Shimazu, T. Ozawa, *Arch. Biochem. Biophys.*, **1998**, 357, 231-239.
25. A. Rivero-Müller, A. De Vizcaya-Ruiz, N. Plant, L. Ruiz, M. Dobrota, *Chem.-Biol. Interact.*, **2007**, 165, 189-199.
26. R. Alemón-Medina, M. Breña-Valle, J. Muñoz-Sánchez, M. Gracia-Mora, L. Ruiz-Azuara, *Cancer Chemother Pharmacol.*, **2007**, 60, 219-228.
27. A. Eastman, *Biochemistry*, **1986**, 25, 3912-3915.
28. A. M. J. Fichtinger-Schepman, J. L. Van der Veer, J. H. J. Den Hartog, P. H. M. Lohman, J. Reedijk, *Biochemistry*, **1985**, 24, 707-713.
29. E. R. Jamieson, S. J. Lippard, *Chem Rev.*, **1999**, 99, 2467-2498.
30. B. M. Hoffman, *Proc. Natl. Acad. Sci. USA*, **2003**, 100, 3575-3578.
31. B. M. Hoffman, *Acc. Chem. Res.*, **1991**, 24, 164-170.
32. B. M. Hoffman, *Acc. Chem. Res.*, **2003**, 36, 522-529.
33. M. Chikira, M., C. Hee Ng, M. Palaniandavar, *Int. J. Mol. Sci.*, **2015**, 16, 22754-22780.
34. J. C. García-Ramos, R. Galindo-Murillo, A. Tovar-Tovar, A. L. Alonso-Saenz, V.Gómez-Vidales, M. Flores-lamo, L. Ortiz-Frade, F. Cortes-Guzman, R. Moreno-Esparza, A. Campero, L. Ruiz-Azuara, *Chem. Eur. J.*, **2014**, 20, 13730-13741.
35. C. M. Dupureur, J. K. Barton, *Inorg. Chem.*, **1997**, 36, 33–43.
36. A. Paulovicova, U. El-Ayaan, Y. Fukuda, *Inorg. Chim.*, **2001**, 321, 56–62.
37. G.-J. Chen, X. Qiao, P.-Q. Qiao, G.-J. Xu, J.-Y. Xu, J.-L. Tian, W. Gu, X. Liu and S.-P. Yan, *J. Inorg. Biochem.*, **2011**, 105, 119-126.
38. S. Stoll, A. Schweiger, A., *J. Magn. Reson.*, **2006**, 178, 42–55.
39. F. E. Mabbs, *Chem. Soc. Rev.*, **1993**, 22, 313-324.
40. E. Carter, E. L. Hazeland, D. M. Murphy, B. D. Ward, *Dalt. Trans.*, **2013**, 42, 15088.
41. R. Miyamoto, Y. Ohba, M. Iwaizumi, *Inorg. Chem.*,**1992**, 31, 3138–3149.
42. S. Kita, M. Hashimoto, M. Iwaizumi, *Inorg. Chem.*, **1979**, 18, 3432–3438.
43. T. G. Brown, B. M. Hoffman, *Mol. Phys.*, **1980**, 39, 1073–1109.
44. M. E. Owen, E. Carter, G. J. Hutchings, B. D. Ward, D. M. Murphy, *Dalt. Trans.*, **2012**, 41, 11085–11092.
45. A. Schweiger, H. H. Günthard, *Chem. Phys.*, **1978**, 32, 35–61.
46. D. M. Murphy, R. D. Farley, *Chem. Soc. Rev.*, **2006**, 35, 249–268.
47. V. Chechik, E. Carter, D. M. Murphy, Electron Paramagnetic Resonance, *Oxford Chemistry Primers* ,**2016**.
48. K. M. Sharples, E. Carter, C. E. Hughes, K D. M. Harris, J. A. Platts, D. M. Murphy, *Phys. Chem. Chem. Phys.*, **2013**, 15, 15214–15222.
49. N. Ritterskamp, K. Sharples, E. Richards, A. Folli, M. Chiesa, J. A Platts, D. M. Murphy, *Inorg. Chem.*, **2017**, 56, 11862–11875.

Chapter 6: The coordination chemistry of Cu(II) mixed nitrogen donor multidentate (*N*-amine and *N*-imine) ligands investigated by EPR.

Cu^{2+} complexes formed by di(2-picolyl)amine L_1 have been studied with the focus on the coordination chemistry using EPR and ENDOR spectroscopy. To date, EPR has only been used to confirm the coordination of L_1 to various Cu^{2+} centres, but it has not been used to further investigate the impact of the two different nitrogen nuclei on the copper centre. This is a surprise as EPR is a high sensitive tool detecting changes in the conformation and configuration of a molecule. Comparative EPR studies have also been undertaken to investigate the Cu^{2+} complexes formed by tris(2-pyridylmethyl)amine L_2 and tris(2-aminoethyl)amine L_3 since they have shown interesting features based on their multidentate ligand configuration.

6.1 Introduction

Transition metal complexes consisting of multidentate ligands are highly desirable in a range of applications including pharmacology, biology and chemistry.[1–6] In simple terms, multidentate ligands can form more than one bond with the metal ion via the ligand donor groups. However, the possible coordination mode of the ligand and resulting structures depend strongly on many parameters, including i) the number of available donor groups and positions within the ligand structure, ii) on the properties of the chosen metal ion.[7–9] Their ligand structures often contain P, N, O or S integrated as donor groups.[10–13] The binding mode of the multidentate ligands is then tuneable and along with a suitable choice of solvent and temperature, good catalytic activities can be achieved, particularly in the activation of small molecules, *i.e.*, the hydrogenation of CO_2 or the activation of N_2.[14–16] Multidentate ligands have also been used in polymeric chemistry, due to their ability to coordinate to a varies of metal ions in different coordination fashions.[17–20]

A well known example of a multidentate ligand is the Schiff base ligand, which are aldehyde or ketone like compounds in which the carbonyl group is

replaced by an imine.[21] The general structure of Schiff base ligands is given in Scheme 6.1, showing the salicylic Schiff base derivatives salicylaldehybenzylhydrazone and salicylaldehydeacetylhydrazone.[22,23] Schiff bases are of interest due to their biological activity, anti-bacterial activity and coordination properties used in industrial application such as antifouling agents and drug designes.[21,24,25] A common derivative of the Schiff base ligand is di(2-picolyl)amine (labelled **L_1**) and shown in Scheme 6.2.

In the literature a variety of di(2-picolyl)amine **L_1** based transition metal complexes have been prepared and studied over the years. Transition metal ions such as Ni^{2+}, Fe^{2+}, Cu^{2+}, Mn^{2+} and Zn^{2+} have all been studied, and all have in common the fact that **L_1** forms the configuration bases of the resulting complex structure.[7,26–30]

Scheme 6.1 Structures of the Schiff bases salicylaldehydebenzylhydrazone (**A**) and salicylaldehydeacetylhydrazone (**B**).[22,23]

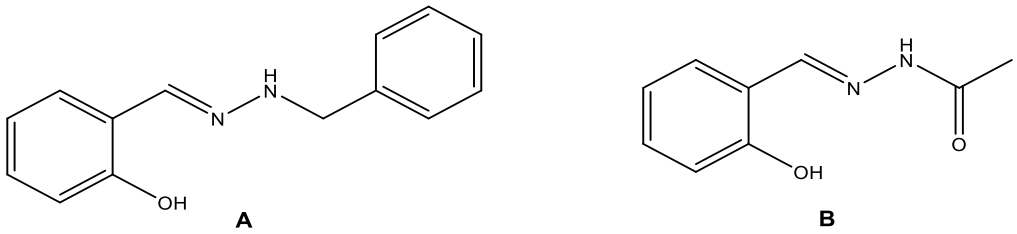

Scheme 6.2 Structure of di(2-picolyl)amine **L_1**, showing the hydrogen labelled H_1, H_2, H_3, H_4, H_5, H_a and H_b.

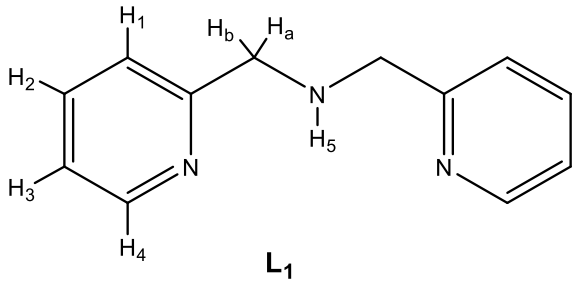

L_1

Sung *et al.*,[31] used di(2-picolyl)sulfide, a derivative of **L_1**, for the reaction with either $CuCl_2$ or $CdCl_2$. The reaction was carried out with one equivalent of di(2-picolyl)sulfide and one equivalent of $CuCl_2$ or $CdCl_2$, respectively, resulting in an mononuclear distorted square pyramidal [Cu^{2+}(di(2-picolyl)sulfide)Cl_2] complex and the binuclear dioctahedral [(di(2-picolyl)sulfide))(Cl)Cd^{2+}(l-Cl)$_2$$Cd^{2+}$(Cl)(di(2-picolyl)sulfide)] complex. This experiment illustrated the influence of the coordination mode by using different transition metal ions.

Furthermore, [Cu(di(2-picolyl)sulfide)Cl_2] was compared to [Cu(**L_1**)Cl_2]. Both complexes revealed a distorted square pyramidal structure. However, the oxidation potential of [Cu(di(2-picolyl)sulfide)Cl_2] was reported to be slightly more positive and the reduction potential was slightly decreased (less positive) than that of [Cu(**L_1**)Cl_2]. Sung et *al.,*[31] suggested that this result might be due to the replaced nitrogen donor atom with the sulfur donor atom.[31,32]

Looking once more at the structural features of di(2-picolyl)amine **L_1**, the multidentate ligand consists of two *N*-pyridyl groups and one secondary *N*-amine group, which acts as backbone for di(2-picolyl)amine. Cu^{2+} salts, such as $CuCl_2$, $Cu(NO_3)_2$, $Cu(SO_4)_2$, $CuClO_4$ and $Cu(BF_4)_2$, all react with **L_1** (Cu^{2+}:**L_1**, 1:1), resulting in the coordination of the two *N*-imine and one *N*-amine along with one counterion in the equatorial plane. The second counterion is coordinated axially to the Cu^{2+} centre, forming a distorted square pyramidal geometry.[32–36] The bis-ligated complex [Cu(**L_1**)$_2$]$^{2+}$, bearing two **L_1** ligands, have also been studied. Palaniandavar *et al*.,[37] for example synthesised a [Cu(**L_1**)$_2$]$(BF_4)_2$ complex, with two equivalents of di(2-picolyl)amine (**L_1**) ligands and one equivalent of $Cu(BF_4)_2$. Interestingly, Palaniandavar *et al*.,[37] reported that two different geometries have been observed in the same unit cell, which are distorted *trans*-facial octahedral and square pyramidal. Similar structures have been reported by Huang *et al*.,[33] for the analogous [Cu(**L_1**)$_2$]$(ClO_4)_2$ complex.

Cu^{2+} complexes consisting of di(2-picolyl)amine or related derivatives have shown promising features in coordination polymer chemistry, catalysis and additionally as potential DNA cleavage complexes.[31,36,38–41] Considering this range of applications that these copper complexes possess, it is important to understand the nature of the multidentate mixed N-donor ligand.

Therefore, the objective of this Chapter is to study the coordination chemistry of the Cu^{2+} complexes formed by di(2-picolyl)amine **L_1** using EPR and ENDOR spectroscopy. To date, EPR has only been used to confirm the coordination of **L_1** to various Cu^{2+} centres, but it has not been used to further investigate the impact of the two different nitrogen nuclei on the copper centre. Furthermore, comparative EPR studies have also been undertaken to investigate the Cu^{2+} complexes formed by tris(2-pyridylmethyl)amine **L_2** and tris(2-aminoethyl)amine **L_3** since they have shown interesting features based on their multidentate ligand configuration.

6.2 Experimental Section

A detailed experimental section was presented previously in Chapter 3. Therefore, only a brief summary of the key experimental points, relevant to this chapter, are given here.

6.2.1 Materials

Copper(II) nitrate trihydrate (hereafter labelled [$Cu(NO_3)_2$]), copper(II) trifluoromethanesulfate (hereafter labelled [$Cu(OTf)_2$]), copper(II) chloride dihydrate (hereafter labelled [$CuCl_2$]), di(2-picolyl)amine (hereafter labelled **L_1**), tris(2-pyridylmethyl)amine (hereafter labelled **L_2**) and tris(2-aminoethyl)amine (hereafter labelled **L_3**), were purchased from *Sigma Aldrich*. In addition, solvents such as dimethylformamide (DMF), chloroform ($CHCl_3$) and methanol (MeOH) were also purchased from *Sigma Aldrich* and used without further purification.

6.2.2 Sample Preparation

[$Cu(L_1)](X)_2$ complexes, X = OTF, Cl, NO_3

For simplicity and brevity, only the preparation of [$Cu(\mathbf{L_1})](NO_3)_2$ is given here. A 1 M stock solution of [$Cu(NO_3)_2$] dissolved in MeOH was prepared and added to a one equivalent solution of **L_1**.[42] The combined solution was stirred overnight. A dark blue solid was obtained and for purification washed with further MeOH and dried.

Variable Ratio Study of [$Cu(NO_3)_2$] with L_1, L_2 and L_3

The variable ratio study was conducted using Cu:L ratios of 1:0, 1:1, 1:2, 1:5, 1:10 and 1:50 of [$Cu(NO_3)_2$] with either L = **L_1**, **L_2** or **L_3**. The general preparation was carried out in a DMF:$CHCl_3$ (1:1) solvent system. A 1 M stock solution of [$Cu(NO_3)_2$] was prepared and added to 1:1, 1:5, 1:10 or 1:50 (Cu^{2+}:L) equivalent solution of the desired ligand. The combined solution was stirred for two hours and if necessary purified.

6.3 Results and Discussion

The copper(II) salts of $[Cu(OTf)_2]$, $[CuCl_2]$ and $[Cu(NO_3)_2]$ were used in the complexation studies of di(2-picolyl)amine **L_1** with Cu^{2+} in a ratio of 1:1. The resulting experimental and simulated spectra recorded at 140 K are shown in Figure 1-2 and E1, Appendix. The spin Hamiltonian parameters extracted by the simulation show similar *g* and *A* values and are listed in Table 6.1. Only the $[Cu(\mathbf{L_1})](NO_3)_2$ complex revealed any resolved ^{14}N superhyperfine pattern and this complex was therefore chosen for further investigation.

The resolution and quality of the EPR spectrum depends, among other factors, on the choice of solvent systems.[43,44] While the dipolar MeOH solvent

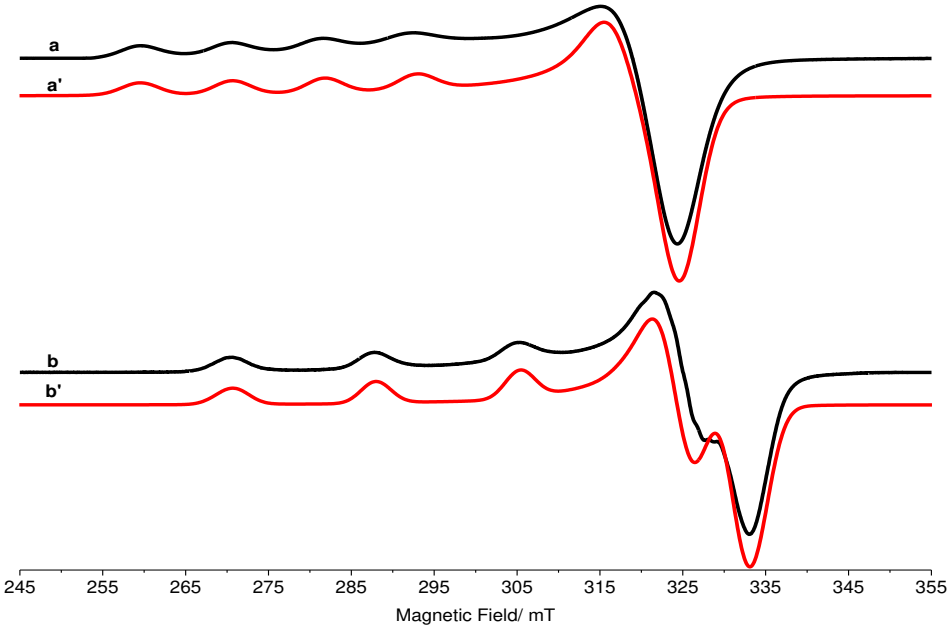

Figure 6.1 Experimental (black) and simulated (red) CW X-band EPR (140 K) spectra recorded in MeOH of a) the $[Cu(NO_3)_2]$ copper salt and b) the $[Cu(\mathbf{L_1})NO_3)_2]$ complex (Cu:**L_1** ratio of 1:1). The simulation parameters are listed in Table 6.1.

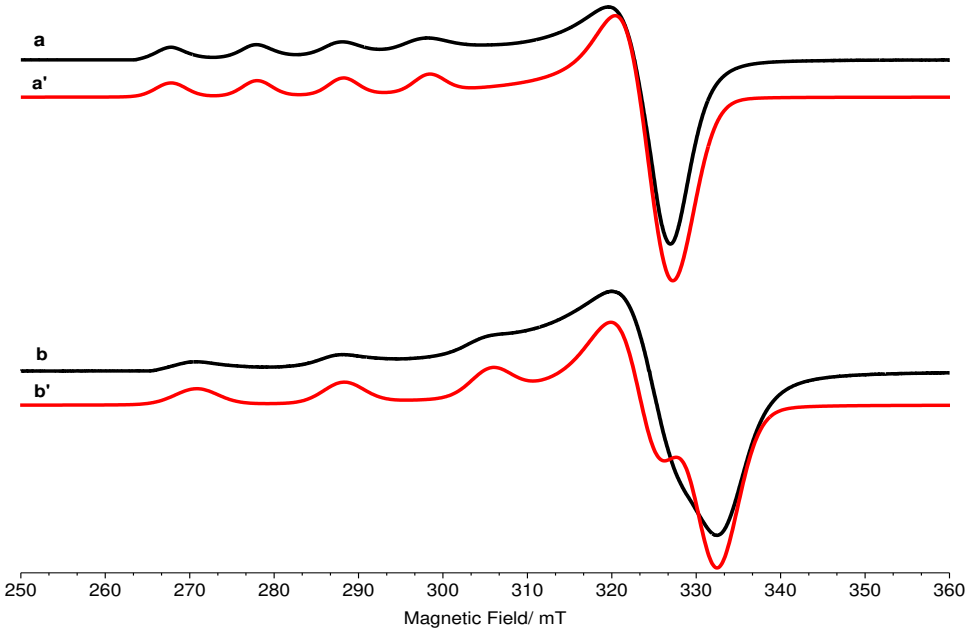

Figure 6.2 Experimental (black) and simulated (red) CW X-band EPR (140 K) spectra recorded in MeOHof a) the $[Cu(OTf)_2]$ copper salt and b) the $[Cu(\mathbf{L_1})(OTF)_2]$ complex (Cu^{2+}:$\mathbf{L_1}$) ratio of 1:1). The simulation parameters are listed in Table 6.1.

gives a poorly defined spectrum of $[Cu(\mathbf{L_1})](NO_3)_2$ (Figure 6.1), a better resolved EPR spectrum is observed with the weakly coordinating solvent system DMF:$CHCl_3$ (Figure 6.3). While the MeOH based solvent system gives values of $g_{iso} = 2.129$ and $a_{iso} = 204$ MHz, the weakly coordinating solvents such as DMF:$CHCl_3$ produces different values, in the latter case with $g_{iso} = 2.127$ MHz and $a_{iso} = 207$ MHz (Table 6.1).[43,45]

Table 6.1 Experimental **g** and ^{Cu}**A** spin Hamiltonian parameters for $[Cu(\mathbf{L_1})]^{2+}$,$[Cu(\mathbf{L_1})_2]^{2+}$, $[Cu(\mathbf{L_2})](NO_3)_2$,$[Cu(\mathbf{L_3})](NO_3)_2$ and other spin Hamiltonian parameters of multidentate Cu^{2+} complexes.

	solvent	g_1	g_2	g_3	A_1	A_2	A_3	**ref**
				Cu^{2+} salts				
$[Cu(NO_3)_2]$	DMF:$CHCl_3$	2.084	2.084	2.400	20	20	400	*t.w*
	MeOH	2.088	2.088	2.425	50	50	370	*t.w*
[Cu(OTf)2]	MeOH	2.084	2.084	2.425	15	15	370	*t.w*
	THF:DMF	2.083[a]	2.083[a]	2.412[a]	13.1[b]	13.1[b]	403.4[c]	46
$[CuCl_2]$	THF:DMF	2.061[a]	2.061[a]	2.316[a]	54.8[b]	54.8[b]	457.8[c]	46
				Ratio 1:1 of $[Cu(\mathbf{L_1})](NO_3)_2$				
$[Cu(\mathbf{L_1})](NO_3)_2$	MeOH	2.060	2.068	2.258	35	40	538	*t.w*
$[Cu(\mathbf{L_1})](NO_3)_2$	DMF:$CHCl_3$	2.060	2.068	2.253	35	40	547	*t.w*
$[Cu(\mathbf{L_1})](OTf)_2$	MeOH	2.070	2.070	2.255	32	32	540	*t.w*
$[Cu(\mathbf{L_1})]Cl_2$	MeOH	2.063	2.063	2.234	45	45	530	*t.w*
				Ratio 1:2 of $[Cu(\mathbf{L_1})](NO_3)_2$				
$[Cu(\mathbf{L_1})_2](NO_3)_2$	DMF:$CHCl_3$	2.061	2.061	2.238	37/30	37/30	520	*t.w*
				Ratio 1:50 of $[Cu(L_2)](NO_3)_2$				
$[Cu(\mathbf{L_2})](NO_3)_2$	DMF:$CHCl_3$	2.050	2.070	2.267	-	-	540	*t.w*
				Ratio 1:50 of $[Cu(L_3)](NO_3)_2$				
$[Cu(\mathbf{L_3})](NO_3)_2$	DMF:$CHCl_3$	2.09	2.19	2.00	330	350	180	*t.w*
				reference complexes				
	solvent	g_1	g_2	g_3	A_1	A_2	A_3	**ref**
$[Cu(\mathbf{L_1})](NO_3)_2$		2.097	2.097	2.207				42
$[Cu(\mathbf{L_1})](H_2O)_2]^{2+}$	H_2O:Glycrol	[d]2.062	[d]2.065	[d]2.262	[e]46	[e]70	[f]556	36
$[Cu(\mathbf{L_1})_2](BF_4)_2$	MeOH:H_2O	[d]2.052	[d]2.052	[d]2.243				33,37
$[Cu(\mathbf{L_1})_2](ClO_4)_2$	MeOH:H_2O	2.067	2.013	2.234				33
$[Cu(\mathbf{L_1})_2]^{2+}$	H_2O:Glycrol	[d]2.046	[d]2.072	[d]2.243	[e]30	[e]42	[f]535	36
$[Cu(en)_2](OTf)_2$	CH_3CN: THF	[g]2.040	[g]2.046	[g]2.202	[h]-78.0	[h]-82.0	[h]-602.0	47
$[Cu(en)_2](NO_3)_2$		[g]2.059	[g]2.059	[g]2.189				48
$[Cu(bpp)(NO_3)_2]$	CH_3CN	2.060	2.114	2.287				49
$[Cu(bpp)(H_2O)(NO_3)_2]$	CH_3CN	2.060	2.060	2.287			175	49
[Cu(bpcp)]	DCM:Hexan	2.281	2.170	2.050	280	58.8	257.6	50

^{Cu}A is given in MHz [a]±0.004, [b]±3 MHz, [c]±6 MHz, [d]±0.003, [e]±10 MHz, [f]±3 MHz, [g]±0.005, [h]±5 MHz, [i]±3 MHz . $\mathbf{L_1}$ = di(2-dipicolyl)amine, $\mathbf{L_2}$ = tris(2-pyridylmethyl)amine, $\mathbf{L_3}$ = tris(2-aminoethyl)amine, en = 1,2-diaminoethane, bpp = 2,6-bis(pyrazol)pyridine, bpcp = 1,4-bis[o-(pyrydine-2-carboxamidophenyl)]-1,4-dioxabutane.

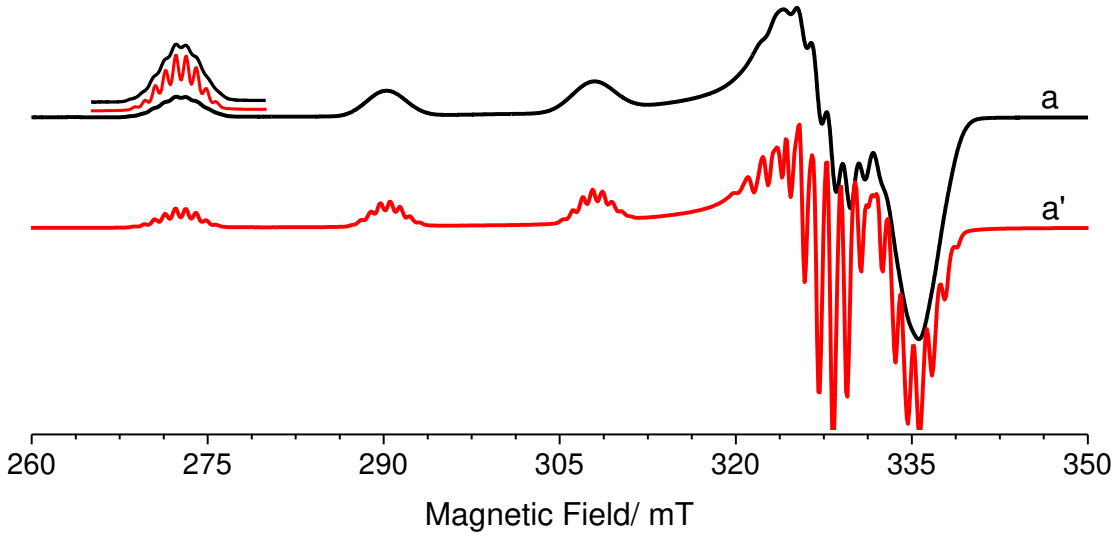

Figure 6.3 Experimental (black) and simulated (red) CW X-band EPR spectra (140 K) of $Cu(NO_3)_2$:**L_1** (formed at a 1:1 ratio) dissolved in DMF:$CHCl_3$.

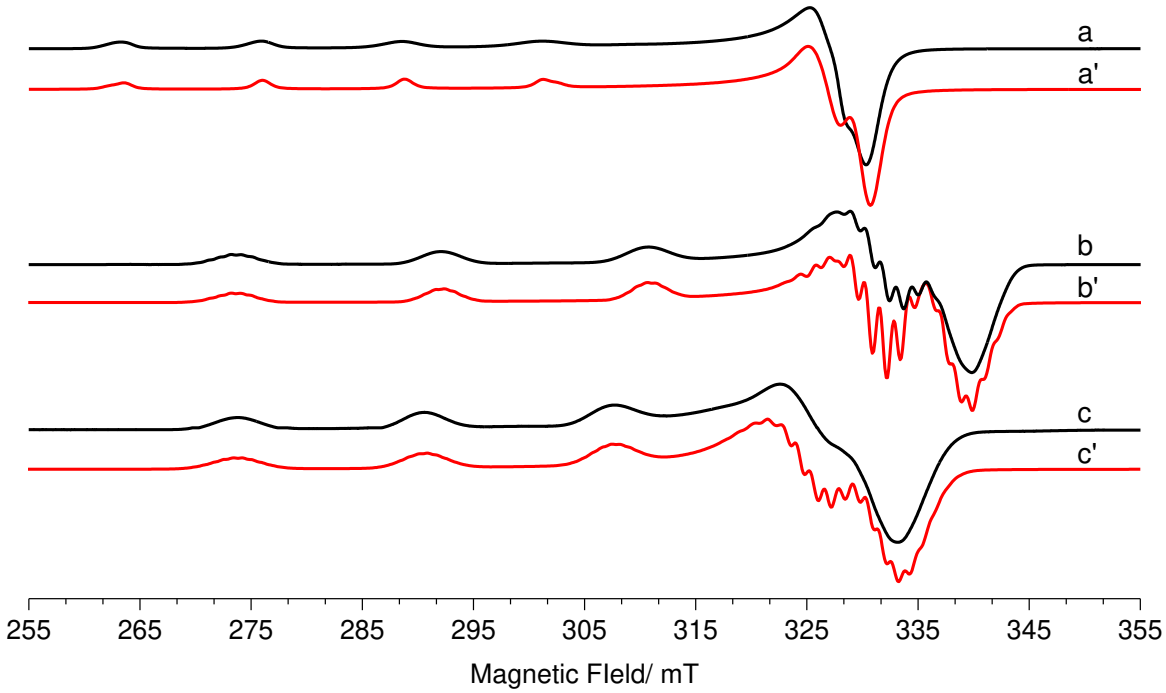

Figure 6.4 Experimental (black) and simulated (red) CW X-band spectra of the [$Cu(NO_3)_2$]:**L_1** formed at ratios of a) 1:0, b) 1:1 and c) 1:2 dissolved in DMF:$CHCl_3$.

6.3.1 CW EPR spectra of $[Cu(NO_3)_2]$,$[Cu(L_1)](NO_3)_2$ and $[Cu(L_1)_2](NO_3)_2$

The experimental and simulated CW X-band EPR spectra of $[Cu(NO_3)_2]$, $[Cu(\mathbf{L_1})](NO_3)_2$ and $[Cu(\mathbf{L_1})_2](NO_3)_2$, obtained at $[Cu(NO_3)_2]$:$\mathbf{L_1}$ ratios of 1:0, 1:1 and 1:2, respectively, are shown above in Figure 6.4a, b and c respectively. The resulting spin Hamiltonian parameters are listed in Table 6.1. The $[Cu(\mathbf{L_1})](NO_3)_2$ complex reveals a decrease in the g_3 value ($\Delta g_3 = 0.147$) and an increase in A_3 ($\Delta A_3 = 147$ MHz) relative to the unbound $[Cu(NO_3)_2]$ salt. These shifts are indicative for the coordination of the nitrogen groups to the copper centre. The observed ^{14}N superhyperfine pattern for $[Cu(\mathbf{L_1})](NO_3)_2$ in the g_1, g_2 and g_3 regions, are also indicative for nitrogen coordination to the Cu^{2+} in the equatorial plane. This assumption is in agreement with the reported crystal structures[35] of the distorted square pyramidal $[Cu(\mathbf{L_1})](NO_3)_2$ complex, with the unpaired electron located in the d_{xy} ground state.[35,42,51] On the outer $m_I = +3/2$ position of the g_3 component, a ^{14}N superhyperfine pattern of 8 lines (considering the gyromagnetic factor of $^{63/65}Cu$) is revealed and this suggests the presence of three equivalent nitrogen nuclei ($I = 1$). However, it is known that two sets of nitrogen nuclei in the ligands have different electronic structures, specifically one *N*-amine and two *N*-pyridyl groups. Therefore, the ^{14}N couplings would be expected to be different. Unfortunately, the differences between these nitrogen groups are not visible on the CW EPR spectrum and ^{14}N ENDOR measurements are required to determine the differences (see later).

At a ratio of 1:2, the EPR spectrum of bis-ligated complex $[Cu(\mathbf{L_1})_2](NO_3)_2$ appears at the expense of the mono-ligated complex $[Cu(\mathbf{L_1})_2](NO_3)_2$ (Figure 6.4b and c). The g and A values of $[Cu(\mathbf{L_1})_2](NO_3)_2$ reveal a small decrease in g_3 ($\Delta g_3 = 0.015$) and A_3 ($\Delta A_3 = 27$ MHz) compared to $[Cu(\mathbf{L_1})](NO_3)_2$ (Table 6.1). The observed g_3 shift and the change in the signal profile, especially in the parallel region, indicate that a second $\mathbf{L_1}$ ligand coordinates to the copper, forming a new structure due to $[Cu(\mathbf{L_1})_2](NO_3)_2$. The ^{14}N superhyperfine splittings are poorly resolved for $[Cu(\mathbf{L_1})_2](NO_3)_2$ (Figure 6.4c) due to overall broadening of the EPR lines, likely due to the presence of additional ^{14}N couplings from additional nitrogen coordination in the equatorial plane. The reported crystal structure of $[Cu(\mathbf{L_1})](ClO_4)_2$ and $[Cu(\mathbf{L_1})](BF_4)_2$, both reveal two different geometries formed in the same unit cell, which are trans-facial octahedral and

square pyramidal.[33] Huang *et al.*,[33] recorded the CW EPR spectra of $[Cu(\mathbf{L_1}](ClO_4)_2$ and $[Cu(\mathbf{L_1})](BF_4)_2$ dissolved in MeOH. Huang *et al.*,[33] noticed that the EPR spectra of $[Cu(\mathbf{L_1})](ClO_4)_2$ and $[Cu(\mathbf{L_1})](BF_4)_2$ were different to each other, even so both have the same trans-facial octahedral and square-pyramidal solution species. For this reason, they suggested that the solution species contain the respective counterions. Furthermore, as the resulting EPR spectrum of $[Cu(\mathbf{L_1})](ClO_4)_2$ and $[Cu(\mathbf{L_1})](BF_4)_2$, respectively, exhibiting spectral traces of a single Cu^{2+} complex, Huang *et al.*[33] implied that the trans-facial and square pyramidal solution species must have very similar spectra. Applying this conclusion to the present $[Cu(\mathbf{L_1})_2](NO_3)_2$ complex could suggest that the resulting spectrum may be composed of two $[Cu(\mathbf{L_1})_2](NO_3)_2$ species, with trans-facial and square pyramidal geometries. In this case, the square planar structure (equatorial) is formed by two *N*-imine of the pyridyl groups and two *N*-amine groups from the backbone of two $\mathbf{L_1}$ ligands. Further work is required to resolve these structures and confirm the above proposal for $[Cu(\mathbf{L_1})_2](NO_3)_2$.

6.3.2 Overshoot features of $[Cu(L_1)](NO_3)_2$

The angular dependency profile of the $[Cu(\mathbf{L_1})](NO_3)_2$ sample recorded at X-band frequency is shown in Figure 6.5a. Three turning points at off-axis orientations, referred to as “overshoot” features, are visible on the $m_I = -3/2$ transitions at 334 mT, on the $m_I = -1/2$ transition at 327 mT and on the $m_I = +1/2$ transition at 325 mT, labelled with an asterisk. These features arise due to the relatively small *g* and large ^{Cu}A anisotropy and can lead to ambiguities in the interpretation of X-band spectra. The corresponding Q-band CW EPR spectrum is shown in Figure 6.5b and the overshoot features are absent. The ^{14}N superhyperfine splitting is lost due to the greater influence of *g* and ^{Cu}A strain. [47,52,53]

The *g* and *A* values for $[Cu(\mathbf{L_1})](NO_3)_2$ suggest a slight off axial symmetry towards rhombicity for this complex. Similar *g* and *A* values have also been reported for $[Cu(\mathbf{L_1})(H_2O)_2]^{2+}$ by Spencer *et al.*[36] However the recorded CW Q-band spectrum of $[Cu(\mathbf{L_1})](NO_3)_2$ does not show traces of rhombicity. For this reason the spectrum of $[Cu(\mathbf{L_1})](NO_3)_2$ must be recorded at W-band as well.

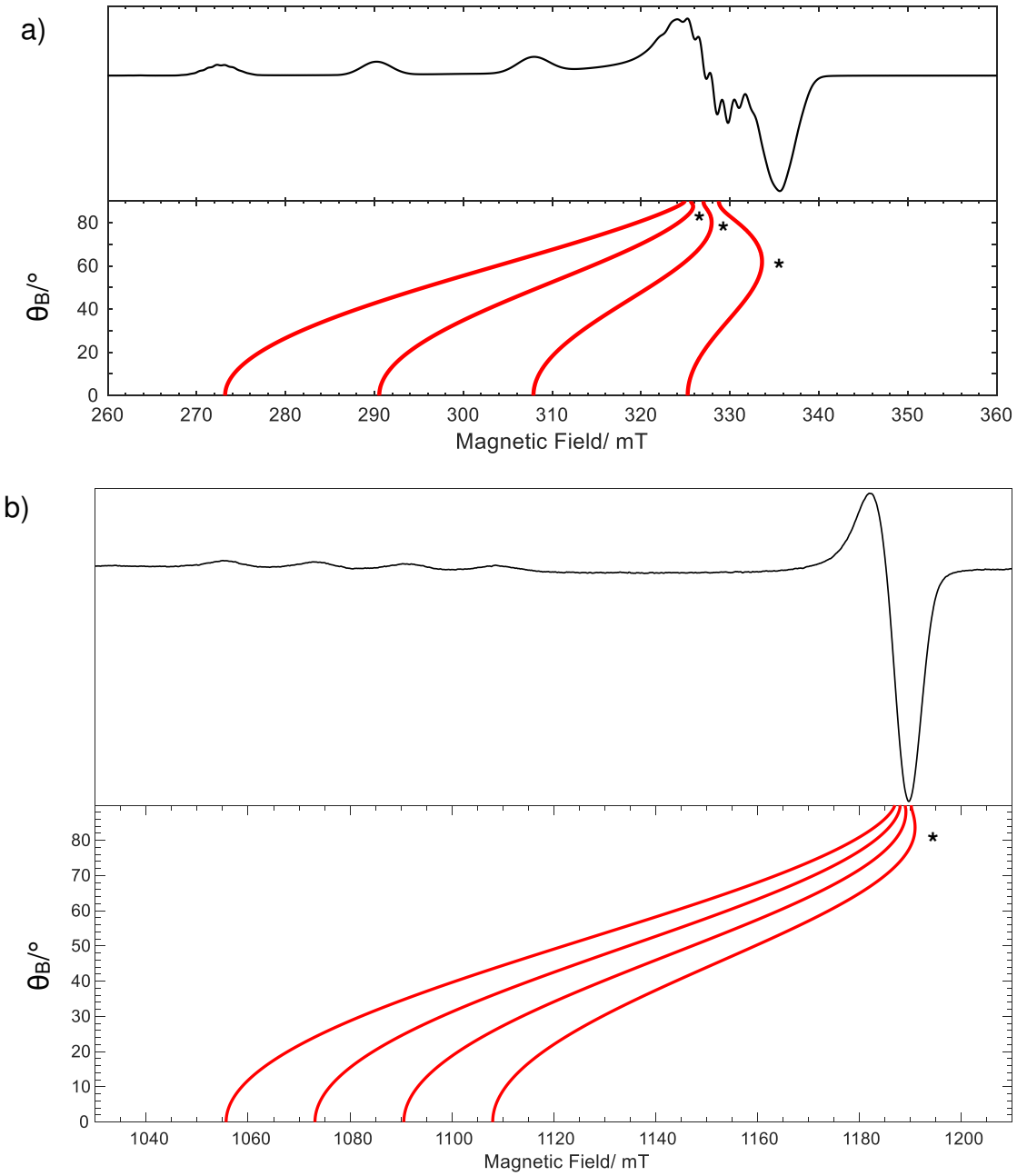

Figure 6.5 CW EPR spectra of [Cu(**L₁**)](NO₃)₂ dissolved in DMF:CHI₃, recorded at a) X- and b) Q-band frequencies. The simulated roadmap for [Cu(**L₁**)](NO₃)₂ at the two frequencies is also shown. The overshoot features are highlighted with an asterisk (*).

*6.3.3 ^{14}N CW Q-band ENDOR of [Cu(**L₁**)](NO₃)₂*

The ^{14}N superhyperfine pattern observed in the CW X-band EPR spectrum of the distorted square pyramidal [Cu(**L₁**)](NO₃)₂ complex (Figure 6.3) contains a rich source of structural information on the coordination mode of [Cu(**L₁**)](NO₃)₂. The crystal structure[35] of [Cu(**L₁**)](NO₃)₂ revealed most of the structural information, for the CW X-band EPR spectrum at low temperature.

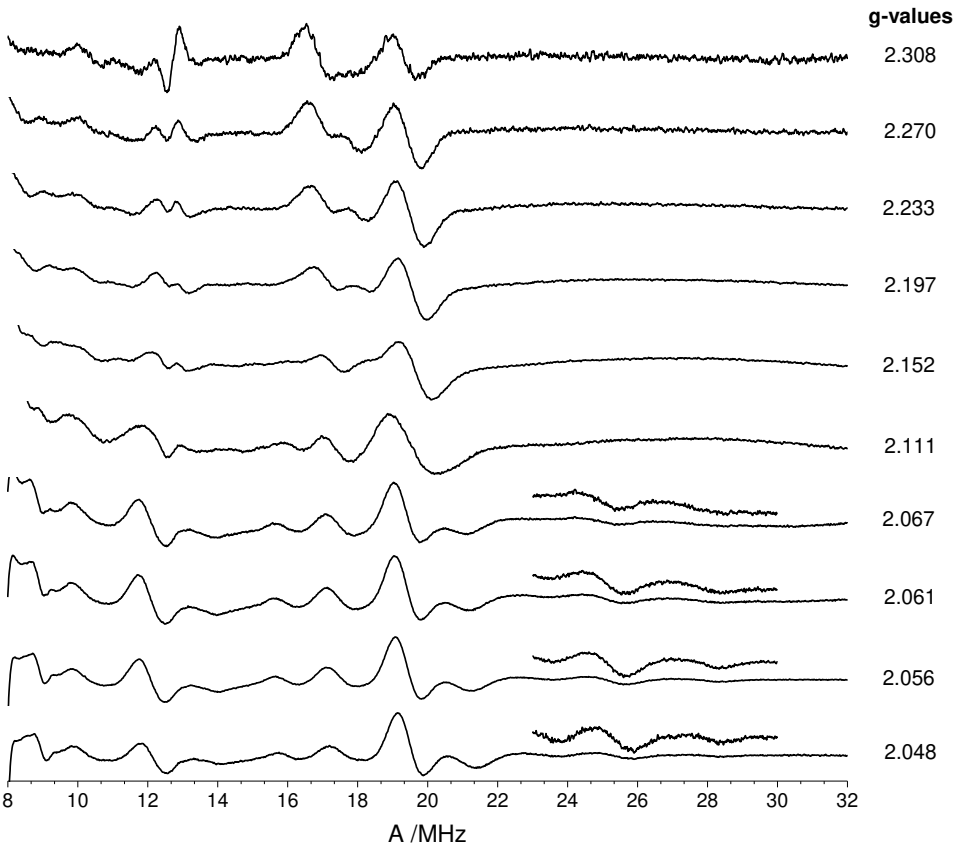

Figure 6.6 Q-band CW ^{14}N ENDOR spectra (10 K) of $[Cu(\mathbf{L_1})](NO_3)_2$ dissolved in DMF-d_7:$CDCl_3$ (1:1) recorded at field positions corresponding to the *g*-values indicated beside each spectrum.

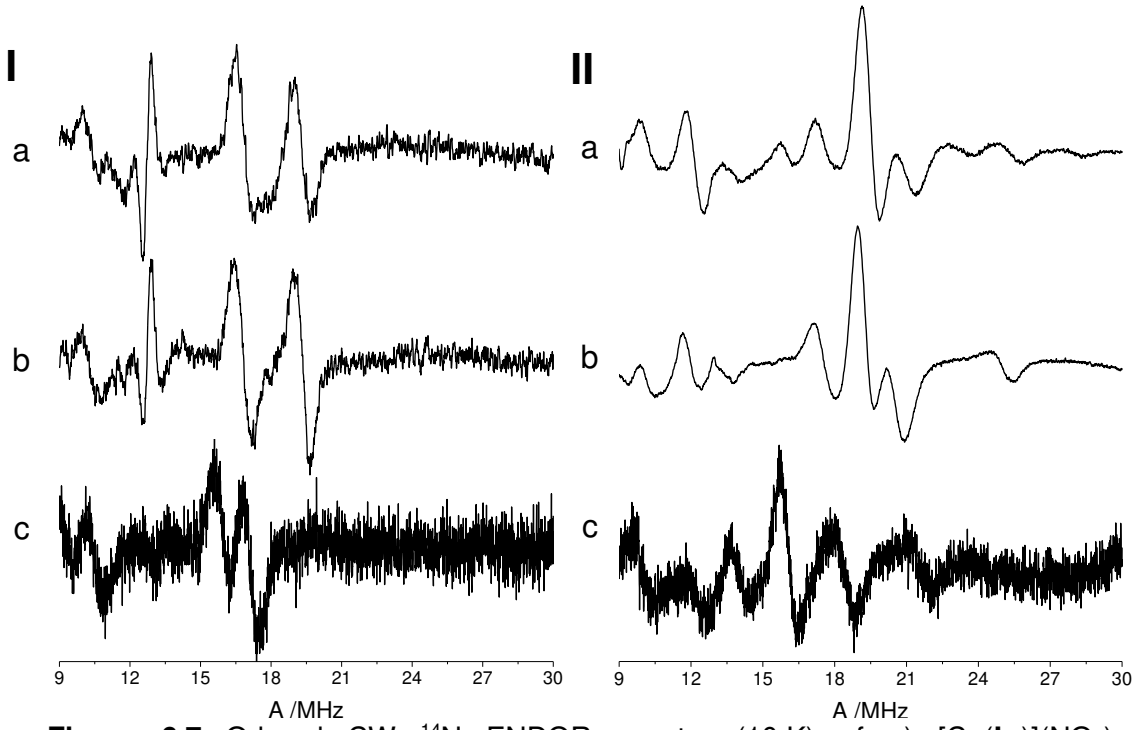

Figure 6.7 Q-band CW ^{14}N ENDOR spectra (10 K) of a) $[Cu(\mathbf{L_1})](NO_3)_2$, b) [Cu(acac)(1,10-phenanthroline)]OTf and c) [Cu(1,2diaminoethane)2](OTf)2[47]. The ENDOR spectra were measured at the field positions corresponding to I) g = 2.30 (labelled I) and g = 2.04 (labelled II).

It is known that the nitrogen nuclei from the pyridyl *N*-imine and *N*-amine groups of the **L₁** backbone are coordinated to Cu^{2+} in the equatorial plane. However, from the X-band EPR spectrum alone it was not possible to distinguish between the two inequivalent nitrogen nuclei. For this reason, CW Q-band ENDOR spectroscopy was used to determine the couplings more accurately. The ^{14}N orientation selective ENDOR measurement of [Cu(**L₁**)]$(NO_3)_2$ were recorded (Figure 6.6). For comparison purposes, the ^{14}N ENDOR spectra of [Cu(acetylacetonate)(1,10-phenanthroline)]$(OTf)_2$ and [Cu(1,2-diaminoethane)$_2$]$(OTf)_2$[47] are also shown in Figure 6.7. These additional and comparative spectra were recorded at g_{II} and $g_{\perp}$ positions. The [Cu(acetylacetonate)(1,10-phenanthroline)]$(OTf)_2$ complex consists of a 1,10-phenanthroline ligand bearing two coordinated *N*-imine nuclei interacting with the copper centre, whereas [Cu(1,2-diaminoethane)$_2$]$(OTf)_2$ consist of only coordinated *N*-amine nuclei interacting with the copper centre. These Cu^{2+} complexes have been studied in depth by EPR spectroscopy and are therefore suitable for comparison in the current complex bearing both coordinated *N*-imine and *N*-amine nuclei.[47,52]

The experimental angular selective CW Q-band ^{14}N ENDOR spectra of [Cu(**L₁**)]$(NO_3)_2$ is shown in Figure 6.6, are deceptively difficult to interpret due to the overlapping couplings from the *N*-imine and *N*-amine nuclei. The spectra are further complicated by the quadrupole interactions. The ^{14}N ENDOR spectrum of [Cu(acetylacetonate)(1,10-phenanthroline)]$(OTf)_2$ produces remarkably similar couplings to those seen in the [Cu(**L₁**)]$(NO_3)_2$ spectra (Figure 6.7a,b), indicating that the *N*-imine couplings in [Cu(**L₁**)]$(NO_3)_2$ are of similar magnitude to those found for other *N*-imine compound systems (i.e., [Cu(acetyl-acetonate)(1,10-phenanthroline)]$(OTf)_2$. Unfortunately, an analogous comparison between [Cu(**L₁**)]$(NO_3)_2$ and the *N*-amine bound system ([Cu(1,2-diaminoethane)$_2$]$(OTf)_2$) is less straightforward. The *N*-amine couplings are clearly smaller (Table 6.2) but owing to the overlap with the larger *N*-imine couplings, it is difficult to unambiguously identify the peaks in the ENDOR spectra. The analysis of the ^{14}N ENDOR spectrum suggest that the hyperfine coupling of the *N*-amine is located at slightly lower frequency than those of the *N*-imine hyperfine coupling of the coordinated di(2-picolyl)amine **L₁** ligand compared to reference complexes (Table 6.2). This observation has been seen for amine and imine nuclei placed in the pseudo planar coordination array of copper complexes. The spin density of

the sp^2 hybridized nitrogen orbitals have been shown to be higher than for the spin density of sp^3 hybridized nitrogen orbitals, the former one shown to have in general larger hyperfine couplings than sp^3 hybridized nitrogen such as amines.[54] Even though, the hyperfine coupling seem to be very similar and causing overlap of the signals as seen in the ^{14}N ENDOR spectra (Figure 6.).

Table 6.2 ^{14}N hyperfine and quadrupole parameters of N2, N4(amine) and N4(aza) Cu^{2+} complex, listed for comparison to $[Cu(\mathbf{L_1})](NO_3)_2$.

Coordination	Complex	A_1[a]	A_2	A_3	Q_1[b]	Q_2	Q_3	***ref***
N4(amine)	$[Cu(en)_2](OTf)_2$	39.35	26.0	26.4	-1.25	0.86	0.39	47
N4(aza)	[Cu(TPP)]	54.2	42.7	44.00	-0.62	0.93	-0.31	55
	$[Cu(BOX)_2]$	39.8	33.1	32.9	-0.57	0.52	0.05	46
N2	$[Cu(BOX)](OTf)_2$	45.6	35.9	36.7	-0.87	0.97	-0.10	46
	$[Cu(BOX)Cl_2$	41.9	32.5	32.8	-0.87	0.97	-0.10	46

^{N}A is given in MHz [a]±0.2 MHz[47] [b]±0.1 MHz[47]. en = 1,2-diaminoethane, BOX = (−)-2,2′-Isopropylidenebis[(4S)-4-phenyl-2-oxazoline].

6.3.4 ^1H ENDOR of $[Cu(\mathbf{L_1})](NO_3)_2$

To complete the CW Q-band ENDOR study of the $[Cu(\mathbf{L_1})](NO_3)_2$ complex, the ^1H ENDOR spectra were recorded at 10 K, and the resulting ENDOR spectra are shown in Figure 6.8. The proton couplings observed for the $[Cu(\mathbf{L_1})](NO_3)_2$ complex are centred around ν_0-ν_L and separated by ^{H}A.[56] The main signals recorded at the field position corresponding to g = 2.307 indicate the presence of three strongly coupled protons. The largest proton coupling appears to be characterised by the tensor ±[7 9 16] MHz and is assigned to the imine proton, labelled H_4 in Scheme 6.2. This coupling is not as big as one would commonly expect for pyridine imine protons. This may be due to the fact that in the primary coordination sphere of the complex, an amine is coordinated in the equatorial plane. It has been observed that axially coordinated amines to Cu^{2+}-Salen type complexes have a slightly decreased proton imine coupling (Table 6.3).[9] However, to confirm or dismiss this assumption for $[Cu(\mathbf{L_1})](NO_3)_2$, further experiments or DFT calculations would be required. The second well resolved tensor ±[2 7 12] MHz has been assigned to the H-amine proton. This tensor is in good agreement with reported proton amine couplings which primarily interact with the Cu^{2+} centre.[47] In the case of indirectly interacting amine protons, the coupling would be weaker and result in smaller couplings.

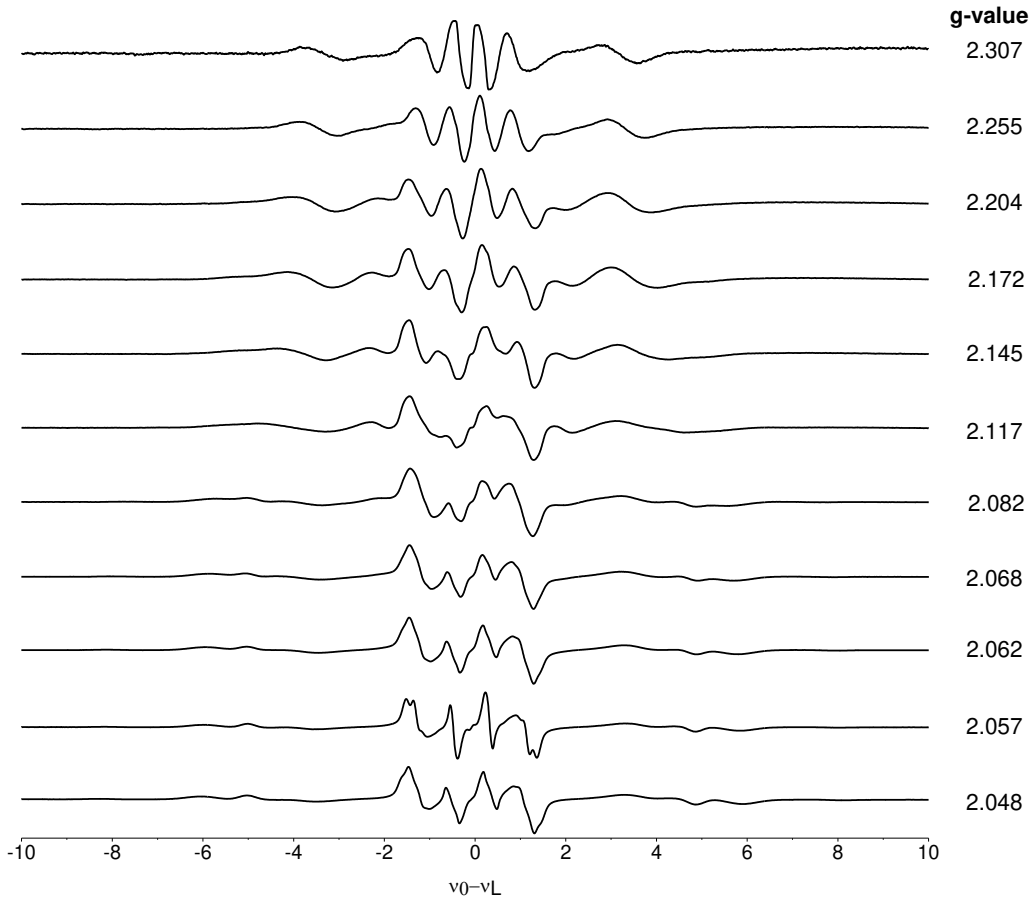

Figure 6.8 CW Q-band ^{1}H ENDOR spectra (10 K) of [Cu(**L$_1$**)](NO$_3$)$_2$ dissolved in DMF-d$_7$:CDCl$_3$ (1:1) recorded at the field positions corresponding to the *g*-values indicated beside each spectrum.

Table 6. 3. ^{1}H arbitrary hyperfine values for [Cu(**L$_1$**)](NO$_3$)$_2$ and other comparative Cu^{2+} complexes.

	Nucleus	A_1	A_2	A_3	α	β	γ	ref
[Cu(**L$_1$**)](NO$_3$)$_2$	H^{imine}	7	9	16	0	90	0	*t.w*
	H^{amine}	2	7	12	0	90	0	*t.w*
	C-H (H^{aromatic})	1.0	1.3	3.0	0	90	0	*t.w*
		reference complexes						
		A_1	A_2	A_3	α	β	γ	ref
[Cu(en)$_2$](OTf)$_2$	H^{amine}	-8.00[a]	5.52	13.65	35	50	0	[47]
	C-H$_{eq}$ (H^{methyl})	-2.63	1.70	4.30	0	60	0	[47]
[Cu(acac)(phen)]CF$_3$SO$_3$	H^{Imine}	2.20[a]	10.05[a]	2.10[b]	0	90[c]	0	[52]
[Cu(salen-3)]	H^{Imine}	17.80[d]	18.55[d]	22.20[d]	-	-	-	[9]
[Cu(salen-3)]MBA	H^{Imine}	16.60[d]	17.20[d]	21.30[d]	-	-	-	[9]
[Cu(BOX)](OTf)$_2$	*α*-1H	-2.1[a]	-1.7[a]	5.9[e]	11	63	34	[46]
	o-H^{Phen}	-3.0[a]	-1.20[a]	1.20[b]	0	11	0	[46]
trans-equatorial [Cu(acac)$_2$(Im)$_2$]	remote H^{amine}	3.15[f]	1.80[f]	1.95[f]	30[g]	20[g]	-30[g]	[44]

t.w = this work. ^{H}A is given in MHz [a]±0.2[47,52] [b]±0.5[52] [c]±15°[52], [d]±0.02[9], [e]±0.1[46], [f]±0.4, [g]±10°. L$_1$ = di(2-dipicolyl)amine, en = 1,2-diaminoethane, salen-3 = N-(3,5-di-tert-butylsalicylidene)-N0-(salicylidene)-cyclohexane-1,2-diaminem, MBA = *S*-methylbenzylamine ,Im = imidazole.

Due to the overlapping ^1H signals, it is not clear if only three strong couplings are present in the ENDOR spectra (Figure 6.8). Between 2 MHz and – 2 MHz, the observed proton couplings are considered as weak proton couplings, presumably resulting from aromatic proton couplings or from the bridging methyl protons, which are not directly interacting with the Cu^{2+} centre. As the $[Cu(\mathbf{L_1})](NO_3)_2$ complex has not be synthesised under inert conditions, it could also be assumed that water is coordinated to copper, even so the crystal structure[35] or EPR spectrum do not indicate the presence of H_2O. However, such occurrence would result in a characteristic proton coupling in the ^1H ENDOR spectra, which has not been observed (Figure 6.8).[46]

To accurate analyse the ^1H ENDOR spectra, DFT calculation and further orientation selective measurement must be conducted. Selective deuteration of $\mathbf{L_1}$ would also help to distinguish between these overlapping proton couplings.[45,57]

6.3.5 Tris(2-pyridylmethyl)amine and tris(2-aminoethyl)amine Cu^{2+} complexes

The structure of di(2-picolyl)amine $\mathbf{L_1}$ was shown earlier in Scheme 6.2. The structures of tris(2-pyridylmethyl)amine $\mathbf{L_2}$ and tris(2-aminoethyl)amine $\mathbf{L_3}$ are illustrated below in Scheme 6.3a, b respectively. In contrast to $\mathbf{L_1}$, tris(2-pyridylmethyl)amine $\mathbf{L_2}$ has an additional pyridylmethyl residue connected to the amine backbone of $\mathbf{L_1}$. Hence, $\mathbf{L_2}$ is considered as a tetradentate ligand with mixed nitrogen functional groups, namely *N*-imine and *N*-amine. In addition, the structural and electronical features of $\mathbf{L_2}$ have also been compared to tris(2-aminoethyl)amine $\mathbf{L_3}$ as this is considered as the amine analogue of $\mathbf{L_2}$.

Scheme 6.3 Structures of the multidentate ligands a) tris(2-pyridylmethyl)amine and b) tris(2-aminoethyl)amine

a)

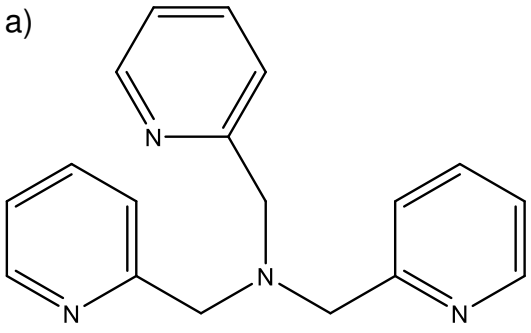

$\mathbf{L_2}$

b)

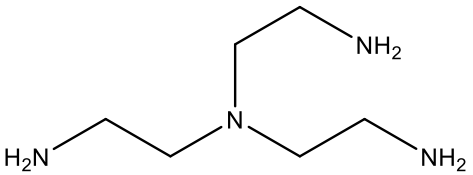

$\mathbf{L_3}$

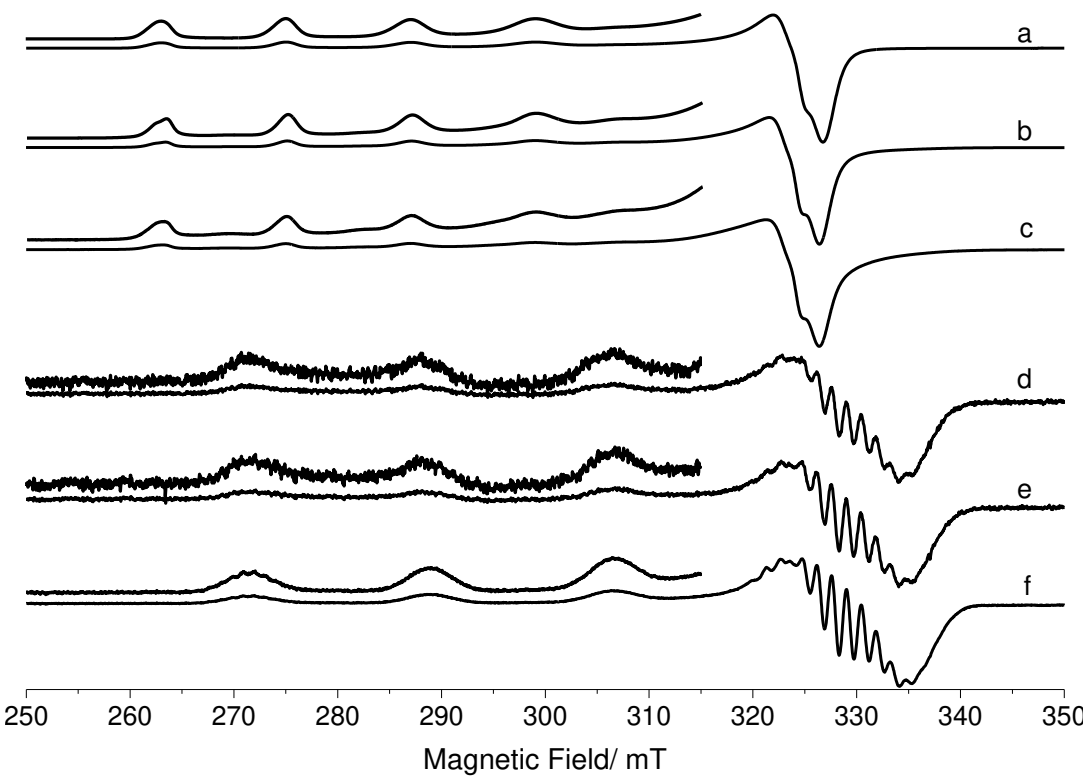

Figure 6.9 CW X-band (140 K) EPR spectra of $Cu(NO_3)_2$ with increasing ratios of the **L_2** ligand; a) 1:0, b)1:1, c) 1:1.5, d) 1:5, e) 1:10 and f) 1:50, dissolved in DMF:$CHCl_3$ (1:1).

The experimental low temperature (140 K) X-band EPR spectra of the $[Cu(NO_3)_2]$:**L_2** complex formed at different ratios (1:0, 1:1, 1:1.5, 1:5, 1:10 and 1:50) are shown in Figure 6.9. The EPR measurement were performed using the solvent system DMF:$CHCl_3$ (1:1). At high ratios (1:5, 1:10), the Cu^{2+} signal intensity was found to be considerably smaller compared to the lower ratios. This is caused by the formation of a variety of Cu^{2+} tris(2-aminoethyl)amine complexes which are insoluble in DMF:$CHCl_3$ resulting in precipitation. Curiously, the Cu^{2+} signal strength recovers again at a ratio of 1:50, and the reason for this is not currently know.

At a ratio of 1:50, the EPR spectrum shows a signal arising from a single Cu^{2+} complex in solution, presumably of the copper $[Cu(\mathbf{L_2})](NO_3)_2$ complex. The spin Hamiltonian parameters extracted by simulation are listed in Table 6.1. The $[Cu(\mathbf{L_2})](NO_3)_2$ complex reveals a decrease in the g_3 ($\Delta g_3 = 0.143$) and an increase in the A_3 ($\Delta A_3 = 140$ MHz) relative to the unbound $[Cu(NO_3)_2]$ salt in the $CHCl_3$:DMF solvent system. These shifts are indicative of the coordination of the **L_2** ligand. In comparison to the distorted square pyramidal $[Cu(\mathbf{L_1})](NO_3)_2$ complex, $[Cu(\mathbf{L_2})](NO_3)_2$ reveals a very small increase in the g_3 value

($\Delta g_3 = 0.009$) and has a similar A_3 value. This observation suggests either the axial coordination or at least weak interaction of one methylpyridine arm with the Cu^{2+} centre.[15,58] Mukhopadhyay *et al.*,[59] studied the structure of the Cu^{2+} tris(2-pyridyl)methyl)amine system, with additional coordinated N_3, *O*-NO or NCS, for the purpose of improving the one-electron reduction and two-electron oxidation potentials. They reported a pseudo octahedral geometry including one of N_3, *O*-NO or NCS. In that case, the tris(2-pyridylmethyl)amine **L₂** complex was always coordinated with three *N*-imine in the equatorial plane and one *N*-amine in the axial position. This observation by Mukhopadhyay *et al.*,[59] does suggest similar coordination for [Cu(**L₂**)]$(NO_3)_2$.

The ^{14}N superhyperfine splitting arising from the [Cu(**L₂**)]$(NO_3)_2$ complex are well resolved and are indicative of ^{14}N superhyperfine interactions from four equivalent nitrogen nuclei ($I = 1$). In the literature, it is commonly observed that the di(2-picolyl)amine ligand forms the base of the conformation and that the residues are either weakly interacting or coordinated perpendicular to the di(2-picolyl)amine base. [7,26–30] In addition, by examining the EPR spectra in Figure 6.9, no obvious indication is given that one ligand is coordinated and subsequently followed by a second ligand. For further clarification, X-ray and ^{14}N ENDOR studies need to be conducted to obtain not only the structural information but to also provide evidence of the inequivalent nitrogen atoms coordinated to Cu^{2+} centre.

Finally it should be noted, that for the [Cu(**L₂**)]$(NO_3)_2$ complex, the *g* and *A* values indicate a slight off axial symmetry towards rhombicity with the electron located in the d_{xy} ground state, giving rise to the observed EPR shape (Figure 6.9). To obtain more accurate *g* and *A* values, the W-band EPR spectrum need to be recorded. Owing to the magnitude of the g_3 and A_3 components, a considerable overshoot appears in the X-band spectrum (Figure E.2, Appendix). This complicates the extraction of the *g* values from X-band data alone.

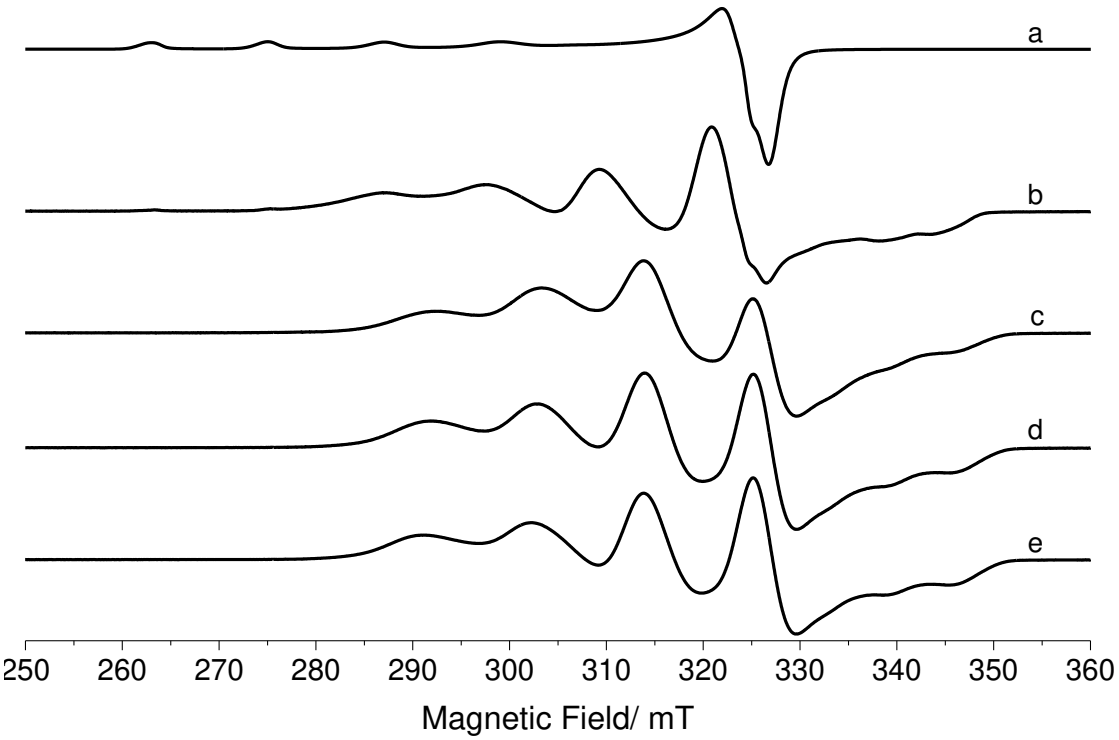

Figure 6.10 CW X-band (140 K) EPR spectra of $Cu(NO_3)_2$ with increasing ratios of the **L_3** ligand: a) 1:0, b) 1:1 c)1:5, d) 1:10, e) 1:50 dissolved in DMF:$CHCl_3$ (1:1).

The experimental CW X-band (140 K) EPR spectra of unbound [$Cu(NO_3)_2$], and the [$Cu(NO_3)_2$]:**L_3** complex bearing increasing ratios of 1:1,1:5, 1:10 and 1:50, dissolved in DMF:$CHCl_3$, are shown in Figure 6.10a-e. At a ratio of 1:1, it is evident that in addition of the copper salt other EPR signals are observed, indicating the formation of a new copper complex formed by coordination of tris(2-aminoethyl)amine **L_3** to the Cu^{2+} centre.

The resulting *g* and *A* values for the new complex are given by the approximate values of $g_1 = 2.09$, $g_2 = 2.19$, $g_3 = 2.00$ and $A_1 = 330$ MHz, $A_2 = 350$ MHz and $A_3 = 180$ MHz. In EPR, systems with well defined axial symmetry are characterised by the *g* values of $g_1=g_2\neq g_3$ (as explained earlier in Chapter 2). In cases where $g_{II}>g_{\perp}$, the symmetry of the complex is usually characterised as pyramidal, octahedral, square planar or square pyramidal. In the current case, the reversed **g** tensor are observed with $g_{II}<g_{\perp}$ and this is typical of a complex bearing a trigonal bipyramidal geometry with a ground state of d_{z^2}.[50,51,60] Further EPR studies such as CW ENDOR and CW W-band EPR need to be carried out to obtain structural information of this complex. An EPR and ENDOR study of related trigonal bipyramidal copper complexes was already reported by Ehsan *et al.*[61] for a series of nitrogen donor tripodal ligands. They

reported that the ligand field at the fifth coordination position affects all of the coordination bonds as well as the spin distribution among the ligands. These ligand field effects on the electronic structures were discussed in reference to the ligand field parameters obtained by EPR.

6.4 Conclusion

Copper complexes with nitrogen based multidentate ligands have been investigated by EPR spectroscopy. In this study, the focus was on three multidentate nitrogen based ligands including di(2-picolyl)amine **L_1**, tris(2-pyridylmethyl)amine **L_2** and tris(2-aminoethyl)amine **L_3**, with the aim to study the mixed nitrogen donor influence on the Cu^{2+} centre using EPR spectroscopy.

The [Cu(**L_1**)]$(NO_3)_2$ complex (Cu^{2+}:**L_1** ratio of 1:1) was characterised by the spin Hamiltonian parameters of $g_1 = 2.060$, $g_2 = 2.068$ and $g_3 = 2.253$ with well resolved ^{14}N superhyperfine interactions to three nitrogen donor groups. ^{14}N CW ENDOR measurements revealed that two different types of nitrogen donors are coordinated to Cu^{2+} (Figure 6.7a), namely the *N*-amine and *N*-imine from the **L_1** ligand (Scheme 6.2). Owing to the overlapping spectra, the spectra could not be reliably simulated. Additionally, the ^1H CW ENDOR spectra of [Cu(**L_1**)]$(NO_3)_2$ also revealed the presence of the coordinated ligand, due to the detection of the characteristic *H*-imine coupling (Figure 6.8 and Figure E.4, Appendix).[25,44,47,52]

For the [Cu(**L_2**)]$(NO_3)_2$ and [Cu(**L_3**)]$(NO_3)_2$ complexes, both were formed at a ratio of 1:50. The ligands **L_2** and **L_3** are similar in structure, however the coordination modes to the copper centre are very different; for [Cu(**L_2**)]$(NO_3)_2$ a d_{xy} ground state occurs, whereas for [Cu(**L_3**)]$(NO_3)_2$ a d_{z^2} ground state is observed (Figure 6.9 and 6.11).

The EPR and ENDOR data presented in this Chapter have been surprisingly difficult to interpret. In previous chapters, a single equivalent nitrogen environment was observed. In the cast of the current multidentate ligands, containing both *N*-imide and *N*-amine nitrogen centres, the resulting spectra are deceptively difficult to analysis. Several of the described complexes have shown evidence for a rhombic distortion and therefore this would need to be investigated using higher frequencies. In the case of [Cu(**L_2**)]$(NO_3)_2$ and [Cu(**L_3**)]$(NO_3)_2$,

further CW and pulsed ENDOR measurements are required to gain further in depth knowledge. To further clarify the mixed nitrogen nature of [Cu(**L**$_1$)](NO$_3$)$_2$ and the other complexes, DFT calculations are also required to complete this study.

6.5 References

1. J. C.Knight, A. J. Amoroso, , P. G. Edwards, , N. Singh, B. D.Ward, *Dalt. Trans.*, **2016**, 45**,** 10630–10642.
2. M. A. Abdulmalic, M. Fronk, B. Bräuer, D. R. T. Zahn, *J. Magn. Magn. Mater.*, **2016**, 419, 17–28.
3. S. J. Smith, R. A. Peralta, R. Jovito, Jr. A. Horn, A. J. Bortoluzzi, C. J. Noble, G. R. Hanson, R. Stranger, V. Jayaratne, G. Cavigliasso, L. R. Gahan, G Schenk, O. R. Nascimento, A. Cavalett, T. Bortolotto, G. Razzera, H. Terenzi, A. Neves, M. J. Riley, *Inorg. Chem.*, **2012**, 51, 2065–2078.
4. Xue, L., Wang, H. H., Wang, X. J. & Jiang, H. *Inorg. Chem.*, **2008**, 47, 4310–4318.
5. J. Krahmer, J., H. Broda, C. Näther, G. Peters, W. Thimm and F. Tuczek, *Eur. J. Inorg. Chem.*, **2011**, 28, 4377–4386.
6. H. E. Wang, M. C. Cheng, S. M. Peng, and S. T. Liu, *Acta Crystallogr. C Struct. Chem.*, **1995**, 51, 198–200.
7. J. England, R. Gondhia, L. Bigorra-Lopez, A. R. Petersen, A. J. P. White and G. J. P. Britovsek, *Dalton Trans.*, **2009**, 27, 5319-5334.
8. D. R., van Staveren, N., Metzler-Nolte, *Chem. Commun.*, **2002**, 13,1406-1407.
9. I. Caretti,E. Carter,I. A. Fallis, D. M. Murphy, S. Van Doorslaer, *Phys. Chem. Chem. Phys.*, **2011**, 13, 45, 20427-20434.
10. R. Viswanathan, M. Palaniandavar , *J. Chem. Soc. Dalton Trans.*, **1995**, 8, 1259–1266.
11. R. Soltek, G. Huttner, L. Zsolnai, A. Driess, *Inorganic Chimica Acta*, **1998**, 269, 143–156.
12. S. T. Liu, H. E. Wang, M. C. Cheng, S. M. Peng, *J. Organomet. Chem.*, **1989**, 376, 333–342.
13. Y. Gou, Z. Zhang, J. Qi, S. Liang, Z. Zhou, F. Yang, H. Liang, *J. Inorg. Biochem.*, **2015**, 153, 13–22.
14. A. Petuker, P. Gerschel, S. Piontek, N. Ritterskamp, F. Wittkamp, L. Iffland, R. Miller, M. van Gastel, U.-P- Apfel, *Dalton Trans.*, **2017**, 46, 13251–1326.
15. A. Petuker, K. Merz, C. Merten, U.-P. Apfel, *Inorg. Chem.*, **2016**, 55, 1183-1191.
16. A. Petuker, M. L. Reback, U.-P. Apfel, *Eur. J. Inorg. Chem.*, **2017**, 3295-3301.
17. M. J. Zaworotko, *Angew. Chemie - Int. Ed.* **2000**, 39, 3052–3054.18. B. Moulton, M. J. Zaworotko, *Chem. Rev.*, **2001**, 101, 1629–1658.
19. W. M. Teles,R. de A. Farani, M. I. Yoshida, A. J. Bortoluzzi, M. Hörner, L. F. de Oliveira, F. C. Machado, *Polyhedron*, **2007**, 26, 1469–1475.
20. E. E. B. De Paula, L. C. Visentin, M. I. Yoshida, L. F. C De Oliveira, F. C. MacHado, *Polyhedron*, **2011**, 30, 213–220.
21. C. M. Da Silva, D. L. da Silva, L. V. Modolo, R. B. Alves, M. A. de Resende,

C. V. B. Martins, A. de Fatima, *J. Adv. Res.*, **2011**, 2, 1–8.
22. L. Pickart, W.H. Goodwin, W. Burgua, T.B. Murphy, D. Johnson, *Biochem. Pharmacol.*, **1983**, 3868–3871.
23. M. Mohan, A. Kumar, M. Kumar, *Inorganica Chimica Acta*, **1987**, 136, 65-74.
24. K. M. Ananth, M. Kanthimathi, B. U. Nair, *Inorg. Chem.*, **2011**, 50, 6944–6955.
25. D. M. Murphy, I. Caretti, E. Carter, I. A. Fallis, M. C. Göbel, J. Landon, S. van Doorslaer, D. J. Willock, *Inorg. Chem.*, **2011**, 50, 6944–6955.
26. R. S. Rarig, J. Zubieta, *J. Solid State Chem.*, **2002**, 167, 370–375.
27. R. Silavi, A. Divsalar, A. A Saboury, *J. Biomol. Struct. Dyn.*, **2012**, 30, 752–772.
28. J. Masternak, M. Zienkiewicz-Machnik, K. Kazimierczuk, B. Barszcz, *Polyhedron*, **2018**, 142, 93-104.
29. S. Maity, S. Kundu, T. Weyhermüller, P. Ghosh, *Inorg. Chem.*, **2015**, 54, 1300–1313.
30. Y. Gultneh, B. Ahvazi, Y. T. Tesema, T. B. Yisgedu, R. J. Butcher, *J. Coord. Chem.*, **2006**, 59, 1835–1846.
31. N.-D. Sung, K.-Y. Choi, H.-H. Lee, K.-C. Lee, M.-J. Kim, *Transit. Met. Chem.*, **2005**, 30, 273–277.
32. K. Choi, Ryu, H., Sung, N. & Suh, M., *J. Chem. Crystallogr.*, **2003**, 33, 0-3.
33. G.-S. Huang, J.-K. Lai, C.-H. Ueng, C.-C. Su, *Transit. Met. Chem.*, **2000**, 25, 84–92.
34. G.-S.Huang, C.-C. Su, S.-L. Wang, F.-L. Liao, K.-J. Lin, *J. Coord. Chem.*, **2000**, 49, 211–226.
35. K.-Y. Choi, , Kim, B.-R. Ko, *J. Chem. Crystallogr.*, **2007**, 37, 847–852.
36. J. Spencer, J. Stevens, C. Perry, D. M. Murphy, *Inorg. Chem.*, **2018**, 57, 10857–10866.
37. M. Palaniandavar, R. J. Butcher, A. W. Addison, *Inorg. Chem.*, **1996**, 35, 467–471.
38. J. H. Kwon, H. J. Park, N. Chitrapriya, T.-S. Cho, S. Kim, J. Kim, I. H. Hwang, C. Kim, S. K. Kim, *J. Inorg. Biochem.*, **2014**, 131, 79–86.
39. N. Niklas, F. Hampel, G. Liehr, A. Zahl, R. Alsfasser, *Chem. Eur. J.*, **2001**, 7, 5135–5142.
40. L. Carlucci, G. Ciani, S. Maggini, D. M. Proserpio, R. Sessoli, F. Totti, *Inorganica Chimica Acta*, **2011**, 376, 538–548.
41. Olivo, G., M. Nardi, D. Vidal, Barbieri, A, A. Lapi, L. Gomez, O. Lanzalunga, M. Costas, S. Di Stefano, *Inorg. Chem.*, **2015**, 54, 10141–10152.
42. M. Palaniandavar, S. Mahadcvan, M. Köckerling, G. Henkel, *J. Chem. Soc. Dalton Trans.*, **2000**, 2, 1151–1154.
43. K. M. Sharples, E. Carter, C. E. Hughes, K. D. M. Harris, J. A. Platts, D. M. Murphy, *Phys. Chem. Chem. Phys.*, **2013**, 15, 15214–15222.
44. N. Ritterskamp, K. Sharples, E. Richards, A. Follis, M. Chiesa, J. A. Platts, D. M. Murphy, *Inorg. Chem.*, **2017**, 56, 11862–11875.
45. E. Carter, K. M. Sharples, J. A. Platts, D. M. Murphy, *Phys. Chem. Chem. Phys.*, **2015**, 17, 11445.
46. M. E. Owen, E. Carter, G. J. Hutchings, B. D. Ward, D. M. Murphy, *Dalton Trans.*, **2012**, 41, 11085–11092.
47. E. Carter, E. L. Hazeland, D. M. Murphy, B. D. Ward, *Dalton Trans.*, **2013**, 42, 15088.
48. R. Rajan, *J. Chem. Phys.*, **1962**, 37, 1901.

49. V. D. Dolzhenko, N. M. Kurnosov, S. I. Troyanov, Z. Anorg. *Allg. Chem.*, **2014**, 640, 347–351.
50. S. Pandey, P. P. Das, A. K. Singh, R. Mukherjee, *Dalton Trans.*, **2011**, 40, 10758.
51. V. Chechik, E. Carter, D. M. Murphy, Electron Paramagnetic Resonance. *Oxford Chemistry Primers*, **2016**.
52. K. M Sharples, PhD thesis: Structural Characterisation of Cu II Complexes of Biological Relevance and EPR and ENDOR investigation, *Cardiff University*, **2014**.
53. D. J. Awad, F. Conrad, A. Koch, A. Friedrich, A. Pöppl, P. Strauch, *Z. Naturforsch.*, **2010**, 65b, 1121–1127.
54. I. Masamoto, K. Takanori, S. Kita, *Inorg. Chem.*, **1986**, 25, 1546–1550.
55. C. Finazzo, C. Calle, S. Stoll, S. Van Doorslaer, A. Schweiger, *Phys. Chem. Chem. Phys.*, **2006**, 8, 1942–53.
56. D. M. Murphy, R. D. Farley, *Chem. Soc. Rev.*, **2006**, 35, 249–268.
57. H. L. Van Camp, R. H. Sands, J. A. Fee, *J. Chem. Phys.*, **1981**, 75, 2098-2107.
58. E.Carter, K. J. Cavell, W. F. Gabrielli, M. J. Hanton, A. J. Hallett, L. McDyre, J. A. Platts, D. M. Smith, D. M. Murphy,*Organometallics*, **2013**,1924-1931.
59. U. Mukhopadhyay, I. Bernal, S. S. Massoud, F. A. Mautner, *Inorganica Chim. Acta*, **2004**, 357, 3673–3682.
60. B. Murphy, B. Hathaway, *Coord. Chem. Rev.*, **2003**, 243, 237–262.
61. M. Q., Ehsan, , Y. Ohba, , S. Yamauchi, M. Iwaizumi, *Bull. Chem. Soc. Jpn.*, **1996**, 69, 2201–2209.

Chapter 7: Conclusion

Copper has two important oxidation states, namely Cu^{1+} and Cu^{2+}, which play a significant and considerable role in catalytic and biological processes, ranging from copper based enzymes or drugs to industrial or pharmaceutical catalysts. A brief introduction and overview on the general relevance and importance of Cu^{2+} based complexes, with particular relevance to catalysis was given in Chapter 1.

A particular series of Cu^{2+} complexes which have been investigated in this thesis are essentially based on planar compounds, primarily interacting with nitrogen bases that are relevant to biology, or ligands bearing mixed nitrogen functional groups that are coordinated to the Cu^{2+} centre. All these complexes are paramagnetic and therefore are readily studied by EPR spectroscopy. EPR spectroscopy, and the related hyperfine techniques, is a powerful method to study the electronic and geometric structure of these Cu^{2+} complexes, enabling one to obtain not only the information on the local Cu^{2+} centre, and inner coordination sphere, but also the long-range superhyperfine information in the outer coordination sphere of the complex. Both EPR and ENDOR techniques, presented in Chapter 2, therefore offer a unique and unparalleled insight into the structure and electronic properties of paramagnetic (cooper) coordination compounds.

A detailed EPR, ENDOR and HYSCORE investigation of the simple $[Cu(acac)_2]$ complex interacting with an imidazole substrate to form a mono- and bis adduct $[Cu(acac)_2Im_{n=1,2}]$, was presented in Chapter 4. This study was conducted owing to the growing number of cytotoxic Cu^{2+} based complexes which actually contain the acetylacetonate ligand and therefore, a better understanding of how such complexes interact with imidazole (which itself represents the side chain moiety of the amino acid histidine), is extremely important and timely. The work conducted herein found that at a relatively low ratios of Cu to Im, a $[Cu(acac)_2Im_{n=1}]$ mono-adduct was formed as expected. The Im-substrate was found to coordinate to the Cu in the axial position, as confirmed by the small shift in the g_3 value ($\Delta g_z = 0.022$) and the concomitant decrease in the $^{Cu}A_3$ value ($\Delta A_z = 48$ MHz) relative to the unbound $[Cu(acac)_2]$ complex. However, at higher ratios of Cu to Im, a $[Cu(acac)_2Im_2]$ bis-adduct was formed, as instantly revealed

by the superhyperfine patterns observed in the CW EPR spectra, which were indicative to two strongly coordinating nitrogen nuclei. Different structural isomers of the $[Cu(acac)_2Im_2]$ bis-adduct are possible, and the detailed EPR, ENDOR and DFT study enabled us to determine which structure was most favourable in frozen solution; namely the *trans*-equatorial conformer. Three individual sets of ^1H tensors were identified from the ^1H ENDOR spectra and assigned to the H^2/H^4, H^5 and H^1 protons of the Im-substrate. These values were consistent with either a *cis*-mixed plane or *trans*-equatorial structure for $[Cu(acac)_2Im_2]$. However, angular selective ^{14}N ENDOR (both CW and pulsed) provided more detailed insights into the hyperfine and quadrupole values for the coordinating imino N^3 nitrogen, and these parameters were in excellent agreement with the geometry optimized structure for the *trans*-equatorial $[Cu(acac)_2Im_2]$ adduct only. Equally, the hyperfine and quadrupole values for the remote ^{14}N amine nucleus were determined, by simulation of the X-band HYSCORE spectra, and a reasonably good agreement was achieved between theory and experiment. The consequence of these findings from a drug-discovery and design perspective, is that the ability of the coordinating ligand in these commonly used Cu-acac based complexes to flip between *cis*- and *trans*-conformations (*i.e.,* from unbound to Im-bound adducts) must therefore be considered when designing novel cytotoxic Cu^{2+} based complexes for target interactions with proteins bearing imidazole residues owing to this ligand flexibility.

The interaction of simple nitrogen bases coordinating to copper complexes was also explored in Chapter 5, specifically focussing on casiopeina type complexes, which have an important role as potential anticancer drugs. A series of casiopeina complexes with the general formula $[Cu(acac)(N\text{-}N)]^+$ were prepared, and their electronic and structural properties were thoroughly examined using EPR and ENDOR spectroscopy. Within the series of complexes studied, the diimine ligand (N-N) was systematically varied in size using 2,2'-bipyridine (bipy), 1,10-phenanthroline (phen), dipyridophenazine (dppz) and a pyridine substituted 2,2'-bipyridine ligand (Py-bipy). These diimine ligands were selected in light of the fact that the size of the aromatic diimine ligand may influence the therapeutic activity. The EPR spectra were characterised by rhombic *g* and *A* values for $[Cu(acac)(\mathbf{1})]^+$ and $[Cu(acac)(\mathbf{2})]^+$, with predominantly axial parameters for $[Cu(acac)(\mathbf{3})]^+$ and $[Cu(acac)(\mathbf{4})]^+$, indicating that the size of

the diimine ligand can influence symmetry around the copper centre. A very small distortion away from the expected square planar geometry therefore occurs, which was only detected by W-band EPR. Differences between the four complexes were also detected in the ^{1}H ENDOR data. The magnitude of the largest imine hyperfine coupling was found to be sensitive to size and degree of conjugation of the diimine ligand. Larger couplings were observed for smaller aromatic ring systems, *i.e.,* bipy, due to the restricted spin delocalisation. Smaller couplings were observed for larger aromatics ligands (*i.e.,* dppz), where spin delocalisation is clearly more diffuse. This observation was confirmed by ^{14}N ENDOR measurement, revealing a decrease of the largest $^{14N}A_3$ coupling for the [Cu(acac)(**1-4**)]$^{+}$, from 40 MHz (bipy), to 38.7 MHz (phen), to 38,8 MHz (dppz) and to 39.1 MHz (Py-bipy).

This spin distribution in the diimine ligands could provide valuable information on the nature of the DNA intercalation. The π-π interactions involved in the intercalation are likely to be influenced by the extent of spin density distribution onto the ligands, as evidenced by ENDOR spectroscopy. The interaction of these complexes with heterocycle nitrogen based substrates (including imidazole and L-histidine) was also investigated. Unlike the case for [Cu(acac)$_2$], where some degree of ligand rearrangement occurred from cis- to trans- arrangement, the interaction of Im and L-His with [Cu(acac)(N-N)]$^{+}$ was very weak and occurred along the unique axial direction. No such ligand flexibility or rearrangements occur with [Cu(acac)(N-N)]$^{+}$, even in the case of potentially strongly coordinating substrates such as Im.

Copper nitrogen based multidentate ligand complexes have been widely investigated by EPR spectroscopy over the years. In Chapter 6, three multidentate nitrogen ligands, including di(2-picolyl)amine, tris(2-pyridyl-methyl)amine and tris(2-aminoethyl)amine, were studied by EPR and ENDOR spectroscopy. The primary focus and aim of this investigation was to utilise ENDOR spectroscopy to examine copper complexes bearing inequivalent coordinated nitrogen nuclei. The [Cu(di(2-picolyl)amine)](NO$_3$)$_2$ complex was prepared in solution and studied by EPR and ENDOR. Differences between the coordinated *N*-Imine and *N*-Amine groups of the complex, [Cu(di(2-picolyl)amine)](NO$_3$)$_2$ were clearly detected in the ^{14}N ENDOR spectra, since it is known that these two sets of ^{14}N environments produce difference ^{N}A and ^{N}Q

values. Despite this knowledge, a reliable simulation of the experimental ^{14}N ENDOR spectra could not be achieved, indicating a subtle variance in the expected couplings for pure *N*-Imine and *N*-Amine nitrogen nuclei in these multidentate ligands. The complexes [Cu(tris(2-pyridylmethyl)amine)]$(NO_3)_2$ and [Cu(tris(2-aminoethyl)amine)]$(NO_3)_2$ were also prepared and studied by EPR spectroscopy. The coordination modes for these two complexes were notably different, with the former producing the expected square planar type arrangement (characterised by a 'normal' Cu^{2+} EPR signal with $g_{\|} > g_{\perp}$, typical of a d_{xy} ground state) while the latter complex produced a trigonal bipyramidal arrangement (characterised by a reversed Cu^{2+} EPR signal with $g_{\|} < g_{\perp}$ typical of a d_{z^2} ground state).

In conclusion, EPR and ENDOR spectroscopies have been used to study a series of copper based complexes and their interaction with nitrogen based substrates. The broader context of this work comes from the growing relevance of copper complexes that are showing enormous potential as cytotoxic compounds. From a biological perspective, the subtle interactions of these complexes and the variable modes of coordination with biologically relevant bases, needs to be understood. EPR is one of the techniques that can provide this information. The more specific context of the Thesis, however, was to investigate in detail the electronic and structural aspects of various copper complexes including [Cu(acac)$_2$], [Cu(acac)(N-N)]$^+$ and the multidendtate ligand based complex [Cu(^{a}N-^{b}N-^{a}N)], and their interaction with target nitrogen bases. In most cases, the combined use of the EPR techniques including ENDOR and HYSCORE, complimented by DFT, is clearly necessary if not strongly advisable, when determining the structure of the complexes. For example with the [Cu(acac)$_2$Im$_2$] adduct, a variety of structural isomers can be formed in solution, and the combined use of advanced EPR techniques were necessary to unambiguously identify which isomer is present. With some complexes, particularly the family of [Cu(acac)(N-N)] systems, conventional X-band EPR is insufficient to reveal the subtle local distortions around the Cu^{2+} site, due to the different ligands. These complexes would all appear to possess a square planar arrangement, for high frequency EPR can detect the small deviations away from planarity. And finally, the variation in structure of copper complexes bearing

multidendate ligands can be readily examined by EPR, as shown for the family of mixed *N*-amine and *N*-imine ligands.

Overall the work presented in this Thesis has shown the value of advanced EPR spectroscopic techniques when probing the structure of a Cu^{2+} systems. In many cases, EPR is more effective than NMR or X-ray to determine the structure in frozen solutions, particularly when complimented by DFT calculations.

A: Appendix to Chapter 2

A.1. Character table for point group D_{4h}.[1]

D_{4h} (4/*mmm*)	E	$2C_4$	C_2	$2C_2'$	$2C_2''$	i	$2S_4$	σ_h	$2\sigma_v$	$2\sigma_d$		
A_{1g}	1	1	1	1	1	1	1	1	1	1		x^2+y^2, z^2
A_{2g}	1	1	1	−1	−1	1	1	1	−1	−1	R_z	
B_{1g}	1	−1	1	1	−1	1	−1	1	1	−1		x^2-y^2
B_{2g}	1	−1	1	−1	1	1	−1	1	−1	1		xy
E_g	2	0	−2	0	0	2	0	−2	0	0	(R_x, R_y)	(xz, yz)
A_{1u}	1	1	1	1	1	−1	−1	−1	−1	−1		
A_{2u}	1	1	1	−1	−1	−1	−1	−1	1	1	z	
B_{1u}	1	−1	1	1	−1	−1	1	−1	−1	1		
B_{2u}	1	−1	1	−1	1	−1	1	−1	1	−1		
E_u	2	0	−2	0	0	−2	0	2	0	0	(x, y)	

C: Appendix to Chapter 4

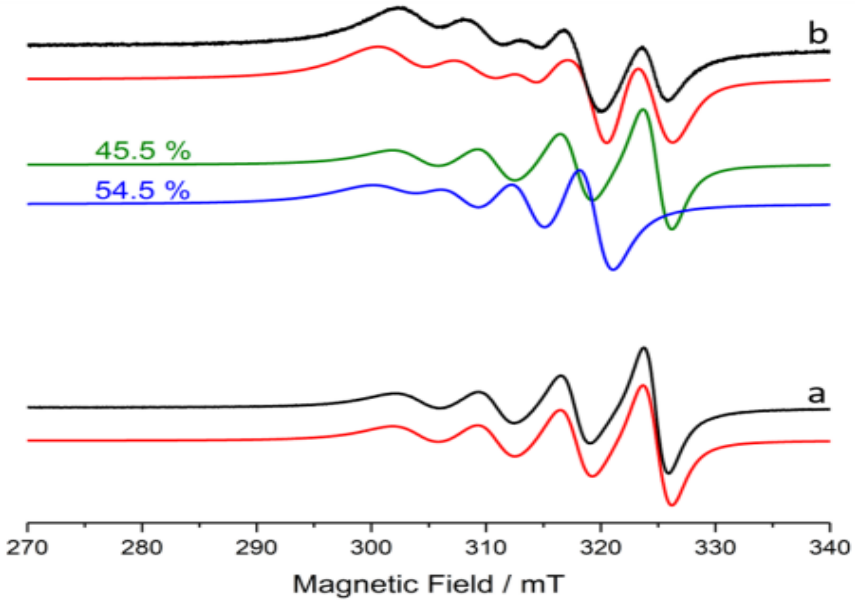

C.1 Experimental (black) and simulated (red) X-band CW EPR spectra (298 K) of $[Cu(acac)_2]$ recorded with a Cu:Im ratios of a) 1:0 and b) 1:10. The deconvoluted simulation of b), shown in the green and blue traces, is due to 45.5 % $[Cu(acac)_2]$ (green) and 54.5 % $[Cu(acac)_2Im]$ (blue). The spectra were recorded in a $CHCl_3$:DMF (1:1) solvent. The simulation parameters are listed in Table 4. 2 (Chapter 4)

C.2 Comment on the DFT energies and basis sets used:

Despite the excellent agreement between experimental data and theoretical prediction for the *trans*-equatorial coordination complex, the latter is predicted to lie ca. 23 kJ mol^{-1} higher in energy than the trans-axial coordination complex. We ascribe this discrepancy to the fact that functional (PBE0) and especially basis set used (EPRII for the light weight p-block elements and core-property CP for Cu) are designed to predict EPR-related properties (**g**-tensor and hyperfine coupling) rather than relative energies.

Cartesian coordinates of the geometry optimized complexes used for the DFT calculation of *g*, *A* and nuclear quadrupole values:

$Cu(acac)_2Im$

CARTESIAN COORDINATES (ANGSTROEM)

Cu	-0.036249	0.032810	-0.722325
O	-1.454303	1.392681	-0.508375
O	1.263384	1.399991	-1.288098
O	1.331577	-1.332404	-1.088392
O	-1.460440	-1.335745	-0.646979
C	-1.303791	2.648559	-0.608756
C	1.083245	2.650951	-1.289826
C	-2.543254	3.464890	-0.321116
H	-3.346446	3.131944	-0.984081
H	-2.867052	3.270560	0.706123
H	-2.379752	4.535503	-0.450944
C	2.283859	3.472889	-1.697265
H	3.104330	3.263296	-1.005135
H	2.607373	3.153984	-2.691837
H	2.076391	4.543757	-1.704746
C	-0.116751	3.309872	-0.957178
H	-0.132904	4.390864	-1.007063
C	-1.276170	-2.586592	-0.588435
C	1.176416	-2.583554	-0.970631
C	-0.036295	-3.241053	-0.698875
H	-0.023566	-4.320999	-0.628644
C	-2.528008	-3.411305	-0.395588
H	-3.221068	-3.193045	-1.212806
H	-2.324188	-4.482467	-0.364535
H	-3.014581	-3.103785	0.534439
C	2.428934	-3.405604	-1.169457
H	3.202551	-3.047023	-0.484890
H	2.260305	-4.471263	-1.008796
H	2.795645	-3.244276	-2.187293
N	0.286512	0.013340	1.525871
C	1.316414	-0.384777	2.340236
C	-0.728520	0.289189	2.311717
C	0.912824	-0.343079	3.647590
H	2.273853	-0.671665	1.931822
H	-1.699767	0.622964	1.972409
H	1.418811	-0.571518	4.571626
N	-0.394610	0.088514	3.611019
H	-0.998856	0.228448	4.405757

***Cis*-mixed plane $Cu(acac)_2Im_2$**

CARTESIAN COORDINATES (ANGSTROEM)

Cu	0.024584	0.123722	0.191301
N	0.365892	-0.651101	-2.000113
C	0.662054	-1.944169	-2.351524
C	0.054226	-0.025818	-3.109196
C	0.531774	-2.097144	-3.706144
H	0.937889	-2.664592	-1.595442
H	-0.241003	1.011508	-3.182204
H	0.670804	-2.943052	-4.359961
N	1.905853	1.001511	0.279943
C	2.266345	2.288446	-0.031500
C	2.986798	0.386712	0.701758
C	3.603041	2.451277	0.207183
H	1.530303	2.989721	-0.392897
H	3.022859	-0.643746	1.023570
H	4.260776	3.297821	0.096511
N	0.142667	-0.861883	-4.176923
H	-0.049284	-0.622188	-5.136772
N	4.044711	1.231084	0.672295
H	4.985811	1.003853	0.952630
O	-0.647614	1.832645	-0.577713
O	-1.800598	-0.713314	0.076298
O	-0.319138	0.552065	2.339210
O	0.822027	-1.613076	0.783811
C	-1.843438	2.059773	-0.942757
C	-2.827952	-0.168005	-0.396676
C	-2.907651	1.150471	-0.910539
H	-3.871080	1.491396	-1.268139
C	-4.078614	-1.020419	-0.395724
H	-3.875693	-1.941033	-0.950021
H	-4.306477	-1.304531	0.635479
H	-4.938835	-0.511048	-0.832623
C	-2.094308	3.460625	-1.458037
H	-3.107979	3.594078	-1.838821
H	-1.918578	4.169008	-0.642738
H	-1.372459	3.688512	-2.248466
C	-0.458274	-0.358992	3.179015
C	0.503063	-2.250669	1.844537
C	-0.093010	-1.726264	2.989975
H	-0.289398	-2.411816	3.805322
C	0.838492	-3.727184	1.808003
H	0.648062	-4.228755	2.758256
H	0.237013	-4.200621	1.025012
H	1.890332	-3.852507	1.533186
C	-1.066078	0.032817	4.514855
H	-2.083815	0.394559	4.340498
H	-1.093572	-0.790908	5.230562
H	-0.491901	0.864210	4.932723

***Trans*-equatorial $Cu(acac)_2Im_2$**

CARTESIAN COORDINATES (ANGSTROEM)

Cu	-0.000744	-0.001280	0.004396
O	-1.399157	1.531154	0.646834
O	1.513256	1.303701	0.446305
O	1.399250	-1.530899	-0.642224
O	-1.513748	-1.304143	-0.438613
C	-1.098235	2.735007	0.911312
C	1.409128	2.529838	0.774146
C	-2.243665	3.703788	1.175686
H	-2.166542	4.591700	0.530353
H	-3.202588	3.202086	0.994672
H	-2.215193	4.057090	2.217787
C	2.721141	3.283402	0.929659
H	3.563343	2.598019	0.777555
H	2.781000	4.100380	0.194967
H	2.789737	3.736358	1.929649
C	0.216920	3.250945	0.995077
H	0.323875	4.308323	1.247029
C	-1.411485	-2.527495	-0.777421
C	1.095182	-2.729579	-0.926001
C	-0.219837	-3.245417	-1.010688
H	-0.327069	-4.298859	-1.278320
C	-2.724196	-3.278332	-0.940023
H	-3.564571	-2.606285	-0.730642
H	-2.816045	-3.671080	-1.963430
H	-2.761843	-4.138140	-0.254737
C	2.239728	-3.697411	-1.198015
H	3.197726	-3.165763	-1.137885
H	2.235447	-4.518597	-0.464555
H	2.136827	-4.153761	-2.193970
N	0.052799	-0.701388	1.873148
C	1.027063	-1.480392	2.462836
C	-0.880104	-0.492358	2.792692
C	0.674471	-1.747310	3.762190
H	1.905713	-1.779131	1.905173
H	-1.779292	0.092594	2.635869
H	1.161772	-2.312487	4.546013
N	-0.540869	-1.111753	3.951612
H	-1.092180	-1.100936	4.801967
N	-0.051180	0.699033	-1.866235
C	-1.044495	1.440628	-2.471708
C	0.902918	0.523689	-2.770711
C	-0.682225	1.718942	-3.766024
H	-1.941618	1.708707	-1.927082
H	1.820965	-0.027556	-2.602425
H	-1.178035	2.264582	-4.558336
N	0.558565	1.128783	-3.935931
H	1.124217	1.136113	-4.776839

***Trans*-axial $Cu(acac)_2Im_2$**

CARTESIAN COORDINATES (ANGSTROEM)

Cu	-0.022628	0.029356	0.009025
O	0.011297	-1.365641	1.434212
O	0.391957	-1.304716	-1.420036
O	0.050631	1.442668	-1.402128
O	-0.521122	1.357976	1.419319
C	0.268762	-2.587806	1.248631
C	0.599604	-2.535130	-1.225420
C	0.256015	-3.444292	2.497299
H	0.475614	-4.493014	2.291864
H	0.991477	-3.048678	3.203778
H	-0.726616	-3.362083	2.970634
C	0.915863	-3.338728	-2.469142
H	0.076544	-3.255414	-3.165825
H	1.790091	-2.900422	-2.959082
H	1.107014	-4.391171	-2.254275
C	0.559279	-3.201075	0.014466
H	0.762087	-4.264512	0.018973
C	-0.657950	2.599600	1.233201
C	-0.167119	2.672522	-1.213170
C	-0.503212	3.281309	0.010864
H	-0.657277	4.352881	0.011852
C	-1.028801	3.397946	2.465245
H	-0.261864	3.243201	3.229278
H	-1.132552	4.464736	2.261535
H	-1.970878	3.012062	2.866503
C	-0.045419	3.543109	-2.445836
H	0.961664	3.433308	-2.859299
H	-0.748440	3.181386	-3.201462
H	-0.240015	4.596601	-2.239912
N	-2.314856	-0.332181	-0.279586
C	-3.092524	-0.746351	-1.330408
C	-3.109295	-0.241254	0.759627
C	-4.387842	-0.905994	-0.914727
H	-2.667353	-0.899588	-2.311239
H	-2.798678	0.057984	1.751421
H	-5.284654	-1.210538	-1.429711
N	-4.381598	-0.579991	0.423749
H	-5.175831	-0.592002	1.043992
N	2.284212	0.365538	0.284724
C	3.176050	0.187858	1.310936
C	2.995588	0.619256	-0.787481
C	4.455351	0.342745	0.847270
H	2.837816	-0.039964	2.310904
H	2.585488	0.797755	-1.772392
H	5.416961	0.282406	1.330997
N	4.322813	0.617125	-0.496311
H	5.073398	0.785732	-1.147363

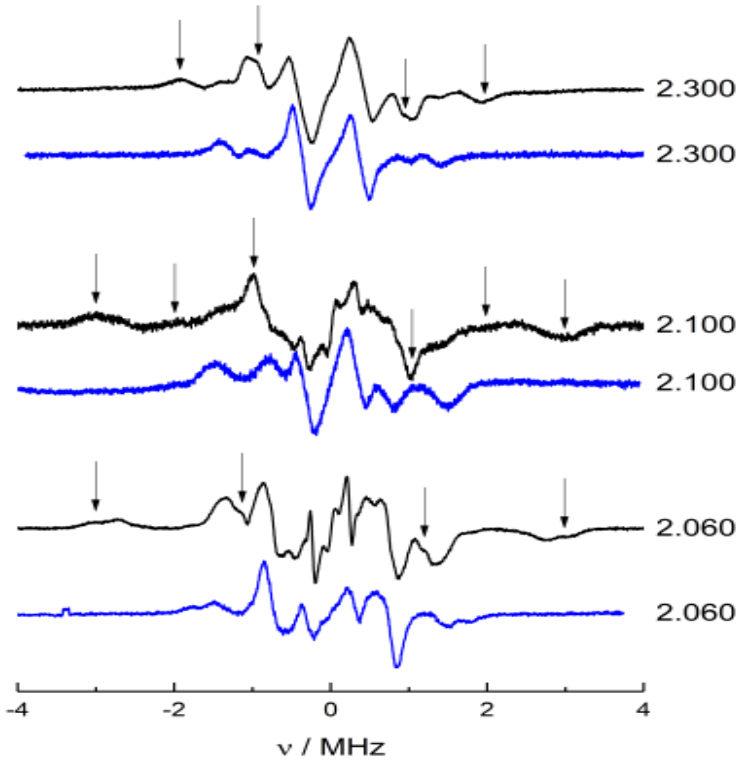

C.3 Q-band CW ^{1}H ENDOR spectra (10 K) of protic [Cu(acac)$_2$Im$_2$] (black) and deuterated [Cu(acac)$_2$(Im-d$_4$)$_2$] (blue) in CDCl$_3$:DMF-d$_7$ (1:1) recorded at the field positions corresponding to g = 2.300, 2.100, 2.060, indicated besides each spectrum. The imidazole derived ^{1}H ENDOR resonances are highlighted with the arrows.

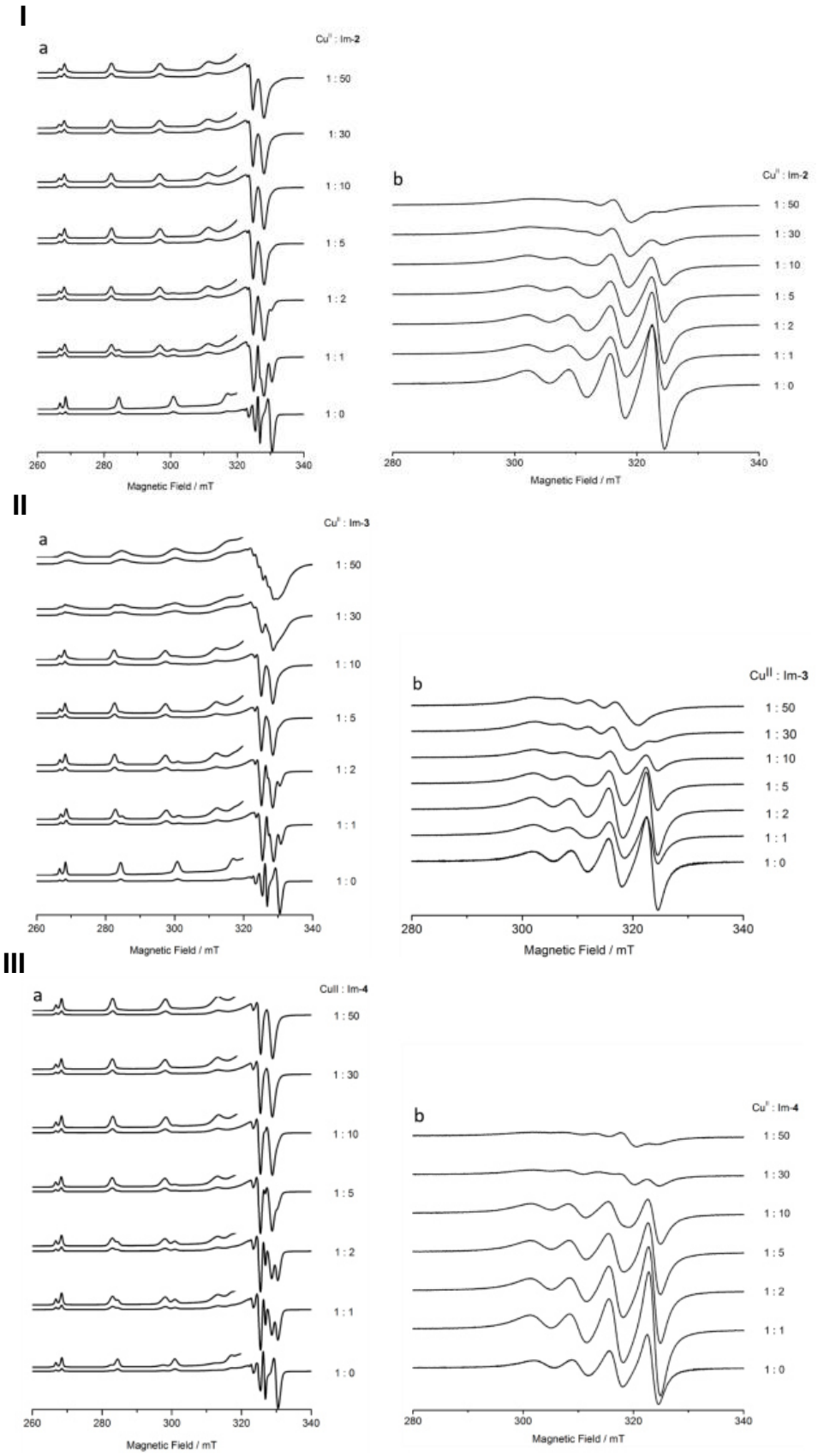

C.4 X-band CW EPR recorded a) 140 K and b) 298 K of [Cu(acac)$_2$] in the presence of increasing molar ratios of I) 2-methyl-imidazole (Im-**2**), II) 4(5)-methyl-imidazole (Im-**3**) and III) benzimidazole (Im-**4**).

D: Appendix to Chapter 5

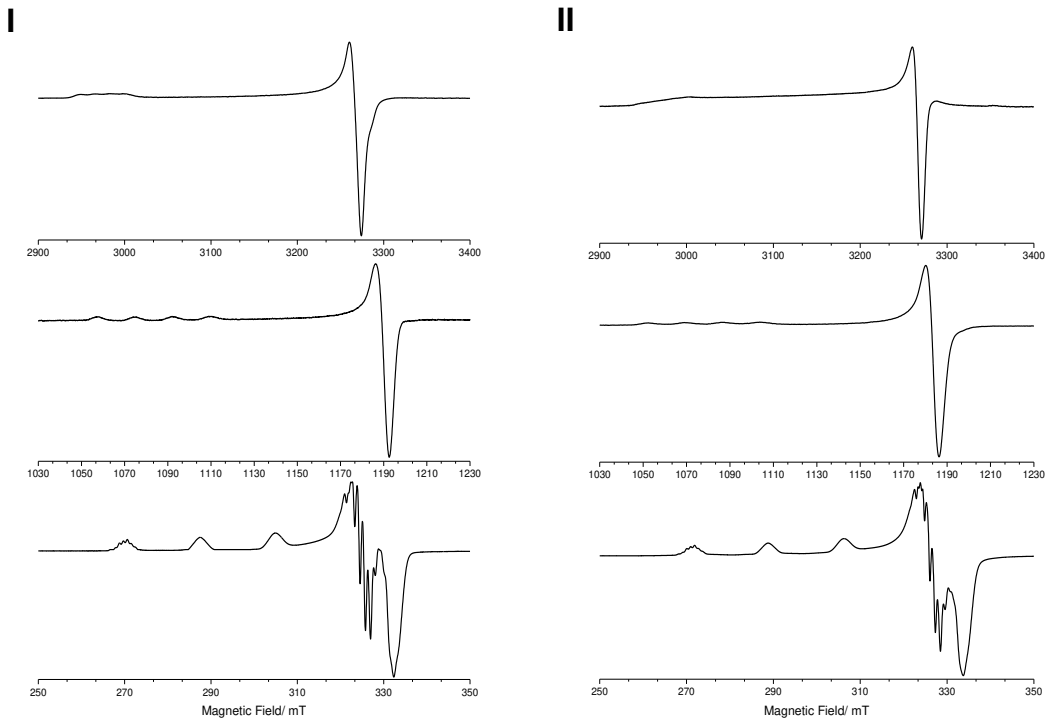

D.1 Multi-frequency CW EPR spectra of I) 1,10-phenanthroline (phen) [Cu(acac)(**2**)]$^{+}$ and II) dipyridophenazine (dppz) [Cu(acac)(**3**)]$^{+}$,recorded at X-, Q- and W-band frequency. All spectra measured at 10 K. All complexes dissolved in EtOH:DMF (1:1).

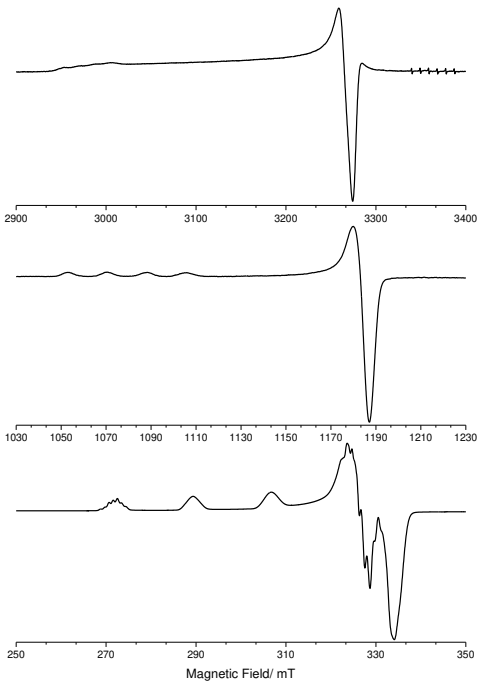

D.2 Multi-frequency CW EPR spectra of 2,3-bis(2-pyridyl)pyrazine (Py-bipy) [Cu(acac)(**4**)]$^{+}$ recorded at X-, Q- and W-band frequency. All spectra measured at 10 K. All complexes dissolved in EtOH:DMF (1:1).

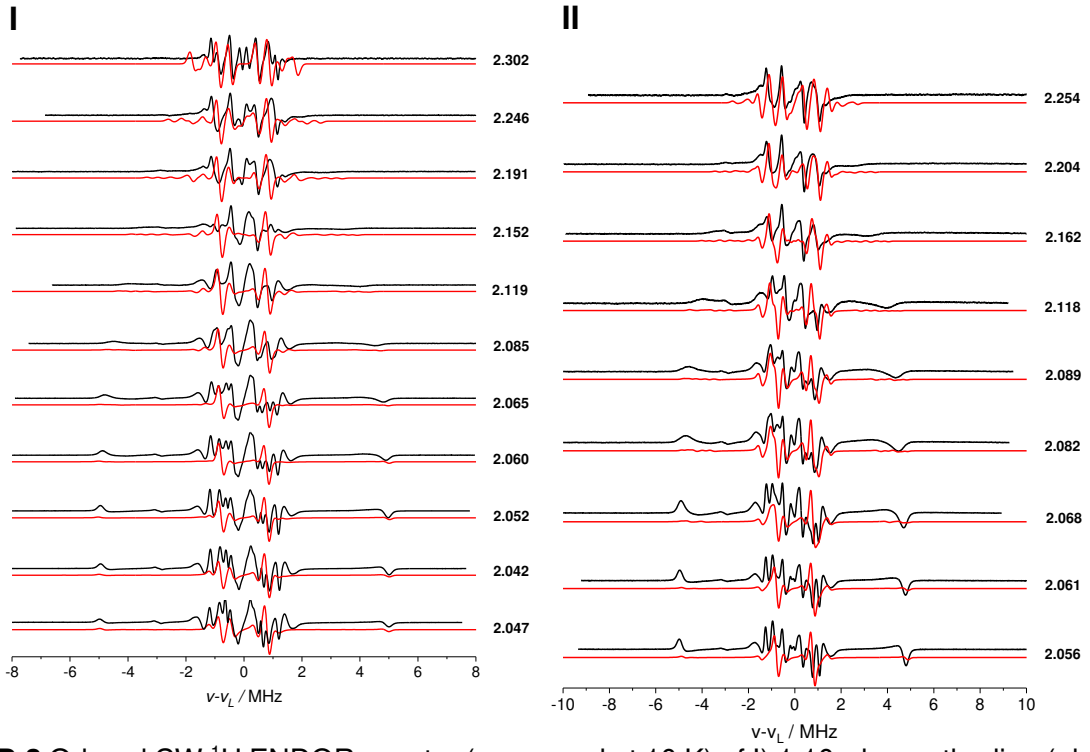

D.3 Q-band CW ^{1}H ENDOR spectra (measured at 10 K) of I) 1,10-phenanthroline (phen) [Cu(acac)(**2**)]$^{+}$ and II) of dipyridophenazine (dppz) [Cu(acac)(**3**)]$^{+}$, dissolved in EtOH:DMF (1:1) recorded at the field positions corresponding to the *g*-values indicated beside each spectrum. Corresponding simulations shown in red trace.

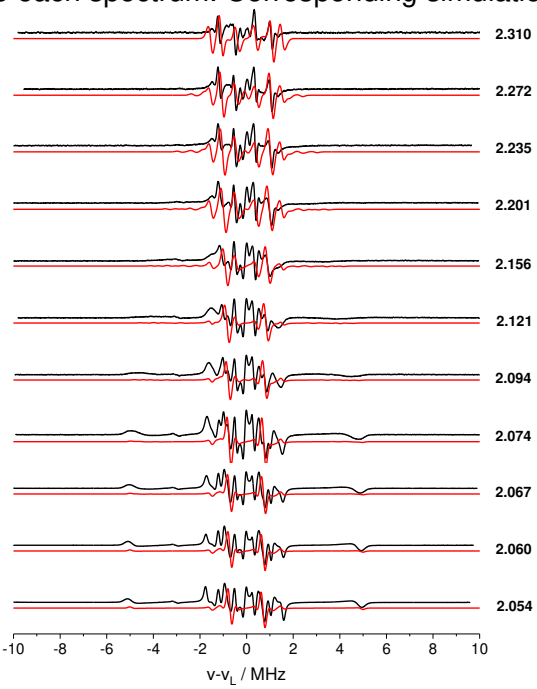

D.4 Q-band CW ^{1}H ENDOR spectra (measured at 10 K) of 2,3-bis(2-pyridyl)pyrazine (Py-bipy) [Cu(acac)(**4**)]$^{+}$ dissolved in EtOH:DMF (1:1) recorded at the field positions corresponding to the *g*-values indicated beside each spectrum shown in black. Corresponding simulations shown in red trace.

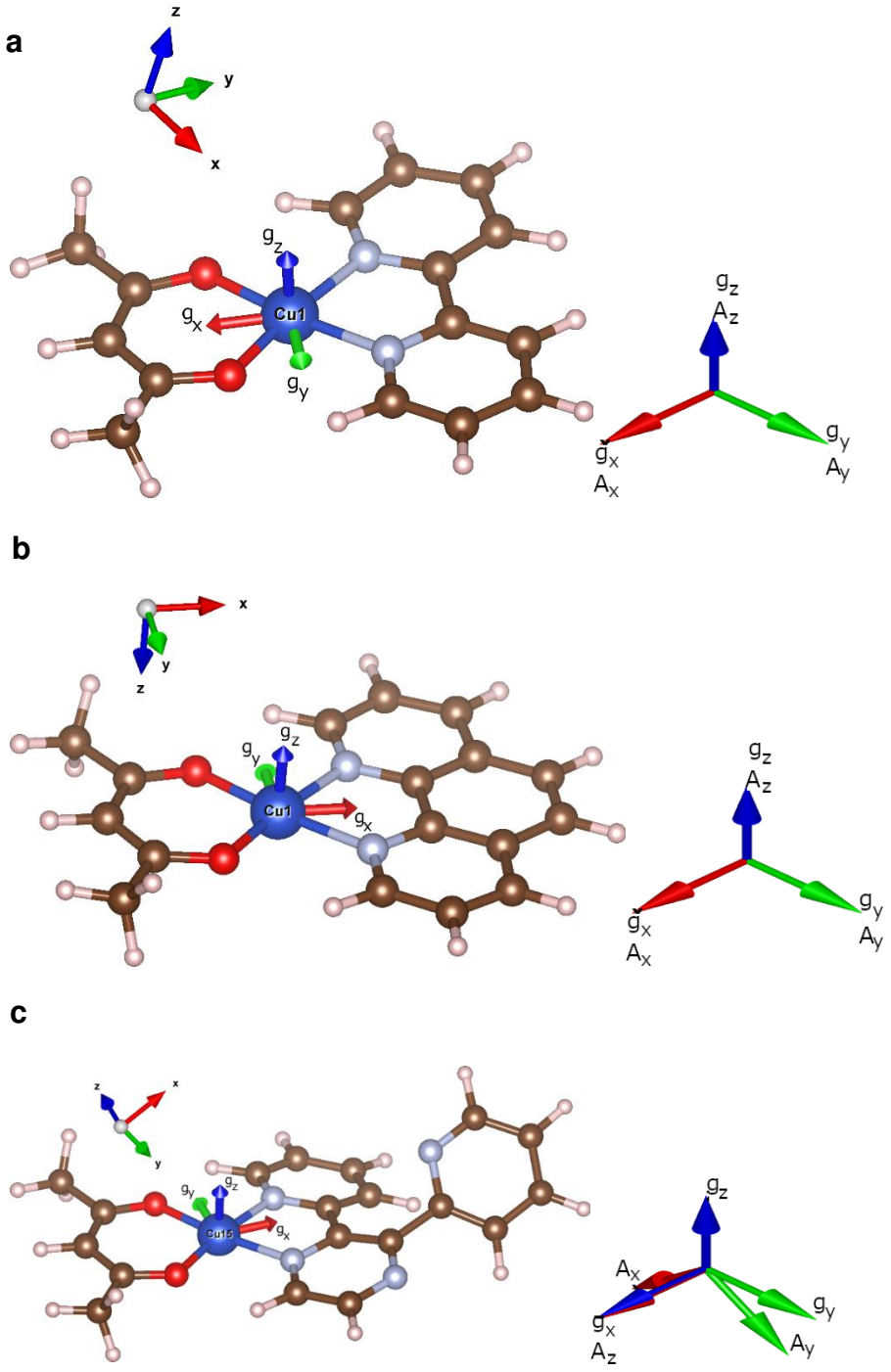

D.5 Geometry optimised structures for the complexes a) 2,2'-bipyridine (bipy) [Cu(acac)(**1**)]$^+$, b) 1,10-phenanthroline (phen) [Cu(acac)(**2**)]$^+$, and c) the pyridine substituted 2,2'-bipyridine (Py-bipy) [Cu(acac)(**4**)]$^+$. The *g*-frame is reported on the Cu atom with the same colour coding as the molecular frame on the right-hand side of the structure: *x* (red), *y* (green) and *z* (blue).

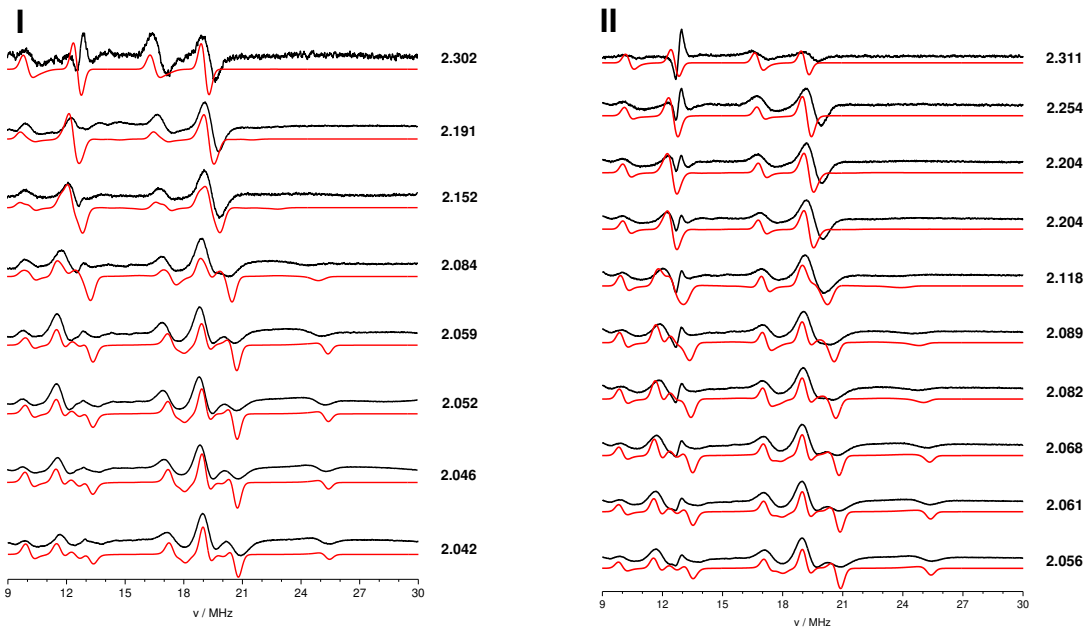

D.6 Q-band CW ^{14}N ENDOR spectra (measured at 10 K) of I) 1,10-phenanthroline (phen) [Cu(acac)(**2**)]$^{+}$ and II) dipyridophenazine (dppz) [Cu(acac)(**3**)]$^{+}$, dissolved in EtOH:DMF (1:1) recorded at the field positions corresponding to the *g*-values indicated beside each spectrum shown in black. Corresponding simulations shown in red trace.

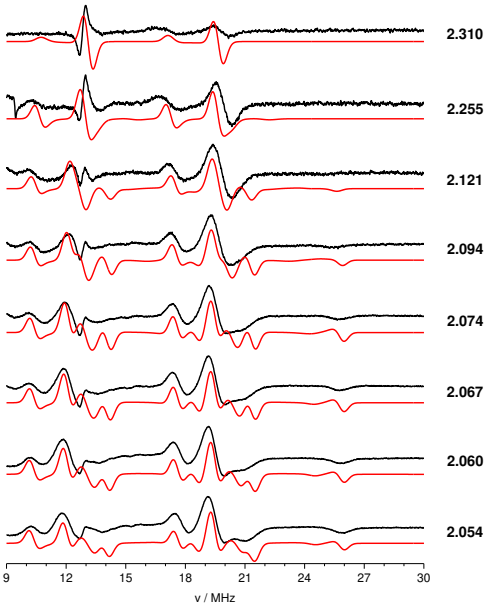

D.7 Q-band CW ^{14}N ENDOR spectra (measured at 10 K) of 2,3-bis(2-pyridyl)pyrazine (Py-bipy) [Cu(acac)(**4**)]$^{+}$ dissolved in EtOH:DMF (1:1) recorded at the field positions corresponding to the *g*-values indicated beside each spectrum shown in black. Corresponding simulations shown in red trace.

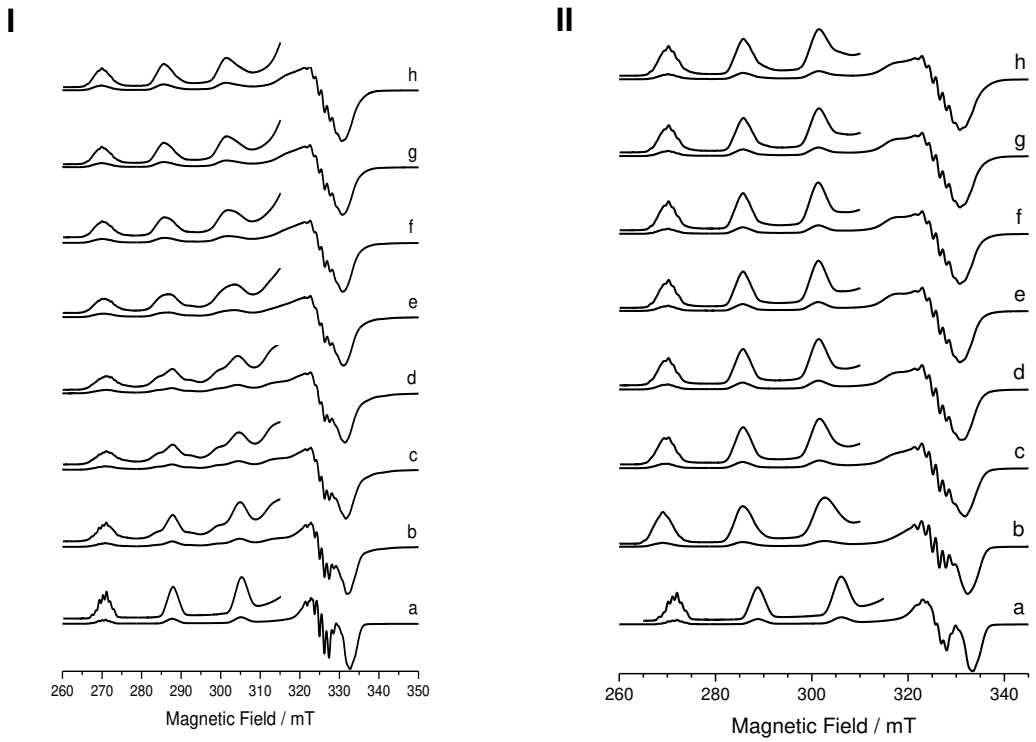

D.8 CW X-band EPR spectra (140 K) of I) $[Cu(acac)(\mathbf{2})]^+$ and II) $Cu(acac)(\mathbf{4})]^+$ recorded with increasing Cu:Im ratios (a) 1:0, (b) 1:2, (c) 1:5, (d) 1:10, (e) 1:30, (f) 1:50, (g) 1:70 and (h) 1:100.

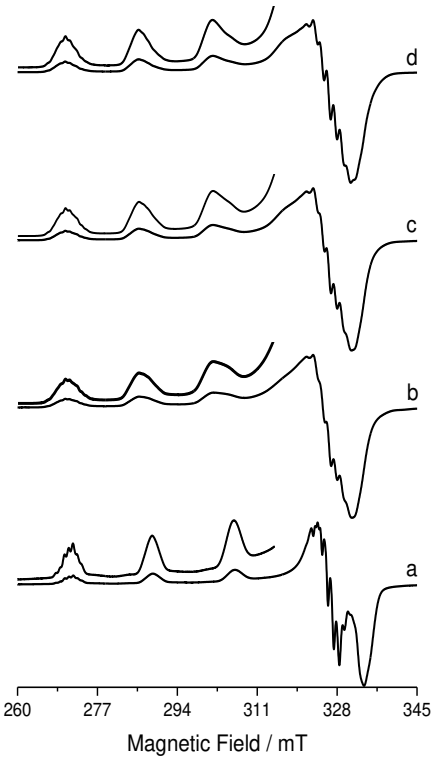

D.9 CW X-band EPR spectra (140 K) of I)$[Cu(acac)(\mathbf{3})]^+$ recorded with increasing Cu:Im ratios (a) 1:0, (b) 1:50, (c) 1:70 and (d) 1:100 and II) $[Cu(acac)(Py\text{-}bipy)]^+$ recorded with increasing Cu:Im ratios (a) 1:0, (b) 1:2, (c) 1:5, (d) 1:10, (e) 1:30, (f) 1:50, (g) 1:70 and (h) 1:100.

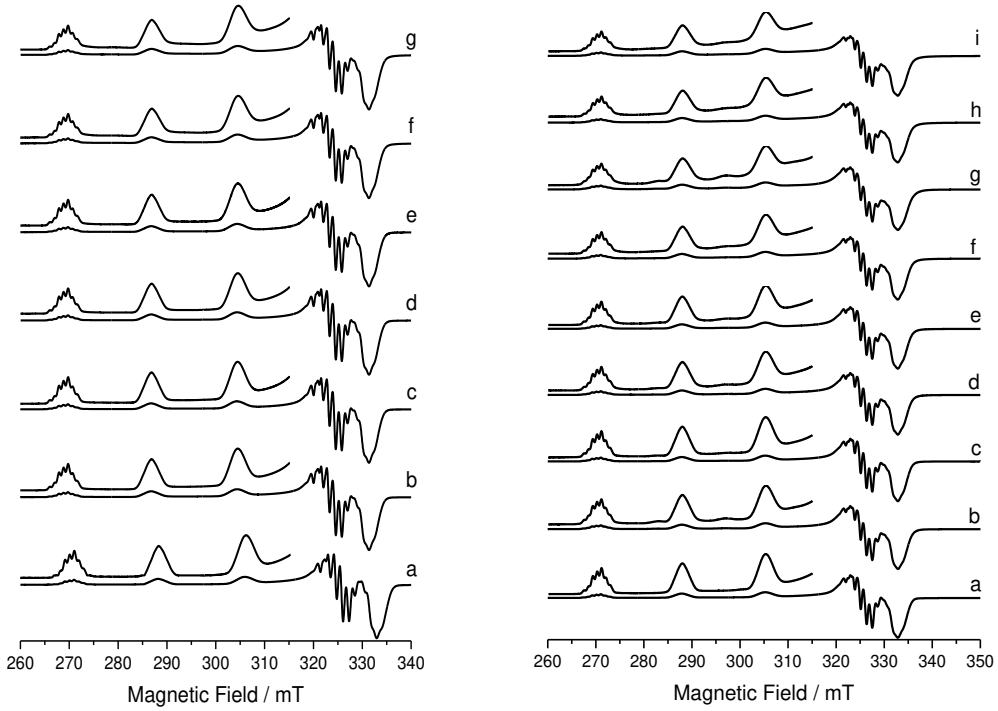

D.10 CW X-band EPR spectra (140 K) of I)[Cu(acac)(**1**)]$^{+}$ recorded with increasing Cu:L-His ratios (a) 1:0, (b) 1:1, (c) 1:2, (d) 1:5, e) 1:10, f) 1:30, g) 1:50 and II) [Cu(acac)(**2**)]$^{+}$ recorded with increasing Cu:L-his ratios (a) 1:0, (b) 1:1, (c) 1:2, (d) 1:5, e) 1:10, f) 1:30, g) 1:50, (h) 1:70 and (i) 1:100.

E: Appendix to Chapter 6

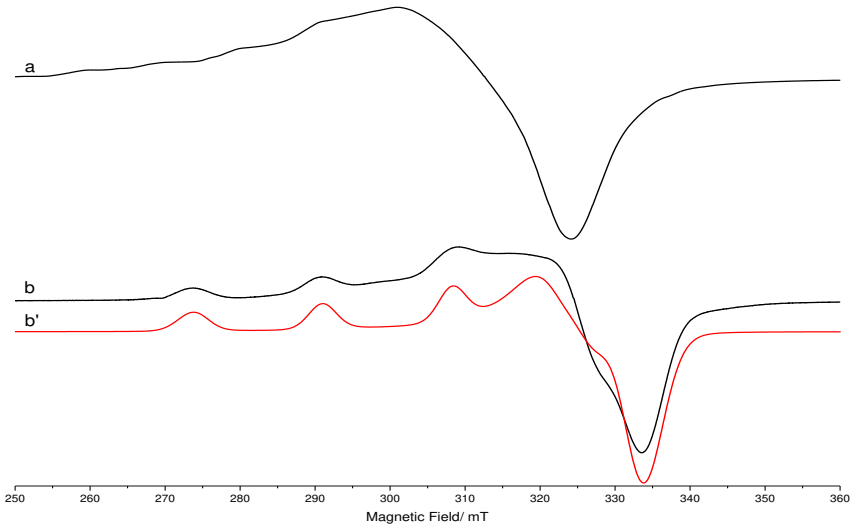

E.1 Experimental (black) and simulated (red) CW X-band EPR spectra of a) [$CuCl_2$] copper salt and b) the [Cu(**L_1**)Cl_2] complex (Cu:**L_1** ratio of 1:1). The spectra were recorded at 140 K in MeOH solvent. The simulation parameters are listed in Table 6. 1, Chapter 6.

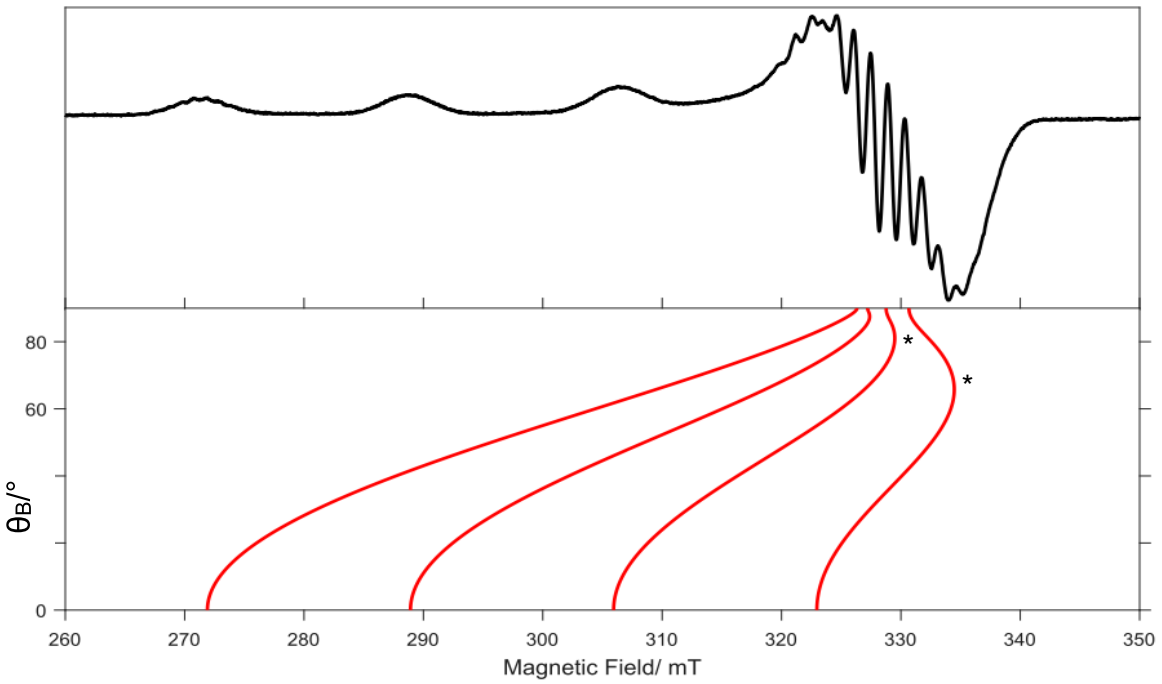

E.2 CW EPR spectra of [Cu(**L_2**)]$(NO_3)_2$ dissolved in DMF:CHI_3 (1:1), recorded at X-band and is given with the corresponding simulated roadmap (red) for [Cu(**L_2**)]$(NO_3)_2$. The overshoot features are highlighted with an asterisk (*).

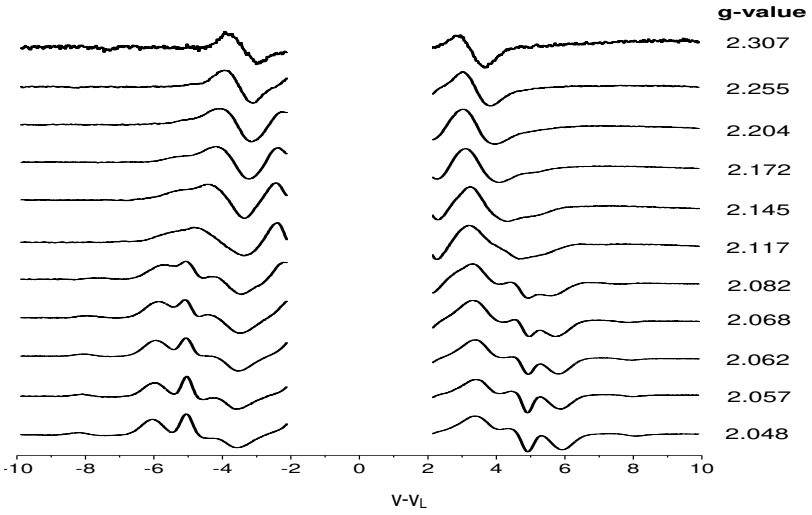

E.3 CW Q-band ^{1}H ENDOR spectra (10 K) showing the proton coupling" of [Cu(di(2-picolylamine)]$(NO_3)_2$ dissolved in DMF-d_7:$CDCl_3$. For clarity, the central part of the spectra, containing proton couplings from the remaining ligand nuclei have been removed.

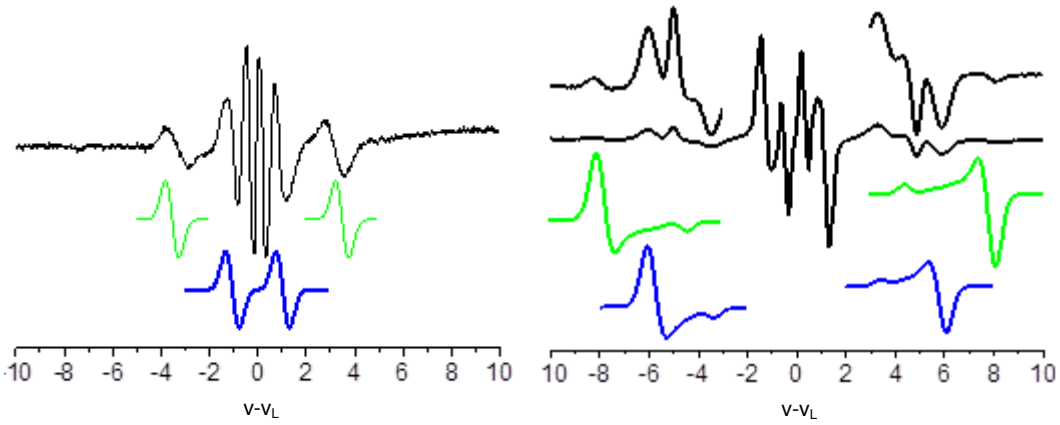

E.4 CW Q-band ^{1}H ENDOR spectra (10 K) of [Cu(L_1)]$(NO_3)_2$ dissolved in DMF-d_7:$CDCl_3$-d_1, recorded at field positions corresponding to a) $g_{//}$ = 2.307 and b) $g_{\perp}$ = 2.048. The simulation for ^{1}H protons of *H*-Imine (green) and *H*-amine (blue).